DEVELOPING THE ^{60}Fe-^{60}Ni SYSTEM FOR EARLY SOLAR SYSTEM CHRONOLOGY

A DISSERTATION SUBMITTED TO THE GRADUATE DIVISION OF THE UNIVERSITY OF HAWAIʻI AT MĀNOA IN PARTIAL FULFILLMENT OF THE REQUIREMENTS FOR THE DEGREE OF

DOCTOR OF PHILOSOPHY

IN

GEOLOGY AND GEOPHYSICS

AUGUST 2015

By:

Myriam Telus

Dissertation Committee:

Gary R. Huss, Chairperson
Kazuhide Nagashima
Alexander N. Krot
G. Jeffrey Taylor
Jonathan P. Williams

Keywords: iron, nickel, aluminum, magnesium, radionuclides, meteorites

To my husband Nathanael, my endless source of inspiration and joy

ACKNOWLEDGEMENTS

I am amazed by how enjoyable graduate school and working toward my Ph.D. has been. For this, I am especially thankful to my advisor Gary Huss. His patience and dedication to helping me grow as a scientist has made this such a rewarding experience. Thanks to all the members of our cosmochemistry group at UH. They are simply the best folks to work with. Thanks to Kazu Nagashima for patiently teaching me to use the ion probe, for working with me on all of my projects and for serving on my dissertation committee. Thanks to Ryan Ogliore for helping me understand proper SIMS data analysis and for traveling all the way to Australia to help with my synchrotron measurements. Thanks to Sasha Krot and Jeff Taylor for serving on my dissertation committee, eagerly discussing ideas with me and for helping me with various aspects of my research. Special thanks to Jonathan Williams, an honorary member of the cosmochemistry group, for hiking all the way from IFA for my dissertation committee meetings. Thanks to Ed Scott for helping with my work on H4 chondrites. Thanks to grad students, Christie Jilly and Caroline Caplan, former postdocs, Manavi Jadhav, Lydie Bonal, Kentaro Makide, Chung-kun Park and Trish Doyle and the assistant lab manager, Aurelien Thomen. They are all part of what makes the cosmochemistry group so special. Thanks to Eric Hellebrand, another honorary member of the group. He has helped all of us with our electron probe analyses. Thanks also to all of my other collaborators including Shogo Tachibana who helped with my Fe-Ni SIMS analyses; Daryl Howard, James Cleverley, and Andy Tomkins who helped with my proposal and analyses at the Australian Synchrotron; and Matt Newville who helped with my analyses at the Advanced Photon Source. I want to acknowledge that funding for my research and education are from

Gary's NASA grant (NNX11AG78G) and my NASA Earth & Space Science Fellowship (NNX11AN62H). Thanks to the Watamull Scholarship and the Gates Millennium Scholarship for their financial support. Thanks also to the Smithsonian and the Meteorite Working Group for supplying the samples for this research.

Many thanks to all the faculty and staff in GG and HIGP, especially Julia Hammer, Jeff Gillis-Davis, John Mahoney, and Przemyslaw Dera who have all helped in some form with my research or served on one of my committees. Thanks to all of the wonderful graduate students who gave me advice and helped me out along the way, especially Elise Rumpf, my wonderful officemate. Thanks also to my previous advisors from UChicago, Nicolas Dauphas, Andy Davis, and Mike Savina for encouraging me to pursue my Ph.D.

Finally, I am especially thankful for my husband Nathanael, my parents, my siblings, Josh, Jessica, Nadeige, Rose, and James, my uncle Yonel, and all of the friends I have made here in Hawaii, especially Ann, Wilfred, Polly, Grace, and Norbert. There are so many people to thank and I am sure that I have missed someone, but you all should know that without your support and your sacrifice this would not have been possible.

ABSTRACT

This dissertation focuses on *in situ* Fe and Ni isotope analyses of chondrules from unequilibrated ordinary chondrites (UOCs) using the ion microprobe in order to constrain the initial $^{60}Fe/^{56}Fe$ ratio of UOC chondrules for early solar system chronology.

Most of the chondrules analyzed for this dissertation do not have resolved excesses in ^{60}Ni. A few chondrules have clear excesses in ^{60}Ni (up to ~30‰) that can only be explained by the decay of ^{60}Fe. However, the isochrons are clearly disturbed as shown by the weak correlation between the excesses in ^{60}Ni and the Fe/Ni ratios. This, along with the discrepancies between the initial ratios inferred from bulk and *in situ* analyses, indicates that the Fe-Ni isotopic system in UOCs was disturbed. Synchrotron X-ray fluorescence maps of Fe and Ni and other trace elements in UOC chondrules confirm this. We found Fe and Ni enrichment along chondrule fractures, indicating extensive open system Fe-Ni redistribution occurred between chondrules and the surrounding matrix. These complications make the Fe-Ni isotope data difficult to interpret. Nevertheless, our data indicate that the initial $^{60}Fe/^{56}Fe$ ratio of UOC chondrules is between 5×10^{-8} and 2.6×10^{-7}.

Our ion microprobe measurements consist of counting Fe and Ni ions from a chondrule and calculating isotope ratios from those counts. However, ratios calculated this way are systematically higher than the true ratio in the sample. The bias increases proportionally with decreasing count rates of the normalizing isotope and can produce linear correlations similar to those of an isochron. This dissertation provides a detailed discussion of the influence of ratio bias on isochrons and it includes re-calculated ratios for several *in situ* studies, including most of the previously published *in situ* Fe-Ni data.

Additionally, a study of the influence of ratio bias on *in situ* ^{26}Al-^{26}Mg ($t_{1/2}$=0.7 Myr) systematics of plagioclase from H4 chondrites is included in this dissertation. We find that ratio bias is not significant for these analyses. We argue that the ^{26}Al-^{26}Mg ages for these chondrites date impact excavation and cooling at the surface of the H chondrite parent body, not cooling at depth as the onion shell model predicts.

TABLE OF CONTENTS

ACKNOWLEDGEMENTS ..... **ii**

ABSTRACT ..... **iv**

LIST OF TABLES ..... **xi**

LIST OF FIGURES ..... **xiii**

CHAPTER 1. INTRODUCTION **1**

1.1 Background 2

1.2 Importance of the ^{60}Fe-^{60}Ni short-lived radionuclide 5

1.3 Dissertation outline 9

CHAPTER 2. *IN SITU* ^{60}Fe-^{60}Ni SYSTEMATICS OF CHONDRULES FROM UNEQUILIBRATED ORDINARY CHONDRITES **11**

2.1 ABSTRACT 12

2.2 INTRODUCTION 13

2.3 METHODS 17

2.3.1 Sample selection 17

2.3.2 Secondary ion mass spectrometry 18

2.3.3 Data analysis 24

2.4 RESULTS 26

2.4.1 Initial ratios with large uncertainties due to low Fe/Ni ratios 27

2.4.2 Initial ratios with large uncertainties due to limited spread in Fe/Ni ratios 27

2.4.3 Unresolved initial ratios, despite high Fe/Ni ratios 29

2.4.4 Resolved initial ratios, but large MSWD values 30

2.4.5 Constraining the initial $^{60}Fe/^{56}Fe$ ratio of UOC chondrules 33

2.4.6 Identifying our best chondrule datasets and constraining upper limits 38

2.4.7 Constraining the upper limit on the initial $^{60}Fe/^{56}Fe$ ratio of UOCs 39

2.5 DISCUSSION 41

2.5.1 Complications from Fe-Ni mobilization in UOC chondrules 42

2.5.2 Interpretation of unresolved initial ratios require caution 44

2.5.3 Constraints from chondrules with high initial ratios and large MSWD values 45

2.5.4 Comparison with ICPMS and TIMS UOC chondrule data 49

2.5.5 Coordinated bulk & *in situ* analyses of UOC chondrules 50

2.5.6 Constraining the source of ^{60}Fe in the early solar system 51

2.5.7 Developing the ^{60}Fe-^{60}Ni system for early solar system chronology 54

2.6 CONCLUSIONS 56

CHAPTER 3. MOBILITY OF IRON AND NICKEL AT LOW TEMPERATURES AND IMPLICATIONS FOR ^{60}Fe-^{60}Ni SYSTEMATICS OF CHONDRULES FROM UNEQUILIBRATED ORDINARY CHONDRITES 57

3.1 ABSTRACT 58

3.2 INTRODUCTION 59

3.3 METHODS 62

3.3.1 Samples 62

3.3.2 XRF mapping and data analysis 63

3.3.3 Electron probe analyses 67

3.4 RESULTS 67

3.4.1 Fe and Ni enrichment in chondrule fractures 67

3.5 DISCUSSION 79

3.5.1 Mechanisms of redistribution of Fe and Ni in UOC chondrites 80

3.5.2 Effects of Fe and Ni redistribution on ^{60}Fe-^{60}Ni systematics 85

3.5.3 Implications for ^{60}Fe-^{60}Ni analyses of UOC chondrules and other meteorite samples 89

3.6 CONCLUSIONS 91

CHAPTER 4. RECALCULATION OF DATA FOR SHORT-LIVED RADIONUCLIDE SYSTEMS USING LESS-BIASED RATIO ESTIMATION 93

4.1 ABSTRACT 94

4.2 INTRODUCTION 96

4.3 BIAS IN ISOCHRONS 100

4.3.1 Propagation of ratio bias through mass-fractionation correction 100

4.3.2 Ratio bias in isochron fitting 104

4.4 RECALCULATING PREVIOUSLY PUBLISHED SIMS DATA 107

4.4.1 Procedure 107

4.4.2 Estimating uncertainties 108

4.5 RESULTS 109

4.5.1 ^{53}Mn-^{53}Cr systematics in pallasite olivines 109

4.5.2 ^{60}Fe-^{60}Ni systematics in sulfides from unequilibrated ordinary chondrites ... 112

4.5.3 ^{60}Fe-^{60}Ni and ^{53}Mn-^{53}Cr systematics in sulfides from enstatite chondrites ... 114

4.5.4 ^{60}Fe-^{60}Ni systematics in chondrules from ordinary chondrites 117

4.5.5 ^{60}Fe-^{60}Ni systematics of more chondrules from ordinary chondrites 119

4.5.6 ^{10}Be-^{10}B systematics in CAIs from CV3 chondrites 123

4.6 DISCUSSION AND CONCLUSIONS 125

CHAPTER 5. REVISITING ^{26}Al-^{26}Mg SYSTEMATICS OF PLAGIOCLASE IN H4 CHONDRITES 129

5.1 ABSTRACT 130

5.2 INTRODUCTION 132

5.3 ANALYTICAL PROCEDURES 135

5.3.1 Sample selection and electron microprobe analyses 135

5.3.2 Ion microprobe measurement conditions and data analysis 136

5.4 RESULTS 139

5.4.1 Ste. Marguerite 139

5.4.2 Forest Vale 143

5.4.3 Beaver Creek 146

5.4.4 Sena 149

5.5 DISCUSSION 151

5.5.1 Comparison with previous measurements 151

5.5.2 Compositional variation and petrology of plagioclase in H4 chondrites 153

5.5.3 Interpretation of the isochron data 156

5.5.4 Comparison with cooling rate data 160

5.5.5 Thermal evolution of the H chondrite parent body 161

5.5 CONCLUSIONS 166

CHAPTER 6. CONCLUSIONS 168

APPENDIX A. SYNTHETIC PYROXENE STANDARDS & FE-NI SIMS CHONDRULE DATA 171

APPENDIX B ADDITIONAL X-RAY FLUORESCENCE MAPS OF UOC CHONDRULES 193

APPENDIX C. RE-CALCULATED SIMS DATA 195

REFERENCES 226

LIST OF TABLES

Table 2.1. All Fe-Ni chondrule SIMS data 35

Table 2.2. Fe-Ni chondrule SIMS data - Filtered according to MSWD values. 37

Table 3.1. Summary of synchrotron XRF mapping 79

Table 4.1. ^{53}Mn-^{53}Cr systematics in pallasite olivines 111

Table 4.2. ^{60}Fe-^{60}Ni systematics in sulfides from unequilibrated ordinary chondrites ... 113

Table 4.3. ^{53}Mn-^{53}Cr systematics in sulfides from enstatite chondrites 115

Table 4.4. ^{60}Fe-^{60}Ni systematics in sulfides from enstatite chondrites 116

Table 4.5. ^{60}Fe-^{60}Ni systematics in chondrules from ordinary chondrites 118

Table 4.6. ^{60}Fe-^{60}Ni systematics of more chondrules from ordinary chondrites 120

Table 4.7. ^{10}Be-^{10}B systematics in CAIs from CV3 chondrites 124

Table 5.1. Al-Mg SIMS data for Ste. Marguerite chondrules 142

Table 5. 2. Al-Mg SIMS data for Forest Vale chondrules 146

Table 5. 3. Al-Mg SIMS data for Beaver Creek chondrules 148

Table 5. 4. Al-Mg SIMS data for Sena chondrules 151

Table Appendix A.1. Synthetic pyroxene standard compositions. 171

Table Appendix A.2. Fe-Ni SIMS data for each chondrule 171

Table Appendix C.1. ^{53}Mn-^{53}Cr pallasite data 198

Table Appendix C.2. ^{60}Fe-^{60}Ni sulfide data Tachibana & Huss (2003b) 199

Table Appendix C.3. ^{53}Mn-^{53}Cr sulfide data (Guan et al. 2007) 203

Table Appendix C.4. ^{60}Fe-^{60}Ni sulfide data (Guan et al. 2007) 204

Table Appendix C.5. ^{60}Fe-^{60}Ni chondrule data (Tachibana et al. 2006) 205

Table Appendix C.6. ^{60}Fe-^{60}Ni chondrule data (Tachibana et al. 2007; Tachibana et al. 2009; Telus et al. 2011a)..... 209

Table Appendix C.7. ^{10}Be-^{10}B CAI data (MacPherson et al. 2003) 223

LIST OF FIGURES

Figure 2.1.Mass scans of ^{60}Ni and ^{61}Ni isotopes and interferences 21

Figure 2.2. Chondrules with low Fe/Ni ratios..... 27

Figure 2.3. Chondrules with limited spread in the Fe/Ni ratios. 28

Figure 2.4. Chondrules with high Fe/Ni ratios, but unresolved initial ratios..... 29

Figure 2.5. Fe-Ni SIMS data for Semarkona chondrule DAP1 30

Figure 2.6. Fe-Ni SIMS data for Bishunpur chondrule BM80 ch13 31

Figure 2.7. Fe-Ni SIMS data for Krymka chondrule KRM9-3 ch11..... 32

Figure 2.8. Fe-Ni SIMS data for QUE97008 chondrule QUE ch5..... 33

Figure 2.9. Initial ^{60}Fe/^{56}Fe ratios of all UOC chondrules..... 37

Figure 2.10. The MSWD values vs. the 2σ-uncertainty on the initial ratios 39

Figure 2.11. SIMS data and Guassian probability distribution for QUE97008 chI..... 40

Figure 2.12. Gaussian probability distributions for best chondrule data 41

Figure 2.13. Constraining the lower limit of the initial ratio for UOC chondrules 48

Figure 3.1. Experimental setup 65

Figure 3.2. X-ray maps for Semarkona chondrule SMK312 chH 70

Figure 3.3. X-ray maps for Semarkona chondrule SMKMT 62231 71

Figure 3.4. X-ray maps for a QUE97008 chondrule..... 72

Figure 3.5. X-ray maps for a EET87735 chondrule..... 73

Figure 3.6. X-ray maps for a MET96503 chondrule 74

Figure 3.7. X-ray maps for a TIL82408 chondrule..... 75

Figure 3.8. X-ray maps for Bishunpur chondrule BM80 ch13 76

Figure 3.9. X-ray maps for Bishunpur chondrule BM23 ch13 77

Figure 3.10. X-ray maps for Krymka chondrule KRM9-4 ch1 78

Figure 3.11. Bleached Fe-rich bleb and opaque nodule from Semarkona chondrules 84

Figure 3.12. Effect of Fe-Ni redistribution on *in situ* analyses..... 87

Figure 3.13. Effect of Fe-Ni redistribution on *bulk* analyses..... 89

Figure 4.1 Schematic isochron diagram produced from ratios that are biased. 97

Figure 4.2. Schematic description of the effect of ratio bias on radiogenic excesses..... 103

Figure 4.3. ^{53}Mn-^{53}Cr systematics in pallasite olivines 111

Figure 4.4. ^{60}Fe-^{60}Ni systematics in sulfides from unequilibrated ordinary chondrites . 114

Figure 4.5. ^{53}Mn-^{53}Cr systematics in sulfides from enstatite chondrites 116

Figure 4.6. ^{60}Fe-^{60}Ni systematics in sulfides from enstatite chondrites..... 117

Figure 4.7. ^{60}Fe-^{60}Ni systematics in chondrules from ordinary chondrites 119

Figure 4.8. ^{60}Fe-^{60}Ni systematics of more chondrules from ordinary chondrites..... 121

Figure 4.9. ^{60}Fe-^{60}Ni systematics of more chondrules from ordinary chondrites..... 123

Figure 4.10. Comparison of ratios calculated from the mean of ratios and total counts 126

Figure 5. 1. H4 chondrite plagioclase compositions..... 139

Figure 5.2. Ste. Marguerite chondrules 140

Figure 5.3. Petrographic relationship between plagioclase grains with high and low An#s.

..... 140

Figure 5.4. Al-Mg SIMS data for Ste. Marguerite chondrules 142

Figure 5.5. Forest Vale chondrules..... 144

Figure 5.6. Al-Mg SIMS data for Forest Vale chondrules 145

Figure 5.7. Beaver Creek chondrules..... 147

Figure 5.8. Al-Mg SIMS data for Beaver Creek chondrules 148

Figure 5.9. Sena chondrules 150

Figure 5.10. Al-Mg SIMS data for Sena chondrules 150

Figure 5.11. Al-Mg systematics of H4 chondrites vs Onion-shell model 164

Figure Appendix B.1. X-ray maps for Semarkona chondrule SMK1805 80040..... 193

Figure Appendix B.2. X-ray maps for Krymka chondrule KRM94 80041 194

Figure Appendix B.3. X-ray maps for Semarkona chondrule SMK1805 ch1..... 195

Figure Appendix B.4. X-ray maps for Krymka chondrule KRM9-3 ch3..... 196

Figure Appendix B.5. X-ray maps for Bishunpur chondrule BM80 ch37 197

CHAPTER 1. **INTRODUCTION**

1.1 Background

The solar system formed from the collapse of a dense molecular cloud of gas, dust, and ice. Over 99% of the original material from the presolar cloud went into forming the Sun. The remaining material that was not accreted onto the Sun formed a disk around it called the protoplanetary disk. Agglomeration of gas, dust and ice in the disk formed planetesimals, bodies 10-100 km in diameter. Collisions between planetesimals and internal heating from radioactive nuclides resulted in the formation of larger differentiated bodies. Protoplanets formed as a result of runaway growth by gravitationally attracting most of the material in their orbital residence. Eventually, most of the material in the disk was consumed by these growing protoplanets. Planet formation is a very energetic process that results in complete melting and alteration of the original components that accreted to form planets. Fortunately, remnants of the original dust and planetesimals in the solar system have been preserved as small bodies called asteroids mainly located 1.5 - 2.3 AU in the Asteroid Belt, which consists primarily of fragments of rock and metal from early planetesimals. Many of these asteroids survived solar system formation with minimal thermal processing.

Asteroids are the parent bodies of most meteorites, fragments of extraterrestrial rocks that survive impact on the Earth. Meteorites vary widely in texture, composition, and thermal history, but they all can be classified as either chondrites or achondrites. Chondrites are primitive stony meteorites. They are sedimentary rocks consisting of an aggregate of material from the protoplanetary disk. They did not experience enough heating to destroy these components. They contain millimeter- to centimeter-sized inclusions called chondrules and calcium- and aluminum-rich inclusion (CAIs).

Chondrules, which are made up of olivine, pyroxene, glass and small blebs of metal and sulfide, make up the bulk of chondrites. Currently, there is no consensus on the exact mechanism for their formation in the protoplanetary disk. CAIs are high temperature condensates and the oldest known material in the solar system. Chondrites also contain matrix that fills the spaces between the chondrules and CAIs. The matrix consists of a fine-grained mixture of hydrated and anhydrous silicates, oxides, Fe-Ni metal, sulfides and organic material. The matrix contains presolar grains, nanometer- to submicron-sized particles that condensed around other stars and were incorporated into the molecular cloud during solar system formation. Chondrules, CAIs, matrix and presolar grains represent remnants of the dust that existed in the Sun's protoplanetary disk. Many chondrites experienced parent body processes, aqueous alteration and/or thermal metamorphism. Achondrites, also called differentiated meteorites, are fragments of planetesimals that underwent significant heating that caused large scale melting of the original planetesimal, resulting in the segregation of high density metals and low density oxides, forming a Fe-Ni rich core and silicate rich mantle. Achondrites include stony, stony-irons, and iron meteorites. They do not generally contain chondrules, CAIs, matrix or presolar grains.

Meteorites provide us with what amounts to an eyewitness account of the events that led to the formation and evolution of the Solar System. The timing of these events is determined through analyses of long- and short-lived radioactive nuclides in meteorites. Long-lived radionuclides have half-lives >100 Myr. These analyses involve measuring the abundance of parent and daughter isotopes of a radionuclide system in a sample and using the radioactive decay law to calculate the age of the sample. The ^{207}Pb-^{206}Pb system

(based on ^{235}U-^{207}Pb and ^{238}U-^{206}Pb systems) is the most commonly used long-lived radionuclide system for absolute ages of meteorites and their components. It provides a resolution of ~1 Myr for early solar system chronology.

Short-lived radionuclides (SLRs), which have half-lives <100 Myr, can provide higher resolution chronology. Due to their very rapid decay rates, SLRs are no longer present in the solar system. They are also known as “extinct” or “fossil” nuclides. The initial abundances of SLRs (defined relative to a stable isotope of the parent nuclide) are inferred through the detection of excesses in the daughter isotope that correlate with the parent-to-daughter isotope ratio. Since the parent nuclide is extinct, isotopic analyses of SLR systems provide quantitative relative ages, not absolute ages, unless anchored to a long-lived chronometer. Most of the major solar system processes including the formation of the first solids, planetesimal accretion and differentiation, and the onset of thermal metamorphism and aqueous alteration occurred within the first 10 million years of solar system formation, making SLRs with half-lives <10 Myr essential for resolving these early events that occurred on such a short timescale. The commonly used SLRs for early solar system chronology are ^{26}Al-^{26}Mg ($t_{1/2}$=0.7 Myr), ^{53}Mn-^{53}Cr ($t_{1/2}$=3.7 Myr) and ^{182}Hf-^{182}W ($t_{1/2}$=8.9 Myr).

In order to use a SLR for high-resolution chronometry, it must meet certain criteria. (1) The SLR must have been distributed homogeneously in the solar system so that differences in the initial abundance for different objects reflect only differences in their formation time. (2) Prior to and/or during formation of the object, there must have been an event that fractionated (or separated) the parent and daughter elements in order to resolve the accumulated radiogenic daughter isotope. (3) There must have been a closed

isotopic system for the nuclides of interest, meaning there should have been no loss or gain of the elements of interest since the event of interest after formation of objects. (4) A precise value for the initial solar system abundance of the SLR (relative to a stable isotope of the parent nuclide) must be known in order to use the radioactive decay equation, $N_t=N_{SS}e^{-\lambda t}$, where N_{SS} is the initial ratio in the solar system, N_t is the initial ratio at a given time, t, and λ is the decay constant of the parent nuclide.

The ^{207}Pb-^{206}Pb systematics of CAIs indicates that they formed 4.568 Gyr ago (e.g., Bouvier et al., 2007). CAIs are the oldest known objects in the solar system; however placing their formation in the context of astronomical observations of star formation (i.e., Class 0, I, II, or III) is difficult. Since the earliest stages of the Sun's evolution occurred extremely rapidly on the scale of ~10 Myr (e.g., Wyatt 2008), solar system formation occurred at least 4.6 Myr ago. Within 1 Myr of the formation of the first solids, accretion and global differentiation of planetesimals occurred, forming Fe-Ni rich cores and silicate rich mantles according to ^{182}Hf-^{182}W systematics of achondrites (e.g., Kleine et al., 2009). The ^{207}Pb-^{206}Pb, ^{26}Al-^{26}Mg, ^{53}Mn-^{53}Cr and ^{182}Hf-^{182}W systematics of basaltic achondrites indicate that magmatism on differentiated bodies occurred 4-10 Myr after CAIs (e.g., Nyquist et al., 2009). The ^{26}Al-^{26}Mg ages of chondrules indicate that most formed 2-3 Myr after CAIs and their chondrite parent bodies accreted soon afterwards (e.g., Kita et al., 2012). Aqueous alteration of chondrite parent bodies began as early as ~2 Myr after CAIs (e.g., Jilly et al., 2014).

1.2 Importance of the ^{60}Fe-^{60}Ni Short-lived Radionuclide System

Iron-60 beta decays to ^{60}Ni via ^{60}Co. It has a half-life of 2.6 Myr (Rugel et al., 2009), making it potentially important for providing additional constraints on the

timescale of early solar system processes. Chemically, Fe is one of the most abundant elements in the solar system. Iron behaves as a siderophile (tendency to form metal), but it is also moderately lithophile (tendency to form silicates or oxides) and chalcophile (tendency to form sulfides), while Ni is mainly siderophile. Iron is a constituent of a wide range of minerals including, oxides, sulfides, metal, and silicates. It is a major constituent of rock forming minerals, olivine and pyroxene. Iron and Ni can be fractionated during melting and crystallization. The ^{60}Fe-^{60}Ni system can potentially be used to date Fe-rich meteoritic components such as Fe-rich silicates and sulfides which cannot be easily analyzed with commonly used short-lived radiochronometers. The former presence of ^{60}Fe in the solar system has been detected in various meteorites through excesses of its daughter isotope ^{60}Ni (^{60}Ni*) that correlate with Fe/Ni ratios. However, in order to use ^{60}Fe-^{60}Ni system for chronology the initial ^{60}Fe/^{56}Fe ratio of the solar system must be constrained.

Iron-60 is also interesting because it is only efficiently produced by stellar nucleosynthesis. This makes it important for constraining the stellar source of short-lived radionuclides. Typically, SLRs in the solar system can have multiple sources including nucleosynthesis in various kinds of stars and particle irradiation. Identifying a possible stellar source for SLRs entails comparing the initial abundances of the different SLRs to abundances predicted by nucleosynthesis models and considering the probability of such stars occurring in a star formation region. An initial ratio of ^{60}Fe/^{56}Fe above galactic background (abundance of SLR inherited from the interstellar medium), estimated to be $<4\times10^{-8}$ (Huss et al., 2009), requires synthesis of ^{60}Fe in a nearby star, ejection into the interstellar medium and subsequent incorporation into the budding solar system (e.g,

Hester and Desch, 2005). Better constraints on the initial $^{60}Fe/^{56}Fe$ ratio of the solar system are required to constrain these models.

The initial $^{60}Fe/^{56}Fe$ ratio of the solar system, $(^{60}Fe/^{56}Fe)_{SS}$, has been estimated from bulk and *in situ* Fe-Ni isotopic analyses of meteorites. Currently, bulk Fe-Ni analyses are carried out using two main methods, ICPMS (Inductively Coupled Plasma Mass Spectrometry) and TIMS (Thermal Ionization Mass Spectrometry). Bulk analyses involve dissolving the sample, separating out the Ni using column chemistry, and then counting the Ni isotopes in the solution using a mass spectrometer. The benefit of this technique is that it permits high-precision results. The drawback is that the sample is completely digested and the petrologic context is lost. Bulk Fe-Ni analyses of meteorites began in the 1980s as a result of interest in isotope anomalies in meteorites. Since CAIs were the first solids to form in the solar system, they were the obvious first choice for determining the $(^{60}Fe/^{56}Fe)_{SS}$ ratio (Birck & Lugmair, 1988). However, CAIs preserve Ni isotope anomalies (non-radiogenic excesses of ^{62}Ni and ^{64}Ni that are nucleosynthetic in origin) that make it difficult to evaluate whether the measured excesses in ^{60}Ni are from the decay of ^{60}Fe or inherited from presolar material. Subsequently, bulk Fe-Ni analyses have been done for differentiated meteorites, including eucrites (e.g., Shukolyukov & Lugmair, 1993a), angrites (e.g., Tang and Dauphas, 2012), ureilites (e.g., Quitté et al., 2010), and iron meteorites (e.g., Bizzarro et al., 2007), and for chondrules (e.g., Tang and Dauphas, 2015). In summary, the $(^{60}Fe/^{56}Fe)_{SS}$ value inferred from bulk Fe-Ni analyses is $<3\times10^{-8}$, which does not require a recent injection of material from a nearby star prior to solar system formation. This initial abundance indicates that ^{60}Fe in the solar system was inherited from the interstellar medium.

In situ ^{60}Fe-^{60}Ni analyses are carried out using secondary ion mass spectrometry (SIMS), often called an ion probe. With this technique, the sample surface is sputtered using a primary high-energy ion beam (often O^- or Cs^+), producing secondary ions from the sample that are extracted into a mass spectrometer. Using the SIMS can preserve the petrologic context of the analyses, but the precision is significantly lower compared to bulk Fe-Ni analyses due to the very small volume sampled. The first published study of *in situ* Fe-Ni measurements (Kita et al., 2000) focused on chondrule olivine from unequilibrated ordinary chondrites (UOCs), but they could not resolve excesses in ^{60}Ni in the chondrules they measured. Subsequently, Tachibana and Huss (2003) and a host of other SIMS studies (e.g., Mostefaoui et al, 2005; Tachibana et al., 2006; Guan et al., 2007; Mishra et al., 2010) reported evidence for ^{60}Fe in troilite and chondrule pyroxenes from ordinary and enstatite chondrites. These studies inferred high values for the $(^{60}Fe/^{56}Fe)_{SS}$ ratio of up to 1×10^{-6}, orders of magnitude higher than the ratio inferred for the ISM and the values inferred from bulk analyses. The high $(^{60}Fe/^{56}Fe)_{SS}$ ratio is very interesting because it would be consistent with a stellar source for ^{60}Fe (e.g., Williams 2010). However, Telus et al. (2012a) shows that many of the results from these early SIMS studies were in error due to improper data analysis that produced a significant positive bias in the Ni isotope ratios. After correcting the data, most of the originally reported excesses in ^{60}Ni disappeared or were much lower than the original estimates. Nevertheless, evidence for ^{60}Fe still exists and SIMS analyses still give higher initial ratios than bulk analyses (e.g., Telus et al., 2012a; Mishra and Goswami, 2014). The discrepancies between bulk and *in situ* analyses are likely due to late-stage Fe-Ni redistribution (Telus et al., 2015a).

1.3 Dissertation Outline

The research presented in this dissertation represents a concerted effort to better constrain the $(^{60}Fe/^{56}Fe)_{SS}$ ratio and understand the analytical techniques and samples best suited for this endeavor.

Chapter 2 discusses the ^{60}Fe-^{60}Ni systematics of chondrules from unequilibrated ordinary chondrites (UOCs). In order to constrain the $(^{60}Fe/^{56}Fe)_{SS}$ ratio, I measured the *in situ* Fe-Ni isotopic composition of olivine and pyroxene in UOC chondrules using the ion microprobe at the University of Hawaii. Despite the complications from Fe-Ni redistribution, we can place constraints on the upper and lower limits of the initial $^{60}Fe/^{56}Fe$ ratio of UOCs. Preliminary data for this study are published in conference abstracts (Huss et al., 2010a, 2010b; Telus et al., 2011a, 2011b, 2011c; Chen et al., 2013; Telus et al., 2013a, 2013b; Telus et al., 2015b). This chapter is currently being prepared for publication (Telus et al., 2015c).

Chapter 3 presents synchrotron X-ray maps that were collected at the Australian Synchrotron and the Advanced Photon Source (Telus et al., 2015a). I carried out this study in order to evaluate whether the Fe-Ni system remain closed in UOC chondrules. The X-ray maps show that Fe and Ni mobility is extensive along fractures within many UOC chondrules, indicating that there was significant exchange of Fe and Ni between chondrules and matrix at the low metamorphic temperatures experience by UOCs. Preliminary data for this study are published in conference abstracts (Telus et al., 2014c 2014d)

Chapter 4 is a study on the influence of ratio bias in ion probe analyses of short-lived radionuclides (published as Telus et al., 2012a). Ion probe analyses of short-lived

radionuclides often involve low count rates, which make these analyses susceptible to ratio bias, which increases proportionally with decreasing count rates of the normalizing isotope. We describe how ratio bias affects the inferred initial $^{60}Fe/^{56}Fe$ ratios. We also report recalculated results for published SIMS studies of various SLR systems, including most of the previously published Fe-Ni data for sulfides and chondrules. Preliminary data for this study are published in conference abstracts (Huss et al., 2011; Telus et al., 2012b).

Chapter 5 is a study on ^{26}Al-^{26}Mg systematics of plagioclase from H4 chondrites and implications for the onion-shell parent body (published as Telus et al., 2014a). This study stems directly from my work on ratio bias and previous *in situ* Al-Mg analyses by Zinner and Göpel (2002). Preliminary data for this study are published in conference abstracts (Telus et al., 2012c; Telus et al., 2014b).

CHAPTER 2. *IN SITU* ^{60}Fe-^{60}Ni SYSTEMATICS OF CHONDRULES FROM UNEQUILIBRATED ORDINARY CHONDRITES

2.1 Abstract

The initial $^{60}Fe/^{56}Fe$ ratio of chondrules from unequilibrated ordinary chondrites (UOCs) can potentially constrain the initial $^{60}Fe/^{56}Fe$ ratio of the solar system, which is necessary to help constrain the stellar source of short-lived radionuclides and to use the ^{60}Fe-^{60}Ni ($t_{1/2}$=2.6 Myr) system for early solar system chronology. We made *in situ* analyses of the Fe-Ni isotopic composition of ferromagnesian silicates in chondrules from UOCs using the ion microprobe. We did not find resolved excesses of ^{60}Ni for most of the chondrules we analyzed. Four chondrules have excesses in ^{60}Ni of up to ~30‰; however, the correlations with the Fe/Ni ratios are weak, making their data difficult to interpret. In order to determine which chondrules provide the best constraints on the initial $^{60}Fe/^{56}Fe$ ratio of UOC chondrules, we filtered the data to only include chondrules that have initial ratios with 2σ uncertainties $<3\times10^{-7}$ and isochrons with MSWD values between 0.5 and 1.5. The initial ratios for our best chondrule are mostly unresolved, except for one, which has an initial ratio of $(2.2\pm1.5)\times10^{-7}$. Assuming the initial ratios for our best chondrules sample a single homogeneous reservoir, we infer an upper limit of 2.6×10^{-7} for $^{60}Fe/^{56}Fe$ at the time UOC chondrules formed. Large excesses in ^{60}Ni from some of our chondrules indicate that the initial ratio for UOC chondrules cannot be less than 5×10^{-8}, which is inconsistent with initial ratios of $<3\times10^{-8}$ inferred from bulk analyses of chondrules. Complications from Fe-Ni redistribution require that both bulk and *in situ* Fe-Ni analyses be interpreted with caution and indicate that the Fe-Ni isotopic analyses of UOC chondrules may be of only limited use for constraining the initial $^{60}Fe/^{56}Fe$ ratio of the solar system.

2.2 Introduction

The ^{60}Fe-^{60}Ni short-lived radionuclide system ($t_{1/2}$=2.6 Myr) has been of interest in cosmochemistry and astrophysics for several reasons, including its potential for constraining early solar system chronology (e.g., Shukolyukov and Lugmair, 1993b; Tang and Dauphas, 2012b), its potential as a heat source for planetary differentiation (e.g., Moskovitz and Gaidos, 2011), identifying the stellar source of short-lived radionuclides (e.g., Huss et al., 2009), and understanding the environmental conditions surrounding the Sun's formation (e.g., Hester and Desch, 2005). The presence of live ^{60}Fe in the early solar system has been inferred through excesses in ^{60}Ni that correlate with the Fe/Ni ratios in various meteorites (e.g., Shukolyukov and Lugmair, 1993a; Tachibana et al., 2006; Tang and Dauphas, 2012a; Mishra and Goswami, 2014). The initial ^{60}Fe/^{56}Fe ratio, $(^{60}Fe/^{56}Fe)_0$, for each sample is determined from the excesses in ^{60}Ni that correlate with the Fe/Ni ratios. The $(^{60}Fe/^{56}Fe)_0$ ratio can then be used to constrain the initial solar system ^{60}Fe/^{56}Fe ratio, $(^{60}Fe/^{56}Fe)_{SS}$, as long as the age of the sample has been determined independently, the Fe-Ni system has remained closed, and ^{60}Fe was homogeneously distributed in the solar system. The last two criteria are often assumed.

Progress with using the ^{60}Fe-^{60}Ni system for early solar system chronology or for constraining astrophysical models has been severely hindered by discrepancies between initial ratios inferred from bulk and *in situ* Fe-Ni analyses. Bulk Fe-Ni analyses of calcium-aluminum-rich inclusions (CAIs), the first solids to form in the solar system, carried out by Birck and Lugmair (1988), found evidence for excess ^{60}Ni in several inclusions and inferred an initial $(^{60}Fe/^{56}Fe)_{SS}$ ratio of $<1.6\times10^{-6}$. However, since CAIs preserve Ni-isotope anomalies, it is not clear whether the excesses in ^{60}Ni are from the

decay of ^{60}Fe or simply inherited isotope anomalies, which are common in CAIs. Further application of CAIs to constrain the $(^{60}Fe/^{56}Fe)_{SS}$ has been problematic for this reason. Whole rock analyses of eucrites, basaltic achondrites, by Shukolyukov and Lugmair (1993a, 1993b) were the first to show resolved ^{60}Ni excesses that correlate with Fe/Ni ratios. The initial $^{60}Fe/^{56}Fe$ ratios inferred for eucrites Juvinas and Chervony Kut were 4.3×10^{-10} and 3.9×10^{-9}, respectively, implying an 8.3 Myr difference in the crystallization ages of these meteorites (using 2.6 Myr half-life determined by Rugel et al., 2009). However, internal isochrons from analyses of mineral separates do not show a clear correlation between excess ^{60}Ni and the Fe/Ni ratio, indicating the Fe-Ni system did not remain closed for these samples and has been affected by thermal metamorphism (Shukolyukov and Lugmair, 1993a; Quitté et al., 2011). Whole rock analyses of eucrites and diogenites by Tang and Dauphas (2012a) infer an initial ratio of 3.45×10^{-9} at the end of mantle differentiation of the HED (howardite-eucrite-diogenite) parent body. Using the radioactive decay equation and the age of these rocks based on ^{53}Mn-^{53}Cr systematics (Trinquier et al., 2008; Nyquist et al., 2009), they calculate the initial solar system $^{60}Fe/^{56}Fe$ ratio, $(^{60}Fe/^{56}Fe)_{SS}$, to be 1.0×10^{-8}. This is also consistent with initial ratios inferred from bulk analyses of angrites (Quitté et al., 2010; Spivak-Birndorf et al., 2011; Tang and Dauphas, 2012a, 2012b). Bulk analyses of chondrules from unequilibrated ordinary chondrites have also been used to help constrain the $(^{60}Fe/^{56}Fe)_{SS}$ ratio. Excesses in ^{60}Ni are unresolved from zero for most bulk chondrules analyses (Tang and Dauphas, 2012a, Spivak-Birndorf et al., 2012; Chen et al., 2013); however, recent analyses found resolved excess ^{60}Ni in one Semarkona chondrule (Tang and Dauphas, 2015). The $(^{60}Fe/^{56}Fe)_{SS}$ ratios inferred from bulk chondrule analyses are all consistent with $<3\times10^{-8}$.

An initial ratio at this level is more consistent with ^{60}Fe being inherited from the galactic background (i.e., material from the interstellar medium inherited by the Sun's molecular cloud; Huss et al., 2009), and it would be an insignificant source of heat for planetary differentiation (Moskovitz and Gaidos, 2011).

Initial ratios inferred from *in situ* Fe-Ni analyses often paint a different picture. *In situ* analyses of troilite in unequilibrated ordinary chondrites (UOCs) by Tachibana and Huss (2003) found excess ^{60}Ni that correlated with the Fe/Ni ratios. They inferred $(^{60}Fe/^{56}Fe)_0$ for sulfides from Bishunpur and Krymka of $(1\text{-}2)\times10^{-7}$, an order of magnitude higher than initial ratios inferred from bulk analyses. Mostefaoui et al. (2005) analyzed troilite and magnetite from Semarkona and inferred an even higher initial ratio for sulfides of 1×10^{-6}. Researchers shifted toward analyzing Fe-silicates (olivine and pyroxene) from UOC chondrules because sulfides were found to be easily altered by mild thermal metamorphism (Guan et al. 2004, 2007). Tachibana et al. (2006) infer initial ratios of $(2\text{-}3)\times10^{-7}$ from *in situ* analyses of Semarkona and Bishunpur chondrules, while Mishra et al. (2010) inferred higher initial ratios of up to 6×10^{-7} from similar analyses. However, Telus et al. (2012a; Chapter 4) show that the high initial ratios inferred from most of the previous *in situ* Fe-Ni analyses are artifacts from the way the isotope ratios were calculated. Isotope ratios calculated from counting data have a positive bias, and the bias is inversely proportional to the number of counts in the denominator of the ratio (Ogliore et al., 2011). The low Ni contents of our samples can potentially lead to significant ratio bias. The bias was accentuated in the early work because the final ratios were calculated from the mean of ratios calculated from a large number of measurement cycles. When the ratios from various studies (Tachibana and Huss, 2003; Guan et al.

2007; Tachibana et al., 2006, Tachibana et al., 2007; Tachibana et al., 2009; Telus et al., 2011a) were calculated using total counts and bias was suppressed, evidence for ^{60}Fe disappeared for sulfides and for most chondrules (Telus et al., 2012a; Chapter 4). Nevertheless, evidence for ^{60}Fe in some chondrules remains, with inferred initial ratios ranging from 2×10^{-7} (Telus et al., 2012a) to 1×10^{-6} (Mishra and Goswami, 2014, Mishra and Chaussidon 2014), though the isochrons are often not well-constrained. The presence of ^{60}Fe at this abundance in the early solar system is consistent with a recent supernova injection of ^{60}Fe and possibly other short-lived radionuclides in the solar system (Hester and Desch, 2005; Huss et al., 2009; Ouellette et al., 2009; Mishra and Goswami, 2014), although an AGB star of >5 solar masses could also potentially provide the ^{60}Fe (Wasserburg et al., 2006). Also, an abundance of this magnitude would have important implications for planetary differentiation (Moskovitz and Gaidos, 2011).

Here, we present ^{60}Fe-^{60}Ni isotopic data for ferromagnesian silicates in chondrules from unequilibrated ordinary chondrites (UOCs) determined *in situ* using the ion microprobe at the University of Hawai‘i. In interpreting these data, we take into account the clear evidence for late-stage Fe and Ni redistribution in these chondrules, as demonstrated by synchrotron X-ray fluorescence studies (Telus et al., 2015a; Chapter 3). We find that most chondrules do not show resolved excesses of ^{60}Ni, some of this is due to secondary processing. Some chondrules have resolved excesses in ^{60}Ni, and some measured excesses are large (up to ~30‰). “Isochrons” constructed for these chondrules typically show a weak correlation between excess ^{60}Ni and Fe/Ni ratio, indicating that the inferred initial ratios are not reliable. We filtered the data according to MSWD (Mean Squared Weighted Deviation) values and the uncertainties on the initial ratios in order to

determine which data we can interpret. With this filter, again most of the chondrules are unresolved except for one, which has an initial ratio of $(2.2\pm1.5)\times10^{-7}$. Although complications from Fe-Ni redistribution make it difficult to interpret the data, we can place constraints on the upper and lower limits of the initial $^{60}Fe/^{56}Fe$ ratio of UOC chondrules.

2.3 Methods

2.3.1 *Sample Selection*

We analyzed chondrule olivine and pyroxene from unequilibrated ordinary chondrites Semarkona (LL3.00), QUE97008 (L3.05), EET90161 (L3.05), Bishunpur (LL3.1) and Krymka (LL3.2). We analyzed a wide variety of chondrules (Type I, Type II, cryptocrystalline, barred and porphyritic), but most of the chondrules are Type II porphyritic chondrules. Our primary selection criteria was for chondrules with high Fe/Ni ratios to permit resolution of excess ^{60}Ni and large grain sizes to accommodate the ion probe pits. At first, we scanned for suitable chondrules using the electron microprobe (JEOL JXA-8500F) at the University of Hawai‘i (UH). We carried out spot analyses with a 10 μm, 200 nA beam at 20 keV to help constrain the Fe/Ni ratios. However, the Fe/Ni ratios were often difficult to constrain because the Ni content in the pyroxene grains are generally too low to resolve using the electron probe. Therefore, we turned to using the ion probe for a second scan of suitable chondrules determined from the electron probe analyses. We simply checked the Fe/Ni ratio on a few areas of each chondrule using a 3 nA $^{16}O^-$ on the Cameca ims 1280 ion microprobe at UH. This method provided more accurate constraints on the Fe/Ni ratio.

We focused most of our efforts on chondrule pyroxenes from UOCs because pyroxenes have high Fe/Ni ratios (e.g., $>2\times10^5$) and are less susceptible to thermal metamorphism compared to olivine and sulfides. Also, UOCs of petrologic types 3.00 to 3.2 have experienced relatively low metamorphic peak temperatures (<400°C; Huss and Lewis, 1994). Despite all these benefits, X-ray fluorescence maps in Telus et al. (2015a) show that Fe and Ni are mobile in UOCs along chondrule fractures. These fractures are often too fine for us to notice or they are subsurface features we cannot readily detect with the electron probe or ion probe. Therefore, we also carried out X-ray fluorescence mapping at the Australian Synchrotron and the Advanced Photon Source to scan for suitable chondrules that do not show evidence for Fe or Ni mobilization, along with having large grain sizes and high Fe/Ni ratios. Our best chondrules from this survey are SMK1805 chT and SMK312B chQ from Semarkona, a type 3.00 ordinary chondrite. These chondrules met every criterion mentioned above except they show evidence for Fe mobilization along chondrule fractures. We did not find chondrules that meet every criterion. Finding suitable chondrules for SIMS Fe-Ni analyses is challenging and may limit its use for constraining the initial $(^{60}Fe/^{56}Fe)_{SS}$ ratio.

2.3.2 *Secondary ion mass spectrometry*

The UOC chondrules were measured using the Cameca ims 1280 ion microprobe at the University of Hawai‘i (UH). Fe and Ni isotopes were measured as positive ions using a 3-10 nA $^{16}O^-$ beam rastered over 15 μm. Spot sizes ranged from 20-40 μm and spots were presputtered (180 s) to minimize surface contamination. The secondary-ion beam was automatically centered in the field aperture using the dynamic transfer

deflectors at the beginning of each measurement. Terrestrial standards (San Carlos olivine, San Carlos pyroxene, and hypersthene) were generally measured using lower beam currents (1-3 nA) because of their higher Ni contents. We also used synthetic pyroxene standards, JHpx1 and JHpx2 (Appendix A.1.) made in the Volcanology and Experimental Petrology lab at UH. We used two basic SIMS protocols: monocollection and multicollection.

Monocollection: Nickel ions ($^{60}Ni^{+}$, $^{61}Ni^{+}$, and $^{62}Ni^{+}$) were counted sequentially on the monocollector electron multiplier, while the Fe ions ($^{56}Fe^{+}$ or $^{57}Fe^{+}$) were counted on the multicollector Faraday cup (L1) together with ^{60}Ni. The main advantage to using monocollection mode is that the monocollector electron multiplier is large and stable, meaning that changes in the gain of the detector over an analytical session are negligible. Also, any changes in the efficiency of the electron multiplier are cancelled out by taking ratios. The electron multiplier can easily handle all Ni count rates that we encountered (up to 5×10^{4} cps), while typical count rates ranging from 1000 to 100 cps. The disadvantage is that measurement times are longer since each isotope is counted separately, and fluctuation of secondary ion beam intensity either due to primary beam instability or heterogeneity of Ni contents introduces additional errors in measured Ni isotope ratios. For our most recent monocollection analyses, $^{60}Ni^{+}$, $^{61}Ni^{+}$, and $^{62}Ni^{+}$ were counted for 2, 50, and 10 s, respectively. Thus, each cycle for monocollection required at least 64 s (not including the time necessary to switch between the different masses and time for mass calibration and energy scans). Mass calibration was done automatically every 25 cycles, and energy scans were done every 50 cycles in order to account for sample charging. A typical measurement of 100 cycles lasted 2 hours.

Multicollection: In most cases, Fe and Ni ions were measured simultaneously, with $^{60}Ni^{+}$, $^{61}Ni^{+}$, and $^{62}Ni^{+}$ counted on electron multipliers and $^{56}Fe^{+}$ measured on a Faraday cup. Sometimes, we set Ni and Fe on separate B-fields and jumped from one to the other. This minimizes the effects of off-axis aberrations and gives the multicollector electron multipliers a rest every cycle. Mass calibration and energy scans were done automatically every 50 cycles. Each measurement cycle lasted 30 seconds and a measurement consisted of 200 cycles; a typical measurement lasted 2 hours. Multicollection requires half the time of monocollection for similar counting statistics, allowing us to analyze more spots and samples in the same amount of time. However, the multicollector electron multipliers are smaller and appear unable to handle as many counts as the monocollector electron multipler. The multicollector electron multipliers are also less stable with the gains changing throughout the analytical session (average $^{60}Ni/^{62}Ni$ ratio change of ~10‰), especially if they have been bombarded with high counts from Ni-rich phases. Unlike monocollection measurements, the gain changes among multicollection electron multipliers introduce inaccuracy in Ni isotope ratios; thus, a correction for drift in the gain of the detectors must be made using standard-sample bracketing. Chondrule BM80 ch37 was measured in both monocollection and multicollection mode (Table 2.1). Results from the different techniques are consistent for this chondrule.

Molecular interferences: Interferences were often measured during each measurement (via peak jumping) or after each measurement (by deflecting the secondary beam). To resolve major molecular interferences on the Ni isotopes (*e.g.,* $^{44}Ca^{16}O$ on ^{60}Ni, $^{45}Sc^{16}O$ on ^{61}Ni, and $^{46}Ca^{16}O$ on ^{62}Ni), a mass resolving power (MRP) of ~4500 was

used during multicollection analyses and a MRP of 6000-7000 was used during monocollection analyses. However, this does not resolve the ^{60}Ni hydride on ^{61}Ni (requires MRP =8,124). To evaluate the influence of ^{60}NiH on ^{61}Ni, we carried out high-resolution scans with MRPs >8000 during each SIMS session. We consistently found the ^{60}NiH peak and other hydrides (e.g., ^{59}CoH on ^{60}Ni and ^{61}NiH on ^{62}Ni) to contribute significantly less than 1‰ to the Ni isotopes on both standards and samples (e.g., Figure 2.1).

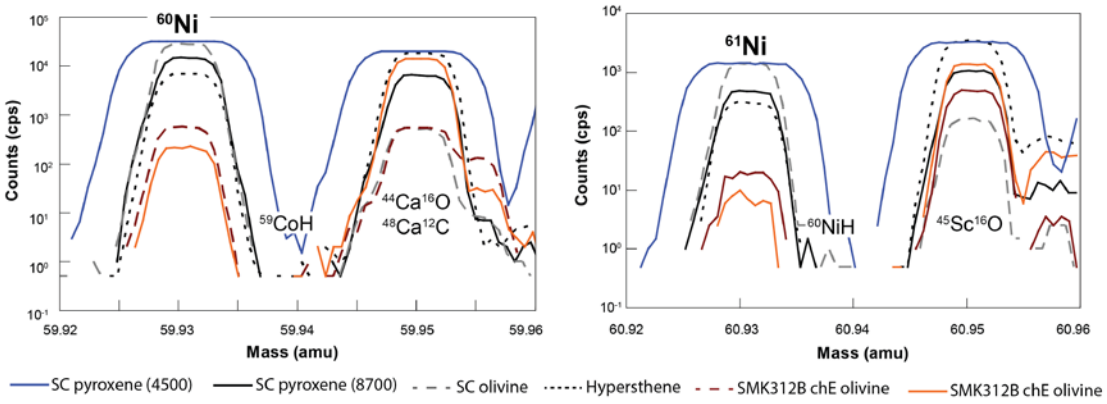

Figure 2.1. Mass scans of ^{60}Ni and ^{61}Ni isotopes and interferences on San Carlos pyroxene and olivine and hypersthene terrestrial standards and also on Semarkona chondrule olivine and pyroxene grains (SMK312B chE). The mass scan for SC pyroxene is shown with mass resolving powers of 4,500 and 8,700. All other scans have MRPs of 8700. Major interferences are resolved with MRP of 4500 and interferences from ^{59}CoH on ^{60}Ni and ^{60}NiH on ^{61}Ni contribute significantly less than 1‰.

We also tried to address the possible influence of unresolved complex molecular interferences on our analyses, such as the $[^{56}Fe^{64}Zn]^{2+}$ interference on ^{60}Ni (resolved with MRP=47,190). To determine the contribution of $[FeZn]^{2+}$ on Ni isotopes, we analyzed a terrestrial sphalerite ((Zn,Fe)S) sample with ~1 wt.% FeO and 65wt.% ZnO. We looked at $[^{57}Fe^{64}Zn]^{2+}$ at mass 60.5 and $[^{56}Fe^{67}Zn]^{2+}$ at mass 61.5 and found <1 cps at both

masses using 10 nA primary beam. We also analyzed one of our chondrules, but did not see any counts at these masses. The counts at mass 60 on sphalerite (<10 cps) can be used as the max contribution of $[^{56}Fe^{64}Zn]^{2+}$ on ^{60}Ni. Even though ^{60}Ni counts for chondrule pyroxenes can be as low as 100 cps, the ZnO concentrations are very low (<200 ppm) and the Fe content very high (~13 wt.%) compared to sphalerite. Therefore, the $[^{56}Fe^{64}Zn]^{2+}$ interference on ^{60}Ni is negligible for our analyses.

Mishra and Chaussidon (2014) used $[^{56}Fe^{57}Fe]^{2+}$ (mass 56.5) as a proxy for $[^{56}Fe^{64}Zn]^{2+}$. If $[^{56}Fe^{57}Fe]^{2+}$ has a high probability of forming, we would expect it to form during analysis of stainless steel. However, we found that counts at mass 56.5 on stainless steel were <10 cps using 5 nA and MRP of 2000. Given the high counts of ^{56}Fe and ^{57}Fe on stainless steel (60 million and 1.4 million, respectively), $[^{56}Fe^{57}Fe]^{2+}$ does not have a high probability of forming during SIMS analyses and, scaling to the Fe content of our chondrules, should contribute no more than 5 cps at mass 56.5, which indicates that counts from $[^{56}Fe^{64}Zn]^{2+}$ at mass 60 should be <5 cps.

We evaluated the $[^{56}Fe_2C]^{2+}$ interference on ^{62}Ni (resolved at MRP=9,383) by analyzing a hypersthene terrestrial standard with a carbon coating and with a gold coating. We anticipated that using the gold coating would reduce the formation of this complex molecular ion if it was forming. However, we found no difference in the $\delta^{60}Ni$ and $\delta^{62}Ni$ compositions of the hypersthene regardless of the type of coating used.

Other complex molecular ions could also potentially be a problem (e.g., $[^{54}Fe_2{}^{12}C]^{2+}$, $[^{54}Cr_2{}^{12}C]^{2+}$, and $[^{52}Cr_2{}^{16}O]^{2+}$ on ^{60}Ni requires MRP >6800; $[^{55}Mn_2{}^{12}C]^{2+}$ and $[^{53}Cr_2{}^{16}O]^{2+}$ on ^{61}Ni requires MRP >8500; $[^{56}Fe_2{}^{12}C]^{2+}$, $[^{54}Fe_2{}^{16}O]^{2+}$, and $[^{54}Cr_2{}^{16}O]^{2+}$ on ^{62}Ni requires MRP >7000). For two of our sessions, we applied a -20 eV energy

offset to reduce the counts from molecular interferences. This should have effectively eliminated any contributions from complex molecular ions. However, the energy offset did not make a measurable difference in the results, and it reduced Ni counts by a factor of ~1.5.

Complications from adjusting the gains of electron multipliers: The gain of the multicollection electron multipliers degrades quickly during a series of measurements. For some time, we were adjusting the voltage on the electron multipliers at various occasions during our SIMS sessions to try to maintain the gain of the detectors. However, we eventually realized that checking the pulse-height distribution, which requires high count rates (1×10^5 cps), and adjusting the voltage on the electron multipliers resulted in short-term gain instability (time scale of many hours) that could not be accounted for. Now, we check the pulse height distribution and adjust the voltage on the electron multipliers in order to optimize the gain of the detectors at the beginning of each SIMS session, and we then refrain from making any further adjustments. We analyze standards several times to characterize the gains at the beginning of the measurement session. Then we measure the standards throughout each day and use sample-standard bracketing to monitor and correct for drift in the gains of the detectors.

Complications from the relative sensitivity factor: Uncertainties in the relative sensitivity factor ($^{56}Fe/^{61}Ni_{true}/\ ^{56}Fe^{+}/^{61}Ni^{+}_{measured}$) can stem from using different beam currents for the standards and samples or using non-matrix-matched standards. The Fe and Ni content of chondrule pyroxene compositions range from 4 to 7 at.% and 0 to 0.01 at.% respectively. The Fe and Ni content for our synthetic standard and hypersthene standard are very similar to those of our chondrules, but we often use San Carlos

pyroxene, which has an Fe content of 1.7 at.% and Ni of 0.03 at.% which is quite different from our samples. To deal with the different sensitivity factors, we apply a relative sensitivity factor correction to the Fe/Ni ratios.

The Fe/Ni ratio varies with time during a SIMS measurement. This can result in variations in the relative sensitivity factor depending on the length of the measurements. To account for this, we measure standards and samples for the same amount of time, even though we don't need all the cycles to get the precision we need on the standards (an alternative strategy is to determine the Fe/Ni sensitivity factor from a limited set of cycles that are always part of the measurement).

2.3.3 *Data Analysis*

Calculating isotope ratios from counting data results in a positive bias that correlates inversely with the number of counts of the normalizing isotope (e.g., Ogliore et al., 2011). Calculating ratios by averaging the ratios from each measurement cycle makes this problem worse because a cycle has fewer counts than the total measurement. The measured Fe/Ni ratios vary by up to one order of magnitude. Because the Fe concentration varies by only a few percent, the variation in Fe/Ni ratio is almost entirely due to the Ni concentration. Thus, the higher the Fe/Ni ratio, the lower the Ni counts and the greater the bias in the Ni-isotope ratio. This produces a correlation on an isotope plot that resembles an isochron. Ratio bias propagates into the slope of the isochron in different ways depending on how the data are reduced. For the ^{60}Fe-^{60}Ni system, an internal mass-fractionation correction using biased ratios produces a positive bias in the slope of the isochron when normalizing with ^{61}Ni, or a small negative bias in the slope

when normalizing with ^{62}Ni (Telus et al., 2012a; Chapter 4). In order to significantly reduce the effect of ratio bias, isotope ratios reported here were calculated from total counts, a less-biased method of calculating ratios (Ogliore et al., 2011). This method involves summing the counts of the numerator isotope over all cycles and dividing by the summed counts of the denominator isotope over all cycles. To further ensure that ratio bias is not an issue, we check that the data normalized to ^{61}Ni and ^{62}Ni, which differ in abundance by a factor of ~3, are consistent.

Since we collected the data in cycles, we were able to include time interpolation and remove anomalous cycles due to spikes in the detector signal from Ni-rich phases, electronic noise, or primary beam dropout. The data were corrected for electron multiplier background (typically measured overnight at the end of the session for 5-10 hours without the primary beam) and electron multiplier deadtime. Drift in the electron multiplier gain was corrected using sample-standard bracketing (for multicollection analyses only). Extraneous counts on the Ni peaks from the tails of interferences were corrected using the tail-to-peak ratio (~1×10^{-5}) determined from measuring counts at the Ni peaks and counts at a few points along the tails, to the low-mass side of each Ni peak. Contributions of tails of interferences onto Ni isotope counts are typically 50-300‰ for ^{60}Ni, 5-20‰ for ^{61}Ni, 20-80‰ for ^{62}Ni, respectively. Uncertainties on the measured ratios include the standard error of the ratios calculated from individual cycles and uncertainties propagated from standard-sample bracketing. This allows us to account for non-statistical cycle-to-cycle variations during the each measurement. To calculate excess in ^{60}Ni, we applied a linear internal mass-fractionation correction (*i.e.*, $\Delta^{60}Ni=\delta^{60}Ni + \delta^{61}Ni$). Reference values of 23.0068 and 3.1884 were used for ^{60}Ni/^{61}Ni and ^{62}Ni/^{61}Ni,

respectively (Chen et al. 2009). There is no significant difference when an external mass-fractionation correction is used instead of the internal mass-fractionation correction. Relative sensitivity factors ($^{56}Fe/^{61}Ni_{true}/\ ^{56}Fe^{+}/^{61}Ni^{+}_{measured}$) for the $^{56}Fe/^{61}Ni$ ratios for olivine and pyroxene were applied based on the $^{56}Fe^{+}/^{61}Ni^{+}$ ratios of standards (San Carlos olivine, San Carlos pyroxene, hypersthene, or synthetic pyroxene) measured by SIMS and the Fe/Ni ratios measured by electron microprobe. The quoted uncertainties on the Fe/Ni ratios are dominated by the uncertainty on the sensitivity factor and are given as 5% of the measured ratios.

The initial $^{60}Fe/^{56}Fe$ ratio for each chondrule is inferred from the error-weighted regression of $^{60}Ni/^{61}Ni$ (or $^{60}Ni/^{62}Ni$) vs. $^{56}Fe/^{61}Ni$ (or $^{56}Fe/^{62}Ni$). Uncertainties on the isochron slopes are reported as 2σ. For chondrules that do not have resolved initial ratios the upper limits are reported as 2σ 1-sided upper limits. For each isochron, we report the mean square weighted deviation (MSWD), which characterizes how well the data fit the regression. Well-correlated regressions will have MSWDs close to 1.

2.4 Results

Initial $^{60}Fe/^{56}Fe$ ratios from our chondrule data fall into four main groups: 1) those with large uncertainties due to low Fe/Ni ratios, 2) those with large uncertainties due to insufficient spread in Fe/Ni ratio, 3) those that have unresolved initial ratios despite having high Fe/Ni ratios, and 4) those with resolved initial ratios, but large MSWD values.

2.4.1 *Initial ratios with large uncertainties due to low Fe/Ni ratios*

The uncertainty on the initial ratios can be quite large if the Fe/Ni ratios are too low. For example, Semarkona chondrule, SMKMT r1, is a porphyritic pyroxene chondrule that has $^{56}Fe/^{62}Ni$ ratios less than 1×10^{5}, with a range of 8×10^{4}. The initial ratio (solid line) is unresolved with an upper-limit of 4×10^{-7} (Figure 2.2). At these Fe/Ni ratios, the uncertainties on the $^{60}Ni/^{62}Ni$ ratios of ~5‰ (or ~3‰ for $^{60}Ni/^{61}Ni$ ratios) do not permit us to resolve an initial ratio of 2×10^{-7} (dashed reference line in Figure 2.2). Including the data for the standards does not provide significantly better constraints on the initial ratio. Four chondrules (SMKMT r1, SMK312B-Q, QUE ch1, BM80 ch18) fall into this category (refer to Table 2.1 for initial ratios and Appendix A for complete data set).

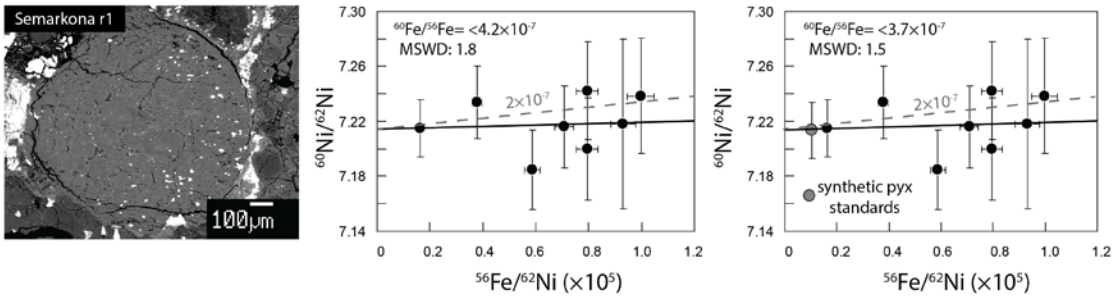

Figure 2.2. Backscattered-electron image for Semarkona chondrule, SMKMT r1, and isochron with and without the standard data. The large uncertainty on the initial ratios is attributed to low Fe/Ni ratios. An initial ratio of 2×10^{-7} cannot be resolved with these uncertainties.

2.4.2 *Initial ratios with large uncertainties due to limited spread in Fe/Ni ratios*

The uncertainties on the initial ratios can be quite large when there is a lack of spread in the Fe/Ni ratios. For example, Krymka chondrule, KRM94 ch3, and Bishunpur chondrule, BM23 ch25, are porphyritic olivine chondrules. They not only have low Fe/Ni

ratios (<1×10^{5}), but they lack significant range in the Fe/Ni ratios (~2×10^{4}). This makes it difficult to constrain the initial ratios for these chondrules. They have upper-limits well over 5×10^{-7}, especially when the standards are not included in the regression. QUE97008 chC is a cryptocrystalline pyroxene chondrule with very high Fe/Ni ratios (up to 1.5×10^{6}), but a relatively limited spread in the Fe/Ni ratios. Six chondrules (QUE chM, QUE chC, BVG ch18, BM23 ch25, KRM94 ch3) fall into this category (see Table 2.1 for initial ratios and Appendix A for complete data sets). The initial ratios for these chondrules are best constrained by including the standard data in the regression (Figure 2.3).

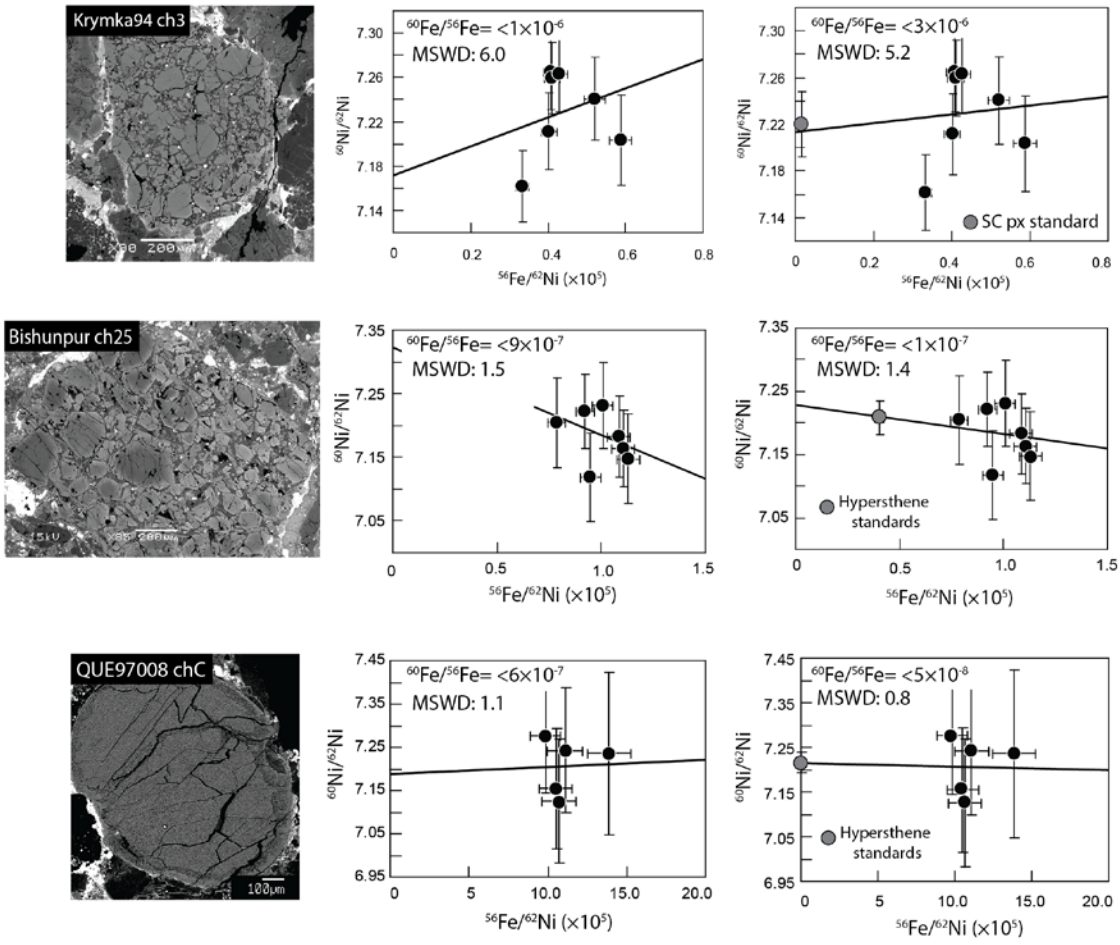

Figure 2.3. Backscattered electron image and Fe-Ni SIMS data for chondrules with initial ratios with large uncertainties due to having a limited spread in the Fe/Ni ratios. Including the standard data in the regression usually significantly reduces the uncertainties.

2.4.3 *Unresolved initial ratios, despite high Fe/Ni ratios*

Some of our chondrules have very high initial ratios, but do not show evidence for excess ^{60}Ni. Krymka chondrule KRM94 ch1 and EET90161 chondrule r1 are large (>1 mm) chondrules with high ^{56}Fe/^{62}Ni ratios (> 8×10^5), but the inferred initial ratios are unresolved from zero (Figure 2.4). Five chondrules (QUE chC, BM23 ch12, BM23 ch9, KRM94 ch1, KRM93 ch1) fall into this category (see Table 2.1 for initial ratios and Appendix A for complete data sets). With such high Fe/Ni ratios, an initial ratio $>2\times10^{-7}$ should easily be resolved, but there is no evidence for such high initial ratios for these chondrules.

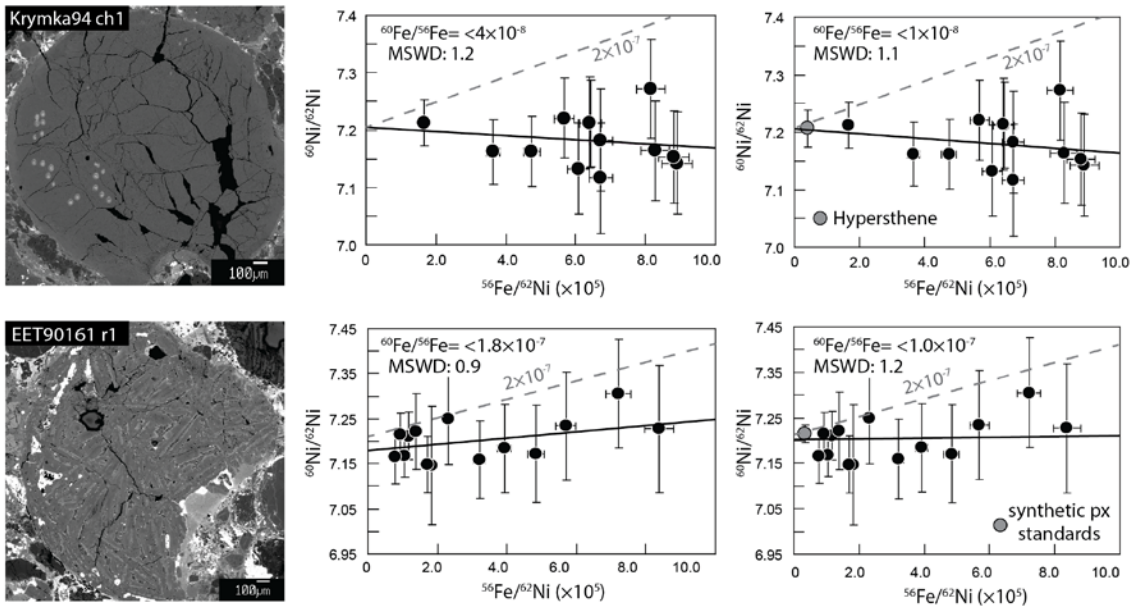

Figure 2.4: Backscattered electron image and Fe-Ni SIMS data for Krymka chondrule KRM94 ch1 and EET90161 chondrule r1. The regressions with and without the standards are shown. Despite the high Fe/Ni ratios, the initial ratios are unresolved from zero and inconsistent with initial ratios $>2\times10^{-7}$.

2.4.4 *Resolved initial ratios, but large MSWD values*

Four of the chondrules we analyzed have resolved initial ratios; however the MSWD values are much greater than 1, indicating the correlation between the ^{60}Ni excesses and the Fe/Ni ratios is weak . Semarkona chondrule, DAP1, is a ~1 mm bleached radial-pyroxene chondrule with sulfide stringers that stretch across the entire length of the chondrule (Figure 2.5). For our SIMS analyses, we targeted areas between sulfide stringers. The bleached regions are fairly obvious and easy to avoid. However, submicron sulfide grains that are scattered throughout the chondrule could not always be avoided with our spot size. Iron-Ni isotopic data for DAP1 were collected during three separate sessions. In every case, excesses in ^{60}Ni are present, but do not correlate well with the Fe/Ni ratio. The initial ratios inferred from these analyses are mostly consistent (see Table 2.1). The initial ratio inferred from our most recent analysis of this chondrule is $(1.9\pm1.0)\times10^{-7}$, but the MSWD is 3.8 (Figure 2.5). The average ^{60}Ni excess (from all spot analyses) is ~14‰ and the maximum excesses range up to ~20±7‰. Including the hypersthene standards in the regression increases the initial ratio by a factor of ~1.5.

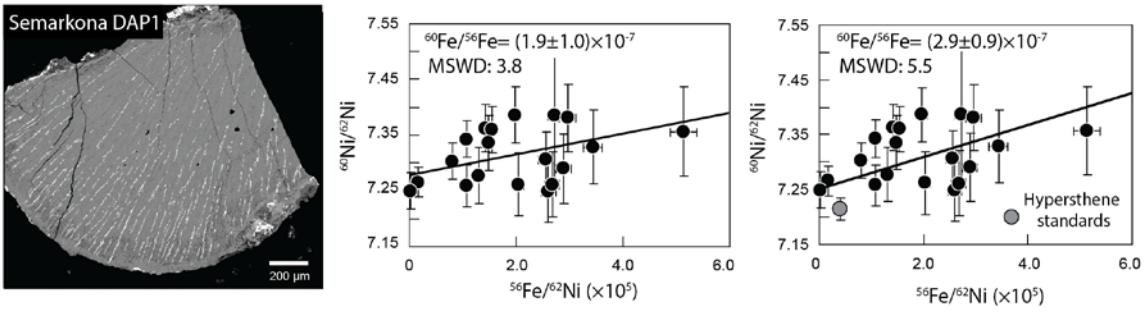

Figure 2.5: Backscattered electron image and Fe-Ni SIMS data for Semarkona chondrule DAP1. The regressions with and without the weighted mean of the standard data are shown. The ^{60}Ni/^{62}Ni and the Fe/Ni ratios are weakly correlated.

Bishunpur chondrule BM80 ch13 is a porphyritic olivine and pyroxene chondrule (~750 μm across) with glassy mesostasis (Figure 2.6). We measured both olivine and pyroxene grains. We aimed to avoid Fe-rich veins for our spot analyses. The synchrotron map for this chondrule shows that 4 spots analyses are clearly compromised by extraneous Fe-Ni material (Telus et al., 2015a; Chapter 3). These spots were excluded for the regression in Figure 2.6. The initial ratio of $(1.1\pm0.6)\times10^{-6}$ inferred from the chondrule data alone is quite large and implies an intercept of -10‰, which is unlikely. The regression with the standards ($(3.8\pm3.4)\times10^{-7}$; MSWD of 1.8) provides the best constraint for the initial ratio of this chondrule (Figure 2.6). The average ^{60}Ni excess (from all spot analyses) is ~6‰, with maximum excesses of ~15±14‰.

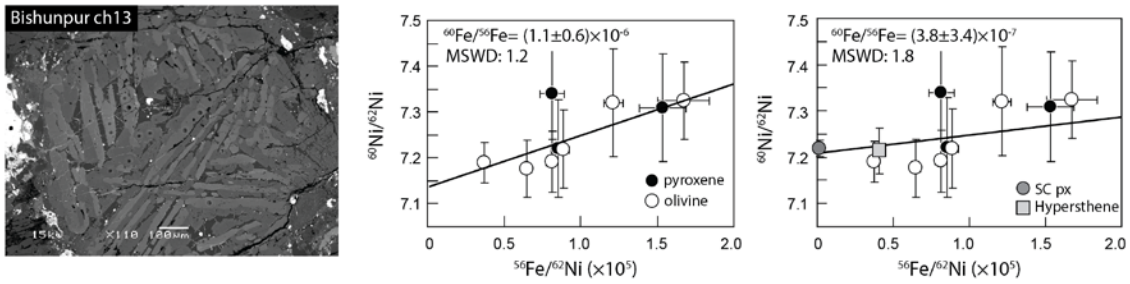

Figure 2.6: Backscattered electron image and Fe-Ni SIMS data for Bishunpur porphyritic olivine-pyroxene chondrule BM80 ch13. The regression without the standards gives a very high initial ratio of $(1.1\pm0.6)\times10^{-6}$. When the weighted mean of the standards is included in the regression, the initial ratio of $(3.8\pm3.4)\times10^{-7}$ with an MSWD of 1.8 is inferred. Including both the San Carlos pyroxene and hypersthene standards provides a better constraint on the initial ratio in this case.

Krymka chondrule KRM93 ch11 is a large (>1 mm) heavily fractured cryptocrystalline pyroxene chondrule (Figure 2.7). Submicron sulfide blebs are also pervasive in this chondrule and were impossible to avoid for our spot analyses. We aimed to avoid large fractures but many of the fine fractures could not be avoided. This

chondrule was analyzed on two separate occasions. The initial ratio inferred from the combined datasets and including hypersthene terrestrial standards is $(2.7\pm1.0)\times10^{-7}$ (Figure 2.7). Without the standards, the slope of the combined data is $(1.9\pm1.2)\times10^{-7}$. These values are very similar to those for SMKDAP1 (Figure 2.5). The MSWD values for these regressions are ~2, indicating that the Fe-Ni data is not well-correlated. The average of the ^{60}Ni excess (from all spot analyses) is ~6‰, with maximum excesses of ~11±8‰.

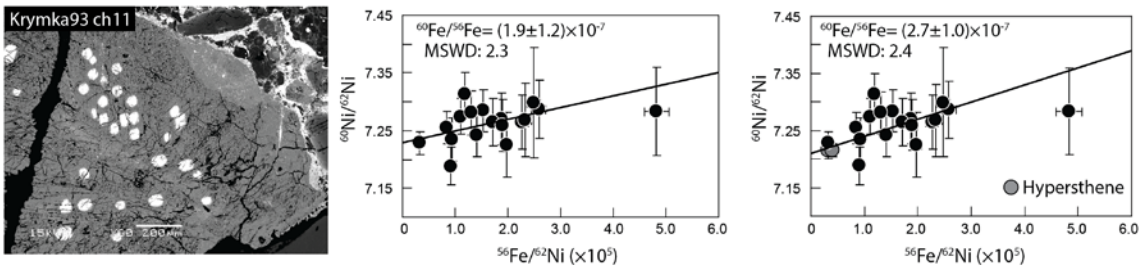

Figure 2.7: Backscattered electron image and Fe-Ni SIMS data for Krymka chondrule KRM9-3 ch11, which was analyzed during two sessions. The weighted mean of the hypersthene terrestrial standard data for both sessions is included in the regression on the right.

QUE97008 ch5 is a porphyritic olivine pyroxene chondrule. The initial ratio inferred for this chondrule is $(1.9\pm0.5)\times10^{-6}$ without the standards and $(1.7\pm0.4)\times10^{-6}$ when the standards are included in the regression (Figure 2.8). This is the highest initial ratio we have inferred from our data. However, the MSWD values are ~4.The average of the ^{60}Ni excess (from all spot analyses) is ~16‰, with maximum excesses of ~30±15‰. This chondrule was not analyzed for Fe-Ni distribution at the synchrotron because the grains are too small to suppress the Fe and Ni signal from the stainless steel bullet they are mounted in. Therefore, we cannot comment on the degree to which this sample has been affected by Fe-Ni redistribution.

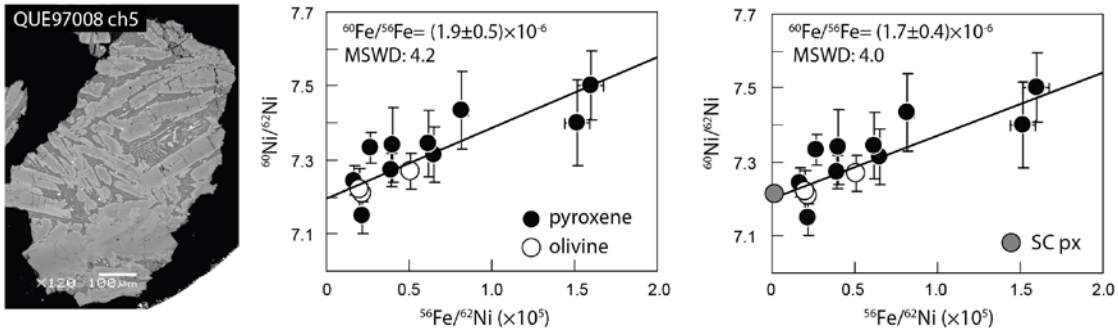

Figure 2.8. Backscattered electron image and Fe-Ni SIMS data for QUE97008 chondrule QUE ch5. The weighted mean of the San Carlos pyroxene terrestrial standard data is included in the regression on the right.

2.4.5 *Constraining the initial $^{60}Fe/^{56}Fe$ ratio of UOC chondrules*

In order to evaluate the influence of ratio bias on the initial ratios, we regressed the data for each chondrule using ratios normalized to ^{61}Ni and ^{62}Ni. To better constrain the initial ratio, we also regressed the data for each chondrule with and without the standards. The initial ratios inferred from these four different regressions are listed in Table 2.1.

It is important to calculate the initial ratios using both the ^{61}Ni and ^{62}Ni normalization to monitor the extent of ratio bias, which propagates into the isochron differently depending on how the mass-fractionation correction is made and depending on which normalizing isotope is used (Telus et al., 2012a). An internal mass-fractionation of biased ratios using ^{62}Ni/^{61}Ni results in under-correcting the ^{60}Ni/^{61}Ni ratios and introducing a positive bias in the inferred initial ratio. When the ^{62}Ni normalization is used instead, an internal mass-fractionation correction results in over-correcting the ^{60}Ni/^{62}Ni ratios, producing a negative bias in the initial ratio. Also, since ^{62}Ni has more counts, using it as the normalizing isotope generally gives results that are less biased.

When ratio bias is accounted for by summing the counts from each cycle of a measurement instead of averaging the counts from each cycle (Ogliore et al., 2011), the choice of normalizing isotope for the nickel isotope ratios (^{61}Ni or ^{62}Ni) does not change the result. However, the uncertainty for ratios normalized to ^{62}Ni is systematically larger than for ratios normalized to ^{61}Ni due to the mass-fractionation correction (the uncertainty on the ^{61}Ni/^{62}Ni ratio is multiplied by 2). Initial ratios determined from ratios normalized to ^{61}Ni and ^{62}Ni are consistent (see Table 2.1).

Determining the initial ratio with and without the standards is important because the intercept for most of the regressions is not well-constrained. Including the standards often helps to better constrain the initial ratios, especially when the range in the Fe/Ni ratios is not sufficiently large (e.g., Figure 2.3).

We determined which of the four regressions for each chondrule provides the best estimate of the initial ratio by filtering the results in Table 2.1 according to the regression with the MSWD values closest to 1. For example, the best regression for chondrule SMKMT r1 is the one with an MSWD of 1.0, while the best regression for QUE ch5 is the one with the MSWD of 4.0 (Table 2.1). In general, regressions using the ^{62}Ni normalization have the lowest MSWD values because the uncertainty is greater than for the ^{61}Ni normalization (see above). The results of this filter are shown in Figure 2.9 and listed in Table 2.2. With this filter, we see that a few chondrules have resolved initial ratios; most have initial ratios that are unresolved from zero.

Table 2.1. Regressions for Fe-Ni chondrule data calculated using the ^{61}Ni and ^{62}Ni normalized ratios. Also regressions for each chondrule determined with and without the standard data. The most reliable regression determined from the MSWD values is highlighted in grey.

Chondrule Name	Normal-ization	Initial ratio ($\times10^{-7}$) without standards	MSWD	Initial ratio ($\times10^{-7}$) with standards	MSWD
SMK312B-E	^{61}Ni	-0.3019 ± 2.229	2.1	-0.6632 ± 1.184	1.6
	^{62}Ni	-0.3387 ± 3.732	0.8	-0.5438 ± 1.962	0.9
SMK312B-Q	^{61}Ni	-1.122 ± 6.879	0.8	-2.499 ± 3.008	0.9
	^{62}Ni	-1.003 ± 11.49	0.3	-1.817 ± 4.911	0.7
SMK1805-T	^{61}Ni	-1.749 ± 2.560	2.0	-2.141 ± 1.014	1.7
	^{62}Ni	-1.960 ± 4.278	0.8	-1.892 ± 1.682	0.9
SMKMT r1	^{61}Ni	0.5088 ± 2.528	4.2	0.6778 ± 1.687	2.4
	^{62}Ni	0.4992 ± 3.909	1.8	0.6794 ± 2.609	1.0
SMKDAP1	^{61}Ni	1.875 ± 0.6247	9.0	1.991 ± 0.6200	9.0
	^{62}Ni	1.867 ± 0.9670	3.8	2.131 ± 0.9502	4.1
SMKDAP1	^{61}Ni	0.5344 ± 1.063	2.7	0.5184 ± 1.023	2.6
	^{62}Ni	0.5389 ± 1.642	1.1	0.5264 ± 1.578	1.1
SMKDAP1	^{61}Ni	0.8177 ± 1.653	2.3	-0.2069 ± 1.553	2.8
	^{62}Ni	0.8012 ± 2.564	1.0	-0.3010 ± 2.396	1.2
SMKDAP2	^{61}Ni	-0.9043 ± 0.9316	2.9	-0.7488 ± 0.9185	2.9
	^{62}Ni	-0.8963 ± 1.437	1.2	-0.7397 ± 1.417	1.2
SMKDAP2	^{61}Ni	-0.9802 ± 0.9917	2.6	-1.140 ± 0.9104	2.4
	^{62}Ni	-0.3218 ± 1.489	1.4	-0.6844 ± 1.279	1.4
SMK1805-1	^{61}Ni	2.407 ± 1.803	1.7	0.7765 ± 1.390	2.7
	^{62}Ni	2.401 ± 2.785	0.7	0.7613 ± 2.141	1.2
SMK1805-1	^{61}Ni	-2.884 ± 2.459	0.9	0.3319 ± 0.7820	1.7
	^{62}Ni	-2.867 ± 3.756	0.3	0.3405 ± 1.207	0.7
QUE ch3	^{61}Ni	0.8940 ± 1.028	2.2	0.8066 ± 1.022	2.2
	^{62}Ni	1.123 ± 1.638	1.1	1.027 ± 1.626	1.1
QUE ch5	^{61}Ni	19.57 ± 3.298	9.7	17.19 ± 2.590	9.4
	^{62}Ni	19.37 ± 4.988	4.2	17.09 ± 3.928	4.0
QUE chK	^{61}Ni	-2.078 ± 2.110	2.3	-1.503 ± 1.573	2.2
	^{62}Ni	-1.993 ± 3.143	1.0	-1.445 ± 2.342	0.9
QUE chI	^{61}Ni	0.7651 ± 2.116	1.0	-1.199 ± 1.623	0.4
	^{62}Ni	0.7632 ± 3.284	0.4	-1.200 ± 2.515	0.6
QUE chM	^{61}Ni	-0.3816 ± 16.96	0.4	4.560 ± 3.245	0.4
	^{62}Ni	-0.4072 ± 26.11	0.2	4.542 ± 5.006	0.2
QUE chC	^{61}Ni	0.4591 ± 3.583	2.6	-0.0890 ± 0.4092	2.0
	^{62}Ni	0.1493 ± 5.531	1.1	-0.0888 ± 0.6553	0.8
QUE chF	^{61}Ni	-0.1319 ± 0.7659	5.5	0.5424 ± 0.6639	7.2
	^{62}Ni	-0.1230 ± 1.179	2.3	0.5439 ± 1.022	3.0
QUE ch6	^{61}Ni	-0.5273 ± 1.157	1.9	0.0129 ± 0.7840	1.8
	^{62}Ni	-0.5389 ± 1.784	0.8	0.0079 ± 1.210	0.7
QUE ch1	^{61}Ni	-13.49 ± 6.768	0.7	-7.655 ± 3.805	0.9
	^{62}Ni	-13.49 ± 10.43	0.3	-7.659 ± 5.874	0.4

EET r1	^{61}Ni	-0.0331	± 0.7306	2.2	-0.6490	± 0.5327	1.7
	^{62}Ni	-0.0313	± 1.132	0.9	-0.6434	± 0.8252	0.7
EET r4	^{61}Ni	-0.1802	± 2.245	1.4	-1.973	± 1.332	1.3
	^{62}Ni	-0.2447	± 4.792	0.6	-2.700	± 2.831	0.6
BM80 r40	^{61}Ni	2.090	± 4.051	0.7	-4.277	± 1.382	2.5
	^{62}Ni	2.017	± 6.296	1.2	-4.245	± 2.142	1.0
BM23 ch13	^{61}Ni	0.1442	± 1.238	1.8	-0.2648	± 0.5793	1.6
	^{62}Ni	0.1470	± 1.912	0.7	-0.2599	± 0.8949	0.7
BM23 ch9	^{61}Ni	-0.1790	± 1.141	2.1	-0.5852	± 0.6553	2.0
	^{62}Ni	-0.1899	± 1.764	0.9	-0.5814	± 1.012	0.8
BM23 ch25	^{61}Ni	-13.41	± 14.75	3.7	-4.708	± 3.822	3.3
	^{62}Ni	-13.38	± 22.49	1.5	-4.698	± 5.884	1.4
BM23 ch12	^{61}Ni	-1.147	± 1.280	2.1	-1.375	± 0.9420	1.9
	^{62}Ni	-1.145	± 1.980	0.9	-1.362	± 1.458	0.8
BVG ch1	^{61}Ni	1.131	± 1.384	2.9	-2.107	± 1.006	8.3
	^{62}Ni	1.153	± 2.146	1.2	-2.092	± 1.529	3.4
BVG ch18	^{61}Ni	5.263	± 13.23	2.0	-3.107	± 4.197	1.9
	^{62}Ni	5.141	± 20.51	0.8	-2.374	± 6.127	0.8
BM80 ch18	^{61}Ni	-4.670	± 5.418	4.8	-1.038	± 3.281	4.5
	^{62}Ni	-4.539	± 8.347	2.0	-0.9507	± 5.063	1.9
BM80 ch37	^{61}Ni	2.899	± 4.426	1.9	1.683	± 3.146	1.9
Mono	^{62}Ni	3.271	± 6.345	0.9	1.718	± 4.453	0.9
BM80 ch37	^{61}Ni	0.8464	± 15.16	0.6	1.720	± 2.472	0.5
Multi	^{62}Ni	0.5863	± 23.10	0.2	1.724	± 3.801	0.2
BM80 ch37	^{61}Ni	1.341	± 3.136	1.7	1.088	± 1.927	2.2
Combined	^{62}Ni	1.438	± 4.615	0.8	0.6334	± 2.843	1.2
BM80 ch13	^{61}Ni	11.18	± 4.054	2.8	3.803	± 2.199	4.3
	^{62}Ni	11.21	± 6.284	1.2	3.816	± 3.379	1.8
KRM94 ch1	^{61}Ni	-0.3866	± 0.5111	3.0	-0.4081	± 0.3611	2.7
	^{62}Ni	-0.3878	± 0.7903	1.2	-0.4070	± 0.5582	1.2
KRM94 ch3	^{61}Ni	15.67	± 11.69	14	3.908	± 4.429	12
	^{62}Ni	12.79	± 18.01	6.0	3.729	± 6.839	5.2
KRM93 ch1	^{61}Ni	0.8169	± 1.597	0.0	-0.2521	± 0.3746	0.5
	^{62}Ni	0.8279	± 2.492	0.0	-0.2524	± 0.5783	0.1
KRM93 ch11	^{61}Ni	1.691	± 2.832	1.3	2.243	± 1.528	0.9
	^{62}Ni	1.686	± 4.372	0.6	2.238	± 2.353	0.4
KRM93 ch11	^{61}Ni	2.765	± 0.666	18.7	2.441	± 0.578	17.6
	^{62}Ni	2.110	± 1.228	2.7	2.750	± 1.063	2.8
KRM93 ch11	^{61}Ni	2.752	± 0.6432	14.3	2.399	± 0.540	12.9
Combined	^{62}Ni	1.921	± 1.162	2.2	2.655	± 0.969	2.3

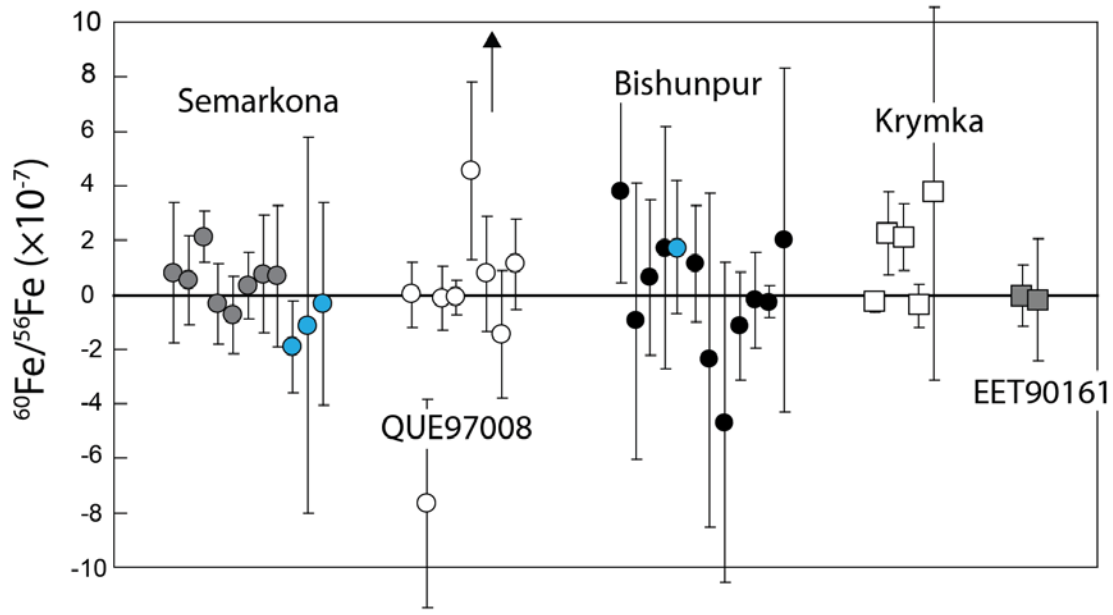

Figure 2.9. Initial $^{60}Fe/^{56}Fe$ ratios of UOC chondrules. The data for each chondrule were regressed in four different ways. The regression from Table 2.1 with the MSWD value closest to 1 is considered the best regression for each chondrule. These regressions are listed in Table 2.2. The upward-pointing arrow points to where chondrule QUE97008 ch5 plots ($(^{60}Fe/^{56}Fe)_0 = 1.7\times10^{-6}$). The blue points were measured in monocollection mode, while all other measurements were in multicollection mode. There are no systematic differences between monocollection and multicollection analyses.

Table 2.2. Initial $^{60}Fe/^{56}Fe$ ratios for various UOC chondrules. Filtered according to MSWD values from Table 2.1. Data highlighted in grey have MSWD values between 0.5 and 1.5 and uncertainties $<3\times10^{-7}$.

Semarkona (LL3.00)				
Chondrule	**$^{60}Fe/^{56}Fe$ $\times10^{-7}$ (2σ)**	**MSWD**	**UL[a]**	**Avg. $\delta^{60}Ni$‰ (2SD)[b]**
SMK312B-E	-0.3 ± 3.7	0.8	2.7	-2.0 ± 23.9
SMK312B-Q	-1.1 ± 6.9	0.8	3.7	-6.9 ± 17.6
SMK1805-T	-1.9 ± 1.7	0.9	-0.5	-5.3 ± 21.6
SMKMT r1	0.7 ± 2.6	1.0	2.8	0.7 ± 5.4
SMK DAP1	2.1 ± 1.0	4.1	-	13.7 ± 13.7
[d]SMK DAP1	0.5 ± 1.6	1.1	1.9	1.6 ± 19.2
[d]SMK DAP1	0.8 ± 2.6	1.0	2.9	-4.5 ± 12.6
SMK DAP2	-0.7 ± 1.4	1.2	0.4	0.9 ± 10.5
[d]SMK DAP2	-0.3 ± 1.5	1.4	0.9	-5.2 ± 21.8
SMK1805 ch1	-0.3 ± 1.2	0.7	1.3	3.3 ± 22.1
[d]SMK1805 ch1	0.8 ± 2.1	1.2	2.5	-0.3 ± 9.3
QUE97008 (L3.05)				
Chondrule	**$^{60}Fe/^{56}Fe$ $\times10^{-7}$ (2σ)**	**MSWD**	**UL[a]**	**Avg. $\delta^{60}Ni$‰* (2SD)[b]**

QUE ch3	1.1 ± 1.6	1.1	2.5	2.5 ± 19.0
QUE ch5	17.1 ± 3.9	4.0	-	15.6 ± 24.9
QUE chK	-1.4 ± 2.3	0.9	0.5	-0.9 ± 7.8
QUE ch I	0.8 ± 2.1	1.0	2.5	-2.5 ± 4.4
QUE chM	4.6 ± 3.2	0.4	-	3.6 ± 2.1
QUE chC	-0.1 ± 0.7	0.8	0.4	-1.1 ± 17.7
QUE chF	-0.1 ± 1.2	2.3	0.8	4.6 ± 14.3
QUE ch6	0.0 ± 1.2	0.7	1.0	1.5 ± 8.4
QUE ch1	-7.7 ± 3.8	0.9	-	-3.0 ± 5.7
EET90161 (L3.05)				
Chondrule	**^{60}Fe/^{56}Fe ×10^{-7} (2σ)**	**MSWD**	**UL[a]**	**Avg. δ^{60}Ni‰* (2SD)[b]**
EET r1	0.0 ± 1.1	0.9	0.9	-3.4 ± 1.8
EET r4	-0.2 ± 2.2	1.4	1.7	-4.1 ± 5.4
Bishunpur (LL3.1/3.15)				
Chondrule	**^{60}Fe/^{56}Fe ×10^{-7} (2σ)**	**MSWD**	**UL[a]**	**Avg. δ^{60}Ni‰* (2SD)[b]**
BM80 r40	2.0 ± 6.3	1.2	4.5	-2.9 ± 8.5
BM23 ch13	-0.3 ± 0.6	1.6	0.2	-2.4 ± 16.1
BM23 ch9	-0.1 ± 1.8	0.9	1.3	-3.9 ± 16.4
BM23 ch12	-1.1 ± 2.0	0.9	0.5	-5.8 ± 17.7
BM23 ch25	-4.7 ± 5.9	1.4	0.9	-3.6 ± 11.4
BVG ch1	1.2 ± 2.1	1.2	2.9	-9.5 ± 23.0
BVG ch18	-2.4 ± 6.1	0.8	2.7	-2.6 ± 7.0
BM80 ch18	-1.0 ± 5.0	1.9	3.1	-0.4 ± 30.8
[c]BM80 ch37	0.6 ± 2.8	1.2	3.0	3.3 ± 50.3
[d]BM80 ch37	1.7 ± 4.4	0.9	4.4	4.5 ± 55.5
[d]BM80 ch37	1.7 ± 2.5	0.5	3.7	5.4 ± 12.4
BM80 ch13	3.8 ± 3.4	1.8	-	0.1 ± 23.1
Krymka (LL3.2)				
Chondrule	**^{60}Fe/^{56}Fe ×10^{-7} (2σ)**	**MSWD**	**UL[a]**	**Avg. δ^{60}Ni‰* (2SD)[b]**
KRM94 ch 1	-0.4 ± 0.8	1.2	0.3	-3.6 ± 12.1
KRM94 ch 3	3.7 ± 6.8	5.2	4.7	1.3 ± 10.7
KRM93 ch 1	-0.2 ± 0.4	0.5	0.1	-3.7 ± 5.8
[c]KRM93 ch 11	2.7 ± 1.0	2.3	-	6.2 ± 8.0
[d]KRM93 ch 11	2.2 ± 1.5	0.9	-	4.4 ± 5.8
[d]KRM93 ch 11	2.8 ± 1.1	2.8	-	0.4 ± 12.0

[a] UL: Upper limit (×10^{-7}) is calculated from the 2σ-1-sided upper limit of the Gaussian distribution for each initial ratio. [b] Averaged excess ^{60}Ni (δ^{60}Ni‰*) of all spot analyses for each chondrule. [c] Combined data from different SIMS sessions. [d] Duplicate analyses during different SIMS session.

2.4.6 *Identifying our best chondrule datasets and constraining upper limits*

In order to identify which chondrules provide the best constraints on the initial ^{60}Fe/^{56}Fe ratio of UOC chondrules, we placed further constraints on the filtered data

plotted in Figure 2.9. We consider chondrules with uncertainties on their inferred initial $^{60}Fe/^{56}Fe$ values of less than 3×10^{-7} and MSWD values between 0.5 and 1.5 to provide the best data (Figure 2.10a). These filters allow us to choose chondrules that have well-correlated isochrons and relatively small uncertainties. For example, chondrules with large uncertainties due to low Fe/Ni ratios (Figure 2.2) or lack of spread in the Fe/Ni ratios (Figure 2.3) are filtered out, and chondrules with poorly correlated data (Figures 2.5-2.8) are also filtered out. The results of this second filter are highlighted in grey in Table 2.2 and shown in Figure 2.10b. Now, only one chondrule (KRM93 ch11) is resolved $(2.2\pm1.5)\times10^{-7}$, while the others are unresolved from zero.

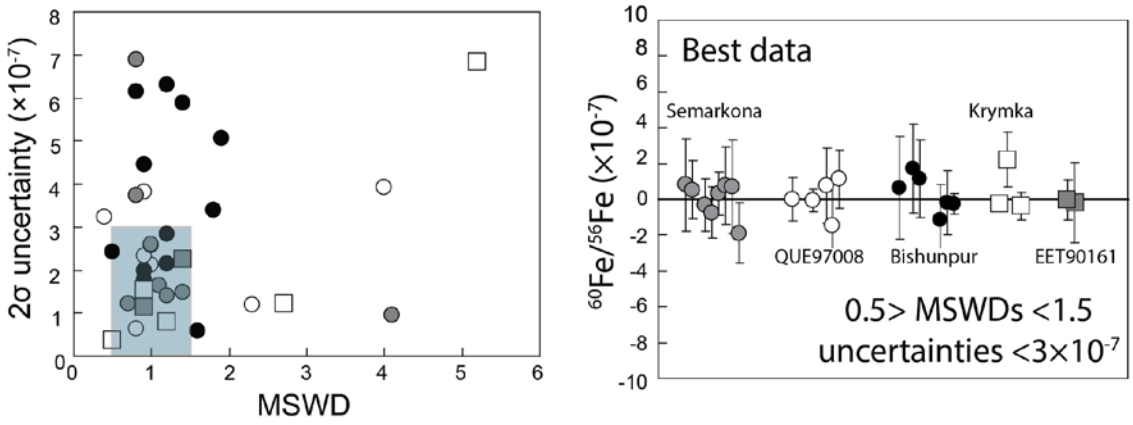

Figure 2.10. The MSWD values vs. the 2σ-uncertainty on the initial $^{60}Fe/^{56}Fe$ ratios from Table 2.2 (a) and initial ratios when the data are filtered according to MSWD values between 0.5 and 1.5 and 2σ-uncertainties $<3\times10^{-7}$ (b).

2.4.7 *Constraining the upper limit on the initial $^{60}Fe/^{56}Fe$ ratio of UOC chondrules*

To constraint the upper limits of chondrules with unresolved initial ratios listed in Table 2.2, we use the slope of the regression and the 1σ-uncertainty to draw a Gaussian distribution and determine the initial ratio at which 95% of the distribution is below that value. This calculation gives the 2σ 1-sided upper limit on the initial ratio. Figure 2.11 is

an example of the SIMS data, the Gaussian distribution and upper limit for one of these chondrules. The 2σ 1-sided upper limit for each chondrule is listed in Table 2.2 under the column labeled "UL".

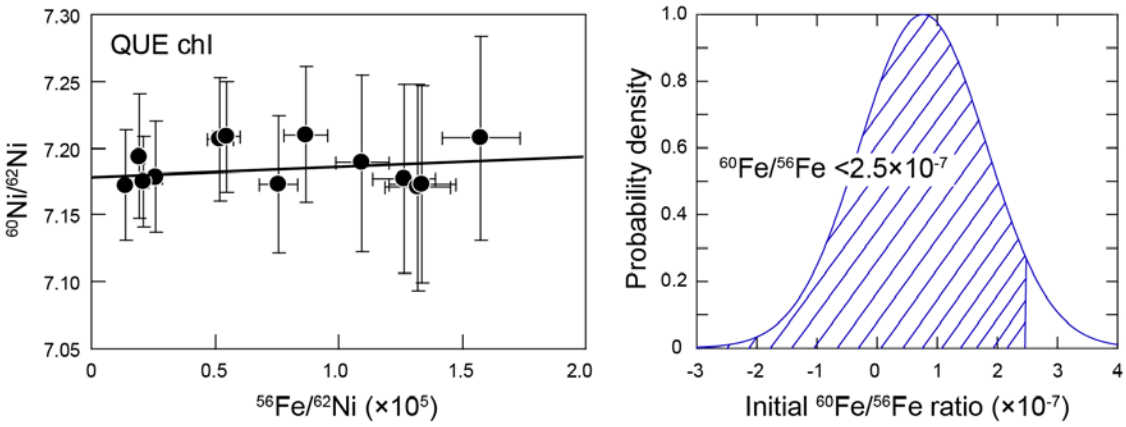

Figure 2.11. Fe-Ni SIMS data and Gaussian probability distribution function for QUE97008 chondrule chI.

If we assume that the initial ratios for all of these chondrules reflect their formation time, and not secondary processing, we can constrain the upper limit on the ^{60}Fe/^{56}Fe ratio at the time the chondrules formed. The Gaussian distributions produced to determine the upper limits for each chondrule (e.g., Figure 2.11) can be summed to give a distribution for the entire data set. The individual distributions for the chondrules in Table 2.2 and their sum are shown in Figure 2.12. The 2σ 1-sided upper limit for the summed distribution is 2.6×10^{-7}, consistent with the resolved initial ratio of $(2.2\pm1.5)\times10^{-7}$ for Krymka chondrule KRM93 ch11. If all the data are truly from a single original population, this value is the upper limit on the ^{60}Fe/^{56}Fe ratio in the region where and when the chondrules in ordinary chondrites formed. But we have reason to believe that many of the chondrules are not pristine, in which case a basic assumption of this

calculation is violated. We will return to trying to constrain the initial ratio when UOC chondrules formed below, after we discuss the complications from Fe-Ni redistribution that must be taken into account.

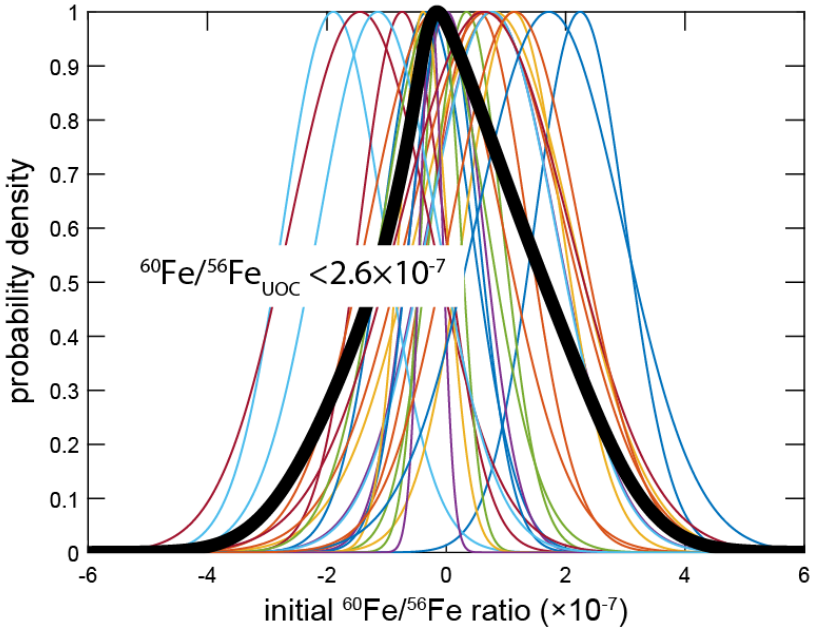

Figure 2.12. Gaussian probability distributions for each of our best chondrules (color). The sum of the distributions (black) gives an upper limit of 2.6×10^{-7} for the initial $^{60}Fe/^{56}Fe$ ratio of UOC chondrules. This assumes these chondrules sample a single distribution and have not been affected by secondary processing.

2.5 Discussion

We have presented Fe-Ni SIMS data of UOC chondrules that were collected over the past several years (Table 2.1; Figure 2.9). Most of the chondrules do not show resolved excesses in ^{60}Ni (Figure 2.4) and those that do mostly have poorly constrained regressions (Figures 2.5-2.8). We have identified our best dataset as chondrules that have initial ratios with 2σ uncertainties $<3\times10^{-7}$ and MSWD values between 0.5 and 1.5 (Table 2.2; Figure 2.10). Our best data can potentially give constraints on the initial $^{60}Fe/^{56}Fe$ ratio of UOC chondrules. However, when we take into account complications from Fe-Ni

redistribution (Telus et al. 2015a), placing constraints on the initial ratio proves to be difficult. Nevertheless, we have placed some constraints on the upper limit of the initial ratio using chondrules from our best dataset and we have placed constraints on the lower limit using chondrules with resolved excesses in ^{60}Ni.

2.5.1 *Complications from Fe-Ni mobilization in UOC chondrules*

It is often assumed that olivine and especially pyroxene remained closed for Fe and Ni in chondrules from UOCs because volume diffusion of Ni in these phases should be insignificant at the low peak temperatures experienced by these chondrites. However, Fe and Ni X-ray fluorescence maps presented by Telus et al. (2015a) show clear evidence for extensive open-system Fe-Ni redistribution between UOC chondrules and the surrounding matrix. All UOCs regardless of petrologic type and regardless of whether fall or find show enrichment of Fe and/or Ni along chondrule fractures, with the finds showing the most extensive Fe-Ni mobilization. The mobilization of Fe and Ni along chondrule fractures indicates that grain boundary diffusion and/or fluid transport is the dominant mechanism for Fe-Ni redistribution. The X-ray maps indicate that grain boundary diffusion and/or fluid transport can redistribute Fe and Ni over hundreds of microns. Late-stage and low-temperature exchange of Fe and Ni between chondrules and matrix was likely facilitated by aqueous alteration on the parent body and/or by terrestrial weathering.

Bulk Fe-Ni analyses of chondrules are especially vulnerable to this alteration because chondrule fractures cannot be avoided. For bulk analyses, extraneous Fe will increase the Fe/Ni ratios, resulting in points moving to the right on the isochron diagram and resulting in a lower inferred initial ratio. Extraneous Ni will decrease the Ni isotope

ratios, moving points toward the intercept on the isochron diagram, but not necessarily changing the initial ratio. However, moving points toward the intercept can make excesses in ^{60}Ni difficult to resolve. Most likely, extraneous Fe and Ni are incorporated simultaneously during bulk analyses. This would move points down the isochron (from adding Ni) and to the right (from adding Fe), resulting in a lower inferred initial ratio (Telus et al., 2015a; Chapter 3). Attempts to alleviate this issue by leaching chondrules prior to chemical digestion may not remove all of the extraneous material and leaching may also result in removing Fe and Ni from the olivine and pyroxene grains themselves. Loss of Fe during leaching will move points to the left on the isochron diagram, while loss of Ni will move points to the right. If Ni is more readily leached than Fe (Quitté et al., 2011), then leaching will also result in lower inferred initial ratios as this produces artificially high Fe/Ni ratios. Additionally, any incorporation of matrix material during sample preparation will result in lowering the inferred initial ratio.

In situ analyses that incorporate extraneous Fe will have higher Fe/Ni ratios, moving points to the right on the isochron diagram and resulting in lower inferred initial ratios. Incorporation of extraneous Ni will decrease the Fe/Ni ratio and decrease excess ^{60}Ni and move points toward the intercept along the original slope. Similar to results for bulk analyses, incorporating both extraneous Fe and Ni will result in lower inferred initial ratios. Extraneous Fe and Ni in chondrule fractures may not affect all spot analyses. If one could isolate only those measurements that did not incorporate extraneous Fe and Ni, reliable results could be obtained. But a mixture of “good” points and “bad” points will give poorly correlated isochrons (Telus et al., 2015a; Chapter 3). Also, lattice diffusion of Ni from olivine or pyroxene into sulfide or metal blebs can also result in poorly

correlated isochrons if some SIMS spots incorporate metal/sulfide blebs located within pyroxene grains, while others do not.

2.5.2 *Interpretation of unresolved initial ratios require caution*

The ability of our *in situ* analyses to resolve initial ratios is limited by the uncertainties on the Ni isotope ratios. Initial ratios $>2\times10^{-7}$ should be resolved with *in situ* analyses if the Fe/Ni ratios are sufficiently high. However, chondrules may not show resolved excesses in ^{60}Ni if they formed after a significant amount of ^{60}Fe had already decayed. For instance, if the initial solar system $^{60}Fe/^{56}Fe$ ratio was 2×10^{-7}, then chondrules that formed >2.6 Myr years after solar system formation (i.e., after 1 half-life of ^{60}Fe) would have an initial ratio of $<1\times10^{-7}$, which we cannot readily resolve with the current *in situ* techniques.

On the other hand, synchrotron maps from Telus et al. (2015a; Chapter 3) indicate that redistribution of Fe and Ni can result in lower inferred initial ratios. For example, Krymka chondrule KRM94 ch1 has high $^{56}Fe/^{62}Ni$ ratios (up to 1×10^{6}), but the inferred initial $^{60}Fe/^{56}Fe$ ratio is $<4\times10^{-8}$ (Figure 2.4). It has a MSWD value between 0.5 and 1.5 and an uncertainty $<3\times10^{-7}$, so it is considered one of our best chondrules (Table 2.2, Figure 2.10). However, synchrotron XRF maps of this chondrule show extensive Fe-Ni mobilization along the chondrule fractures, with many of our spot analyses overlapping these fine fractures (Figure 3.9 in Chapter 3). This indicates that the low initial ratio for this chondrule likely does not reflect its true initial ratio. Telus et al. (2015a) also found that almost all chondrules from UOC finds show extensive Fe-Ni redistribution; thus, *in situ* analyses of chondrules from QUE97008 and EET90161 may also be compromised in

this way. Bulk analyses of chondrules from finds (Tang and Dauphas, 2012a, Spivak-Birndorf et al., 2012a,2012b) are also likely affected by extraneous Fe and Ni.

2.5.3 *Constraints from chondrules with high initial ratios and large MSWD values*

Four of the chondrules reported in this study have resolved initial ratios of up to 1.7×10^{-6} (Figures 2.5-2.8). However the ^{60}Fe-^{60}Ni systems for these chondrules have been disturbed as indicated by the poor correlation between the excesses of ^{60}Ni and the Fe/Ni ratios. The initial ratios for these chondrules are not reliable and should not simply be taken at face value. Nevertheless, the observed excesses in ^{60}Ni and the Fe/Ni ratios can be used to place constraints on the initial ^{60}Fe/^{56}Fe ratios.

These chondrules have ^{60}Ni excesses of up to ~30‰ (Table 2.2). The presence of excess ^{60}Ni at this level in Fe-rich objects strongly indicates that the excesses come from the decay of ^{60}Fe. Also, nonradiogenic Ni isotope anomalies are not this large (e.g., Chen et al., 2009) and would have been homogenized by the melting and crystallization that produced chondrules.

Redistribution of Fe and Ni can decrease the δ^{60}Ni values, but it cannot increase them. Decreases in δ^{60}Ni can be achieved by adding terrestrial Ni, while increasing δ^{60}Ni would require additional input of only ^{60}Ni and not the other Ni isotopes, which is highly unlikely. Therefore, we can take the highest δ^{60}Ni values as a signature of the true initial ^{60}Fe/^{56}Fe ratios prior to Fe-Ni redistribution.

It is possible that redistribution of Fe and Ni resulted in the high initial ratios inferred from *in situ* analyses. This could occur by decreasing the Fe/Ni ratio via preferential loss of Fe or by concentrating the radiogenic nickel in specific phases. This

would mean that the Fe/Ni ratios during the decay of ^{60}Fe were higher than what we now observe. To constrain the lowest initial ^{60}Fe/^{56}Fe ratio that could have produced the observed excesses in ^{60}Ni, we investigated the plausible range of Fe/Ni ratios that could have been present in these samples.

The highest ^{56}Fe/^{62}Ni value we have measured for chondrules with resolved initial ratios is ~5×10^5 and the highest ^{56}Fe/^{62}Ni we have measured for chondrules overall is 1×10^6. Constraining the highest possible Fe/Ni ratio prior to Fe-Ni redistribution is not straightforward, but we know that the initial Fe/Ni ratios of chondrule Fe-silicates cannot be infinitely large since their values are limited by partitioning among phases. Melting and recrystallization produce high Fe/Ni ratios in pyroxenes and change the bulk Fe/Ni ratio. Diogenites, cumulate orthopyroxenes from Vesta, are a good example of this because they experienced Fe-Ni fractionation during Vesta core formation and during magmatic differentiation that formed these rocks. Their pyroxenes can have Ni contents ranging from 20 ppm to 100 ppm (Mittlefehldt, 1994). We carried out electron probe analyses of pyroxene from the Johnstown diogenite (200nA, 20keV, 10um) and found Fe content of ~12 wt.% and Ni content of ~15 ppm, corresponding to an ^{56}Fe/^{62}Ni ratio of 3×10^5. This is not very different from the ^{56}Fe/^{62}Ni ratios we have measured for chondrule pyroxenes.

Pyroxenes with extremely high Fe/Ni ratios are likely those that crystallized in the presence of metal under reducing conditions, allowing Ni to mainly partition into the metal phase. Pyroxenes from lunar rocks (norites or Ti-basalts) fit these criteria and may provide better constraints on the highest possible Fe/Ni ratio for pyroxene; however, since the Ni content is often below the detection limit, electron probe and INAA

(instrumental neutron activation analyses) data on pyroxenes from lunar rocks do not normally report values for Ni content. Nevertheless, based on the high Fe content of pyroxenes from late-stage Ti-basalts and the low Ni content (below the detection limit) in the coexisting olivine grains, pyroxene in these rocks likely have extremely high Fe/Ni ratios ranging from ~4×10^3 to ~4×10^5 or $^{56}Fe/^{62}Ni$ ratios of ~1×10^6 to 1×10^7 (Charles Shearer; personal discussion). This is up to 1 order of magnitude higher than $^{56}Fe/^{62}Ni$ ratios we have observed from SIMS analyses of chondrule pyroxenes.

We take a $^{56}Fe/^{62}Ni$ ratio of 1×10^7 as an upper limit for the highest possible Fe/Ni ratio and use this in conjunction with the 30‰ excesses in ^{60}Ni to place constraints on the initial $^{60}Fe/^{56}Fe$ ratio of UOCs. Figure 2.13 compares initial ratios of 1×10^{-8}, 5×10^{-8}, 1×10^{-7} and 2×10^{-7} with the data for all chondrules with resolved initial ratios. An initial ratio of 1×10^{-8} requires $^{56}Fe/^{62}Ni$ ratios ~2×10^7 to produce excess ^{60}Ni of 30‰. This is too high compared to what we consider plausible Fe/Ni ratios for pyroxenes. An initial ratio of 5×10^{-8} requires $^{56}Fe/^{62}Ni$ ratios of ~4×10^6 to produce excess ^{60}Ni of ~30‰, consistent with the highest plausible Fe/Ni ratio for pyroxene. An initial ratio of 1×10^{-7} requires $^{56}Fe/^{62}Ni$ ratios of 2×10^6 to produce excess ^{60}Ni of ~30‰. This is higher than Fe/Ni ratios we have observed from our SIMS analyses, but within the range of ratios that are plausible.

From this exercise, we place a lower limit of 5×10^{-8} on the initial $^{60}Fe/^{56}Fe$ ratio for these chondrules (the maximum permissible initial ratio is harder to constrain and is not discussed here). This means that decreasing the Fe/Ni ratio by losing Fe or concentrating anomalous Ni can potentially produce the high initial ratios inferred from *in situ* analyses provided that the true initial ratio was at least ~5×10^{-8}. The mechanism

for decreasing the Fe/Ni ratio is not clear, but may involve redistribution of Ni from pyroxenes into secondary metal/sulfide blebs during thermal metamorphism. *In situ* analyses of pyroxenes that include these secondary phases will have apparently low Fe/Ni ratios, but relatively high δ^{60}Ni values (see Figure 3.13 in Chapter 3). This will move points to the left on the isochron plot. This has been observed for metal and chromite in eucrite Juvinas (Quitté et al., 2011).

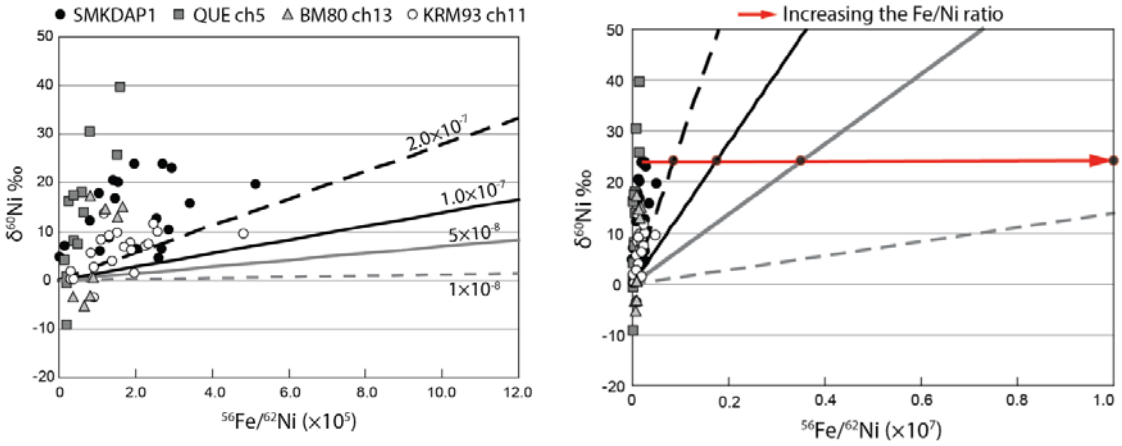

Figure 2.13. Fe-Ni SIMS data for chondrules with resolved initial ratios, but large MSWD values (Figures 2.5-2.8) on the left. Comparison of various initial ratios with this data illustrates that large excesses in ^{60}Ni of ~30‰ require initial ^{60}Fe/^{56}Fe ratios of at least 5×10^{-8} (right), assuming a ^{56}Fe/^{62}Ni ratio of 1×10^{7} is the highest plausible value for pyroxenes.

Due to complications from Fe-Ni mobilization, it is difficult to constrain the initial ^{60}Fe/^{56}Fe ratio of UOCs. Since Fe and Ni have been redistributed, we cannot simply average the initial ratios from numerous chondrules to determine the upper limit for UOCs. Nevertheless, the upper limit of 2.6×10^{-7} for UOC chondrules inferred from summing the Gaussian distributions of the initial ratios (Figure 2.12) is consistent with the initial ratio of $(2.2\pm1.5)\times10^{-7}$ from the only resolved value in our best dataset

(KRM93 ch11). Therefore, we take 2.6×10^{-7} to be our best estimate of the upper limit on the initial $^{60}Fe/^{56}Fe$ ratio of UOC chondrules. We constrain the lower limit to be 5×10^{-8} based on excesses in ^{60}Ni of ~30% from chondrules with resolved initial ratios, but large MSWDs (Figure 2.13). Previously reported *in situ* Fe-Ni systematics of UOC chondrules by Mishra and Goswami (2014) Mishra and Chaussidon (2014) tend to give higher initial ratios than the best data reported in this study (Table 2.2, Figure 2.10). Since both studies use similar analytical techniques, data analyses and samples, the apparent discrepancy between *in situ* analyses from this study and previous SIMS studies from Mishra remains unclear.

2.5.4 *Comparison with ICPMS and TIMS UOC chondrule data*

Bulk analyses of NWA5717 (UG3.05) and QUE97008 (L3.05) chondrules do not have resolved excess ^{60}Ni and do not show any correlation between excess ^{60}Ni and the Fe/Ni ratios (Tang and Dauphas, 2012a; Spivak-Birndorf et al., 2012a; Chen et al., 2013). Chondrules from Chainpur (LL3.4) also do not show resolved excess ^{60}Ni (Spivak-Birndorf et al., 2012b; Tang and Dauphas, 2012a); however, this is likely because this chondrite experienced significant thermal metamorphism with a peak temperature >400°C (Huss and Lewis, 1994). The initial $^{60}Fe/^{56}Fe$ ratio for UOCs inferred from these studies are all consistent with $<3\times10^{-8}$, inconsistent with initial ratios between 5×10^{-8} and 2.6×10^{-7} inferred from this study.

Tang and Dauphas (2015) focused their most recent bulk chondrule analyses on those from Semarkona because they show the least evidence for Fe-Ni mobilization. They analyzed 6 chondrules and found evidence for excess ^{60}Ni ($0.051\pm0.043\varepsilon$) in one, a

Type II (Fe-rich) Semarkona chondrule. From their data, they infer an initial $^{60}Fe/^{56}Fe$ ratio for UOCs of $(5.39\pm3.27)\times10^{-9}$, consistent with estimates of $<3\times10^{-8}$ inferred from previous bulk chondrule studies. Based on preliminary results from synchrotron Fe and Ni X-ray fluorescence mapping of UOC chondrules that found that 5 out of 16 (or 31%) of Semarkona chondrules were affected by Fe-Ni mobilization (abstract by Telus et al., 2013b), Tang and Dauphas (2015) argue that most bulk analyses of Semarkona chondrules should be unaffected by Fe-Ni redistribution. However, additional synchrotron X-ray maps of Semarkona chondrules by Telus et al. (2015a) show that 17 of 27 (or 63%) of chondrules from Semarkona exhibit clear evidence for Fe and/or Ni mobilization. Tang and Dauphas (2015) also argue that parent-body disturbance will produce low Fe/Ni ratios and that chondrules with high Fe/Ni ratios should give reliable results. However, Telus et al. (2015a) show that Fe-Ni mobilization introduces extraneous Fe and Ni into the chondrule which increases the Fe/Ni ratio (from adding Fe) and moves points toward the intercept (from adding Ni), resulting in artificially high Fe/Ni and low $\delta^{60}Ni$ values. Therefore, contrary to what Tang and Dauphas (2015) argue, most Semarkona chondrules have been affected by Fe-Ni mobilization, which will most likely lower the inferred initial $^{60}Fe/^{56}Fe$ ratios.

2.5.5 *Coordinated bulk & in situ analyses of UOC chondrules*

In collaboration with researchers at Caltech, we carried out coordinated bulk and *in situ* Fe-Ni analyses of chondrules from QUE97008 and Semarkona (QUE ch3, QUE ch5, and DAP1). The bulk analyses were done using thermal ionization mass spectrometry and the results were reported by Chen et al. (2013). The chondrules were

broken and fragments were reserved for *in situ* analysis. The chondrules were first washed in ethanol and HCl to remove metal or sulfide from the surface or in cracks and then were dissolved in strong acids. Their Ni extraction procedures are described in Chen et al. (2009). Initial $^{60}Fe/^{56}Fe$ ratios inferred from their bulk analyses are unresolved from zero, although relatively high ratios of up to 1×10^{-7} are permitted by the data (Chen et al., 2013).

The *in situ* data for these chondrules are reported in this study. The data for QUE ch3 gives an upper limit of 2.1×10^{-7} (Table 2.2), which is consistent with the bulk chondrule data. However, the *in situ* data for DAP1 and QUE ch5 are not consistent with the bulk data. The *in situ* data for these chondrules give initial ratios of $(2.1\pm1.0)\times10^{-7}$ (Figure 2.5) and $(1.7\pm0.4)\times10^{-6}$ (Figure 2.8), respectively, up to two orders of magnitude higher than the initial ratios inferred from the bulk analyses. Again, the large MSWDs of 4.1 and 4.0, respectively, reflect a poor correlation between the excesses in ^{60}Ni and the Fe/Ni ratios. The discrepancies between bulk and *in situ* analyses of the same chondrules are further indications that the Fe-Ni system for UOC chondrules is disturbed.

2.5.6 *Constraining the source of ^{60}Fe in the early solar system*

Iron-60 in the early solar system could have been inherited from the interstellar medium or from ejecta from a dying star. The abundance of ^{60}Fe in the galactic background is constrained by comparing abundances determined from galactic chemical evolution models with present day ^{60}Fe abundances in the galaxy determined from gamma-ray spectroscopic observations. Present-day gamma ray emission flux analyses by Wang et al. (2007) determined the $^{60}Fe/^{26}Al$ ratio is 0.148, which corresponds to a

$^{60}Fe/^{26}Al$ ratio of 0.53 when the decay rates are taken into account (using half-life of 2.6 Myr determined by Rugel et al., 2009). Using the mass of ^{26}Al in the galaxy (2.8 $M_{\odot}$; Diehl et al., 2006), an abundance of ^{60}Fe in the galaxy of 1.5 $M_{\odot}$ is calculated. Assuming the galaxy has solar metallicity, the abundance of ^{60}Fe in the galaxy is converted to a $^{60}Fe/^{56}Fe$ ratio in the galaxy of 4.6×10^{-7}. However, this is probably not valid because the metallicity of the galaxy toward the galactic center (where most of the measured ^{60}Fe is located) is almost certainly higher than solar. To determine a more accurate $^{60}Fe/^{56}Fe$ ratio of the galactic background at the time of solar system formation using the gamma ray emission data, one must determine the ^{56}Fe abundance in the galaxy at that time. This is where models of galactic chemical evolution come in. Huss et al. (2009) estimate the abundance of ^{56}Fe in the galaxy at the time of solar system formation by using a galactic chemical evolution model to track the buildup of metals from when the galaxy formed (12 Gyr) to when the solar system formed (4.6 Gyr). They infer an initial $^{60}Fe/^{56}Fe$ ratio of $<4\times10^{-8}$.

A $(^{60}Fe/^{56}Fe)_{SS}$ ratio above galactic background points towards a stellar origin for ^{60}Fe. During stellar nucleosynthesis, ^{60}Fe is produced via slow-neutron capture (s-process) on ^{59}Fe, which has a very short half-life of 44 days. For efficient production of ^{60}Fe, the neutron density must exceed ~30 billion in order to get significant neutron capture on ^{59}Fe through s-process nucleosynthesis (Limongi and Chieffi, 2006). This requires temperatures between 4×10^{8} and 2×10^{9} degrees.

Injection of ^{60}Fe into the budding solar system from a single stellar source has been modeled for asymptotic giant branch (AGB) stars and type II supernovae (SNII). The protosolar molecular cloud could have incorporated material from the wind of an

AGB star. Wasserburg et al. (2006) modeled the abundances of short-lived radionuclides in the envelopes of low and intermediate mass AGB stars ($1.5M_{\odot}$-$3M_{\odot}$and $M_{\odot}$; solar metallicity). The high temperatures necessary for production of ^{60}Fe are achieved in the He shell of a $5M_{\odot}$ AGB star, where the $^{60}Fe/^{56}Fe$ ratio is estimated to $\sim 1\times10^{-6}$. The temperatures in the envelopes of low mass AGB ($<3M_{\odot}$) stars are not sufficient for ^{60}Fe production; however, some nuclear processing can occur through Cool Bottom Processing, which involves mixing between material from the cool envelope and hotter and denser layers. Wasserburg et al. (2006) calculate initial $^{60}Fe/^{56}Fe$ ratios of 4×10^{-8} to 2×10^{-7} for the envelopes of low mass AGB stars.

Massive stars between $11M_{\odot}$ and $33M_{\odot}$ die as type II supernovae. Ejecta from the supernovae explosion could have potentially been incorporated during solar system formation. Presupernova, conditions for ^{60}Fe production are achieved during hydrostatic burning in the C and He burning shells (Limongi and Chieffi, 2006). Explosive nucleosynthesis of ^{60}Fe is most efficient when shock waves generated from the supernova pass through the C burning shell. Nucleosynthesis models indicate that ^{60}Fe is produced copiously by massive stars (e.g., Limongi and Chieffi, 2006). In order to better match abundances determined from isotope analyses of meteorites, mixing at the C/O burning shell and fall back of a significant fraction of ejecta back onto the supernova remnant (Takigawa et al., 2008). Wasserburg et al. (2006) calculate an initial $^{60}Fe/^{56}Fe$ ratio of $\sim 2\times10^{-3}$ for the ejected stellar envelope of a 15 $M_{\odot}$ supernova source.

The high initial ratios inferred from *in situ* analyses by Mishra and Goswami (2014) and Mishra and Chaussidon (2014) are consistent with a SNII or intermediate mass AGB star, while initial ratios of $<3\times10^{-8}$ inferred from bulk analyses (e.g., Tang and

Dauphas, 2015) are more consistent with galactic background as the source for ^{60}Fe in the solar system. An initial ratio for UOCs between 5×10^{-8} and 2.6×10^{-7} inferred from our data does not provide strong constraints on the $(^{60}Fe/^{56}Fe)_{SS}$ ratio, but it indicates that a supernova may not be a necessary source for ^{60}Fe as inferred from previous SIMS analyses (e.g., Tachibana and Huss, 2003; Mishra and Goswami, 2014). Nevertheless, a supernova source is often preferred to an AGB source based on the probability of their encounter with young stellar objects. A supernova source for ^{60}Fe is more likely (Williams and Gaidos, 2007) because young stellar objects form in clusters where massive stars are common and supernovae tend to occur prior to the dispersion of stellar clusters. AGB stars have a lower probability of being the source of ^{60}Fe in the solar system (Kastner and Myers, 1994) because they are much older objects and not associated with star formation regions.

2.5.7 *Developing the ^{60}Fe-^{60}Ni system for early solar system chronology*

Constraining the initial ^{60}Fe/^{56}Fe ratio of the solar system is necessary for using the ^{60}Fe-^{60}Ni system for chronology. Although analytical issues from ratio bias have been addressed (Telus et al., 2012a; Chapter 4), some discrepancies between *in situ* and bulk analyses of UOC chondrules remain. Excesses of up to ~30‰ in ^{60}Ni that are measured from *in situ* analyses (Figure 2.13) should be easily resolved in bulk analyses, but they are not, even when the same chondrules are analyzed by both techniques (Section 2.5.5). Late-stage open-system redistribution of Fe and Ni was prevalent and provides some explanation for these discrepancies (Telus et al., 2015a; Chapter 3). This alteration can easily compromise bulk and *in situ* analyses, resulting in either lower inferred initial

ratios or poorly correlated isochrons. Given the complications with Fe-Ni redistribution, UOCs may not be appropriate samples for constraining the $(^{60}Fe/^{56}Fe)_{SS}$ ratio.

Our best approach in moving forward with ^{60}Fe-^{60}Ni analyses is to make a greater effort in identifying suitable samples prior to isotope analyses. For now, it is not clear which samples have escaped late-stage, low-temperature Fe-Ni mobilization. At least 60% of chondrules from Semarkona show evidence for this alteration. Although this is the least amount observed for any UOC, it is still indicates that the majority of these chondrules have been compromised. Semarkona may be the best UOC to use for Fe-Ni studies, but each sample should be characterized thoroughly prior to isotopic analyses to confirm that it has not been affected by Fe-Ni mobilization. *In situ* analyses can potentially avoid extraneous Fe-Ni in chondrule fractures if samples are thoroughly characterized. Bulk analyses must also take special precaution to avoid or remove contamination.

Synchrotron X-ray fluorescence analyses provide the sensitivity, resolution, and efficiency for analyzing the distribution of Fe and Ni, at least in regards to Fe-Ni enrichment along chondrule fractures. Another benefit to the synchrotron analyses is that they provide subsurface information of Fe and Ni distribution, which is not readily available from electron microscopy. Iron-Ni redistribution in chondrules from other chondrite groups (e.g., CO3s) should also be investigated to determine if they can provide better constraints. Finally synchrotron analyses of other important samples such as angrites and eucrites, which have been used to constrain the initial $^{60}Fe/^{56}Fe$ solar system ratio, should also be carried out.

2.6 Conclusions

To constrain the initial $^{60}Fe/^{56}Fe$ ratio of the solar system, we measured the Fe-Ni system *in situ* in chondrule olivine and pyroxene in unequilibrated ordinary chondrites (UOCs) using the ion microprobe. Most chondrules do not have resolved excesses in ^{60}Ni. A few chondrules have resolved excess of up to 30‰; however, the initial $^{60}Fe/^{56}Fe$ ratios are poorly constrained (Table 2.1; Figure 2.9). Initial ratios inferred from our best data (i.e., initial ratios with MSWDs between 0.5 and 1.5 and 2σ uncertainties $<3\times10^{-7}$) are mostly unresolved from zero except for one chondrule which has an initial ratio of $(2.2\pm1.5)\times10^{-7}$ (Table 2.2; Figure 2.10). We use the chondrules from our best data set to infer an upper limit of 2.6×10^{-7} (Figure 2.12) and the excesses in ^{60}Ni from chondrules with resolved initial ratios to infer a lower limit of 5×10^{-8} (Figure 2.13). Initial ratios for UOCs between 5×10^{-8} and 2.6×10^{-7} are inconsistent with bulk analyses, which infer initial ratios of $<3\times10^{-8}$. The initial ratios inferred from this study do not necessarily require a supernova source for ^{60}Fe. A low mass AGB star is a viable source. The discrepancies between bulk and *in situ* analyses likely stem from complications due to late-stage open-system Fe-Ni mobilization (Telus et al., 2015a; Chapter 3). Therefore, UOCs may not be the best samples for constraining the initial $^{60}Fe/^{56}Fe$ ratio of the solar system.

CHAPTER 3. **MOBILITY OF IRON AND NICKEL AT LOW TEMPERATURES AND IMPLICATIONS FOR ^{60}Fe-^{60}Ni SYSTEMATICS OF CHONDRULES FROM UNEQUILIBRATED ORDINARY CHONDRITES**

Submitted in its present form as Telus, M., G. R. Huss, R. C. Ogliore, K. Nagashima, D. L. Howard, M. G. Newville, and A. G. Tomkins (2015), Geochimica et Cosmochimica Acta.

3.1 Abstract

The Fe and Ni isotopic composition of ferromagnesian silicates in chondrules from unequilibrated ordinary chondrites (UOCs) have been used to estimate the initial abundance of the short-lived radionuclide, ^{60}Fe, in the early solar system. However, these estimates vary widely, and there are systematic discrepancies in initial ^{60}Fe/^{56}Fe ratios inferred from *in situ* and bulk analyses of chondrules. A possible explanation is that the Fe-Ni isotope system in UOC chondrules has not remained closed (a necessary condition for isotopic dating), and Fe and Ni have been redistributed since the chondrules formed. In order to evaluate this, we collected high-spatial-resolution X-ray fluorescence (XRF) maps of UOC chondrules to better understand the distribution and mobility of Fe and Ni at the low metamorphic temperatures of these chondrites. We used synchrotron X-ray-fluorescence microscopy to map the distribution of Fe, Ni and other elements in portions of 71 chondrules from 8 UOCs (types 3.00-3.2). The synchrotron XRF maps show clear enrichment of Fe and/or Ni in fractures ranging down to micrometer scale in chondrules from all UOCs analyzed for this study regardless of petrologic type and regardless of whether fall or find, indicating that there was significant exchange of Fe and Ni between chondrules and matrix and that the Fe-Ni system was not closed. Sixty percent of chondrules in Semarkona (LL3.00) have Fe and Ni enrichment along fractures, while 80-100% of chondrules analyzed from the other UOCs show these enrichments. Mobilization was likely a result of fluid transport of Fe and Ni facilitated by aqueous alteration on the parent body and/or during terrestrial weathering. *In situ* and bulk Fe-Ni analyses that incorporate extraneous Fe and Ni from chondrule fractures will result in lowering the initial ^{60}Fe/^{56}Fe ratios.

3.2 Introduction

Iron-60 is a short-lived radionuclide that is produced efficiently only by stellar nucleosynthesis. Its former presence in the solar system has been inferred through excesses in the daughter isotope, ^{60}Ni, that correlate with the Fe/Ni ratios in various meteorites (e.g., Shukolyukov and Lugmair, 1993a; Tachibana et al., 2006; Tang and Dauphas, 2012; Mishra and Goswami, 2014). An initial abundance of ^{60}Fe above galactic background implies that material synthesized in one or more stars that died just before the solar system formed (e.g., supernovae) was incorporated into the early solar system. A precise measurement of the initial solar system ^{60}Fe/^{56}Fe ratio, $(^{60}Fe/^{56}Fe)_{SS}$, could help identify the environment in which the solar system formed such as in an area of cluster star formation like Orion or in relative isolation like in Taurus Auriga (Hester and Desch, 2005). Additionally, the rapid decay rate of ^{60}Fe ($t_{1/2}$ = 2.6 Myr; Rugel et al., 2009) potentially makes it a useful tool for dating early solar system processes that fractionate Fe and Ni, such as chondrule formation, aqueous alteration, and planetary differentiation. Since Fe is a major element in many meteoritic components, the ^{60}Fe-^{60}Ni system can potentially be used for dating objects that cannot be easily dated by other methods (e.g., chondrule ferromagnesian silicates and sulfides).

A well-constrained $(^{60}Fe/^{56}Fe)_{SS}$ is necessary in order to use the ^{60}Fe-^{60}Ni system to determine the stellar source of short-lived radionuclides or to use it for early solar system chronology. It is also important for thermal models of planetesimals (e.g., Moscovitz and Gaidos, 2011; Henke et al., 2012; 2013; Monnereau et al., 2013; Mare et al., 2014) because the rapid decay of ^{60}Fe is thought to generate significant internal heat (Moskovitz and Gaidos, 2011). To determine $(^{60}Fe/^{56}Fe)_{SS}$, it is critical to identify

materials for measurement that recorded the abundance of ^{60}Fe when they formed and have remained unaltered since that time. Components of primitive chondrites (e.g., chondrules, sulfides, and magnetite) are attractive targets because they formed early in solar system history and have experienced relatively little thermal processing (e.g., Tachibana et al., 2006; Tang and Dauphas, 2012). But differentiated meteorites have also been used (e.g., Dauphas et al., 2008; Quitté et al., 2011). Ferromagnesian silicates in chondrules from unequilibrated ordinary chondrites (UOCs) have been used to constrain $(^{60}Fe/^{56}Fe)_{SS}$ because: 1) the silicates (particularly pyroxenes) are relatively resistant to metamorphism and aqueous processing, 2) Fe-rich pyroxenes have high Fe/Ni ratios, and 3) chondrules in UOCs have been dated to 1-3 Myr after calcium-aluminum rich inclusions (CAIs), the first solids to form in the solar system (Kita and Ushikubo, 2012, Connelly et al., 2012).

In situ and bulk methods have been used to measure ^{60}Fe-^{60}Ni systematics of UOC chondrules. *In situ* methods, such as secondary ion mass spectrometry (SIMS), also known as the ion microprobe, measure chondrules in polished thick and thin sections, keeping the petrographic context intact. This method produces an internal isochron, which is constructed from the Fe/Ni ratio and Ni isotopic composition of each measured spot. The Fe/Ni ratios and excesses in ^{60}Ni correlate positively on an isochron diagram (e.g., $^{60}Ni/^{62}Ni$ vs. $^{56}Fe/^{62}Ni$) for an undisturbed chondrule. The slope of the isochron gives the initial $^{60}Fe/^{56}Fe$ ratio for that chondrule, $(^{60}Fe/^{56}Fe)_0$, and the intercept gives the initial $^{60}Ni/^{61}Ni$ ratio. The $(^{60}Fe/^{56}Fe)_{SS}$ can be constrained from the chondrule $(^{60}Fe/^{56}Fe)_0$ ratios using the radioactive decay law ($N_0=N_{SS}e^{-\lambda t}$; where t and λ are for the time and decay constant, respectively) and the UOC chondrule ages from ^{207}Pb-^{206}Pb and

^{26}Al-^{26}Mg chronometers. *In situ* Fe and Ni isotopic measurements of UOC chondrules show that a few chondrules have resolved ^{60}Ni excesses that correspond to $(^{60}Fe/^{56}Fe)_0$ ratios ranging from 1×10^{-7} (Telus et al., 2012a; Chapter 4) to 1×10^{-6} (Mishra and Goswami, 2014). However, the isochron diagrams for these chondrules show weak correlations between excesses in ^{60}Ni and the Fe/Ni ratios. The presence of ^{60}Fe at these abundances in the early solar system are higher than estimates for the galactic background, implying that a dying star, likely a supernova, was the source of ^{60}Fe and possibly other short-lived radionuclides (Hester and Desch, 2005; Huss et al., 2009; Ouellette et al., 2009).

Bulk techniques, such as thermal ionization mass spectrometry (TIMS) or inductively coupled plasma mass spectrometry (ICPMS) measure purified Fe and Ni extracted from dissolved chondrules. These measurements can be used to construct a "whole-rock" isochron, where each chondrule is a point on the isochron. The assumption with a whole-rock isochron is that all measured samples formed at the same time from the same initial material. If this assumption is valid, the whole-rock isochron gives the $^{60}Fe/^{56}Fe$ ratio at the time the chondrules formed. Again, the $(^{60}Fe/^{56}Fe)_{SS}$ is constrained from the $(^{60}Fe/^{56}Fe)_0$ ratios of the chondrules using the radioactive decay law and the chondrule ages. Bulk TIMS and MC-ICPMS measurements of UOC chondrules are consistent with $(^{60}Fe/^{56}Fe)_0 < 3\times10^{-8}$ (Spivak-Birndorf et al., 2012a,b; Tang and Dauphas, 2012; Chen et al., 2013; Tang and Daupas, 2015), at least an order of magnitude lower than values inferred from some SIMS data, indicating that the source of ^{60}Fe is likely from galactic background instead of a recent injection from a nearby stellar source.

Both *in situ* and bulk measurements of UOC chondrules assume that ^{60}Fe was distributed homogeneously in the solar nebula and that the Fe-Ni system remained closed since chondrule formation. One possible explanation for the poorly correlated *in situ* data and the discrepancies between *in situ* and bulk chondrule data is that our assumption of closure of the Fe-Ni isotopic system is incorrect. In order to evaluate whether the Fe-Ni system remained closed in UOC chondrules, we need to better understand the distribution and mobility of Fe and Ni at the low metamorphic temperatures (peak temperatures <450 °C) experienced by UOCs. Here, we present results from synchrotron X-ray fluorescence (XRF) mapping of Fe, Ni and other elements in chondrules from very primitive UOCs. The synchrotron provides the sensitivity and spatial resolution necessary to rapidly map abundances of trace elements (e.g., Ni in olivine and pyroxene) at large scales (e.g., Dyl et al., 2014). Our results show that chondrules from UOCs have been severely affected by low-temperature Fe-Ni mobilization.

3.3 Methods

3.3.1 *Samples*

We analyzed chondrules from the least metamorphosed UOCs (petrologic types 3.00 to 3.2). We analyzed witnessed falls, Semarkona (LL3.00), Bishunpur (LL3.1) and Krymka (LL3.2), which should not have been significantly affected by terrestrial weathering. We also analyzed chondrules from thin sections of Antarctic finds QUE97008 (L3.05), EET87735 (L3.05), EET90080 (L3.05), MET96503 (L3.1), and TIL82408 (LL3.1). Antarctic meteorites are given weathering grades of A, B, or C, to indicate minor, moderate or severe rusting, respectively. The Antarctic meteorites we

studied have all been classified as weathering grade B, except QUE97008 which has a weathering grade of A (Meteoritical Bulletin Database: http://www.lpi.usra.edu/meteor/metbull.php). We mapped a variety of chondrule types, including type I (Fe-poor) and II (Fe-rich) chondrules, with porphyritic (coarse-grained) and radiating/cryptocrystalline (fine-grained) textures. Most of the chondrules we analyzed are >500 μm across. Most of our samples are standard 1-inch-round glass thin sections. One sample, (DAP-1), is mounted in epoxy within a stainless steel bullet. In total, we mapped 71 UOC chondrules. Some of these chondrules were previously analyzed for ^{60}Fe-^{60}Ni systematics by SIMS. Mineral compositions were identified using the scanning electron microscope and/or the electron microprobe at the University of Hawai‘i (UH).

3.3.2 *XRF mapping and data analysis*

We collected XRF maps of UOC chondrules using both the Australian Synchrotron in Melbourne, Victoria and the Advanced Photon Source at the Argonne National Laboratory in Chicago, Illinois. The measurement conditions and data analyses are described below. In some cases, electron probe spot analyses were done at UH to verify observations from the XRF maps. The beam conditions for the electron probe analyses are described in Section 2.3.

Australian Synchrotron XFM beamline We collected X-ray maps of 70 UOC chondrules at the Australian Synchrotron XFM beamline (Paterson et al., 2011). The XFM beamline is equipped with a Maia energy-dispersive detector, a large solid-angle, 384-detector array (Ryan et al., 2010). The detector is situated between the sample and the incident

beam (Figure 3.1A). The samples were placed 10 mm away from the detector. The incident beam passes through a hole in the detector and passes through the sample. The sample emits fluorescent X-rays at various energies that are counted by the detector. The maps were collected during two separate sessions. The main difference between the two sessions is that the X-ray beam energy for the first session was 12.5 keV and that for the second session was 11.7 keV. These energies allowed us to resolve Ni X-rays from the elastic and inelastic scattered X-rays (i.e., Rayleigh and Compton scattering), which were at ~11-12 keV. An incident X-ray beam at these energies allows us to map the X-ray fluorescence of elements from Ca to Zn with the Maia detector (the Maia currently is not sensitive for elements with K-shell binding energies below those of Ca). At the beginning of each session, we analyzed standard metal foils (Mn, and Pt) to calibrate the X-ray energies and establish elemental quantitation. We collected low-spatial-resolution maps of each thin section for navigating to each chondrule. High-resolution maps of chondrules were collected using an incident X-ray beam focused to ~2 μm. We used various dwell times, mostly, between 31 and 63 msec. The pixel size was 2 μm. Under these conditions, the chondrule maps required ~0.5 to ~2.5 hours. This technique is beneficial for rapid large-scale mapping of elements Z > Ca. The detection limit for Ni should be ~50 ppm; however, the high Fe/Ni ratios in olivine and pyroxene result in significant overlap of Ni Kα peaks (7.46 keV) and Fe Kβ peaks (7.06 keV), degrading detection limits for Ni X-rays (to >400 ppm), and making it difficult to resolve the trace amount of Ni in these phases. However, Ni concentrations at grain boundaries and in cracks were clearly detected.

GeoPIXE^{TM} spectral data processing software was used to generate quantitative elemental maps of the chondrules. GeoPIXE fits the spectra using dynamic matrix analysis that deconvolves each spectrum according to the contributions from each element, background, scatter and pile up. Ryan (2001) provides a thorough explanation of this algorithm. This program allows us to estimate the concentrations of trace elements, even when they are small peaks on the shoulders of larger peaks (*e.g.*, Ni Kα on Fe Kβ). Corrections for background, interferences, pileup, elastic and inelastic scatter were applied (see Ryan et al., 1990 for details). Because the synchrotron X-ray beam passes through the thin sections, the resulting maps are integrations over the entire 30-µm thickness of the thin section.

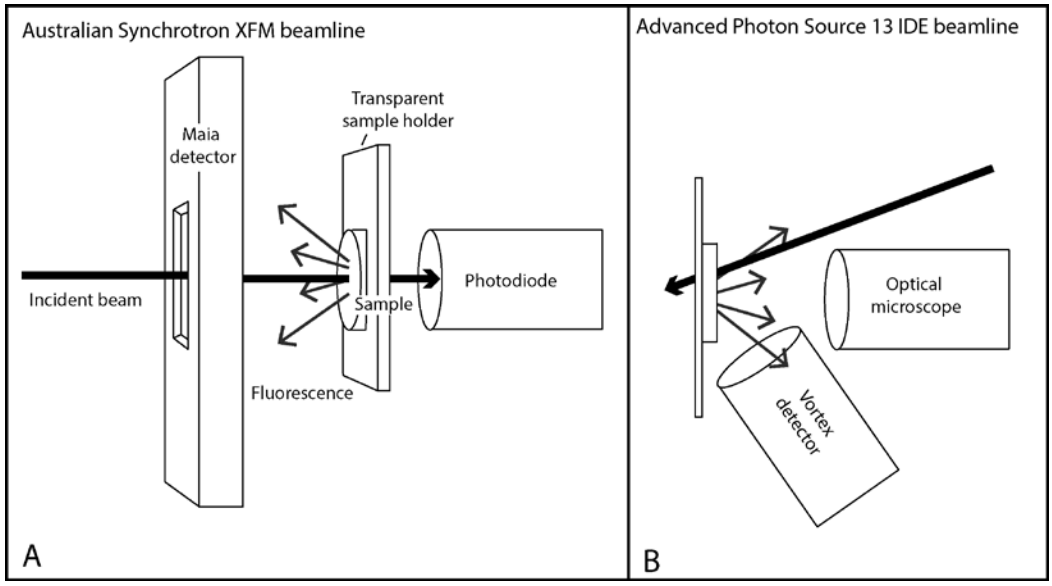

Figure 3.1. Schematic illustration of the experimental setup at the Australian Synchrotron (A) and the Advanced Photon Source (B). The photodiode at the AS is used for alignment.

Advanced Photon Source GSECars 13IDE beamline In another effort to resolve variations in the Ni concentration within chondrule olivine and pyroxene, we collected region-of-interest X-ray fluorescence maps at the APS GSECars (GeoSoilEnviro

Consortium on Advanced Radiation Sources, University of Chicago) beamline 13-IDE. Region of interest maps assign X-rays of a certain energy range to certain elements. For instance, X-rays of energies between 5.673 and 6.109 keV are assigned to Mn Kα. The Cr and Mn X-ray maps often appear very similar (see Figures 3.2, 3.3, and 3.6). This is because the Cr Kβ peak (5.947 keV) overlaps within the region of interest for Mn. Data collection is very similar to that used at the Australian Synchrotron; the main differences are the energy resolution, configuration, and saturation of the detectors. At the APS, we used a 4-element, energy-dispersive, Vortex detector that is situated at ~90 degrees relative to the incident beam (Figure 3.1B). This geometry significantly reduces background from elastic and inelastic scattered X-rays. To further reduce background from scattered X-rays, we covered the detector with a collimator. We placed ~150 μm thick piece of Al foil in front of the detector to reduce saturation of the detectors. This reduced the signal from Fe Kα by a factor of 50, allowing us to push the detector closer to the sample and detect relatively more of the Ni signal. The detector set up and efforts to reduce saturation and background allowed for an increase in the spectral resolution of about a factor of 2 or 0.2 keV compared to the Australian Synchrotron.

The beam energy was set to 9 keV to maximize sensitivity to Ni. This set up allowed us to analyze elements from Cr to Ni. Dwell time was normally 50 ms, but we also used 100 ms in a few cases. Beam size and pixel size were 2 μm. The position of the detector was adjusted prior to each map to keep the count rate from Fe Kα low enough so that the deadtime of the detector was below 40%. We mapped 23 chondrules with this technique; all except 1 were previously analyzed at the Australian Synchrotron. The X-ray maps from the APS were processed using Larch, an open-source spectral processing

and analysis software (http://cars.uchicago.edu/xraylarch/). Corrections for changes in the beam intensity, deadtime, and background were applied using this software (Newville, 2013).

3.3.3 *Electron probe analyses*

Contamination of Ni from the glass substrate was a concern for the XRF analyses. Therefore, we used the JEOL JXA-8500F electron microprobe at UH (focused beam at 100 nA and 20kV) to analyze the glass substrate of each thin section to determine the potential contribution of the glass substrate to the Ni X-ray signal from our synchrotron analyses.

We used the electron probe under the same conditions to verify observations from our synchrotron analyses. We put the focused beam on chondrule fractures. However, in most cases, the analytical volume of the beam is much larger than the crack. Therefore the results do not provide reliable information regarding the exact concentration of Fe or Ni in the crack. They only provide an idea about the relative abundance of Fe or Ni in the crack compared to the glass substrate (e.g., Ni content in chondrule fractures is higher or similar to Ni content in the glass).

3.4 Results

3.4.1 *Fe and Ni enrichment in chondrule fractures*

Figures 3.2 to 10 show Ca, Cr, Mn, Fe, and Ni X-ray maps along with backscattered-electron images for various chondrules from both the Australian

Synchrotron (AS) and the Advanced Photon Source (APS) analyses. The figures are arranged in order of the petrologic type of the host meteorite. The elemental maps have been stretched in order to make variations noticeable. Additional Fe, Ni and Cr maps can be found in Appendix B.

Semarkona (LL3.00), the least metamorphosed UOC in our collections, shows clear evidence for Fe-Ni mobilization in 60% of the chondrules studied. Semarkona is a witnessed fall and so has not experienced significant terrestrial weathering. Figure 3.2 shows a porphyritic pyroxene chondrule with Fe and Ni concentrated in fine fractures throughout the pyroxene grains. Many porphyritic chondrules from Semarkona show no obvious signs of Fe-Ni enrichment along chondrule fractures. For those that do, Fe-Ni enrichment is limited to discrete small regions that do not stretch across the entire chondrule (Appendix B. 1). The most extensively altered Semarkona chondrule is a bleached radiating-pyroxene chondrule (Figure 3).

QUE97008 (L3.05) is an Antarctic find of weathering grade A. Again, Fe and Ni are enriched along fine fractures in olivine and pyroxene grains (Figure 3.4). The Fe and Ni concentrations appear to decrease with distance from the edge of the chondrule, indicating that the matrix is the source of Fe and Ni in the fractures. With the exception of one barred chondrule, all chondrules studied, whether porphyritic or radiating/cryptocrystalline, show extensive mobilization of Fe and Ni. EET87735 (L3.05), EET90080 (L3.05), MET96503 (L3.1) and TIL82408 (LL3.1) are Antarctic finds of weathering grade B. All chondrules studied from these chondrites show extensive evidence of Fe and Ni mobilization, with Fe and Ni enrichments along cracks

permeating the mineral grains at all scales (e.g., Figure 3.5-3.7). Again, the matrix appears to be the source of Fe and Ni in the chondrule fractures.

In Bishunpur (LL3.1), a witnessed fall, porphyritic chondrules show limited enrichments of Fe and Ni along chondrule fractures (Figure 3.8), but the degree of alteration is definitely more extensive than that in Semarkona. We analyzed two radiating/cryptocrystalline chondrules from Bishunpur, and they both show evidence for extensive Fe-Ni mobilization (e.g., Figure 3.9). Among the Bishunpur chondrules studied, three showed no obvious signs of Fe-Ni mobilization.

Every chondrule that we analyzed from Krymka shows clear evidence for Fe-Ni mobilization that is often more extensive than Bishunpur chondrules, but less extensive than chondrules from Antarctic meteorites. Alteration for radiating/cryptocrystalline chondrules (e.g., Figure 3.10) is often more extensive than that for porphyritic chondrules (Appendix B. 2).

Table 3.1 lists all the meteorites analyzed for this study and the percentage of chondrules from each chondrite that show clear evidence for Fe and Ni enrichment along chondrule fractures. Synchrotron XRF maps show clear enrichments of Fe and Ni in chondrule fractures from all of the meteorites analyzed for this study regardless of petrologic type (Figures 3.2-3.10; Table 3.1). The majority of chondrules studied in all meteorites showed enrichments of Fe and Ni in fractures.

The high concentrations of Fe and Ni in the chondrule fractures were confirmed for several chondrules with electron probe spot analyses along the cracks. The FeO and NiO concentrations inferred from electron microprobe measurements of cracks (>1 wt% and >0.3 wt%, respectively) cannot be from the glass substrate, which has < 2000 ppm

and <100 ppm Fe and Ni, respectively. Again, the results for the Fe and Ni content in the cracks are not accurate because the analytical volume of the beam is much larger than the cracks. This simply tells us that the Fe and Ni content in the chondrule fractures are much larger than in the glass substrate.

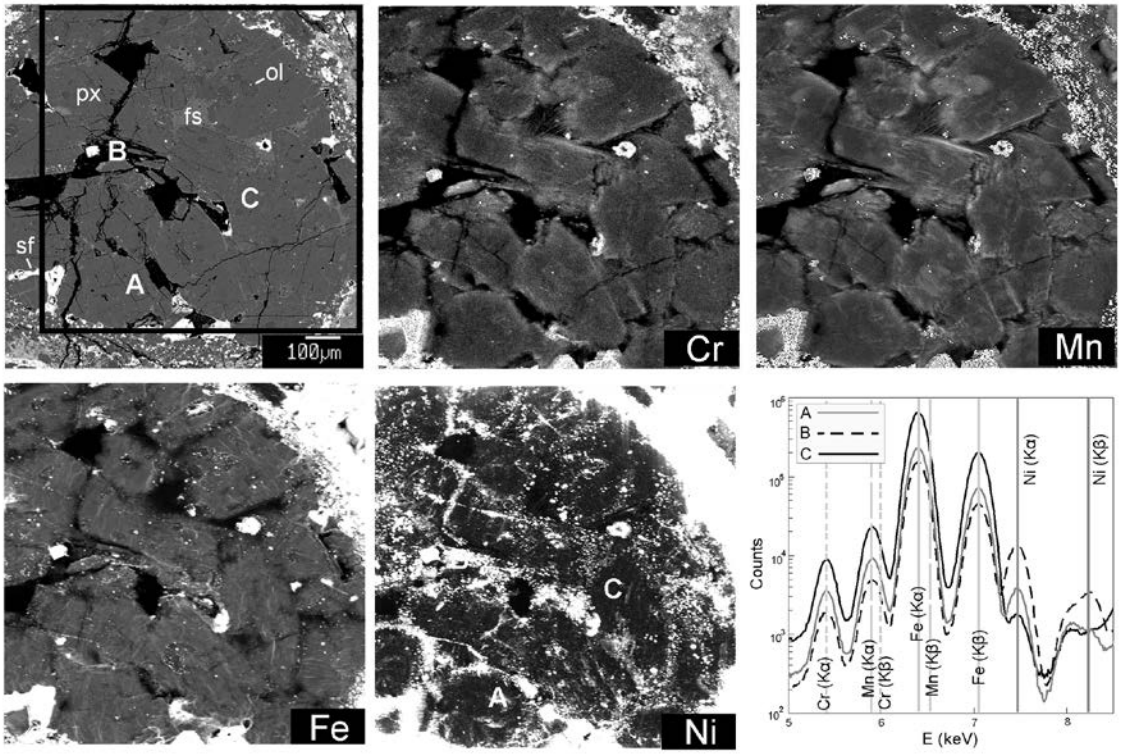

Figure 3.2. Backscattered-electron (BSE) image and elemental maps for a type I porphyritic pyroxene chondrule from Semarkona (SMK312 chH) obtained at the APS (ol: olivine, px: pyroxene, fs: feldspar, and sf: sulfide). The X-ray maps show that Fe is concentrated in blebs and along fine fractures in the pyroxene grains. Nickel is concentrated in blebs throughout the chondrule. Nickel is also associated with fine fractures. Spectra for the regions labeled on the BSE map are shown. Chromium and Mn show minor zoning and enrichment in what appears to be relict grains. It is possible that some of the Mn signal is from overlap with Cr (see explanation in Section 2.2.2). Variations in Ni for the regions labeled on the BSE image and Ni map are highlighted in the spectra. The signal from the Fe-rich phases should be interpreted with caution because the deadtime in these regions were very high (>75%).

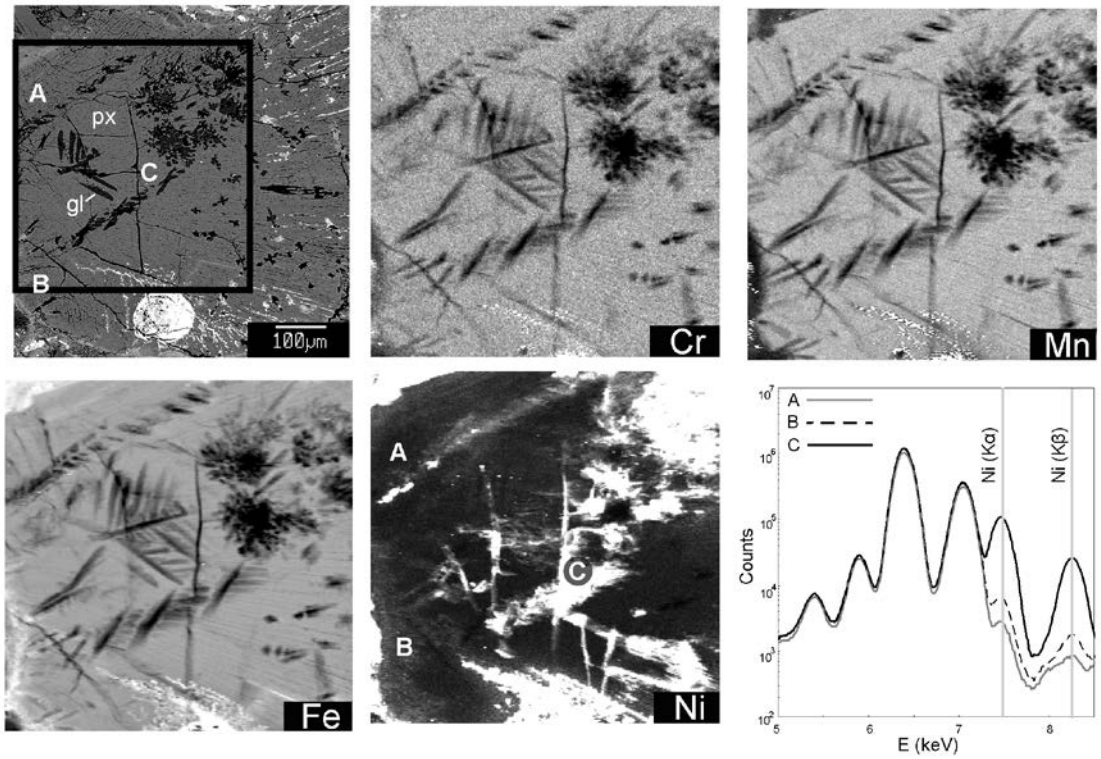

Figure 3.3. BSE image and elemental maps for a type II radial pyroxene (px) chondrule from Semarkona (SMKMT 62231) analyzed at the APS. Nickel is mostly concentrated along fractures, euhedral silica glass laths (gl), Fe-rich veins and the Fe-rich rim. Nickel is also enriched in bleached zones along the chondrule rim (see spectrum for spot B). Chromium and Mn distributions look very similar, but there are a few differences (e.g., upper right and lower left of X-ray maps). It is possible that some of the Mn signal is from overlap with Cr (see explanation in Section 2.2.2). Variations in Ni for the regions labeled on the BSE image are highlighted in the spectra.

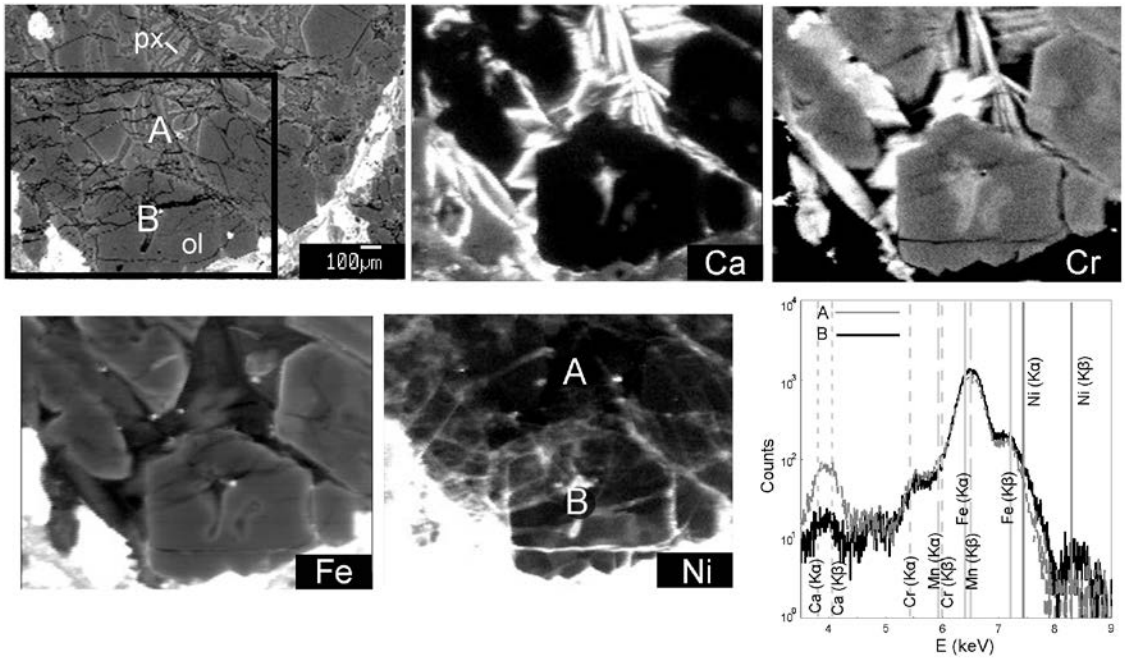

Figure 3.4. BSE image and elemental maps of a type I porphyritic olivine-pyroxene (px: pyroxene and ol: olivine) chondrule from QUE97008 analyzed at the AS. Iron and Ni are concentrated in along the numerous fine fractures. As the Ni map shows, the Fe- and Ni-bearing fractures occur at all scales down to the smallest scale visible on the image. Iron zoning is apparent in the olivine crystals. Chromium is concentrated in pyroxene grains. Variations in Ni for the regions labeled on the BSE image are highlighted in the spectra.

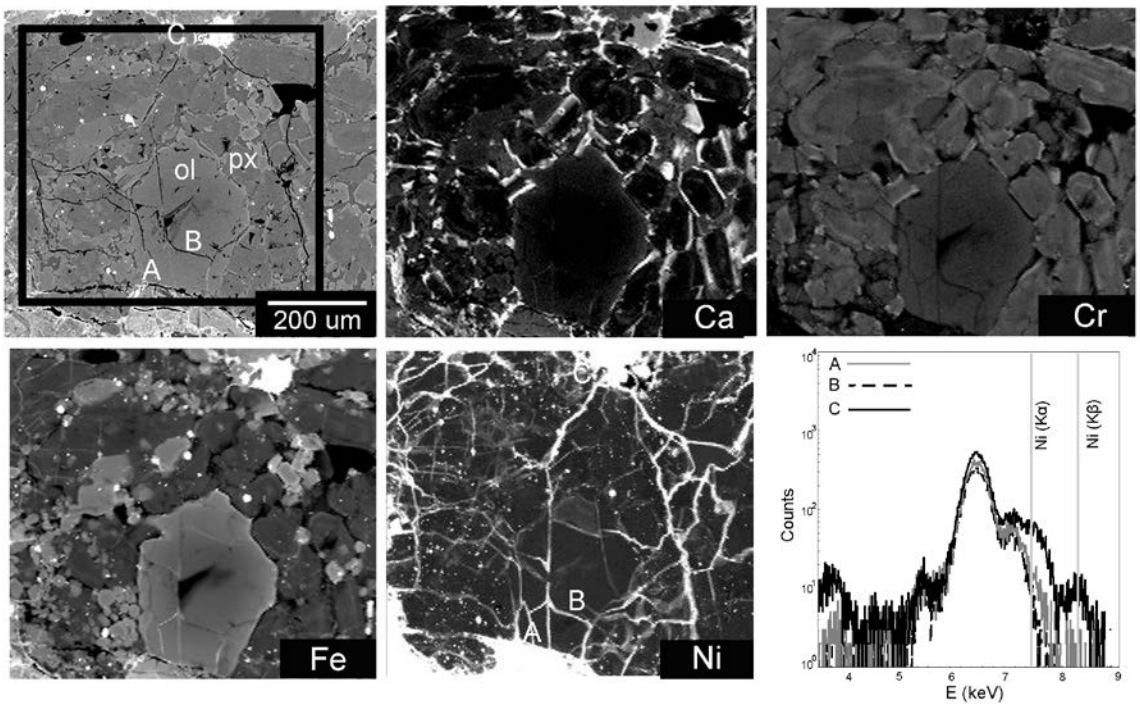

Figure 3.5. BSE image and elemental maps for EET87735 (EET87735 chF), a type II porphyritic olivine (ol) and pyroxene (px) chondrule analyzed at the AS. Iron shows compositional zoning in both olivine and pyroxene, while Cr compositional zoning occurs only in pyroxene. This chondrule has Fe-rich veins that emanate from the matrix. This can be seen in fractures of the large olivine grain. Nickel-rich veins cut across the entire chondrule, from one side to the other. Iron and Ni are also concentrated in blebs scattered throughout the chondrule. Spectra for the regions labeled on the BSE image are shown.

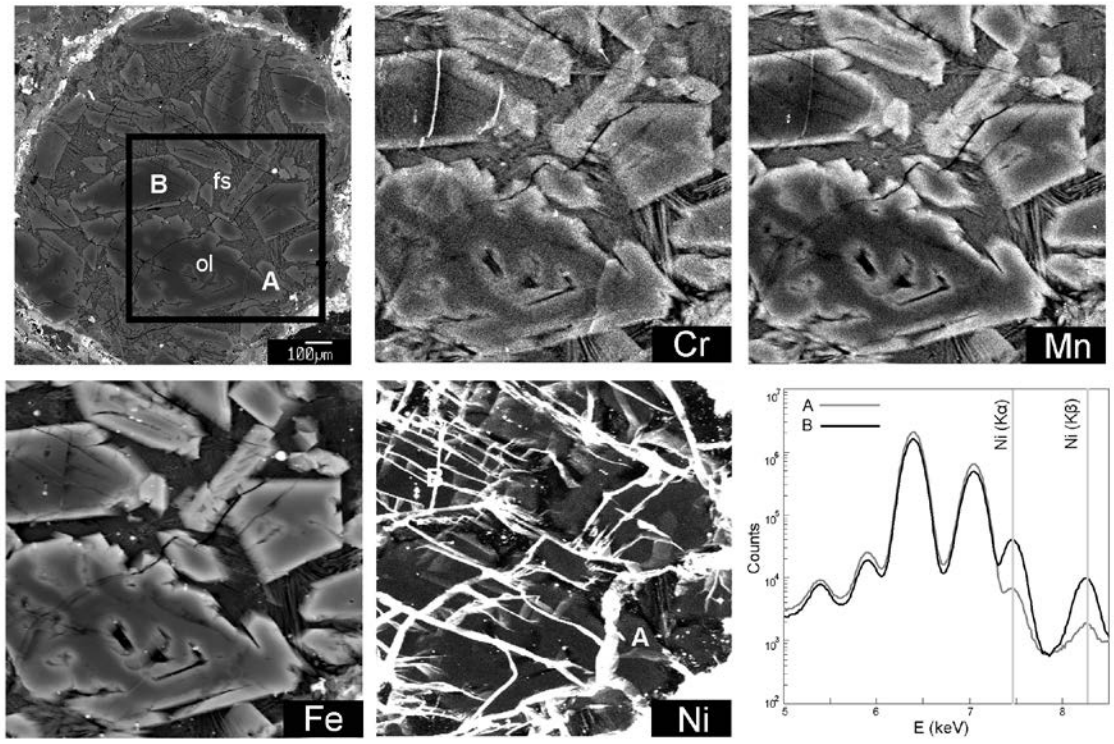

Figure 3.6. BSE image and elemental maps for MET96503 (MET96503 62224), a type II porphyritic olivine chondrule analyzed at the APS (ol: olivine and fs: feldspar). Iron and Cr have similar zoning in the olivine grains. Nickel enrichment in the chondrule fractures is also associated with Ni-rich blebs. Nickel variation in olivine is not resolved. Iron, Cr and even Mn are also concentrated in blebs and along chondrule fractures. It is possible that some of the Mn signal is from overlap with Cr (see explanation in Section 2.2.2). Variations in Ni for the regions labeled on the BSE image are highlighted in the spectra.

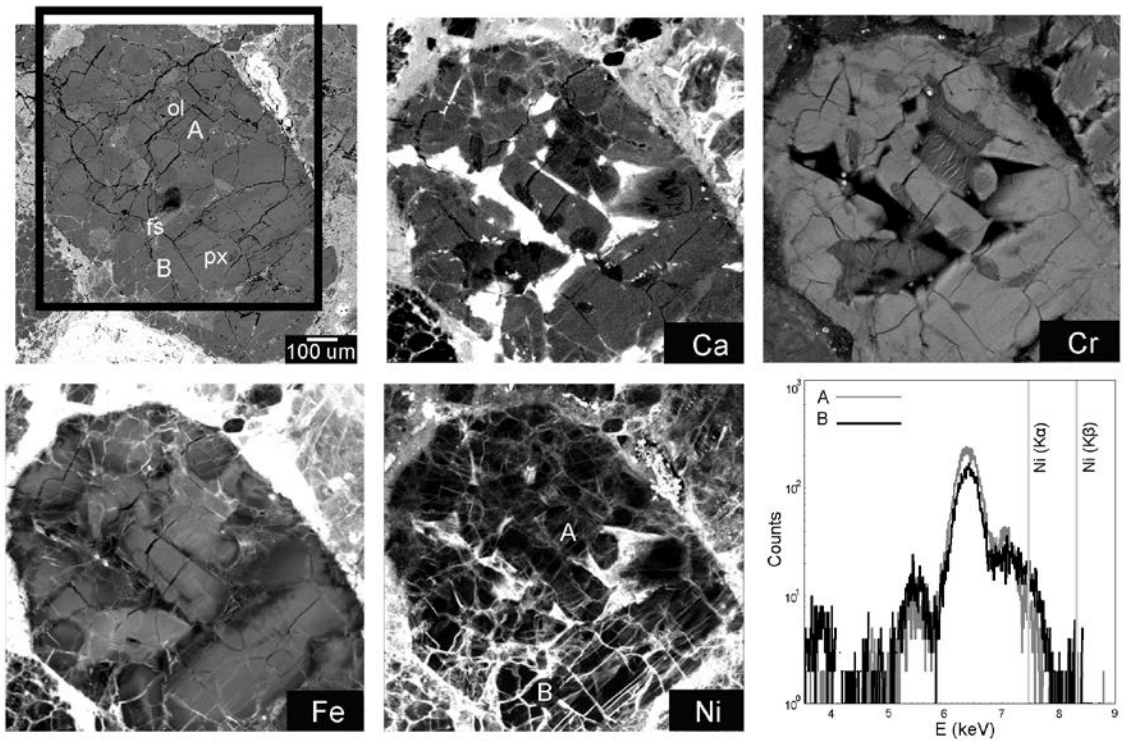

Figure 3.7. BSE image and elemental maps for TIL82408 (TIL 80074), a type I porphyritic pyroxene chondrule analyzed at the AS (ol: olivine, px: pyroxene, and fs: feldspar). There is extensive Fe, Ni and Ca enrichment along chondrule fractures (Ca signal from the mesostasis has been stretched to saturation in order to point out Ca in fractures). Chromium shows exsolution features in olivine, but it is homogeneous in pyroxene. Variations in Ni for the regions labeled on the BSE image are highlighted in the spectra.

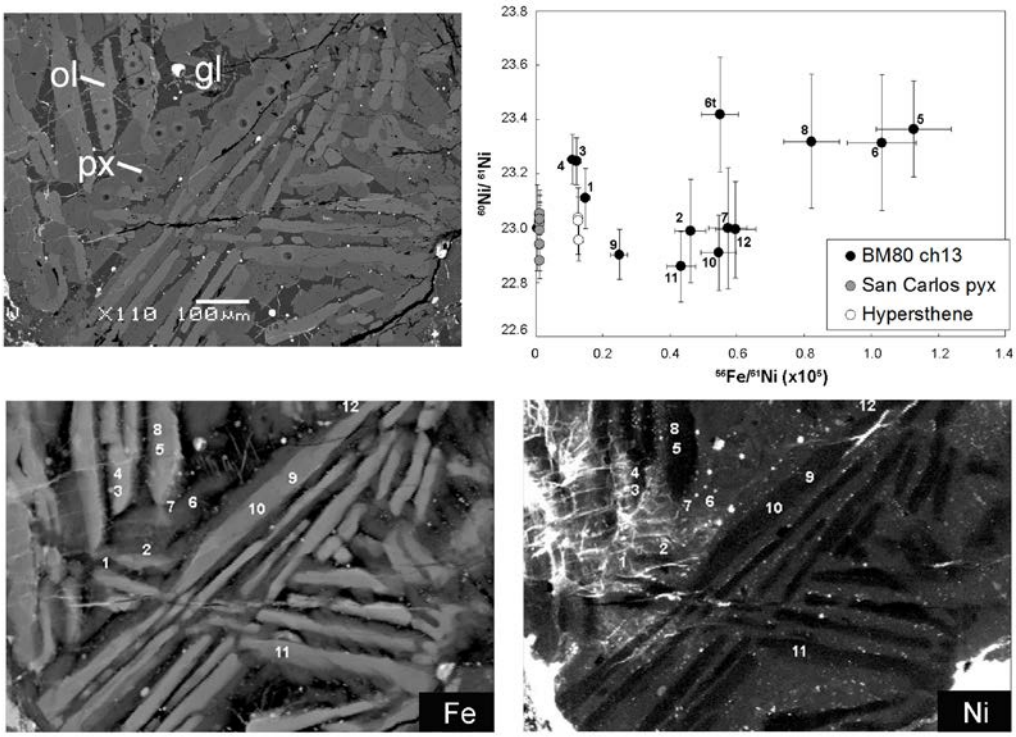

Figure 3.8. BSE image, SIMS data, and elemental maps for Bishunpur chondrule (BM80 ch13), a type II porphyritic olivine-pyroxene chondrule that was mapped at the AS (ol: olivine, px: pyroxene, and gl: glass). Iron and Ni enrichment can be observed along the cracks. Black ovals in the BSE image are from ion probe analyses. SIMS spots in the Ni enriched region (e.g., 1, 2, 3 and 4) have some of the lowest Fe/Ni ratios. Spot 6t is on and 6 are on the same spot. Hypersthene and San Carlos pyroxene are terrestrial standards.

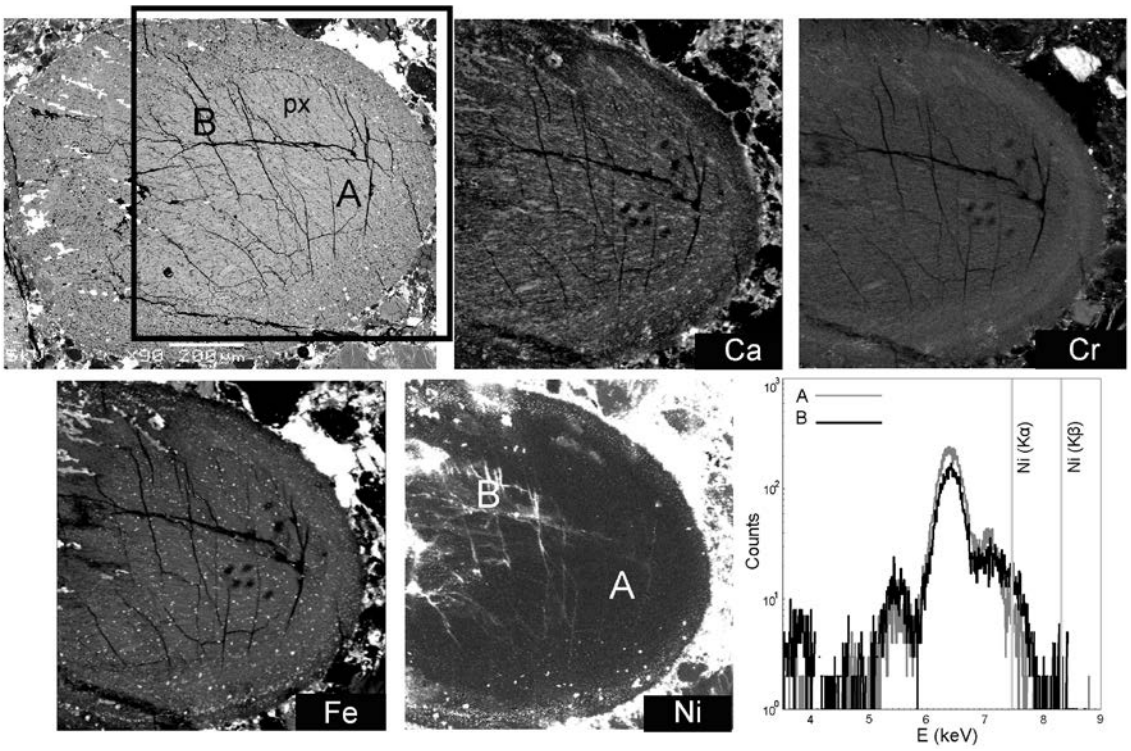

Figure 3.9. BSE image and elemental maps for Bishunpur (BM23 ch13), a type II bleached radial pyroxene (px) chondrule analyzed at the AS. Nickel is enriched along chondrule fractures. The Ni concentration in the fractures decreases with increasing distance from Fe-rich phases within the chondrule. Calcium and Cr appear to be correlated. Chromium is also enriched in the rim and Fe is enriched in sulfide blebs. Variations in Ni for the regions labeled on the BSE image are highlighted in the spectra. Black ovals in the X-ray maps are from ion probe analyses.

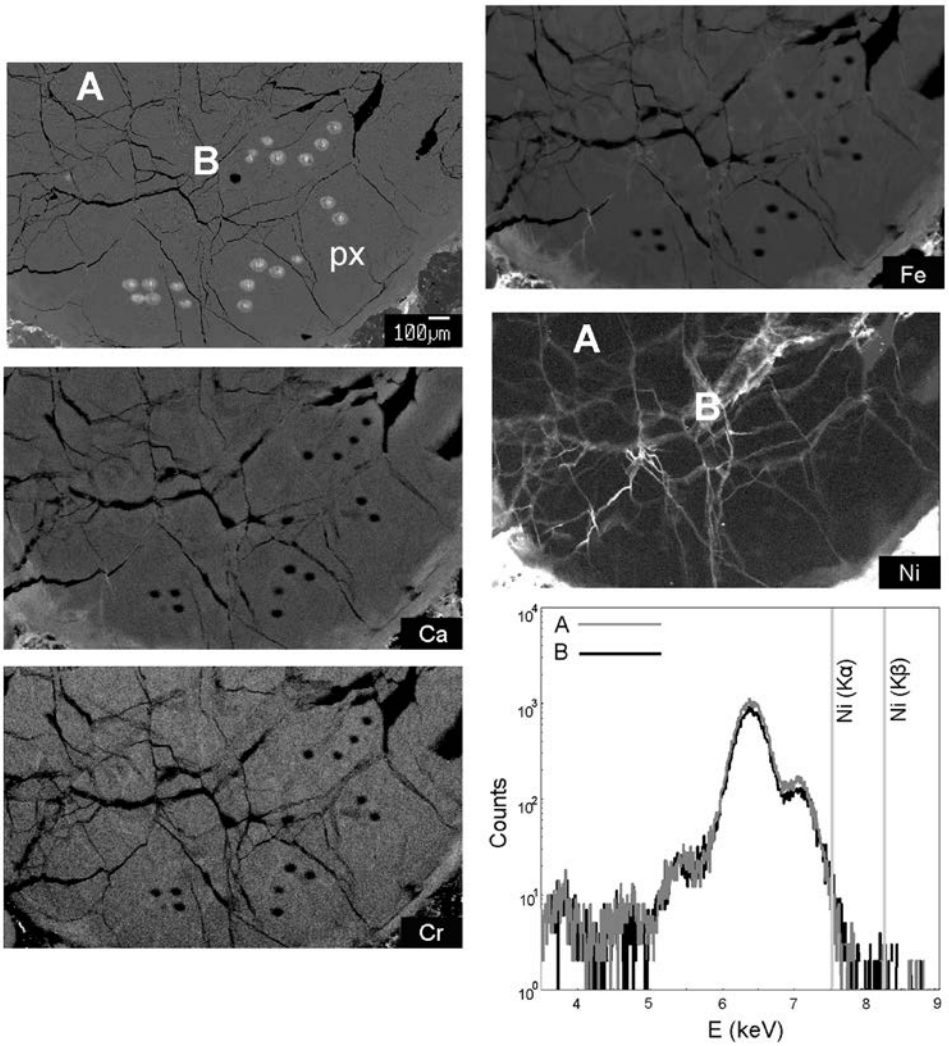

Figure 3.10. BSE image and elemental maps for Krymka chondrule (KRM9-4 ch1), a type II cryptocrystalline pyroxene (px) chondrule that was analyzed at the AS. Iron and Ni enrichment can be observed along the cracks. Iron and Ca are enriched in the bleached rim. Variations in Ni for the regions labeled on the BSE image are highlighted in the spectra. White ovals in the BSE image (black ovals in the X-ray maps) are from ion probe analyses, which may have been affected by Fe and Ni mobilization.

Table 3.1. Summary of synchrotron XRF mapping showing the percentage of chondrules from each UOC that show clear evidence for Fe and Ni mobilization

Chondrite	Type	Fall/Find & Year[1]	Total # of chondrules analyzed	% that show Fe and/or Ni mobilization
Semarkona	LL3.00	Fall, 1940	27	60
QUE97008	L3.05	Find, 1997	8	88
EET87735	L3.05	Find, 1987	2	100
EET90080	L3.05	Find, 1990	3	100
MET96503	L3.1	Find, 1996	5	100
TIL82408	LL3.1	Find, 1982	1	100
Bishunpur	LL3.1	Fall, 1985	14	79
Krymka	LL3.2	Fall, 1946	11	100

[1]Meteoritical Bulletin Database (http://www.lpi.usra.edu/meteor/metbull.php)

3.5 Discussion

Although the concentration of Ni in chondrule olivine and pyroxene is often below the detection limit, our synchrotron analyses provide important insight into the mobility of Fe and Ni in UOC chondrules. Our main observation is of Fe and Ni enrichment along chondrule fractures in UOCs regardless of petrologic type and regardless of whether fall or find (Table 3.1; Figures 3.2-3.10). In some cases, Fe and Ni enrichment in chondrule fractures appears to decrease with increasing distance from the matrix (e.g., Figures 3.4 and 3.6), indicating open system Fe-Ni exchange between chondrules and surrounding matrix. These observations provide substantial evidence for pervasive late-stage redistribution of Fe and Ni in UOC chondrules. Late stage redistribution of Fe and Ni is a possible cause for the poor correlation between excess

^{60}Ni and the Fe/Ni ratios of many *in situ* analyses and the discrepancies between *in situ* and bulk analyses, as we will discuss below.

3.5.1 *Mechanisms of redistribution of Fe and Ni in UOC chondrites*

There are various mechanisms for Fe-Ni mobilization in chondrules, including lattice diffusion, grain boundary diffusion, and fluid transport. Lattice diffusion involves redistribution of Fe and Ni through vacancies in the crystal lattice. The Ni concentration in chondrule silicates is at the trace level, olivine typically < 500 ppm and pyroxene typically < 200 ppm, making it difficult to assess the influence of lattice diffusion on the Ni distribution in these phases. Although Ni concentrations are too low to map Ni in olivine, Cr concentrations are high enough to analyze. Experimental diffusion studies of Cr in olivine and orthopyroxene indicate that Cr is essentially immobile in these phases below ~400 °C (Ito and Ganguly, 2006; Ganguly et al., 2007). The Ni diffusion rate in olivine is similar to the Fe-Mg interdiffusion rate and approximately 3 times faster than diffusion of Cr at temperatures below 700 °C (Petry et al., 2004; Chakraborty, 2010). Grossman and Brearley (2005), show that Cr begins to diffuse out of Fe-rich olivine and form chromite grains in type 3.05 chondrites and has mostly left olivine in type 3.1 chondrites. Since Ni diffuses faster than Cr in olivine, prolonged thermal metamorphism can potentially cause Ni diffusion out of olivine and concentrate it in Ni-rich metal and/or sulfide inclusions. Our Fe-Ni ion probe analyses focus on pyroxene instead of olivine because pyroxene generally has higher Fe/Ni ratios than olivine and should be more resistant to metamorphism. The Fe-Mg interdiffusion in Fe-rich orthopyroxene at 700 °C is slower by a factor of ~2.5 compared to olivine (Cherniak and Dimanov, 2010) and Cr diffusion in orthopyroxene at that temperature is slower than in olivine by a factor of ~2

(Ganguly et al., 2007; Cherniak and Dimanov, 2010). Although, experimental data for Ni diffusion in pyroxene is lacking, we expect lattice diffusion of Ni in pyroxene is slower than in olivine by a factor of 2-3 and therefore not significantly affected by thermal metamorphism at the peak temperatures of type 3.00 – 3.2 UOCs (200-400 °C; e.g., Huss and Lewis, 1994).

Grain boundaries and defects in a crystal function as short-circuit diffusion paths, producing another possible mode of redistributing elements in UOCs. In the presence of a fluid phase, grain boundary diffusion can be orders of magnitude faster than lattice diffusion (e.g., Klinger and Rabkin, 1999). Thus, diffusion along grain boundaries and cracks could potentially allow Fe and Ni to move large distances (>100 μm) into and out of olivine and pyroxene grains on a relatively short timescale. This diffusion mechanism is consistent with the observation of Fe and Ni enrichment along chondrule fractures from our XRF maps. Currently, there are no studies of grain boundary diffusion of Ni under the conditions relevant to the thermal and/or aqueous processing experienced by UOC chondrules on their parent bodies. Various mechanisms for grain boundary diffusion are discussed in Dohmen and Milke (2010). The mechanism that is the most relevant to UOC chondrules based on our observations is the structural-inhomogeneity model, also called pipe diffusion (Klinger and Rabkin, 1999). This model involves diffusion along dislocations (e.g., fractures), subgrains (e.g., inclusions), and/or lamellar precipitates. Our observations are consistent with the scenario where temperatures within chondrules are low such that lattice diffusion is negligible and diffusion occurs mainly along grain boundaries without much leakage to the adjacent crystals (referred to as type

C kinetics). Mishin and Herzig (1999) provide a detailed explanation of grain boundary diffusion and the different regimes that vary with temperature and annealing times.

During fluid transport, elements are mobilized through dissolution and precipitation of minerals. Some of the FeNi-enriched veins could be a result of precipitation of FeNi-oxides and/or hydroxides from fluid flowing through empty fractures. Fluid transport on UOC chondrite parent bodies has been inferred from the presence of hydrous phases (e.g., phyllosilicates), precipitates (e.g., calcite), and bleached chondrules. The mechanism for fluid transport was mostly likely melting of accreted ices during thermal metamorphism (e.g., Alexander et al., 2012) and/or impacts on the asteroid parent body (e.g., Bland et al., 2014). Bleached chondrules are prevalent throughout UOCs and provide substantial evidence for Fe-Ni mobilization during aqueous alteration (e.g., Figure 3.3). These radial or cryptocrystalline chondrules are readily recognized by porous zones, usually located along the chondrule rim, where mesostasis has been removed. Grossman et al. (2000) carried out an extensive study on the petrological, chemical, mineralogical and H-isotopic composition of bleached chondrules from Semarkona. They observed that bleached zones occur near the chondrule surface or along cracks in the chondrule. They found increases in Fe in the outer zone, the outermost region of a bleached chondrule. Bleached regions are depleted in Na and Al. Sulfur is found in sulfide blebs and stringers located throughout these chondrules, but in the bleached zone, there is some Fe, Na and Al enrichment associated with sulfide blebs and stringers. Bleached zones are enriched in H, Cl and F and their H-isotopic compositions are intermediate between compositions for the unbleached core of the chondrule and the matrix. The Grossman et al. (2000) analyses show that the bleached

zones contain an abundance of Fe-rich smectite that are platy in appearance and appeared to have grown in place. Finally, the bleached zones are also rich in pentlandite, not troilite, which is found in the unbleached core of these chondrules, indicating that the Ni for pentlandite formation must have come from somewhere other than the chondrule.

Overall, our synchrotron XFM observations of two bleached chondrules from Semarkona and two from Krymka are consistent with those of Grossman et al. (2000). The outer zone is enriched in Fe, Ca is enriched in the bleached zone, and Cr shows little to no variations (e.g., Figure 3.10 and Appendix B figures B.3-B.4). The bleached rim of the chondrule from Bishunpur featured in Figure 9 appears to consist of two zones, a Fe-rich inner layer and a Fe- and Ca-poor outer layer. In another bleached chondrule from Bishunpur (Appendix B.5), the bleached zone has been filled with an Fe-Ni-rich phase. Our maps show that Ni is typically enriched in the bleached and outer zones (e.g., Figure 3.3, 3.9, 3.10 and Appendix B Figures B.4-B.5). In Semarkona, the most extensive Ni mobilization occurs in a bleached chondrule (Figure 3.3). Most of the Ni in this chondrule is associated with feathery silica glass laths. The bleached region (see spot labeled B on BSE image) shows enrichment of Ni and there is a small outer zone that is enriched in Fe and Ni (visible in the lower left region of BSE image and X-ray maps). We normally avoid these regions during SIMS analyses, so they do not necessarily affect our *in situ* analyses. However, some open spaces that could be targeted for SIMS analyses (e.g., region labeled "C" in Figure 3.3) are clearly compromised by extraneous Ni. Semarkona chondrules not only experienced dissolution of the mesostasis, but there is also evidence for dissolution of Fe-Ni-rich blebs or nodules (Figure 3.11), which could have been the source of some of the extraneous Fe and Ni in chondrules. Grossman et al.

(2000) concluded that bleaching occurred during fluid transport through the porous matrix and cracks on the parent body. Since Ni mobilization is also associated with bleaching, this lends support for Ni mobilization on the asteroid parent body, although the possibility of mobilization during terrestrial weathering remains.

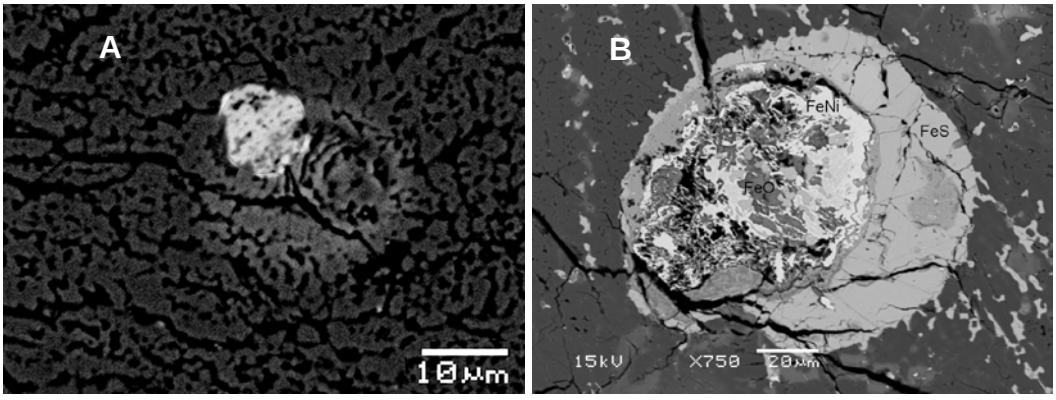

Figure 3.11. Backscatter electron images of an Fe-rich bleb (A) and opaque nodule (B) from Semarkona chondrules (Appendix B.3 and Figure 3.3, respectively). Porous regions within the bleb and nodule are likely due to bleaching as a result of transient fluid, which likely also mobilized Ni. The bright circular region next to Fe-rich bleb is a SIMS pit.

Constraints on the temperature during aqueous alteration are based on the thermodynamic stability of certain phases found in chondrites. For Semarkona, the least metamorphosed UOC, the presence of maghemite and the absence of hematite in chondrule rims and matrix, and the structure of smectite place an upper limit of 260°C for the temperature during aqueous alteration of these chondrites (Alexander et al., 1989). This is consistent with peak temperatures for this chondrite inferred from noble gases in presolar nanodiamonds (Huss et al., 1994), and spectroscopic features of insoluble organic matter (IOM; Cody et al., 2008). For Krymka (LL3.2), the most metamorphosed UOC analyzed in this study, peak temperatures inferred from presolar grains and the IOM indicate aqueous alteration occurred at temperatures below 400°C (Huss et al., 1994; Cody et al., 2008). The evidence from our synchrotron analyses of Fe-Ni mobilization in

these chondrites and the association of Fe-Ni mobilization with bleached chondrules indicates that Fe-Ni mobilization on the parent bodies occurs at temperatures of 260°C or lower.

Terrestrial weathering is another possible mechanism for Fe and Ni enrichment along chondrule fractures. All chondrules from Antarctic finds (except one chondrule from QUE97008) show clear evidence for Fe-Ni enrichment along fractures (Table 3.1). In particular, TIL82408 chondrule in Figure 3.7 shows enrichment of Ca along with Fe and Ni along the chondrule fractures. TIL82408 is the only chondrite analyzed so far that shows evidence for extensive Ca mobilization, which may be indicative of terrestrial weathering. But all Antarctic finds show more evidence of Fe and Ni mobilization than the witnessed falls. Thus, terrestrial weathering has likely overprinted parent body alteration since they both involve fluid transport at low temperatures.

Our observations of Fe-Ni enrichment regardless of petrologic type and regardless of whether fall or find indicate that the mechanism for Fe-Ni mobilization includes both low temperature parent body aqueous alteration and terrestrial weathering.

3.5.2 *Effects of Fe and Ni redistribution on ^{60}Fe-^{60}Ni systematics*

For *in situ* analyses, redistribution of Fe and Ni after the decay of ^{60}Fe affects the isochrons differently depending on whether lattice diffusion, grain boundary diffusion, or fluid transport has taken place. Grain boundary diffusion and fluid transport cause Fe-Ni exchange, with a net addition of Fe and/or Ni to chondrule olivine and pyroxene from the surrounding matrix via fractures in the chondrules. Many of the fractures are very fine and are not readily detected without the assistance of the synchrotron maps (e.g., Figures 3.2 and 3.4). *In situ* measurement spots can easily overlap fine fractures and incorporate

extraneous Fe and/or Ni. The schematic isochron plot in Figure 3.12A illustrates the effect of extraneous Fe and/or Ni on internal isochrons. If a spot analysis incorporates pure Fe from a fracture, the Fe/Ni ratio will be higher than the true value, which will shift the point to the right on the isochron plot and will decrease the inferred initial $^{60}Fe/^{56}Fe$ ratio of the chondrule. Incorporating pure Ni from the fracture will change both Fe/Ni ratio and the Ni-isotope ratio such that the disturbed spot still lies along the original slope but closer to the origin. In reality, chondrule fractures contain both Fe and Ni at some level, and often the concentration of the Ni in the fractures is higher than Ni concentrations in the olivine and pyroxene. Adding both extraneous Fe and Ni in a spot analysis will change the Ni-isotope ratio and the Fe/Ni ratio ("region of possible values" for disturbed analyses is the grey region in Figure 3.12A), resulting in an overall decrease in the inferred initial $^{60}Fe/^{56}Fe$ ratio compared to the original value.

Metal/sulfide inclusions in chondrule olivine and pyroxene are common (e.g., Figures 3.2 and 3.6). They can be difficult to avoid during SIMS analyses because they are often submicron in size and are dispersed throughout the chondrule. During lattice diffusion, Ni from olivine, pyroxene and metal/sulfide can exchange, with a net diffusion of Ni from olivine and pyroxene to metal/sulfide due to the partition coefficients (http://earthref.org/KDD/). This will preferentially remove Ni from Fe-silicates and concentrate it in sulfide/metal blebs within or adjacent to the silicates. Figure 3.12B describes the effect of lattice diffusion on internal isochrons. Extracting Ni from olivine and pyroxene will increase their Fe/Ni ratios. This will move the point to the right on the isochron plot. Exchange of Ni between Fe-silicates and metal/sulfide will lower the Ni-isotopic ratio and also move the point down on the isochron plot. SIMS spot analyses that

only incorporate olivine or pyroxene where Ni has been extracted will thus have a higher Fe/Ni ratio and lower-Ni isotopic composition than the true value. Disturbed points (towards lower-right) have been observed and modeled in ^{26}Al-^{26}Mg systematics of high Al/Mg phase (anorthite) and low-Al/Mg phases in a CAI from Allende, a metamorphosed chondrite (LaTourrette and Hutcheon, 1999; Ito and Messenger, 2010).

Lattice diffusion will hardly change the Fe/Ni ratio and Ni-isotopic composition of metal. If a spot analysis incorporates metal blebs, this will move the point towards the intercept on the isochron. Sulfides are more complicated because they can be primary or secondary phases. Primary troilite is usually Ni-poor, while secondary sulfide is Ni-rich (pentlandite). Spot analyses that incorporate primary sulfide blebs will move points towards the intercept. A spot analysis that overlaps secondary sulfide inclusions that contain Ni extracted from the bulk silicate will have a Fe/Ni ratio that is lower that the true value, moving the spot to the left on the isochron plot (Figure 3.12B). Altogether, lattice diffusion will result in a poor correlation between the Ni isotopic composition and the Fe/Ni ratio.

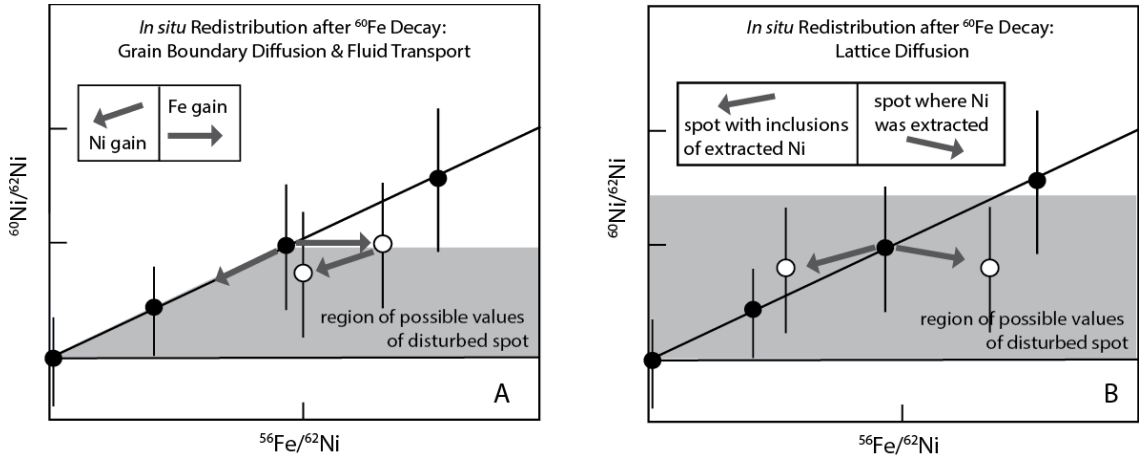

Figure 3.12. Schematic diagram illustrating the region of possible ^{60}Ni/^{62}Ni and ^{56}Fe/^{62}Ni ratios for chondrule spot analyses affected by Fe and/or Ni enriched fractures from grain boundary diffusion (A), and Ni exchange from silicates into metal/sulfide inclusions

during lattice diffusion (B). Error bars have been drawn to illustrate the effect of redistribution on our ability to resolve excesses in ^{60}Ni.

Bulk Fe-Ni analyses of chondrules can be influenced by fluid transport of Fe and Ni. Extraneous Fe and Ni in bulk meteorites are usually attributed to contamination from terrestrial weathering. However, mobilization of Fe and Ni through late-stage low-temperature aqueous processing on the ordinary chondrite parent body also occurred, as discussed above. Both terrestrial contamination and parent body aqueous alteration involve fluid transport of Fe and/or Ni and can result in Fe and/or Ni enrichment along chondrule fractures and void spaces. Figure 3.13A shows that during fluid transport the chondrule as a whole will gain Fe and/or Ni, changing both the Ni-isotope composition and the Fe/Ni ratio, and resulting in a lower inferred initial ^{60}Fe/^{56}Fe ratio for the chondrule.

A common approach for removing extraneous material in chondrule fractures and pore spaces is to wash the chondrules with a mild acid, usually ethanol and HCl, prior to dissolving them for wet chemistry. Some bulk studies wash the chondrule before crushing (e.g., Tang and Dauphas, 2012) and others wash after crushing the chondrule (e.g., Chen and Papanasstassiou, 2013). This procedure helps remove extraneous Fe-Ni rich material from chondrule fractures, but it also has the potential to leach Fe and Ni from the chondrule. For instance, Quitté et al. (2011) found that washing 150 mg of Bouvante (eucrite) in acetone for 5 minutes in an ultrasonic bath leached over 30% of the total Ni. If leaching removes any of the original Fe and Ni from the chondrule, or fails to remove all of the extraneous Fe and Ni, the resulting isotopic measurement will not give reliable results (e.g., Figure 3.13B). If Ni is more readily leached than Fe (Quitté et al.,

2011), this will preferentially move the data point to right on the isochron diagram, resulting in lower initial $^{60}Fe/^{56}Fe$ ratios.

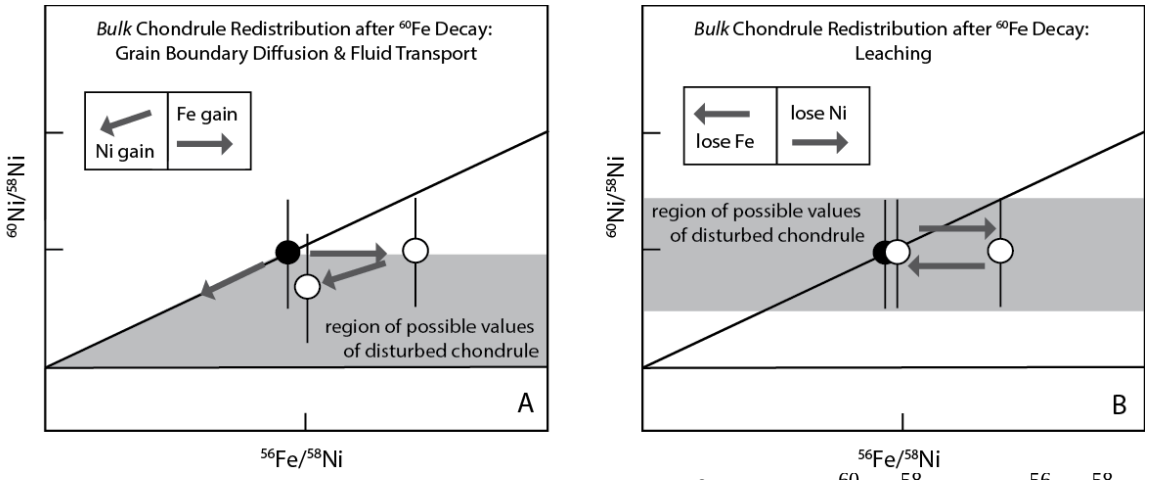

Figure 3.13. These diagrams illustrate the region of possible $^{60}Ni/^{58}Ni$ and $^{56}Fe/^{58}Ni$ ratios for bulk chondrule analyses affected by Fe and/or Ni enriched fractures from grain boundary diffusion (A), and Fe and Ni extraction from the chondrule during leaching (B). Error bars have been drawn to illustrate the effect of redistribution on our ability to resolve excesses in ^{60}Ni.

3.5.3 *Implications for ^{60}Fe-^{60}Ni analyses of UOC chondrules and other meteorite samples*

Low-temperature mobilization of Fe and Ni in chondrules from type 3.00 – 3.2 UOCs calls into question whether these are actually the appropriate samples for constraining the initial $^{60}Fe/^{56}Fe$ ratio of the solar system. Appropriate samples must have remained closed systems since the chondrules formed in order for the derived date to be relevant to chondrule formation, the event that can be dated by the Pb-Pb system and other isotopic techniques. Our observations show that most chondrules from type 3.0-3.2 UOCs have experienced open-system exchange of Fe and Ni, either on the parent body or on Earth, or both.

Ion probe analyses of UOC chondrules have been of both falls and finds. There are discrepancies between SIMS analyses from different groups. Mishra and Goswami

(2014) and Mishra and Chaussidon (2014) found evidence for ^{60}Fe in many UOC chondrules with initial ^{60}Fe/^{56}Fe ratios ranging from 2×10^{-7} to 1×10^{-6}, whereas Telus et al. (2012a) found that very few chondrules show clear evidence for ^{60}Fe, with those that do giving initial ratios of 1×10^{-7} to 3×10^{-7}. The source of inconsistencies from different SIMS groups is still unclear. Some of our SIMS analyses clearly overlap Fe-Ni rich fractures within the chondrules (e.g., Figures 3.8 and 3.10). The work presented here indicates that this overlap can explain the poor correlation between excess ^{60}Ni and the Fe/Ni ratios of many of the SIMS analyses (e.g., Telus et al., 2012a). The chondrule featured in Figure 3.8 was analyzed with the SIMS prior to collecting the elemental maps at the synchrotron. SIMS spots 1 through 4 clearly overlap a region enriched in extraneous Ni. These spots also have some of the lowest Fe/Ni ratios. However not all of the spots with low Fe/Ni ratio or low Ni-isotope ratios are obviously affected by extraneous Ni, such as spots 9, 10 and 11. Eliminating points that have been clearly contaminated does not improve the correlation between the Fe/Ni and Ni-isotope ratios. Chondrules that do not show resolved excess ^{60}Ni, despite high Fe/Ni ratios, may have experienced extensive redistribution of Fe and Ni. Future ion probe analyses can potentially avoid these fracture and altered areas by thoroughly characterizing each chondrule prior to isotopic analyses. It may be possible to identify suitable spots within chondrules from the most primitive UOCs for Fe-Ni measurements. However, it is still not clear from our analyses whether secondary processing has affected Ni within the silicates, away from the chondrule fractures. If this is shown to have occurred, UOC chondrules would be inappropriate for determining the initial ^{60}Fe/^{56}Fe ratio of the solar

system. Otherwise, unbleached, fracture-free ferromagnesian chondrule silicates may yet offer a reliable estimate of the initial $^{60}Fe/^{56}Fe$ ratio of the solar system.

Bulk Fe-Ni analyses of UOC chondrules from falls and finds infer initial ratios $<3\times10^{-8}$ (Spivak-Birndorf et al., 2012a,b; Tang and Dauphas, 2012; Chen et al., 2013; Tang and Dauphas, 2015), 1-2 orders of magnitude lower than what is inferred from SIMS analyses. In order to avoid being compromised by extraneous material in chondrule fractures, the chondrules are washed in weak acids prior to analyses. Although washing chondrules helps with removing surficial material, it is not clear how effective this is for removing material in fine fractures. If washing does not remove all extraneous material in chondrule fractures, the extra Fe and Ni will generate erroneously lower initial ratios (Figure 3.13B). Prolonged washing in acid may leach Fe and Ni from silicates, which can also compromise these analyses. Given the prevalence of Fe-Ni enrichment in UOC chondrules, it is likely that these analyses have been compromised by Fe-Ni mobility. Other types of meteorites may potentially be better candidates for studying ^{60}Fe-^{60}Ni systematics. However, each sample needs to be characterized in detail to determine whether Fe and Ni have remained undisturbed by solid-state diffusion, aqueous alteration, and/or terrestrial weathering.

3.6 Conclusions

Identifying samples suitable for Fe-Ni analyses is critical for constraining the initial $^{60}Fe/^{56}Fe$ ratio of the solar system and for the continued development of the ^{60}Fe-^{60}Ni chronometer. We have focused our Fe-Ni ion probe analyses on chondrules from UOCs in order to avoid complications from Fe-Ni redistribution. However, synchrotron

X-ray fluorescence maps collected at the Australian Synchrotron and the Advanced Photon Source show substantial evidence for Fe and Ni mobilization along chondrule fractures in UOCs regardless of petrologic type or whether fall or find (Table 3.1, Figures 3.2-3.10). Even Semarkona, the least metamorphosed UOC chondrite, shows evidence for Fe-Ni mobilization. Our synchrotron X-ray data provides evidence for significant exchange of Fe and Ni between chondrules and matrix, which provides some explanation for the weak correlation between excess ^{60}Ni and the Fe/Ni ratios from *in situ* analyses (Figure 3.12) and for the discrepancies between *in situ* and bulk Fe-Ni analyses (Figure 3.13). Late-stage Fe-Ni mobilization was likely facilitated by fluid considering the large distances (>100 um) that Fe and Ni have been redistributed in many chondrules. Iron-nickel redistribution on this scale requires caution in collecting and interpreting *in situ* and bulk Fe-Ni data. *In situ* analysis may still be appropriate for these analyses if chondrule fractures are avoided with a high degree of care. Otherwise, UOC chondrules may not be suitable for constraining the initial ^{60}Fe/^{56}Fe of the solar system.

CHAPTER 4. **RECALCULATION OF DATA FOR SHORT-LIVED RADIONUCLIDE SYSTEMS USING LESS-BIASED RATIO ESTIMATION**

Published in its present form as Telus, M., G. R. Huss, R. C. Ogliore, K. Nagashima, and S. Tachibana (2012), Meteoritics and Planetary Science, 47, 2013-2030.

doi: http://dx.doi.org/10.1111/j.1945-5100.2012.01411.x

4.1 Abstract

Ratios determined from counting a subset of atoms in a sample are positively biased relative to the true ratio in the sample (Ogliore et al., 2011). The relative magnitude of the bias is approximately equal to the inverse of the counts in the denominator of the ratio. SIMS studies of short-lived radionuclides are particularly subject to the problem of ratio bias because the abundance of the daughter element is low, resulting in low count rates. In this paper, we discuss how ratio bias propagates through mass-fractionation corrections into an isochron diagram, thereby affecting the inferred initial ratio of short-lived radionuclides. The slope of the biased isochron can be either too high or too low, depending on how it is calculated. We then reanalyze a variety of previously published data sets and discuss the extent to which they were affected by ratio bias. New, more accurate, results are presented for each study. In some cases, such as for ^{53}Mn-^{53}Cr in pallasite olivines and ^{60}Fe-^{60}Ni in chondrite sulfides, the apparent excesses of radiogenic isotopes originally reported disappear completely. Many of the reported initial ^{60}Fe/^{56}Fe ratios for chondrules from ordinary chondrites are no longer resolved from zero, though not all of them. Data for ^{10}Be-^{10}B in CAIs were only slightly affected by bias because of how they were reduced. Most of the data sets were recalculated using the ratio of the total counts, which increases the number of counts in the denominator isotope and reduces the bias. However, if the sum of counts is too low, the ratio may still be biased and a less-biased estimator such, as Beale's estimator, must be used. Ratio bias must be considered in designing the measurement protocol and reducing the data. One can still collect data in cycles to permit editing of the data and to monitor and correct for changes in ion-beam intensity, even if total counts are used to calculate the final ratio.

The cycle data also provide a more-robust estimate of the systematic uncertainties in the data.

4.2 Introduction

Secondary ion mass spectrometry (SIMS) is an important tool for understanding short-lived isotopic systems and for constraining early solar system chronology. The SIMS technique, like many other analytical techniques, is fundamentally a sampling experiment: a subsample of a parent population is measured in order to estimate certain parameters of the source population (*e.g.* an isotope ratio). It is typically assumed that these sampled ratios are unbiased estimates of the true isotope ratios in the object. When the number of counts of the denominator isotope is large, this assumption is generally safe, but when the number of counts is low, the expectation value of the ratio calculated from the measurement can be significantly higher than the true ratio in the object (see, *e.g.*, Pearson 1910). Count rates of the denominator isotope during SIMS measurements of short-lived-radionuclide systems are often low, particularly when parent/daughter elemental ratios are high, making the isotope ratios susceptible to ratio bias. In this paper we refer to the bias as the expectation value of the measured isotope ratio minus the true ratio in the object. Ogliore et al. (2011) discusses the issue of ratio bias as it applies to SIMS measurements. They show that positive bias in isotope ratios inferred from counting data can be significant and can result in incorrect inferences about the objects. The relative bias (the bias divided by the true ratio) in ratio estimation is approximately equal to the inverse of the number of counts in the denominator (assumed to be Poisson distributed). For example, if the number of total counts of the denominator isotope is 200, the bias of the estimated ratio will be 5‰. The more counts of the denominator isotope, the smaller the bias and the closer the estimated ratio is to the true ratio that the investigator seeks to measure.

Ratio bias is particularly insidious in SIMS measurements of short-lived radionuclide systems where statistical bias from low counts in the denominator isotope can produce a correlation similar to an isochron with a positive slope (Figure 4.1a). The bias increases as the number of denominator counts decreases. In the example in Figure 4.1a, the counts of ^{55}Mn have been held constant for each set of data, so the x-axis of the plot is effectively 1/^{52}Cr, producing a perfect correlation. In a real system, the ^{55}Mn counts will also vary, which weakens the correlation. But for many natural systems, the parent/daughter element ratio is controlled primarily by variations in the daughter element abundance and the system approaches the modeled case. As we will show below, unrecognized ratio bias can easily be interpreted as evidence for the presence of a short-lived nuclide when the sample formed.

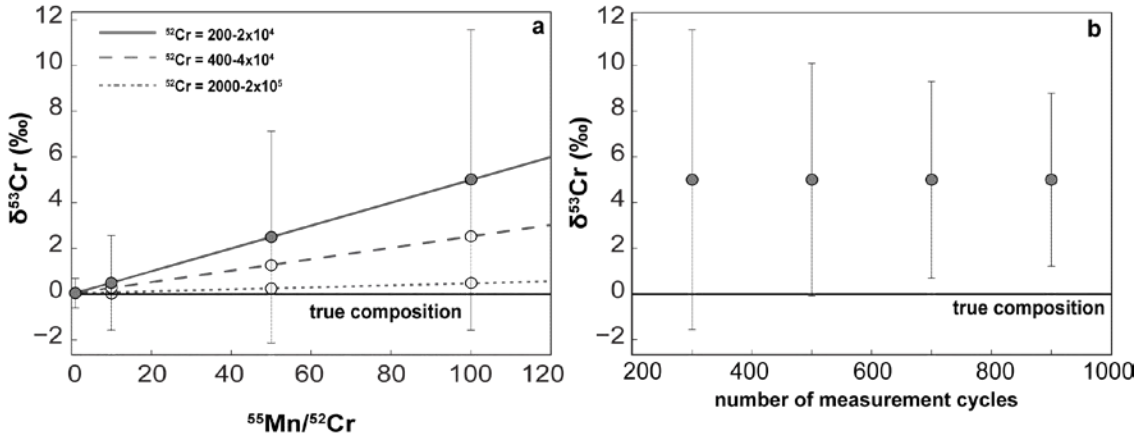

Figure 4.1. Panel (a) shows a generic example of an isochron-like diagram produced from ratios that are biased due to averaging ratios for individual measurement cycles. We set the number of cycles to 300, the count time for ^{52}Cr and ^{53}Cr to 3 and 20 seconds, respectively, and the ^{55}Mn counts per cycle to 2×10^4. Each line represents a different set of ^{52}Cr rates. As the count rate for the denominator decreases, the positive bias on the ^{53}Cr/^{52}Cr ratios increases, resulting in calculated ratios that are significantly higher than the true composition (solid black line). The bias from low ^{52}Cr counts also affects the ^{55}Mn/^{52}Cr ratio, but even the largest plotted shift in ^{55}Mn/^{52}Cr (5‰) does not show up on the diagram. The uncertainties (2σ) for one data set are shown in (a). Panel (b) shows that the bias in an isotope ratio does not decrease by averaging an increasing number of ratios,

but the statistical uncertainty in the inferred ratio does decrease. Improving the precision with more ratios does not decrease the bias.

Averaging the ratios from many cycles of a measurement is especially prone to ratio bias, because the counts obtained over the measurement are divided up amongst the individual ratios, resulting in a lower number of counts for each ratio. For instance, if a measurement is partitioned into 100 cycles, the ratio calculated by the mean of these 100 ratios will have a relative positive bias about 100 times larger than the ratio determined from dividing the total counts of the numerator isotope by the total counts of the denominator isotope. Increasing the number of ratios (while maintaining the same number of counts per ratio) improves the statistical uncertainty, but it does not decrease the bias (Figure 4.1b). If one averages 300 ratios with a mean of 200 counts in the denominator of each ratio, the estimated ratio will have an expectation value 5‰ greater than the true value and a statistical uncertainty of ±6.6‰ (the highest gray point in Figure 1a). However, if one averages 900 ratios, the estimated ratio will still be 5‰ larger than the true ratio even though the uncertainty has decreased to ±3.8‰ (Figure 4.1b). Totaling the counts before calculating the ratios will lower the bias. However, either method can be significantly biased if the counts in the denominator are low. The data for many of the published SIMS studies of short-lived radionuclide systems have been calculated using the mean of the ratios, implying that the published ratios may be significantly affected by statistical bias.

The most effective way to avoid ratio bias is to ensure that there are enough counts of the denominator isotope in each cycle of the measurement. In cases where this cannot be achieved, calculating ratios from the total counts will usually suffice to eliminate the effect of ratio bias. When the counts per cycle are very low, Beale's

estimator, a method that takes into account the total counts of the isotopes and the correlation between the numerator and denominator isotopes, will provide more accurate estimated ratios, since it is less biased (Ogliore et al., 2011). Coath and Steele (2012) proposed another ratio estimator with low bias. Determining the number of counts necessary to avoid biased ratios depends on the accuracy required to clearly observe the desired effects (*e.g.,* excesses in radiogenic isotopes).

In this paper, we discuss the effect of ratio bias on isochron slopes, and we report recalculated results for the data published in Hsu et al. (2005) on ^{53}Mn-^{53}Cr systematics of pallasites, in Tachibana and Huss (2003) and Guan et al. (2004) on ^{60}Fe-^{60}Ni systematics of sulfides from ordinary and enstatite chondrites, and in Tachibana et al. (2006) and subsequent abstracts from the University of Hawai‘i on ^{60}Fe-^{60}Ni systematics of silicates from ordinary chondrites. We also recalculated some of the data reported in Mishra et al. (2010) on ^{60}Fe-^{60}Ni systematics of silicates from ordinary chondrites, and data for ^{10}Be-^{10}B systematics of CAIs from CV chondrites published by MacPherson et al. (2003). We corrected for possible biases in the published isotopic ratios by calculating the ratios using the total counts instead of averaging the ratios from each cycle. For the ^{10}Be-^{10}B data, we also used Beale's estimator to calculate the ratios. The data reported here should be used in place of those reported in the original publications. We hope that re-evaluating these datasets will encourage other researchers to re-visit their data. The new data will provide much needed clarification on the abundances of short-lived radionuclides in the solar system.

4.3 Bias in Isochrons

The radiogenic excess of the daughter isotope is determined by calculating the ratio of the daughter isotope to a normalizing isotope of the same element and then correcting for instrumental mass fractionation and intrinsic mass fractionation in the sample. To make an isochron, the mass-fractionation-corrected isotope ratios are plotted as a function of the parent/daughter elemental ratio and the error-weighted regression, the isochron, is computed. The slope of the isochron gives the initial abundance of the radioactive parent (*e.g.*, Faure and Messing, 2005). To predict the effect of ratio bias in the slope of the isochron, it is necessary to understand how the ratio bias propagates through the entire analysis. Here we describe the correction for instrumental and natural mass fractionation and determine how the isochron slope is affected by ratio bias.

4.3.1 *Propagation of Ratio Bias through Mass Fractionation Correction*

In a system with only one isotope ratio available (*e.g.*, ^{10}Be-^{10}B and ^{53}Mn-^{53}Cr), the correction for mass fractionation is done "externally". (The ^{53}Mn-^{53}Cr system is typically treated as a one-ratio system because only ^{52}Cr and ^{53}Cr are free from interferences, leaving one ratio for the mass fractionation correction.) The correction is done by comparing the measured ratio in the sample to the measured ratio in a standard of similar mineralogy and known isotopic composition. The difference between the ratio measured in the standard and the true composition of the standard corresponds to the instrumental mass fractionation, and this difference is applied to the ratio for the unknown, using an appropriate mass-fractionation law. If the ratios for the standard and unknown are unbiased, any resulting difference between the true ratio for the standard and the corrected ratio for the unknown is considered an isotope anomaly. If the anomaly

is an excess of the daughter isotope of a short-lived radionuclide, and if the excesses among several measurements correlate with the parent/daughter elemental ratio, there is evidence for the former presence of the short-lived radionuclide in the sample, and its abundance at the time the sample formed is given by the slope of the isochron. If the isotope ratio for either the standard or the unknown is biased, the calculation of excess radiogenic daughter and the slope of the isochron are compromised. Typically, the standard has a higher abundance of the daughter element than does the unknown. Therefore, if the data are gathered in the same way for both, ratio bias will affect the measured ratio for the unknown more than for the standard and the difference between the biases would appear as an excess of the radiogenic daughter isotope.

When two isotope ratios are available (*e.g.*, ^{26}Al-^{26}Mg, ^{60}Fe-^{60}Ni systems), the correction for mass fractionation can be done "internally". One ratio, the one that does not include the radiogenic daughter isotope, is used to estimate the mass fractionation, and the fractionation inferred from that ratio is applied to the other ratio using an appropriate mass-fractionation law. The difference between the mass-fractionation-corrected ratio and the normal isotope ratio is the isotope anomaly. As in the case described above, if this anomaly is an excess of the daughter isotope and is correlated with the parent/daughter elemental ratio, there is evidence for the former presence of the short-lived radionuclide, and its abundance at the time the sample formed is given by the slope of the isochron.

Figure 4.2 describes schematically the effect of ratio bias on the inferred radiogenic excess for the ^{26}Al-^{26}Mg and ^{60}Fe-^{60}Ni systems. Figure 4.2a shows magnesium isotopes plotted as delta values with ^{24}Mg as the normalizing isotope. The normal

isotopic ratios, without mass fractionation or isotopic anomalies, plot on the horizontal flat line. Two cases of mass-dependent fractionation are illustrated by the gray symbols and solid lines. Here we arbitrarily define excesses of the heavy isotopes relative to normal magnesium as a positive mass fractionation and excesses of light isotopes as negative mass fractionation. The biases introduced into δ^{25}Mg and δ^{26}Mg from low counts in ^{24}Mg will be the same. The open symbols in Figure 4.2 represent the additional effect of a positive statistical bias on the mass-fractionated ratios. If an internal mass-fractionation correction is done using the biased ^{25}Mg/^{24}Mg ratio, represented by the dashed lines, the inferred value for δ^{26}Mg will be negative. This will decrease any real excess of radiogenic ^{26}Mg inferred for the measurement. However, if one does an external mass-fractionation correction, the system will behave like the ^{10}Be-^{10}B and ^{53}Mn-^{53}Cr systems and any bias will be positive, increasing the inferred excess of radiogenic ^{26}Mg. In general, because the ^{24}Mg count rate is approximately 10 times higher than the count rates of ^{25}Mg and ^{26}Mg, ratio bias is not a significant issue in the ^{26}Al-^{26}Mg system, but this should be verified for each new measurement.

Figure 4.2a can also be used to illustrate the situation where the radiogenic daughter isotope is between the two isotopes used for the fractionation correction (*e.g.*, if ^{25}Mg were radiogenic). If the ^{26}Mg/^{24}Mg ratio is used for the mass fractionation correction, the inferred degree of mass fractionation will be lower (still higher than the true value), and the fractionation-corrected ^{25}Mg/^{24}Mg would have a positive bias.

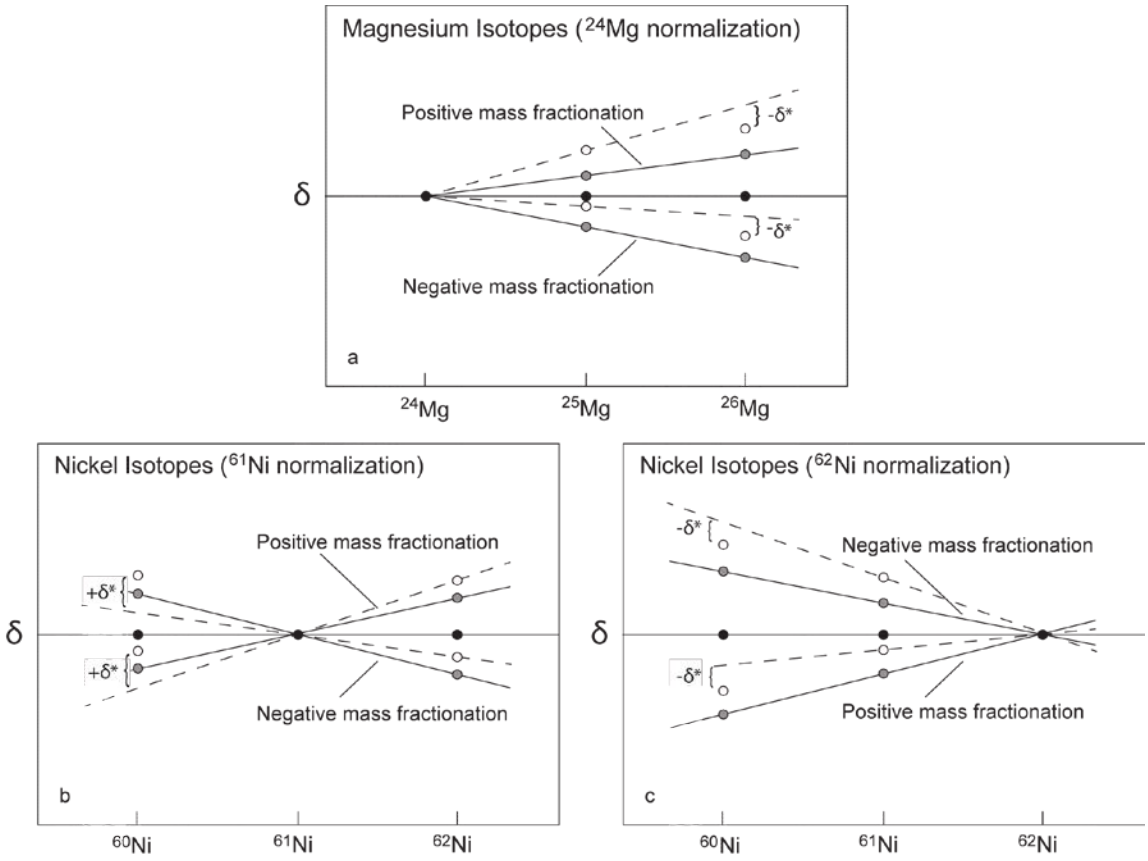

Figure 4.2. Schematic description of the effect of ratio bias on the measured radiogenic excess for three cases. In all panels, the isotope ratios are depicted as delta values relative to the listed normalizing isotope. The horizontal line in each plot represents a normal isotopic composition. Gray symbols and solid sloping lines illustrate linear mass fractionation. Positive mass fractionation is arbitrarily defined as a relative enrichment of heavy isotopes and negative mass fractionation as an enrichment of light isotopes. The open symbols show a hypothetical bias in the mass-fractionated ratios, and the dashed lines show the linear mass fractionation that would be inferred from the biased ratio. Inferred excesses or deficits in the radiogenic isotope relative to the calculated mass fractionation line are shown by the labeled brackets. a) The ^{26}Al-^{26}Mg system (^{24}Mg normalization): A ratio bias introduced by low counts in ^{24}Mg would result in the calculation of a deficit in δ^{26}Mg, which would reduce an inferred excess of ^{26}Mg due to decay of ^{26}Al. b) The ^{60}Fe-^{60}Ni system (^{61}Ni normalization): A ratio bias introduced by low counts in ^{61}Ni would result in a more extreme inferred mass fractionation. This would translate into calculation of an excess in δ^{60}Ni in addition to the bias already present in δ^{60}Ni, resulting in a larger inferred excess of radiogenic ^{60}Ni. c) The ^{60}Fe-^{60}Ni system (^{62}Ni normalization): A ratio bias introduced by low counts in ^{62}Ni would result in the calculation of a deficit in ^{60}Ni, which would decrease an inferred excess of radiogenic ^{60}Ni.

Figure 4.2b illustrates the nickel isotopes plotted as delta values normalized to ^{61}Ni. Again, mass fractionation is shown by the solid lines and gray symbols. The bias introduced by low counts of ^{61}Ni is the same for δ^{60}Ni and δ^{62}Ni. In this case, if the mass fractionation correction is done using the measured δ^{62}Ni, δ^{60}Ni will be overcorrected (dashed lines). The inferred excess in δ^{60}Ni will be the sum of the bias in the ^{60}Ni/^{61}Ni ratio and that in the ^{62}Ni/^{61}Ni ratio. Because ^{61}Ni is the least abundant isotope being measured, the ratio bias will be large in an absolute sense as well. For the ^{61}Ni normalization, an external fractionation correction will be less biased (all other things being equal) because the bias only contributes once to the final ratio.

Figure 4.2c illustrates the nickel isotopes normalized to ^{62}Ni. This case is analogous to that for the magnesium isotopes (Figure 4.2a). A bias in the ^{61}Ni/^{62}Ni ratio will result in an over-correction for mass fractionation in the ^{60}Ni/^{62}Ni ratio, which in turn will produce a negative isotope anomaly in δ^{60}Ni. However, once again, if an external mass fractionation correction is used, any bias in the ^{60}Ni/^{62}Ni ratio will be positive. For a given measurement, the total bias in δ^{60}Ni after an internal mass-fractionation correction introduced by normalizing to ^{61}Ni will be larger in magnitude than that introduced by normalizing the ^{62}Ni for two reasons: 1) the abundance of ^{61}Ni is ~3 times lower than the abundance of ^{62}Ni, and 2) the effect of bias on the mass fractionation correction is twice as great in the ^{61}Ni normalization.

4.3.2 *Ratio Bias in Isochron Fitting*

Once the excess of the radiogenic isotope is determined, the abundance of the radiogenic isotope relative to that of the normalizing isotope of that element is plotted as a function of the parent/daughter elemental ratio (see Figs. 3-9 below). Since both ratios

have analytical uncertainties, the equation of the fitted line is determined by solving the weighted least-squares problem. Generally, this is solved by the York method (York, 1966) or an equivalent formulation (*e.g.*, Ludwig, 2006). The effects of biased isotope ratios on an isochron can differ significantly, depending on the isotope system. We consider several cases explicitly below, but this treatment is not intended to be comprehensive.

Consider the simplest case where the isotope ratios are biased due to low denominator counts and there are no complications from an internal mass-fractionation correction. Consider further that the isochron is being constructed from several measurements of a single mineral with different parent/daughter elemental ratios. In this case, the differences in parent/daughter ratio will be due almost exclusively to the variable abundance of the daughter element. An isochron plot is then effectively a plot of the isotope ratio versus the inverse of the daughter-element abundance. In this case, the bias will correlate precisely with the elemental ratio and an array with a positive slope will be generated without any contribution from an excess of the radiogenic isotope. This is observed in some of the ^{53}Mn-^{53}Cr data discussed below.

If the isochron is produced from several minerals with different compositions, the effect of bias on the regression will be similar. Except, in this case, the correlation will be less precise than in the situation with a single mineral discussed above. There will be a general correlation because the abundance of major elements typically varies by a factor of two to three while the abundance of a trace element can vary by orders of magnitude.

We now turn to the case where ratios are corrected internally for mass fractionation. For the ^{26}Al-^{26}Mg system, isochrons are typically generated from several

minerals with different Al/Mg ratios. A slightly negative bias in the $^{26}Mg/^{24}Mg$ ratio will correlate with the inverse of the ^{24}Mg counts during the measurement. The resulting effect on the isochron will depend on the mineral composition and the measurement conditions, but will typically lower the inferred $^{26}Al/^{27}Al$ initial ratio. Fortunately, for most ^{26}Al-^{26}Mg measurements, the count rates are sufficiently high that the slight negative bias on the ratios is not significant.

For the ^{60}Fe-^{60}Ni system where the normalizing isotope is ^{61}Ni, bias in the isochron can be a severe problem, both because of the low number of counts and because the internal mass-fractionation correction amplifies the effect, as described above. In many samples measured to date, the spread in Fe/Ni ratios that permit calculation of an isochron comes from abundance variations in the trace-element nickel from spot to spot in the same mineral. In this case, the isochron plot will be similar to a plot of the nickel isotope ratio versus the inverse of the nickel abundance, and the array will have a well-correlated positive slope due to significant ratio bias. However, if the data are reduced using ^{62}Ni as the normalizing isotope, the bias will be slightly negative and the isochron slope will be lower than the true value or negative if there is no radiogenic nickel. We observe this behavior in most of the ^{60}Fe-^{60}Ni data we review below.

The effect of ratio bias on an isochron slope can be approximated mathematically using certain simplifying approximations and data from any given measurement. The published online supplement derives the relevant equations and provides an example for determining the bias in the isochron of an actual dataset (Telus et al., 2012a). We also provide an example of the complete calculation of ratios and isochron for the ^{60}Fe-^{60}Ni systematics of an E-chondrite sulfide.

4.4 Recalculating Previously Published SIMS Data

4.4.1 *Procedure*

We have access to the original data from each of the studies discussed in this paper; these studies were carried out by a number of coworkers in collaboration with Gary Huss. To the extent possible, we corrected the measured data and edited the data in the same way as they were edited originally. In most cases, were able to reproduce the original published numbers. We recalculated the final ratios using the following prescription:

1) Data were corrected for deadtime and detector background and were edited, as much as possible, as they were in the original paper.
2) If data were collected in monocollection mode by peak jumping (most of the data), time interpolation was applied in the same way as in the original data analysis.
3) The same mass-fractionation corrections were applied.
4) The means of the individual ratios and the standard error of the means were calculated.
5) The counts from cycles for each isotope were summed and the results were used to calculate the isotope ratios.
6) The final reported ratios are those calculated from the total counts, and the uncertainties are the standard errors of the mean of the individual ratios (we discuss the uncertainties further below).

4.4.2 *Estimating Uncertainties*

A robust estimate of our measurement uncertainties is required to understand the cosmochemical implications of our work. A given measurement has different types of uncertainty: 1) statistical uncertainty due to counting statistics of the secondary ions, also called Poisson noise; 2) variations in the secondary ion signal not attributable to counting statistics that occur on timescales significantly shorter than the measurement (*e.g.*, varying parent-daughter elemental ratio, noise bursts); and 3) systematic uncertainty that decreases the accuracy of the measurement due to phenomena like non-linearity in the detector, inaccurate deadtime correction, or imperfect background measurements. We cannot evaluate the systematic uncertainties from the data, so we will not consider them further here. The statistical uncertainty of a ratio (1) is well-known and is easily derived from the standard error propagation equation. If the numbers of counts for isotopes in the ratio are reasonably large and the numerator and denominator counts are uncorrelated and normally distributed, the statistical standard deviation of the ratio r = y/x is approximately:

$$\sigma(r) \approx r\sqrt{\left(\frac{1}{y}+\frac{1}{x}\right)}$$

When calculating ratios by summing the counts of one isotope and dividing by the summed counts of another, the above expression represents the minimum total uncertainty of the measurement. An additional contribution from sources other than Poisson noise (such as those discussed in #2, above) must be accounted for. In this work, we estimate the contribution from other sources of uncertainty by looking at the data collected in the individual cycles during the measurement.

Isotope data are typically collected in a number of short cycles in order to monitor the effects of drift in signal strength, changes in mass fractionation, etc. If drifts in signal strength can be adequately sampled, they can be corrected for relatively easily with time interpolation. After editing the data to remove highly anomalous cycles and correcting for drift, the variability among individual ratios is a good estimate of the total uncertainty from sources 1) and 2) described above. The standard error of the measured ratios is a reasonable measure of how well the mean of the ratios is known when the data are sampled from a single parent distribution with a well-defined mean. Even though the individual cycle ratios can be significantly biased when the denominator counts are low, in most cases, the variability of the data is independent of whether or not the data are biased (Ogliore et al., 2011). It is therefore appropriate to continue to use the standard error of the measured ratios as an estimate of the total uncertainty (from 1 and 2) in the final ratio.

4.5 Results

4.5.1 *^{53}Mn-^{53}Cr systematics in pallasite olivines (Hsu et al., 1997, Hsu, 2005; Tomiyama and Huss, 2005, and Tomiyama et al., 2007)*

After a study of phosphates in the Springwater pallasite that appeared to show evidence of live ^{53}Mn when the pallasites formed was published (Hutcheon and Olsen, 1991), the Caltech ion probe group carried out a study of the ^{53}Mn-^{53}Cr system in pallasite olivines. The olivine measurements appeared to show excesses of ^{53}Cr that correlated with the ^{55}Mn/^{53}Cr ratio, and the inferred $(^{53}Mn/^{55}Mn)_0$ ratios for the olivines when they formed were $(0.6\text{-}2.0)\times10^{-5}$ (Table 3.1; Hsu et al., 1997; Hsu, 2005). These

results were consistent with those found for phosphates in Springwater (Hutcheon and Olsen, 1991) and implied that pallasites must have cooled much more quickly than generally believed, calling into question the origin of pallasites at the core-mantle boundary of the parent asteroids (e.g., Hsu et al., 1997; Hsu, 2005). However, subsequent measurements of olivine in pallasites by other techniques and by higher transmission ion probes were unable to confirm high $(^{53}Mn/^{55}Mn)_0$ ratios (Lugmair and Shukolyukov, 1998; Tomiyama and Huss, 2005; Tomiyama et al., 2007).

For this paper, we have re-reduced the data gathered by Hsu et al. (1997), which was published in Hsu (2005). We recalculated the isotope ratios using total counts, instead of the mean of the ratios. The data were reduced and edited in exactly the same way as in the original work; the only change was the way the final ratios were calculated. The results are shown in Figure 4.3 and Table 4.1. In all measurements, the $^{53}Cr/^{52}Cr$ was lower in the recalculated results (Figure 4.3). When the newly calculated data were regressed on a ^{53}Mn-^{53}Cr isochron diagram, all evidence for extinct ^{53}Mn disappeared (Figure 4.3, Table 4.1). The olivine data reported by Hsu et al. (1997) and Hsu (2005) are all biased and the inferred initial ratios are artifacts of that bias. The complete recalculated data set is available in Appendix C. Data reported by Tomiyama and Huss (2005) and Tomiyama et al. (2007) were not significantly affected by ratio bias because, in those studies, the count rates for the chromium isotopes were much higher than in the Caltech study (*i.e.*, ^{52}Cr counts per cycle were between 2,200 and 22,000 for the Tomiyama et al. (2007) and between 100 and 800 for the Caltech study). With the re-reduced data, none of the ion probe studies show evidence of in situ decay of ^{53}Mn in pallasites.

Table 4.1. $(^{53}Mn/^{55}Mn)_0$ ratios for pallasite olivines

Meteorite	Mean of Ratios[1]	Ratio of Total Cts
Albin	$(1.3\pm1.0)\times10^{-5}$	$(-0.0\pm0.9)\times10^{-5}$
Brenham	$(1.9\pm1.3)\times10^{-5}$	$(0.2\pm1.3)\times10^{-5}$
Eagle Station	$(0.6\pm0.8)\times10^{-5}$	$(-0.1\pm1.0)\times10^{-5}$
Glorieta Mountain	$(1.5\pm1.0)\times10^{-5}$	$(0.4\pm1.1)\times10^{-5}$
Imilac	$(0.8\pm0.8)\times10^{-5}$	$(-0.3\pm0.9)\times10^{-5}$
Springwater	$(0.9\pm0.6)\times10^{-5}$	$(0.3\pm0.5)\times10^{-5}$

[1] Hsu et al. (1997) and Hsu (2005)

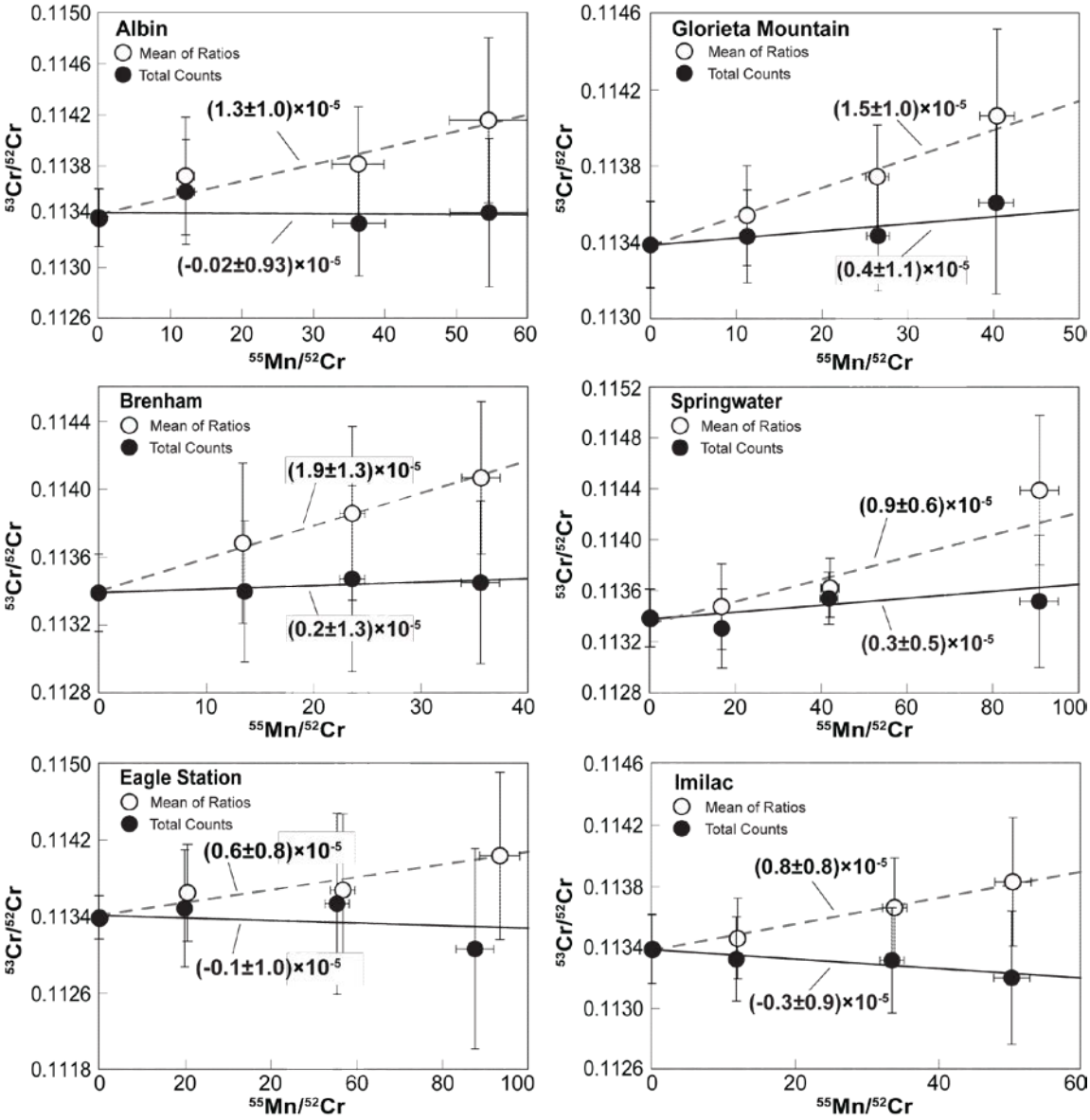

Figure 4.3. ^{53}Mn-^{53}Cr isochron diagrams for the pallasite data reported by Hsu et al. (1997) and Hsu (2005). The open symbols and dashed isochrons show the data as originally reported, calculated using the means of the ratios from individual cycle data. The solid symbols and solid isochrons show the ratios calculated from total counts. When the data are reduced properly, all evidence for extinct ^{53}Mn disappears.

4.5.2 *^{60}Fe-^{60}Ni systematics in sulfides from unequilibrated ordinary chondrites (Tachibana and Huss, 2003a, 2003b)*

The first paper to claim clear evidence for the presence of ^{60}Fe in chondritic materials was Tachibana and Huss (2003). In this paper, $(^{60}Fe/^{56}Fe)_0$ ratios of $(1\text{-}2)\times10^{-7}$ were reported for troilite from unequilibrated chondrites Bishunpur (LL3.15) and Krymka (LL3.2) (Table 4.2). The initial ^{60}Fe/^{56}Fe ratio for the solar system estimated from the troilite data range from $(2.8\text{-}4.0)\times10^{-7}$. The results were apparently confirmed by Mostefaoui et al. (2003, 2004, 2005), who found even higher initial ratios for sulfides from Semarkona (LL3.0) using NanoSIMS. Tachibana and Huss (2003) calculated the nickel-isotope ratios using the mean of the ratios from the individual measurement cycles. The published ratios were normalized to ^{61}Ni because the uncertainty for ratios normalized to ^{62}Ni is systematically larger than for ratios normalized to ^{61}Ni due to the mass fractionation correction.

We re-reduced the Tachibana and Huss (2003) data using the total counts. The data were reduced and edited exactly as they were for the original publication; only the method of calculating the ratios changed. The initial $(^{60}Fe/^{56}Fe)_0$ ratios reported in Table 4.2 are slightly different than those in the original publication because we did not take into account the correlated component of the uncertainties in the current work. This makes for a fair comparison between the two data reduction methods in Table 4.2. We found that the ^{60}Ni/^{61}Ni ratios are distinctly lower and the ^{60}Ni/^{62}Ni ratios are marginally higher than the original values calculated from the means of the measured ratios (Figure

4.4), as expected (Figure 4.2). For the recalculated data, the inferred $(^{60}Fe/^{56}Fe)_0$ ratios are unresolved from zero, independent of the normalizing isotope (Table 4.2, Figure 4.4). We conclude that the initial ratios reported by Tachibana and Huss (2003) were strongly affected by ratio bias and that there is no longer evidence for the presence of ^{60}Fe when these samples formed. The complete recalculated data set is available in the online material.

Table 4.2. $(^{60}Fe/^{56}Fe)_0$ ratios for troilites from unequilibrated ordinary chondrites.

Sample	**^{61}Ni Normalization ($\times10^{-7}$)**		**^{62}Ni Normalization ($\times10^{-7}$)**	
	Mean of Ratios[1]	Ratio of Total Cts	Mean of Ratios	Ratio of Total Cts
Bish-Tr41	1.10 ± 0.32[2]	**0.16 ± 0.37**	0.12± 0.40	**0.21± 0.63**
Bish-Tr2	1.06 ± 0.66[2]	**-0.04 ± 0.79**	-0.28 ± 1.17	**-0.04 ± 1.36**
Bish-Tr47	1.28 ± 0.67[2]	**0.48 ± 0.77**	0.36 ± 1.16	**0.37 ± 1.34**
Krm-Tr1	1.82 ± 0.78[2]	**-0.23 ± 0.96**	-0.61 ± 1.34	**-0.12 ± 1.67**
Krm-Tr12	1.64 ± 0.93[2]	**-0.12 ± 0.96**	-0.71 ± 1.57	**-0.12 ± 1.65**

[1] Tachibana and Huss (2003)

[2] These values differ slightly from those in Tachibana and Huss (2003) because the analysis done for the current paper did not take into account the correlated component of the errors. The data in this table differ only in the method of ratio calculation and are directly comparable.

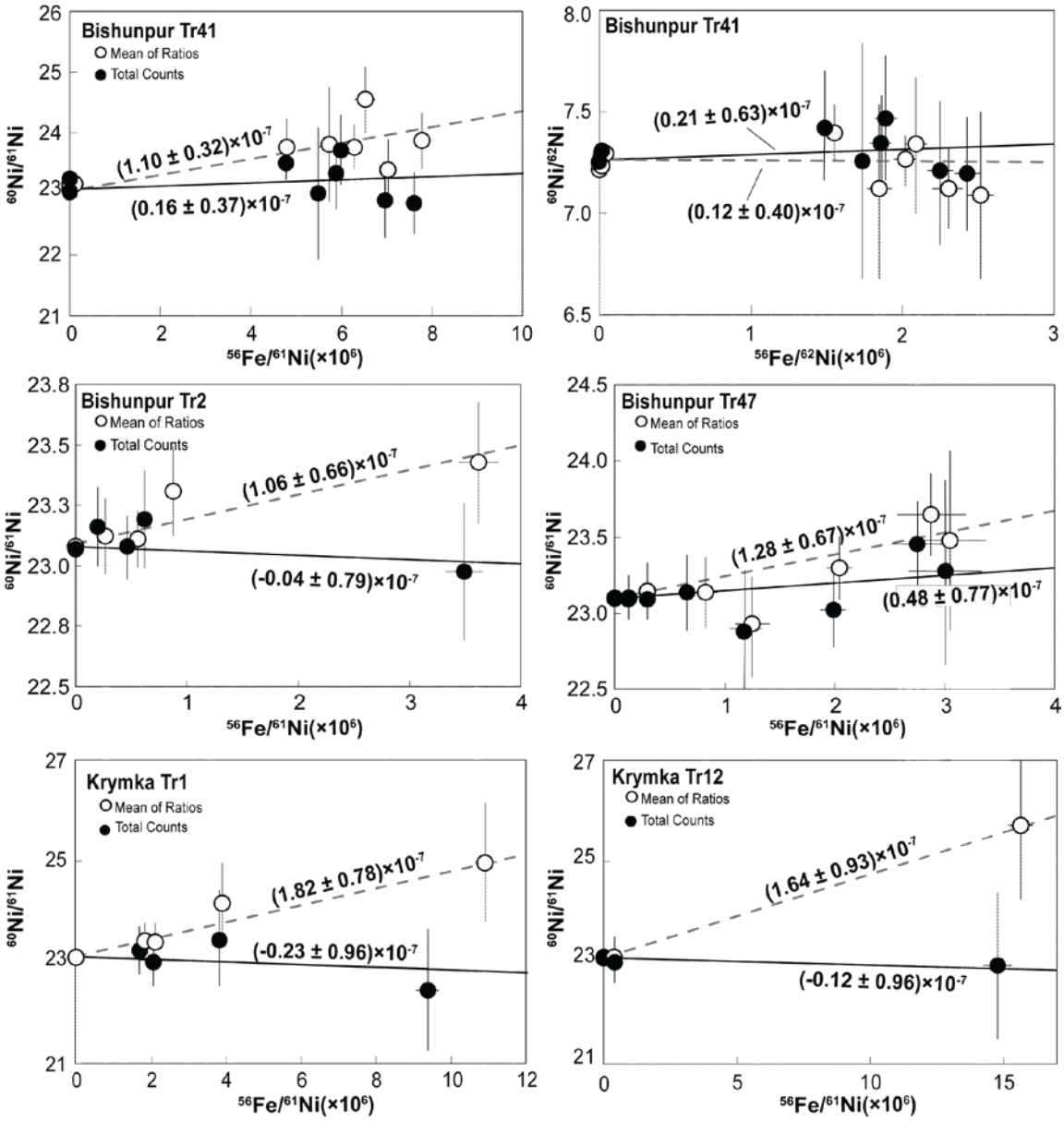

Figure 4.4. $^{60}Ni/^{61}Ni$ versus $^{56}Fe/^{61}Ni$ for troilite from Bishunpur and Krymka (Tachibana and Huss, 2003). $^{60}Ni/^{62}Ni$ versus $^{56}Fe/^{62}Ni$ is also shown for Bishunpur Tr41. The open symbols and dashed lines show the original results. The solid symbols and solid lines show the data reduced using total counts.

4.5.3 *^{60}Fe-^{60}Ni and ^{53}Mn-^{53}Cr systematics in sulfides from enstatite chondrites (Guan et al., 2003a, 2003b, 2004a, 2004b, 2007).*

Guan et al. (2007) measured the ^{60}Fe-^{60}Ni and ^{53}Mn-^{53}Cr systems in sulfides from enstatite chondrites to further constrain the initial abundance of ^{60}Fe in the solar system

and to investigate possible correlations between ^{60}Fe-^{60}Ni and ^{53}Mn-^{53}Cr systems. Some of these results were also reported in various abstracts (Guan et al., 2003a, 2003b, 2004a, 2004b). Sulfides from ALHA77295, MAC88136, and Qingzhen (all EH3) were measured using a Cameca ims-6f at ASU. Large variations were found in the $(^{60}Fe/^{56}Fe)_0$ and $(^{53}Mn/^{55}Mn)_0$ ratios of $(2\text{-}20)\times10^{-7}$ and $(2\text{-}7)\times10^{-7}$, respectively, but there was no clear correlation between ^{60}Fe-^{60}Ni and ^{53}Mn-^{53}Cr systems. These authors also found that the $^{60}Ni/^{61}Ni$ ratios did not correlate with the $^{56}Fe/^{61}Ni$ ratios. Although the ^{60}Fe-^{60}Ni system may be disturbed, they concluded that there was clear evidence for the presence of ^{60}Fe in these sulfides.

Isotope ratios for these measurements were originally calculated using the mean of the ratios. We recalculated some of the data using total counts (Tables 4.3 and 4.4). Although we were not able to precisely match the published data in our recalculations, our values using the means of the ratios are similar to the published ratios. The counts per cycle for ^{52}Cr in sphalerite for these measurements range from 20 to 80, so the ratios calculated from the mean of individual ratios are too high. Using total counts, $^{53}Cr/^{52}Cr$ ratios were lower (Figure 4.5) and the inferred $(^{53}Mn/^{55}Mn)_0$ ratios dropped, although there is still clear evidence for the former presence of ^{53}Mn in one of the sulfides (Table 4.3).

Table 4.3. $(^{53}Mn/^{55}Mn)_0$ ratios for sulfides from enstatite chondrites.

Sample	**Mean of Ratios[1]** ($\times10^{-7}$)	**Ratio of Total Cts** ($\times10^{-7}$)
M3641-1	4.56 ± 0.75[2]	3.42 ± 0.83
M3645-5	1.75 ± 0.50[2]	0.41 ± 0.58

[1] Guan et al. (2007)

[2] These initial ratios do not match the published values because we were unable to fully duplicate the original data

reduction. The data in this table differ only in the method of ratio calculation and are directly comparable.

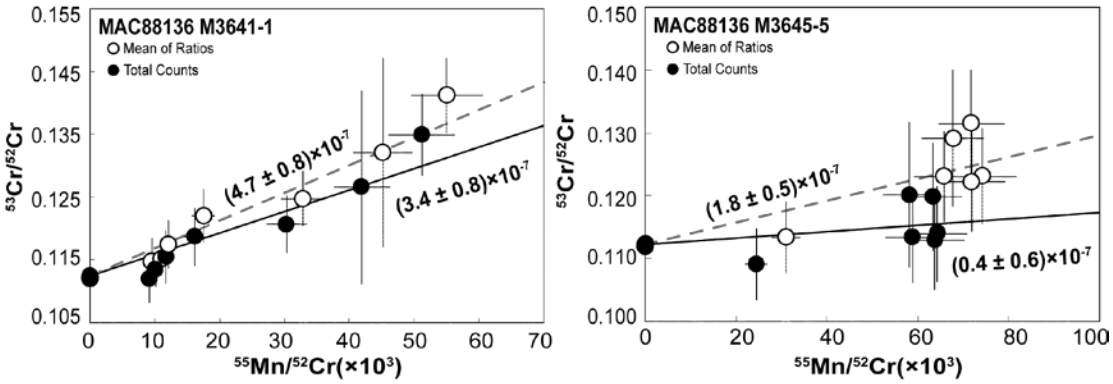

Figure 4.5. ^{53}Mn-^{53}Cr vs ^{55}Mn/^{52}Cr for two of the sulfides reported by Guan et al. (2007). The open symbols and dashed lines show the data calculated using the means of the ratios from individual cycle data. The solid symbols and solid lines show the ratios calculated from total counts.

For the Fe-Ni system, counts per cycle for ^{61}Ni ranged from 4 to 100 (~3× higher for ^{62}Ni). The ^{60}Ni/^{61}Ni ratios calculated from total counts are lower, while the ^{60}Ni/^{62}Ni ratios were similar or slightly higher than those determined from means of the ratios (Figure 4.6, Table 4.4), as expected (Figure 4.2). The $(^{60}Fe/^{56}Fe)_0$ ratios for these sulfides are no longer resolved from zero; there is no longer clear evidence for the presence of ^{60}Fe in these sulfides. Data for the individual measurements are available in the online material.

Table 4.4. $(^{60}Fe/^{56}Fe)_0$ ratios for sulfides from enstatite chondrites.

Sample	^{61}Ni Normalization (×10^{-7})		^{62}Ni Normalization (×10^{-7})	
	Mean of Ratios[1]	Ratio of Total Cts	Mean of Ratios	Ratio of Total Cts
M3641-2	8.5 ± 6.1[2]	**1.8 ± 9.0**	0.4 ± 10.0	**1.8 ± 14**
QZ02-3	6.1 ± 2.1[2]	**-4.2 ± 2.9**	-6.7 ± 3.6	**-4.0 ± 4.7**

[1] Guan et al. (2007)

[2] These initial ratios do not match the published values because we were unable to fully duplicate the original data reduction. The data in this table differ only in the method of ratio calculation and are directly comparable.

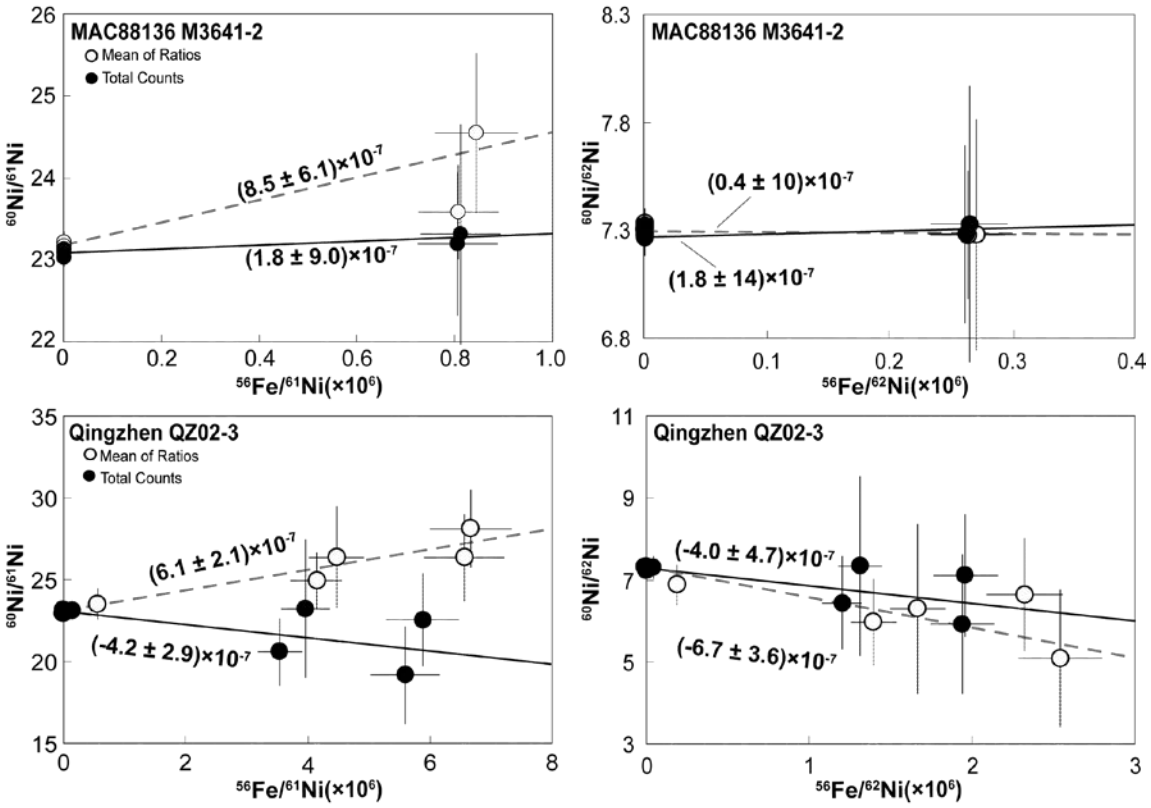

Figure 4.6. $^{60}Ni/^{61}Ni$ versus $^{56}Fe/^{61}Ni$ and $^{60}Ni/^{62}Ni$ versus $^{56}Fe/^{62}Ni$ for two sulfides reported by Guan et al. (2007). The open symbols and dashed lines in the two left panels show the ^{61}Ni normalization that was originally published and the open symbols and dashed lines in the two right panels show the same data normalized to ^{62}Ni. The solid symbols and solid lines show the data reduced using total counts.

4.5.4 *^{60}Fe-^{60}Ni systematics in chondrules from ordinary chondrites (Huss and Tachibana, 2004; Tachibana et al., 2005; Tachibana et al., 2006)*

Measurements of sulfides in unequilibrated chondrites apparently showed that the ^{60}Fe-^{60}Ni systematics is easily disturbed by secondary processing (Guan et al., 2004b, 2007). Because of this, Huss and Tachibana (2004) decided to look at Fe-rich silicates, which should be less susceptible to metamorphic disturbance. They found that Fe-rich pyroxene can have very high Fe/Ni ratios, particularly the fine-grained radiating pyroxene chondrules. Huss and Tachibana (2004) reported the first data from a chondrule to show evidence of ^{60}Fe. They measured a radiating pyroxene chondrule using the ASU

Cameca ims 6f. In order to confirm this measurement, they re-measured the chondrule using the Cameca ims 1270 at the Geological Survey of Japan. The two data sets gave very similar results, giving them confidence that the data were robust and correct (Table 4.5). Tachibana et al. (2005, 2006) measured some additional pyroxene-rich chondrules from Semarkona (LL3.00) and Bishunpur (3.15) and found evidence of ^{60}Fe in all of them. They reported $(^{60}Fe/^{56}Fe)_0$ ratios of $(2\text{-}4)\times10^{-7}$ for the chondrules (Figure 4.7, Table 4.5) and inferred that the initial ratio for the solar system was in the range of $(0.5\text{-}1.0)\times10^{-6}$. The counts-per-cycle for BIS21, which gave the highest $(^{60}Fe/^{56}Fe)_0$ ranges from 10 to 100 for an average of ~200 cycles.

We recalculated the data reported by Huss and Tachibana (2004) and Tachibana et al. (2005, 2006) using total counts. As expected, the ^{60}Ni/^{61}Ni ratios are lower than the previously published values, while the ^{60}Ni/^{62}Ni ratios are higher than those determined using mean of ratios (Figure 4.7). The inferred $(^{60}Fe/^{56}Fe)_0$ ratios for the chondrules are also significantly lower. Once again, the choice of normalizing isotope for the nickel isotope ratios (^{61}Ni or ^{62}Ni) does not change the result, although it does change the uncertainty for the reasons described above.

Table 4.5. $(^{60}Fe/^{56}Fe)_0$ ratios for chondrules from unequilibrated ordinary chondrites.

Sample	**^{61}Ni Normalization ($\times10^{-7}$)**		**^{62}Ni Normalization ($\times10^{-7}$)**	
	Mean of Ratios	Ratio of Total Cts	Mean of Ratios	Ratio of Total Cts
SMK 1-4 (ASU)	4.2 ± 1.7	**1.0 ± 2.0**	1.3 ± 3.1	**0.8 ± 2.3**
(GSJ)	2.6 ± 1.0	**0.6 ± 1.1**	0.2 ± 1.7	**0.6 ± 1.9**
All Data	2.7 ± 1.0[2]	**0.7 ± 1.1**	0.2 ± 1.6	**0.7 ± 1.8**
SMK 2-1	2.0 ± 1.1[1,2]	**-1.3 ± 1.5**	-4.7 ± 2.0	**-1.2 ± 2.6**
SMK 2-4	2.8 ± 2.3[1,2]	**-0.2 ± 2.8**	-1.4 ± 3.8	**-0.2 ± 4.7**
BIS21	4.4 ± 2.5[1,2]	**-1.7 ± 2.7**	-3.5 ± 4.0	**-1.6 ± 4.6**

[1] Tachibana et al. (2006)

[2] Some of these values differ slightly from those in Tachibana et al. (2006) because the analysis done for the current paper did not take into account the

correlated component of the errors. The data in this table differ only in the method of ratio calculation and are directly comparable.

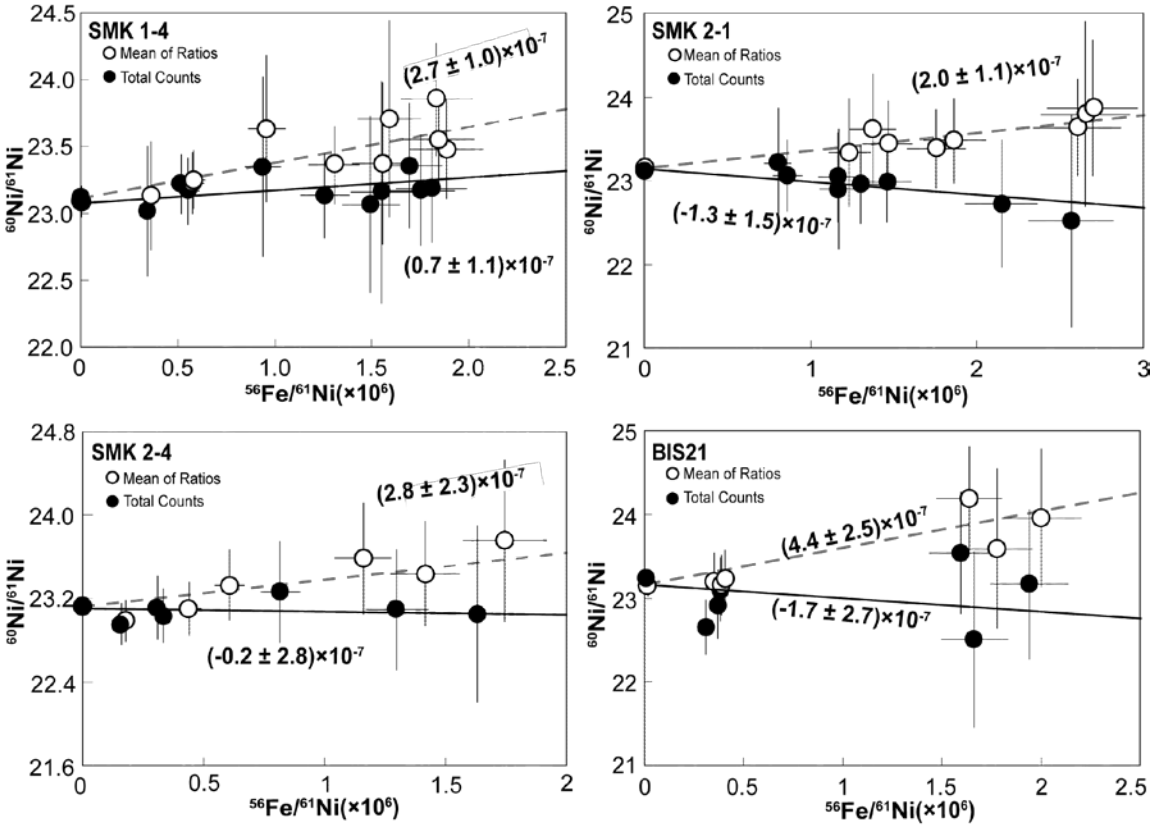

Figure 4.7. $^{60}Ni/^{61}Ni$ versus $^{56}Fe/^{61}Ni$ for the chondrules from Tachibana et al. (2006). The data calculated from the mean of the ratios are shown in open symbols and dashed lines, and the recalculated data are shown in solid symbols and solid lines. Reducing the data using total counts results in significantly lower nickel-isotope ratios and lower inferred $(^{60}Fe/^{56}Fe)_0$ ratios.

4.5.5 *^{60}Fe-^{60}Ni systematics of more chondrules from ordinary chondrites (Tachibana et al., 2007, 2009; Huss et al., 2007, 2010a, 2010b; Mishra et al., 2009, 2010; Telus et al., 2011).*

In this section, we review ^{60}Fe-^{60}Ni data gathered at the University of Hawai‘i and reported prior to our learning about ratio bias. Data for seven chondrules from Semarkona and Bishunpur were reported by Tachibana et al. (2007). They reported $(^{60}Fe/^{56}Fe)_0$ ranging from $(1\text{-}2)\times10^{-7}$. Six of these chondrules were also measured for ^{26}Al-^{26}Mg systematics (Huss et al. 2007). A subset of these data along with new data obtained using

the Cameca ims 4f at the Physical Research Laboratory (PRL) in Ahmedabad, India were subsequently published by Mishra et al. (2009, 2010). Mishra et al. (2010) inferred an initial $^{60}Fe/^{56}Fe$ ratio for the early solar system of ~4×10^{-7} (using the revised half-life of 2.6 Myr for ^{60}Fe; Rugel et al., 2009).

We re-reduced the data gathered at the University of Hawai‘i using total counts (Table 4.6). Counts per cycle for ^{61}Ni among the low-Ni points ranged from 10 to 250 (~3× higher for ^{62}Ni) for typically 200 cycles. We found that the $^{60}Ni/^{61}Ni$ ratios are lower and the $^{60}Ni/^{62}Ni$ ratios are similar to or slightly higher than the original values (Figure 4.8). The inferred $(^{60}Fe/^{56}Fe)_0$ ratios are also lower. None of the seven chondrules from Tachibana et al. (2007) show evidence for the former presence of ^{60}Fe (Table 4.6). The Al-Mg data gathered at UH were also recalculated using total counts, and these data were not found to be significantly biased. The data for the other chondrules measured at PRL were not available for this paper. Although the Fe-Ni data were reduced using total counts (Mishra, personal communication), we suspect that they may also be affected by bias because they were collected using the ims 4f, which has significantly lower transmission than the ims 1280.

Table 4.6. $(^{60}Fe/^{56}Fe)_0$ ratios for chondrules from unequilibrated ordinary chondrites

Sample	^{61}Ni Normalization ($\times10^{-7}$)		^{62}Ni Normalization ($\times10^{-7}$)	
	Mean of Ratios	Ratio of Total Cts	Mean of Ratios	Ratio of Total Cts
BIS 32	1.9 ± 1.1[1,2]	**0.0 ± 1.3**	-0.1 ± 1.9	**0.1 ± 2.1**
SMK 1-5	3.2 ± 1.6[1,2]	**0.1 ± 1.9**	0.0 ± 2.8	**0.1 ± 3.1**
SMK 1-6	0.5 ± 4.2[1,2]	**0.6 ± 3.2**	-3.9 ± 7.1	**0.6 ± 5.4**
SMK 3-6	1.7 ± 1.1[1,2]	**0.6 ± 1.2**	0.5 ± 1.9	**0.6 ± 2.0**
SMK 3-2	2.0 ± 1.9[1]	**0.2 ± 2.0**	0.1 ± 3.0	**0.3 ± 3.4**
BIS-1	0.5 ± 1.0[1]	**-0.5 ± 1.1**	-0.4 ± 1.6	**-0.5 ± 1.8**
BIS-38	1.2 ± 0.9[1]	**0.4 ± 1.1**	-0.2 ± 1.7	**0.4 ± 1.8**
KRM 3-1	1.42 ± 0.21	**1.14 ± 0.22**	0.88 ± 0.32[3]	**0.94 ± 0.33**
KRM 3-9	0.95 ± 0.42	**0.63 ± 0.44**	0.54 ± 0.64[3]	**0.62 ± 0.68**

KRM 3-11	2.76 ± 0.44	**2.35 ± 0.44**	2.36 ± 0.68[3*]	**2.36 ± 0.67**
DAP-1	4.5 ± 1.3	**2.1 ± 1.2**[4]	1.1 ± 1.9	**2.1 ± 1.9**

[1] Tachibana et al., (2007); [2]Mishra et al., (2009, 2010); [3]Tachibana et al., (2009). [4]Telus et al., (2011a, 2011b).

* This value differs slightly from the one published in Tachibana et al. (2009) because we were not able to completely reproduce the original data reduction.

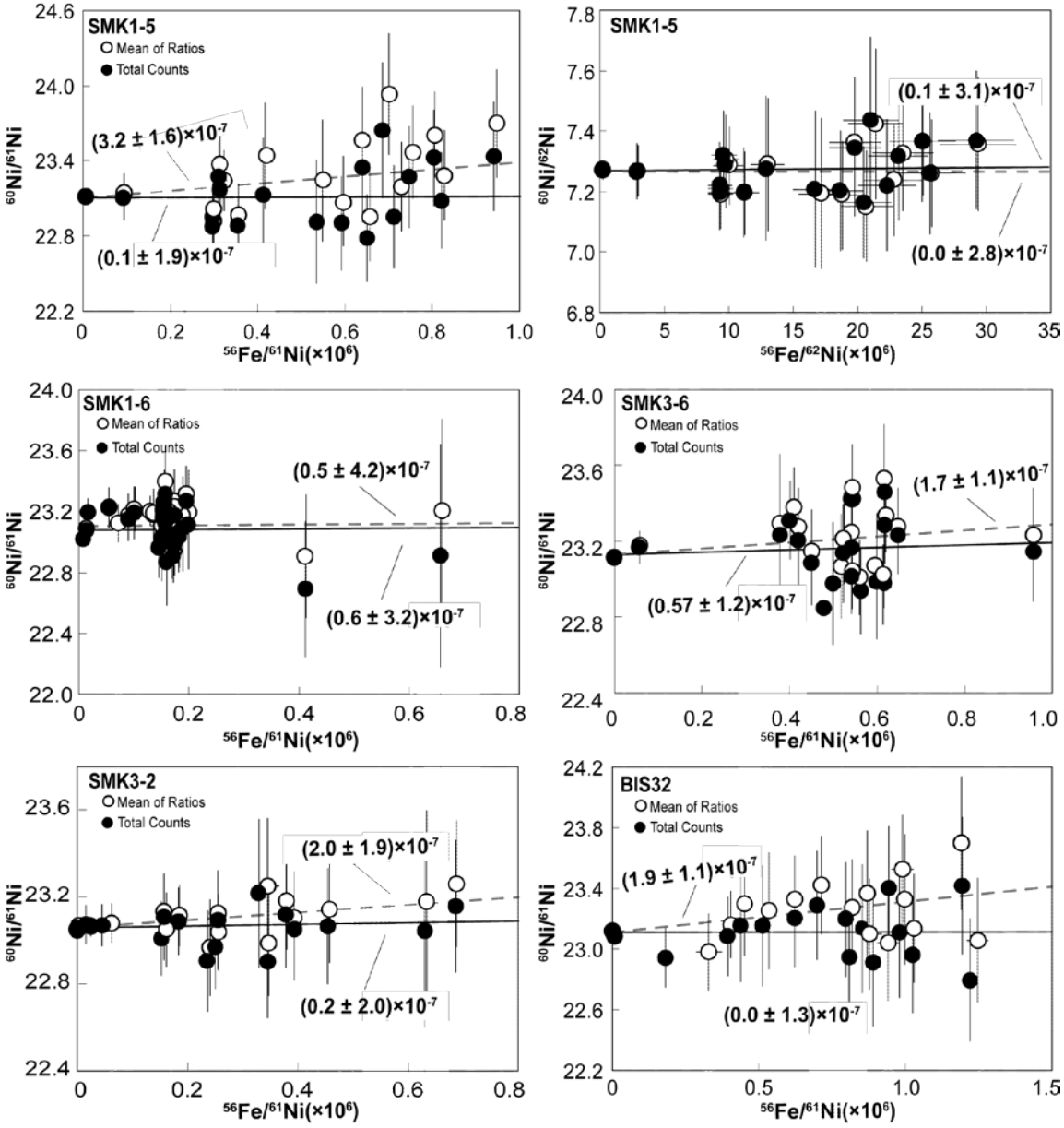

Figure 4.8: $^{60}Ni/^{61}Ni$ versus $^{56}Fe/^{61}Ni$ for the chondrules reported by Tachibana et al. (2007). $^{60}Ni/^{62}Ni$ versus $^{56}Fe/^{62}Ni$ is shown for SMK 1-5. The original published results are shown in open symbols and dashed lines, and the recalculated data are shown in solid

symbols and solid lines. Reducing the data using total counts results in significantly lower nickel-isotope ratios and low inferred $(^{60}Fe/^{56}Fe)_0$ ratios.

Multi-collection measurements of ^{60}Fe-^{60}Ni systematics of chondrules from Krymka (LL3.2) were reported by Tachibana et al. (2009) (Table 4.6). The inferred initial $(^{60}Fe/^{56}Fe)_0$ ratio for these show the least amount of change in nickel-isotope ratios because the count rates for ^{61}Ni were relatively high. For chondrule KRM 3-1, which has the highest $^{56}Fe/^{61}Ni$ ratios, the average counts-per-cycle range from 200 to 400 for 200 cycles. The data were originally reduced using the mean of ratios, but normalized to ^{62}Ni instead of ^{61}Ni. Since ^{62}Ni has more counts, using it as the normalizing isotope generally gives results that are less biased. When reduced using total counts, the three Kyrmka chondrules give resolved initial ratios ranging from $(0.6\pm0.4)\times10^{-7}$ to $(2.4\pm0.4)\times10^{-7}$(Table 4.6, Figure 4.9). As Tachibana et al. (2009) mentions, the correlation between the nickel-isotope ratios and Fe/Ni ratio for chondrules KRM 3-11 and KRM 3-9 are weak (both have $\chi_v^2 > 3$) and suggests the Fe-Ni system in some of these chondrules is disturbed. There is evidence for excess ^{60}Ni at the 2σ level in these chondrules, but one cannot extract a robust estimate of the initial $(^{60}Fe/^{56}Fe)_0$ ratio for when these chondrules formed.

Semarkona chondrule, DAP-1, has been analyzed several times (Huss et al. 2010a, 2010b; Telus et al. 2011a). The most recent data set, measured in multicollection mode at UH, is shown in Table 4.6 and Figure 4.9. The counts-per-cycle for ^{61}Ni range from 40 to 1000 for 200 cycles. When the data are calculated using total counts, the inferred initial $(^{60}Fe/^{56}Fe)_0$ ratio for DAP-1 is $(2.1\pm1.2)\times10^{-7}$ ($\chi_v^2 = 2.5$) (Table 4.6, Figure 4.9). Again, the relatively weak correlation suggests that the Fe-Ni system for this

chondrule is disturbed and cannot give an accurate estimate of the true $(^{60}Fe/^{56}Fe)_0$ for this chondrule.

The ^{60}Fe-^{60}Ni data for all of these chondrules are available in the online material.

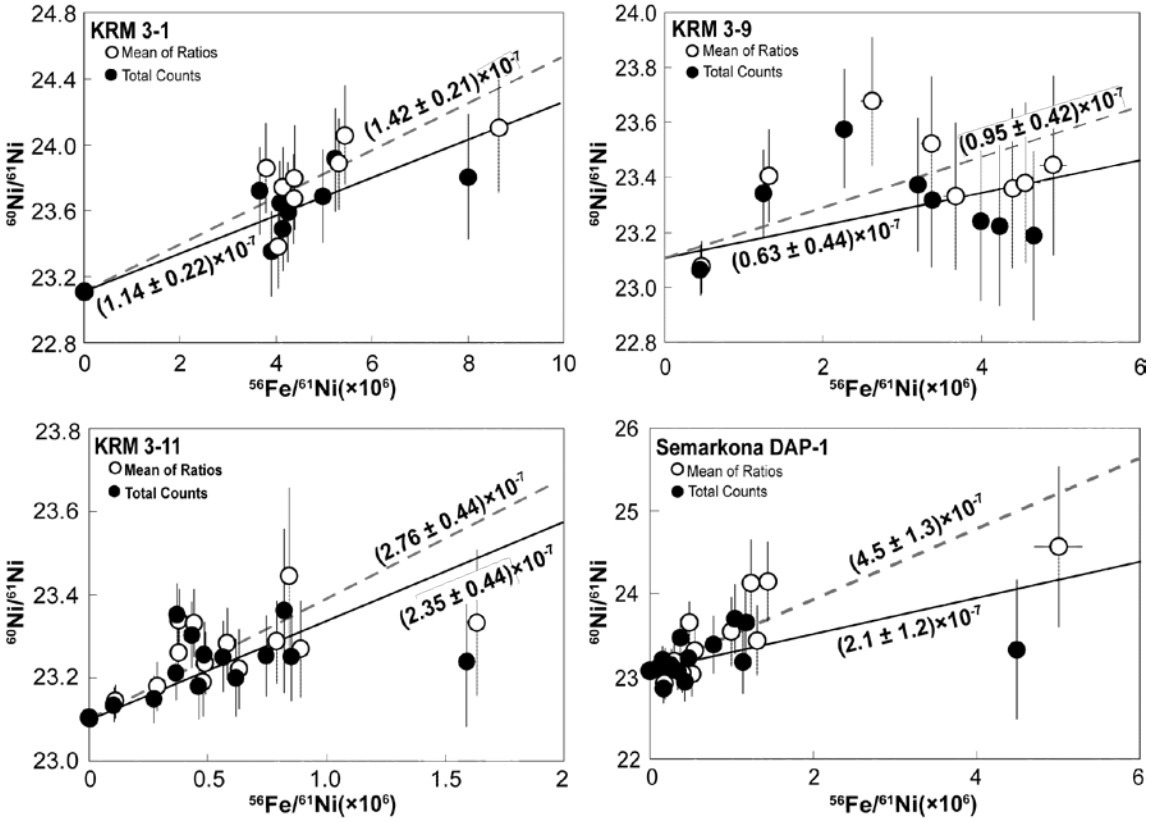

Figure 4.9: $^{60}Ni/^{61}Ni$ versus $^{56}Fe/^{61}Ni$ for Krymka and Semarkona chondrules that were reported in abstracts by Tachibana et al. (2009) and Telus et al. (2011a).

4.5.6 *^{10}Be-^{10}B systematics in CAIs from CV3 chondrites (MacPherson et al., 2001, 2003).*

Another isotope system that gives low count rates in SIMS measurements is the ^{10}Be-^{10}B system ($t_{1/2}$ = ~1.4×10^6 years; Chmeleff et al., 2009). MacPherson et al. (2003) published ^{10}Be-^{10}B data for seven Type A calcium-aluminum inclusions (CAIs) from CV chondrites. All showed clear evidence for ^{10}Be, but the initial abundances of ^{10}Be did not correlate tightly with the initial abundances of ^{26}Al in the inclusions.

The data in this study were collected over as many as 300 cycles, with ^{10}B and ^{11}B counted for 10 seconds and 3 seconds, respectively. The count rates were low enough that many cycles had zero counts. This meant that the data could not be reduced using the mean of the individual cycle ratios. So the counts of each isotope were totaled and the $^{9}Be/^{11}B$ and $^{10}B/^{11}B$ ratios were calculated from the total counts. The total number of counts of ^{11}B used to calculate the $^{10}B/^{11}B$ ratios ranged from 3,000 to 2.4×10^{5} counts in pyroxene and 35 to ~8,500 counts in melilite. According to Figure 4.1 of Ogliore et al. (2011), the positive bias in the published $(^{10}B/^{11}B)_0$ ratios should be insignificant for pyroxene, but up to ~30‰ for melilite. To check the bias, we recalculated all of the ratios from MacPherson et al. (2003) using the Beale's estimator (Beale, 1962; Ogliore et al., 2011), which should reduce the bias to significantly less than a part per million.

The recalculated $^{10}B/^{11}B$ ratios were from ~0.3‰ to ~42‰ lower than the published ratios (excesses relative to normal boron can be as much as 1200‰). New regressions for each inclusion sometimes resulted in very slight revisions in the inferred $(^{10}Be/^{9}Be)_0$ ratios for these CAIs (Table 4.7). The new results do not change the conclusions of the MacPherson et al. (2003) paper in any significant way. The recalculated data are given in the online material.

Table 4.7. $(^{10}Be/^{9}Be)_0$ ratios for Type A CAIs from CV chondrites.

CAI	Initial $^{10}Be/^{9}Be$[1]	$^{10}Be/^{9}Be_{\text{Beale's estimator}}$
Efremovka 6456-1	$(0.76\pm0.16)\times10^{-3}$	$(0.76\pm0.16)\times10^{-3}$
Vigarano 1623-9	$(0.58\pm0.19)\times10^{-3}$	$(0.57\pm0.19)\times10^{-3}$
Vigarano 477-4b	$(0.53\pm0.17)\times10^{-3}$	$(0.53\pm0.17)\times10^{-3}$
Vigarano 477-5	$(0.73\pm0.19)\times10^{-3}$*	$(0.72\pm0.19)\times10^{-3}$
Leoville 3535-3b	$(0.67\pm0.24)\times10^{-3}$	$(0.67\pm0.28)\times10^{-3}$
Allende 3898	$(0.48\pm0.17)\times10^{-3}$	$(0.48\pm0.17)\times10^{-3}$
Axtell 2771	$(0.30\pm0.12)\times10^{-3}$	$(0.29\pm0.13)\times10^{-3}$

[1] MacPherson et al. (2003) [*]A mistake in the original data reduction resulted in an inferred initial ratio of $(0.75\pm0.19)\times10^{-3}$, rather than the value listed in the table.

4.6 Discussion and Conclusions

We have reviewed and re-reduced many of the data sets collected by Gary Huss and his collaborators over the years that could have been subject to bias. As we have shown, many SIMS studies of short-lived radionuclide systems (*e.g.*, ^{26}Al-^{26}Mg, ^{10}Be-^{10}B, ^{53}Mn-^{53}Cr, and ^{60}Fe-^{60}Ni) have unintentionally generated biased data due to the low number of counts in the denominator of the isotope ratios. The re-reduced data presented in this paper should be used instead of the originally published data in all future work. We hope that this paper will prompt others to review their previously reported data and to republish corrected data in cases of serious bias.

A key question is how to evaluate whether or not the ratio bias is significant for a particular study. Cosmochemists are used to evaluating whether or not two measurements are different by looking to see if their uncertainties overlap. If two independent measurements have overlapping uncertainties, they are considered to be indistinguishable at a certain confidence level. It is not valid to use the same test to compare ratios calculated by different methods from the same data to evaluate whether or not the bias is significant. Figure 4.10 shows a ratio calculated from the mean of 100 ratios compared to a ratio calculated from the same data using total counts. The mean of 100 ratios shows a 20‰ positive bias compared to the mean of total counts and the statistical error on both ratios is 23‰ (2σ). The comparison to be made is not between the bias and the error, but

between the bias and the size of the effect that is significant in the study. For example, if the solid line represents the isotopic composition of a mantle reservoir and our hypothesis is that our sample was derived from that reservoir, we would reject our hypothesis at the 2σ level if we calculated the data from the mean of the ratios, but we would not reject the hypothesis if we calculated the ratio from total counts. If a bias of 20‰ does not change the conclusions of the work, then it can be considered insignificant. But if the bias dominates the isotope effects seen in the work, as in many examples shown in this paper, then it must be dealt with even if it is smaller than the 2σ measurement uncertainties. The bias is a systematic shift, not a random fluctuation.

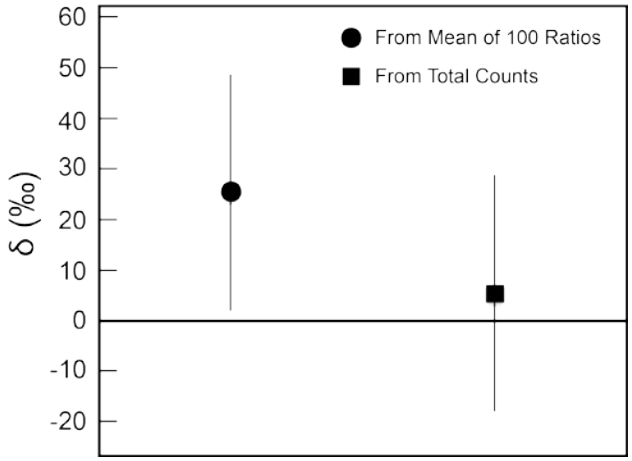

Figure 4.10: Comparison of ratios calculated from the mean of 100 ratios and from total counts with the 2σ statistical error of each ratio. Although the error is larger than the bias, this does not mean that the two ratios are equivalent. The solid line represents a hypothetical isotopic composition that we wish to compare with our data. The ratio calculated from the mean of 100 ratios is resolved at the 2σ level from this composition, but the ratio calculated from total counts is not. The bias is a systematic shift, not the result of a random statistical fluctuation.

For most of the data sets in this paper, we have used total counts to calculate less-biased estimators of the true isotope ratios. But even total counts can lead to biased isotope ratios. Analysts must monitor the number of counts acquired during each

measurement and decide if the bias in the calculated ratios is small enough to be insignificant (*cf.*, Ogliore et al., 2011). If there are not enough counts in the denominator to assure a sufficiently unbiased result, there are other less-biased estimators available. Ogliore et al. (2011) discusses the Beale's estimator (Beale, 1962), which we applied to the ^{10}Be-^{10}B data reported by MacPherson et al. (2003). Beale's estimator noticeably reduced the bias in some of the data, which was initially reduced using total counts. Coath and Steele (2012) discuss another way to handle the bias introduced by a small number of counts.

For future studies, experimental design must take into account the issue of ratio bias. The goal must be to have enough counts of the denominator isotope so that ratio bias is insignificant, e.g. much smaller than the total uncertainty of the measured ratio. Data can still be collected using a large number of measurement cycles to evaluate the performance of the mass spectrometer, heterogeneities in the sample, and electronic noise. The data can be edited, and time interpolation can be applied as before. But if the number of counts per cycle is too low (see Ogliore et al., 2011), the data for all cycles should be totaled before calculating the ratios to minimize the bias. If the number of total counts is still too low, a more sophisticated analysis is required to estimate accurate ratios (*e.g.*, Beale's estimator). Uncertainties calculated from variations among individual ratios are still appropriate to estimate the total uncertainty in the measurement, as discussed above.

As we discussed in the section on Bias in Isochrons, ratio bias can propagate into the slope of the isochron in different ways. For example, when an external mass fractionation correction is applied to biased ratios (*e.g.*, ^{10}Be-^{10}B and ^{53}Mn-^{53}Cr systems),

the resulting isochron is typically positively biased. On the other hand, if an internal mass fractionation correction is applied to biased ratios (*e.g.*, ^{26}Al-^{26}Mg and ^{60}Fe-^{60}Ni systems), the isochron can be either positively or negatively biased, depending on the ratio used for normalization. For instance, in the ^{60}Fe-^{60}Ni system, biased ratios can produce a large positive bias in the isochron when the normalizing isotope is ^{61}Ni or a small negative bias in the isochron when the normalizing isotope is ^{62}Ni (*e.g.*, Figure 4.2). The Tables presented above show that when the data are reduced properly, there is no systematic difference in the results as a function of normalizing isotope. This emphasizes the importance of internal consistency checks during data reduction.

CHAPTER 5. **REVISITING ^{26}Al-^{26}Mg SYSTEMATICS OF PLAGIOCLASE IN H4 CHONDRITES**

Published in its present form as Telus, M., G. R. Huss, K. Nagashima and R. C. Ogliore (2014), Meteoritics and Planetary Science, 49, 929-945.

doi: http://dx.doi.org/10.1111/maps.12304

5.1 Abstract

Zinner and Göpel (1992, 2002) found clear evidence for the former presence of ^{26}Al in the H4 chondrites Ste. Marguerite and Forest Vale. They assumed that the ^{26}Al-^{26}Mg systematics of these chondrites date "metamorphic cooling of the H4 parent body". Plagioclase in these chondrites can have very high Al/Mg ratios and low Mg concentrations, making these ion probe analyses susceptible to ratio bias, which is inversely proportional to the number of counts of the denominator isotope (Ogliore et al., 2011). Zinner and Göpel (2002) used the mean of the ratios to calculate the isotope ratios, which exacerbates this problem. We analyzed the Al/Mg ratios and Mg isotopic compositions of plagioclase grains in thin sections of Ste. Marguerite, Forest Vale, Beaver Creek and Sena to evaluate the possible influence of ratio bias on the published initial ^{26}Al/^{27}Al ratios for these meteorites. We calculated the isotope ratios using total counts, a less-biased method of calculating isotope ratios. The results from our analyses are consistent with those from Zinner and Göpel (2002), indicating that ratio bias does not significantly affect ^{26}Al-^{26}Mg results for plagioclase in these chondrites. Ste. Marguerite has a clear isochron with an initial ^{26}Al/^{27}Al ratio indicating that it cooled to below 450 °C 5.2±0.2 Myr after CAIs. The isochrons for Forest Vale and Beaver Creek also show clear evidence that ^{26}Al was alive when they cooled, but the initial ^{26}Al/^{27}Al ratios are not well constrained. Sena does not show evidence that ^{26}Al was alive when it cooled to below the Al-Mg closure temperature. Given that metallographic cooling rates for Ste. Marguerite, Forest Vale and Beaver Creek are atypical (>5000 °C/Myr at 500 °C) compared to most H4s, including Sena, which have cooling rates of 10-50 °C/Myr at 500 °C (Scott et al., 2014), we conclude that the Al-Mg systematics for Ste. Marguerite,

Forest Vale and Beaver Creek are the result of impact excavation of these chondrites and cooling at the surface of the parent body, instead of undisturbed cooling at depth in the H chondrite parent body, like many have assumed.

5.2 Introduction

The timescale of metamorphism on chondrite parent bodies has important implications for understanding their accretional histories and their structures, and the nature of the heat source for metamorphism. Since closure temperatures vary for different radionuclide systems, the thermal history of a parent body can be constrained by comparing the ages determined from several chronometers. Göpel et al. (1994) used the ^{207}Pb-^{206}Pb system to measure secondary phosphates in several ordinary chondrites. Based on the differences in the Pb-Pb ages of phosphates from the various chondrites, they determined that thermal processing on the chondrite parent bodies occurred over a period of 60 million years. For H chondrites, they found a clear inverse correlation between the age of the phosphates and the petrologic grade of the chondrites. This correlation supports the layered, "onion-shell", model where chondrites with high petrologic type (H6s) cooled slowly in the inner regions of the parent body, while low petrologic types (H3s) cooled rapidly at the surface. Intermediate petrologic types (H5s and H4s) formed in intermediate layers and experienced intermediate degrees of cooling (e.g., Miyamoto et al., 1981). Trieloff et al. (2003) found a correlation between ages determined from ^{244}Pu fission tracks, ^{40}Ar-^{39}Ar, and ^{207}Pb-^{206}Pb dating and petrologic types of H chondrites. These authors constructed a cooling chronology for the H chondrite parent body by combining age determinations from their results and other methods. They concluded that the parent body must have had an onion-shell structure that remained undisturbed for 160 Myr after the formation of calcium-aluminum-rich inclusions (CAIs), the earliest formed solar system solids. The ^{26}Al-^{26}Mg system can also provide a constraint on the thermal history of the chondrite parent body provided that at

least a portion of the parent body cooled to below ~450 °C while ^{26}Al was still alive (LaTourrette and Wasserburg, 1998). This appears to have been the case for Ste. Marguerite (H4), which has clear excess ^{26}Mg in plagioclase that correlates with Al/Mg ratio. Assuming that ^{26}Al was distributed homogeneously in the solar nebula, the corresponding cooling time for this meteorite is ~5 Myr after CAIs, (Zinner and Göpel, 1992, 2002). Given that the Al-Mg systematics of plagioclase are consistent with Pb-Pb systematics of phosphates (Göpel et al., 1994), these authors conclude that the Al-Mg systematics likely date the time when the region of the parent body where H4 chondrites formed cooled down to the closure temperature of the Al-Mg system.

Plagioclase grains in the H4 chondrites have low Mg concentrations (~0.05-0.1 wt.% Mg), so the counts of Mg isotopes during ion probe measurements are also low. This can make Al-Mg measurements susceptible to ratio bias, a deviation from the true ratio. Ratio bias is not a random uncertainty; all ratios are biased in the same direction. Isotope ratios determined from counting a subset of atoms in a sample are subject to a positive bias (i.e., the measured ratio is greater than the true ratio) that is inversely proportional to the number of counts in the denominator of the ratio, ^{24}Mg, in this case (e.g., Ogliore et al., 2011). Isotope ratios from SIMS data are often calculated using the mean of the ratios from many cycles of a measurement. This method of calculating ratios makes the magnitude of the bias larger because the total counts of each isotope are divided into many subsamples (e.g., Ogliore et al., 2011). Using the ratio of the total counts from all cycles of the measurement provides a less-biased method of calculating isotope ratios. Because the results reported by Zinner and Göpel (1992) were calculated using the mean of the ratios (Ernst Zinner, personal communication), we decided that it

would be worthwhile to re-measure these samples using the University of Hawaii Cameca ims 1280 ion microprobe in order to eliminate the possibility that ratio bias has affected these results. Previous measurements were carried out using a Cameca ims 3f ion microprobe (Zinner and Göpel, 1992) and a Cameca NanoSIMS (Zinner et al., 2002).

While we were making these measurements, our colleagues at the University of Hawaii were carrying out a study on the cooling rates of H chondrites using Ni diffusion profiles in cloudy taenite grains (Krot et al., 2012; Scott et al., 2014). Their study shows that Ste. Marguerite, Forest Vale, and Beaver Creek are unusual in that they cooled much more quickly (>5000 °C/Myr) than other H4 chondrites (<50 °C/Myr). These very high cooling rates are not consistent with cooling at depth, as the onion-shell model predicts. This finding may require reevaluation of the interpretation that the ^{26}Al-^{26}Mg system for H4 chondrites records metamorphism of the parent body, as proposed by Zinner and Göpel (2002).

The objective of this study is to better constrain the initial ^{26}Al/^{27}Al ratios, $(^{26}Al/^{27}Al)_0$, determined by Zinner and Göpel (2002) and to re-evaluate how Al-Mg systematics of H4 chondrites fit into the overall picture of the structure and thermal history of the H chondrite parent body. We analyzed thin sections of the fast cooled H4 chondrites, Ste. Marguerite, Forest Vale, and Beaver Creek, which previously showed evidence of ^{26}Al, and of the slow-cooled H4, Sena, which was not previously analyzed for Al-Mg. Overall, we confirm the previous measurements, but we argue that the ^{26}Al-^{26}Mg system gives the time of impact excavation instead of the end of metamorphism for H4 chondrites.

5.3 Analytical Procedures

5.3.1 *Sample Selection and Electron Microprobe Analyses*

Thin sections of Ste. Marguerite (2), Forest Vale (2), Beaver Creek (1) and Sena (1) were analyzed for this study. Aluminum elemental maps of these thin sections were collected with an SEM-EDX (JEOL JSM-5900LV) to screen for a suite of possible targets for Al-Mg isotopic measurements. Once suitable candidates were identified, high-resolution Mg, Fe and Ca elemental maps were collected on these objects using the JEOL JXA-8500F electron microprobe. Since Mg content of plagioclase in these objects is low, Mg distribution maps were helpful for avoiding Mg-rich regions in our SIMS measurements. Magnesium was measured on 3 different spectrometers with a focused beam at 50 nA and 15 kV, with a dwell time of 50 ms. The X-ray maps were set up to resolve 1 μm features. For some of the samples, the electron microprobe was also utilized for quantitative measurements of the Al/Mg elemental ratio. These analyses were carried out with a 10 μm beam at 15-20 nA and 15 kV. Since these measurements damaged the carbon coating, they also served as useful fiducials in the plagioclase for our SIMS analyses: the electron microprobe measurement spots were readily identified with the ion probe by looking at Na or Al ion images.

Since Zinner and Göpel (2002) used plagioclase mineral separates for their Al-Mg isotopic analyses, the petrographic context of these grains is unknown. To get an overview of the composition of plagioclase from each chondrite, we analyzed ~20-25 plagioclase grains from each chondrite using the electron microprobe (10 nA, 15 keV, 10 μm beam). The stoichiometry determined from the electron microprobe measurements shows that the grains analyzed are consistent with feldspar and not glass. The electron

microprobe probe data are compiled in the Supplementary section of Telus et al. (2014a). It includes data for plagioclase, olivine, pyroxene and chromite. Implications of the compositional variations and petrology of plagioclase in Ste. Marguerite and the other chondrites analyzed in this study are described in the Discussion.

5.3.2 *Ion Microprobe Measurement Conditions and Data Analysis*

Aluminum and Mg isotopes were measured with the Cameca ims 1280 ion microprobe at the University of Hawai‘i at Manoa. The procedures for SIMS Al-Mg isotopic measurements of plagioclase are described in detail in Makide et al. (2009). We used a $^{16}O^-$ primary beam at 300-400 pA with 13 kV accelerating voltage (i.e., -13 kV at the source). The spot size was ~10 μm. The $^{27}Al^+$ count rates were ~10^7 cps. The mass resolving power was set to ~3900, which resolves molecular interferences ($^{48}Ca^{2+}$ and $^{23}NaH^+$ from ^{24}Mg and $^{24}MgH^+$ from ^{25}Mg).

Plagioclase from Ste. Marguerite was measured using mono-collection detectors, with $^{27}Al^+$ measured for 2 seconds per cycle on the mono-collector Faraday cup (FC2), $^{24}Mg^+$ for 4 s/cycle on the mono-collector electron multiplier (EM), and $^{25, 26}Mg^+$ for 10 s/cycle on the mono-collector EM. Plagioclase from Forest Vale, Beaver Creek and Sena were measured using a similar set up, but $^{27}Al^+$ (on a multi-collector Faraday Cup, H’2) and $^{25}Mg^+$ (mono-collector EM) were measured simultaneously for 10s/cycle. We switched to this set up because it required less magnetic-field peak jumping. The number of cycles for each measurement varied from 150 to 275. Miyakejima anorthite (An 97) and Lake County plagioclase standards (An 68) were measured to monitor drift in the detectors and to determine the Al-Mg relative sensitivity factors.

Olivine, pyroxene and Cr-spinel were measured to constrain the intercept of the isochrons. These analyses were done using a 3 nA, ~20×15 µm primary beam in aperture-illumination mode. For these measurements, $^{27}Al^{+}$ and $^{24, 25, 26}Mg^{+}$ were all measured with four Faraday cups for 10 s/cycle for 30 cycles. San Carlos olivine, San Carlos pyroxene and Burma spinel were used as standards.

The isotope ratios reported here are calculated from summing the counts of the numerator isotope over all cycles and dividing by the summed counts of the denominator isotope over all cycles. However, ratios were also calculated from the mean of the ratios of individual cycles to permit monitoring of data quality and to compare the magnitude of the ratio bias on the results. Since we collected the plagioclase data in cycles, we were able to include time interpolation and remove anomalous cycles. Reasons for excluding cycles include spikes in the detector signal due to sputtering through a Mg-rich phases during analyses of plagioclase grains, electronic noise, and primary beam dropout. We did not apply a generic filter for outliers. The data were corrected for electron-multiplier deadtime. Relative sensitivity factors ($^{27}Al^{+}/^{24}Mg^{+}_{measured}$ / $^{27}Al/^{24}Mg_{true}$) for the $^{27}Al/^{24}Mg$ ratios for each mineral were applied based on the $^{27}Al^{+}/^{24}Mg^{+}$ ratios measured by SIMS and the Al/Mg ratios from electron microprobe measurements. Correction for instrumental mass fractionation was done by standard-sample bracketing assuming all terrestrial standards have the same Mg-isotope ratios. To calculate the excess in ^{26}Mg, we applied a correction for intrinsic mass fractionation in the samples using an exponential law with coefficient β=0.514 (Davis et al., 2005). Uncertainties on the measured ratios were determined using the standard error of the ratios calculated from individual cycles, which allows us to account for non-statistical cycle-to-cycle variations during the

measurement. The overall uncertainties on the reported Mg isotope ratios include the statistical measurement error and the standard deviation of the standard measurements. Mg-isotope data from Zinner and Göpel (2002) were calculated using a reference $^{26}Mg/^{24}Mg$ value of 0.13945, while our data were calculated using a reference value of 0.13932 (Catanzaro et al., 1966). We shifted all the $^{26}Mg/^{24}Mg$ values from Zinner and Göpel by -0.00013, so that the reference values from the two studies are consistent. This makes it easier to directly compare results from the two studies. For each isochron, we report the mean square weighted deviation (MSWD), which is a measure of how well the data fit the regression. The isochron plots also include $\delta^{26}Mg$ values, the deviation of the mass-fractionation-corrected $^{26}Mg/^{24}Mg$ ratios from the terrestrial $^{26}Mg/^{24}Mg$ value (see Makide et al., 2009 for detailed equations). Uncertainties on the isochron slopes are reported as 2σ.

Finally, for each meteorite, we report the magnitude of the ratio bias based on the ^{24}Mg counts per cycle from the measurements with the highest $^{27}Al/^{24}Mg$ ratios (or the lowest ^{24}Mg counts/cycle). The relative bias in each ratio (the bias divided by the true ratio) is approximately equal to the inverse of the number of counts in the denominator (Ogliore et al., 2011; Coath et al., 2013). The biased ratios are then propagated through the mass fractionation correction and isochron calculation as described in Telus et al. (2012a). In the Discussion, we estimate the magnitude of the bias on each isochron, defined here as the bias in slope divided by the calculated slope (from either total counts or averaging the ratio), and multiplied by 1000 and briefly discuss how ratio bias propagates through the mass fractionation correction and into the final isochrons.

5.4 Results

5.4.1 *Ste. Marguerite*

Our electron microprobe analyses show that the compositions of plagioclase grains from Ste. Marguerite span a wide range from An_4 to An_{89} (Figure 5.1). The distribution of compositions seems to be bimodal with most lying between $An_{10\text{-}15}$ and a few above An_{50}. Most of the grains are associated with chondrules; examples are illustrated in Figure 5.2. Plagioclase with high An# (>50) is almost always associated with plagioclase with low An# (<50) (e.g., Figure 5.3). This relationship was also noted by Kovach and Jones (2010). In some cases, plagioclase compositions within a chondrule are not bimodal. The significance of compositional heterogeneity of plagioclase in Ste. Marguerite is addressed in the Discussion.

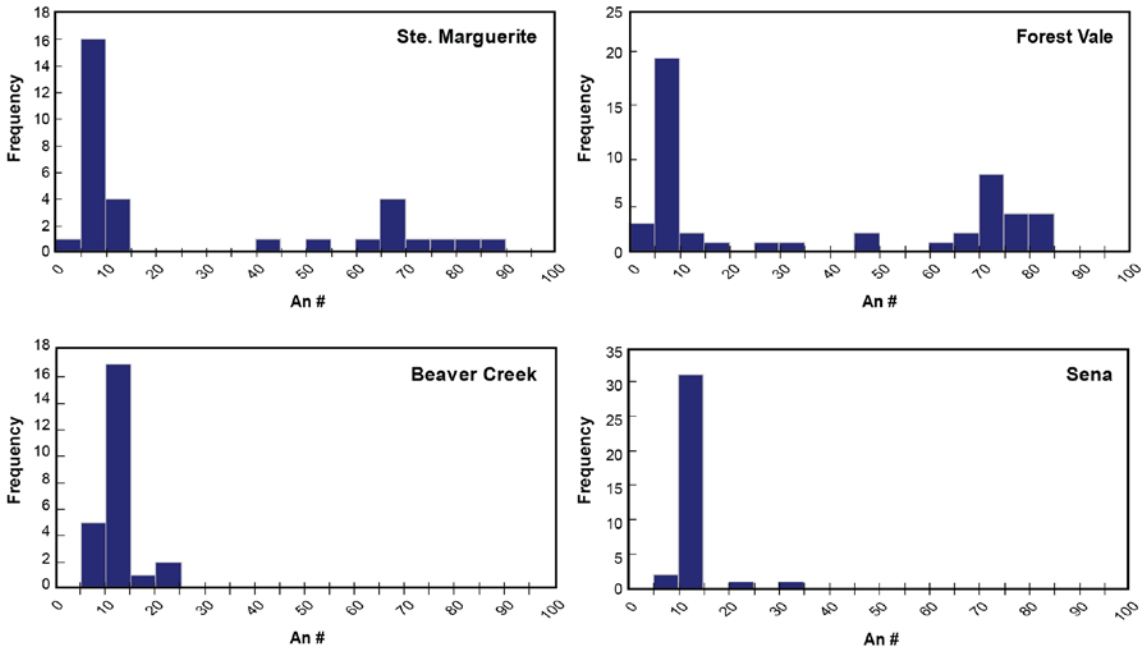

Figure 5.1. Plagioclase composition based on electron microprobe analyses of the H4 chondrites analyzed for this study. Note the bimodal distributions for Ste. Marguerite and Forest Vale.

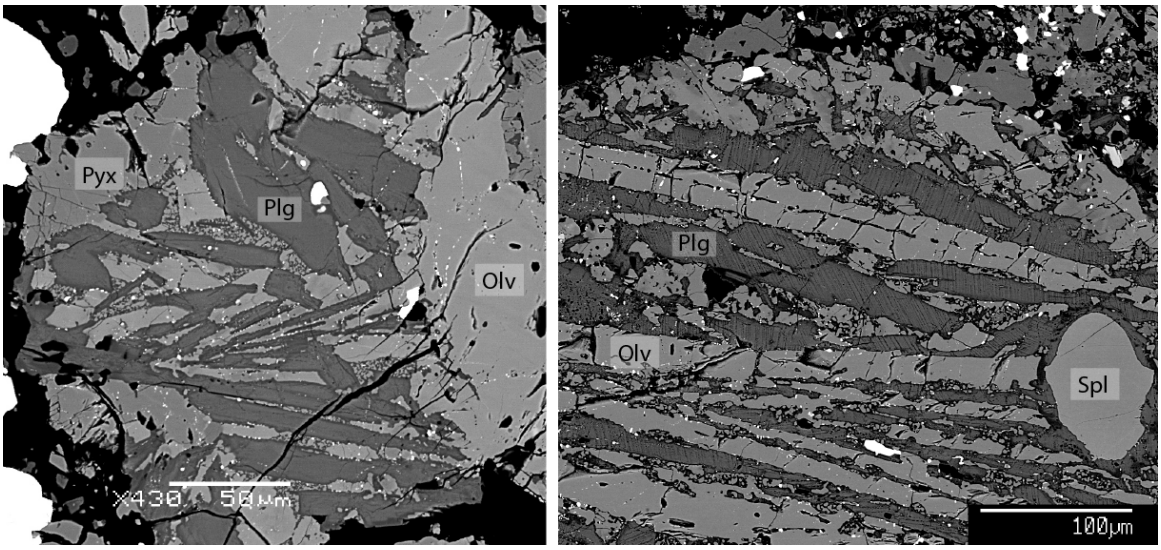

Figure 5.2. Backscattered-electron images of two chondrules from Ste. Marguerite that were analyzed for ^{26}Al-^{26}Mg systematics, (left) SM3-2 and (right) SM2-1 (see Table 5.1). Plagioclase (Plg) grains from Ste. Marguerite analyzed in this study are typically associated with chondrules. Olivine (Olv), pyroxene (Pyx) and Cr-spinel (Spl) grains were measured to constrain the intercept value on the isochron diagram (e.g., see Figure 5.4). Black areas are epoxy.

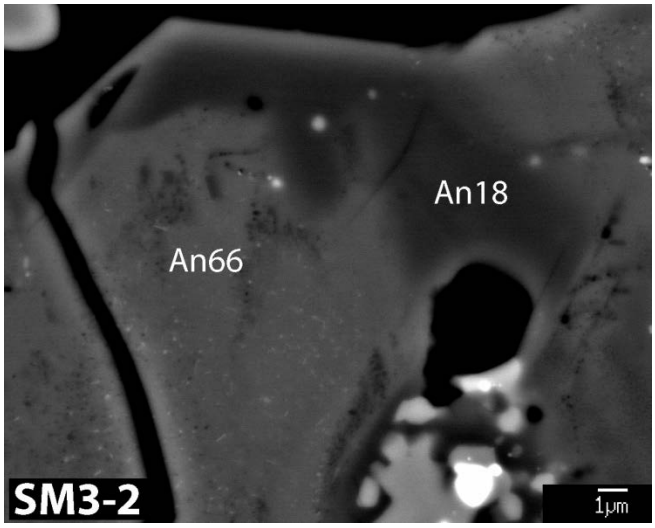

Figure 5.3. Backscattered-electron image of SM3-2 illustrating the petrologic relationship between most of the high and low An# plagioclase grains (the whole chondrule is shown in the left image of Figure 5.2).

Using the ion probe, we measured the Al-Mg isotopic systematics of 8 plagioclase, 7 olivine and 2 spinel grains in Ste. Marguerite (Table 5.1). The ^{26}Mg/^{24}Mg ratio correlates with the ^{27}Al/^{24}Mg ratio, showing that ^{26}Al was once present in this

meteorite. The regression through our SIMS data in Figure 5.4 corresponds to an initial ratio [$(^{26}Al/^{27}Al)_0$] of $(3.0\pm0.5)\times10^{-7}$ (2σ). This is consistent with previous results from Zinner and Göpel (2002), who inferred an $(^{26}Al/^{27}Al)_0$ ratio of $(2.9\pm0.6)\times10^{-7}$ (2σ). Assuming a homogeneous distribution of ^{26}Al, this initial ratio corresponds to isotopic closure of the Al-Mg system in Ste. Marguerite 5.2±0.2 Myr after CAIs, which have $(^{26}Al/^{27}Al)_0$ of 5.25×10^{-5} (Jacobsen et al., 2008; Larsen et al., 2011). An absolute age of 4562.1±0.3 Ma is obtained for Ste. Marguerite by tying the ^{26}Al system in CAIs to a U-isotope-ratio corrected ^{207}Pb-^{206}Pb absolute age of 4567.30±0.16 Ma obtained from CAIs by Connelly et al. (2012).

In Ste. Marguerite, plagioclase grains from PlagA have the highest Al/Mg ratios of > 4000 (see Table 5.1). The ^{24}Mg counts per cycle (150 to 200 cycles) for these measurements are ~20,000. The magnitudes of the ratio biases from averaging the ratios (the inverse of the counts per cycle of ^{24}Mg) and from using total counts (the inverse of the total counts of ^{24}Mg) are very low, $+5\times10^{-5}$ (+0.05‰) and $+4\times10^{-7}$ (+0.4 ppm), respectively.

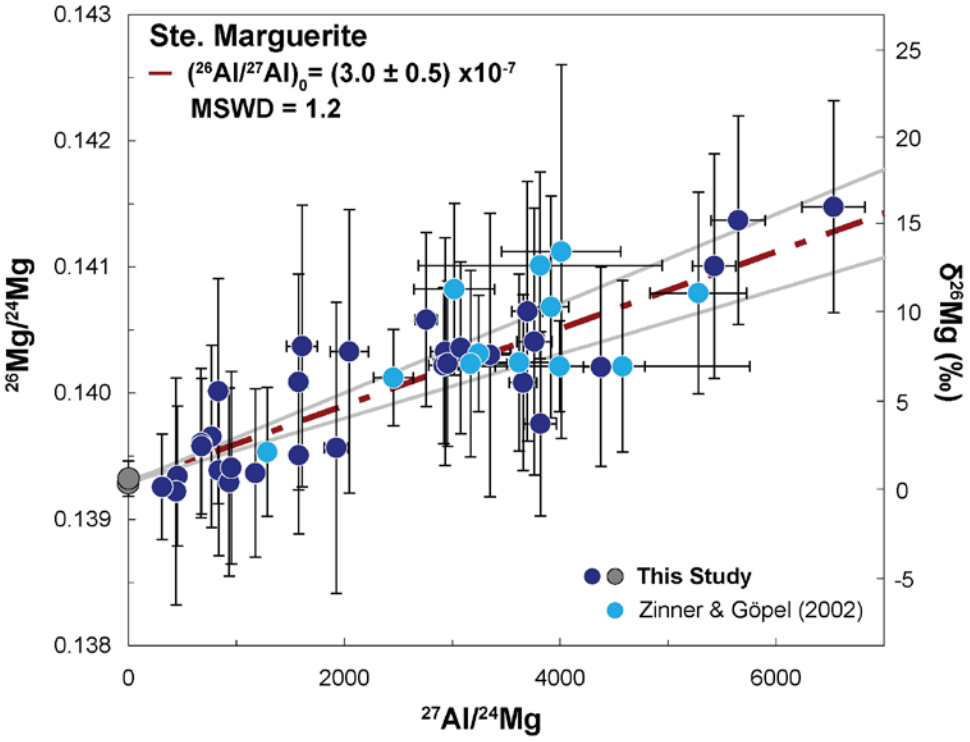

Figure 5.4. $^{26}Mg/^{24}Mg$ vs. $^{27}Al/^{24}Mg$ for plagioclase, olivine, and Cr-spinel grains from H4 chondrite, Ste. Marguerite. The plagioclase data from this study are in dark blue and the olivine and spinel data are shown in grey. The $(^{26}Al/^{27}Al)_0$ inferred from this study is $(3.0\pm0.5)\times10^{-7}$ (2σ) with a MSWD of 1.2. Data from Zinner and Göpel (2002), which are in light blue, are not included in the regression.

Table 5.1. Al-Mg isotopic composition of plagioclase, olivine, pyroxene, and Cr-spinel from Ste. Marguerite

Sample Name/ Mineral	$^{27}Al/^{24}Mg$	$^{26}Mg/^{24}Mg$	Sample Name/ Mineral	$^{27}Al/^{24}Mg$	$^{26}Mg/^{24}Mg$
SM2-1			*SM3-5*		
olv	0.00049 ± 0.00009	0.13929 ± 0.00003	olv	0.00309 ± 0.00067	0.13930 ± 0.00003
	0.00086 ± 0.00017	0.13929 ± 0.00003		0.00195 ± 0.00038	0.13930 ± 0.00003
Cr-sp	3.6 ± 0.11	0.13932 ± 0.00003		0.00220 ± 0.00042	0.13929 ± 0.00003
	3.6 ± 0.11	0.13931 ± 0.00003	plag	456 ± 18	0.13934 ± 0.00055
plag	771 ± 29	0.13966 ± 0.00072		444 ± 25	0.13922 ± 0.00090
	839 ± 47	0.13939 ± 0.00067	*SM3-7*		
	2933 ± 133	0.14033 ± 0.00090	olv	0.00235 ± 0.00047	0.13930 ± 0.00003
	1609 ± 142	0.1404 ± 0.0011		0.00252 ± 0.00048	0.13931 ± 0.00003
	1926 ± 110	0.1396 ± 0.0012	plag	314 ± 14	0.13926 ± 0.00042
	2048 ± 175	0.1403 ± 0.0011		936 ± 43	0.13929 ± 0.00075
Plag-A			*SM3-2*		
olv	0.00168 ± 0.00032	0.13929 ± 0.00003	olv	0.00061 ± 0.00027	0.13930 ± 0.00003
	0.00021 ± 0.00004	0.13930 ± 0.00003	pyx	0.0157 ± 0.0030	0.13933 ± 0.00004

plag	5728 ± 569	0.14138 ± 0.00083	plag	1577 ± 83	0.14009 ± 0.00086
	6623 ± 562	0.14049 ± 0.00084		1177 ± 47	0.13937 ± 0.00067
	5502 ± 287	0.14101 ± 0.00089		675 ± 29	0.13960 ± 0.00059
	3397 ± 228	0.1403 ± 0.0011		678 ± 33	0.13958 ± 0.00054
SM3-1			*SM3-6*		
olv	0.00106 ± 0.00021	0.13929 ± 0.00003	Cr-sp	3.9 ± 0.12	0.13933 ± 0.00003
	0.00059 ± 0.00011	0.13929 ± 0.00003		4.1 ± 0.12	0.13933 ± 0.00003
plag	2922 ± 136	0.14022 ± 0.00062	plag	2759 ± 102	0.14058 ± 0.00069
	2957 ± 109	0.14023 ± 0.00066		1578 ± 74	0.13951 ± 0.00062
SM3-M				833 ± 50	0.14002 ± 0.00089
olv	0.0068 ± 0.0013	0.13929 ± 0.00003		954 ± 59	0.13941 ± 0.00076
	0.0045 ± 0.0010	0.13929 ± 0.00003		3079 ± 175	0.14036 ± 0.00068
plag	3657 ± 129	0.14008 ± 0.00070			
	4378 ± 163	0.14021 ± 0.00079			
	3815 ± 148	0.13976 ± 0.00073			
	3761 ± 161	0.1404 ± 0.0011			
	3696 ± 144	0.1406 ± 0.0010			
$(^{26}Al/^{27}Al)_0$	$(3.0 \pm 0.5)\times10^{-7}$ (2σ)				
MSWD	1.2				

5.4.2 *Forest Vale*

Plagioclase grains in Forest Vale can be associated with chondrules, but many are associated with metal and sulfide assemblages (Figure 5.5). They range in composition from An_3 to An_{84} (Figure 5.1). The distribution of plagioclase compositions appears to be bimodal with about half of the plagioclase compositions lying between $An_{10\text{-}15}$ and the others above An_{50}. Like in Ste. Marguerite, plagioclase with high An# is closely associated with plagioclase with low An# (see example in Figure 5.3).

SIMS data for plagioclase and olivine from Forest Vale are reported in Table 5.2. When plagioclase data are plotted alone on the isochron diagram (Figure 5.6) there is no correlation between the $^{27}Al/^{24}Mg$ and $^{26}Mg/^{24}Mg$ ratios. The average $^{26}Mg/^{24}Mg$ ratio for the plagioclase grains corresponds to a $\delta^{26}Mg$ value of ~8±4 ‰ (grey dashed line in Figure 5.6). This clear excess of ^{26}Mg in the high-Al plagioclase compared to no excess

in high-Mg olivine indicates that the excesses are due to the decay of ^{26}Al. A weighted regression through plagioclase and olivine data gives an $(^{26}Al/^{27}Al)_0$ of $(1.5\pm0.7)\times10^{-7}$ (2σ), which is consistent with the $(^{26}Al/^{27}Al)_0$ of $(1.5\pm0.5)\times10^{-7}$ (2σ) inferred by Zinner and Göpel (2002). The initial ratio corresponds to a time difference of 5.9 (+0.6/-0.4) Myr after CAIs. The large uncertainties on the ^{26}Mg/^{24}Mg ratios for plagioclase in Forest Vale make it difficult to conclude whether or not the Al-Mg systematics are disturbed.

The maximum ratio bias (r/R-1 or (r/R-1)×1000, where r is the calculated ratio and R is the true ratio) in the Forest Vale data is estimated from plagioclase grains from FVMT-17, which have the highest Al/Mg ratio of ~10,000 (see Table 5.2) and ^{24}Mg counts per cycle of ~4800 (200 cycles). When the isotope ratios are calculated from averaging ratios, the ratio bias is $+2\times10^{-4}$ (+0.2‰); and when total counts are used, the ratio bias is $+1\times10^{-6}$ (+1 ppm).

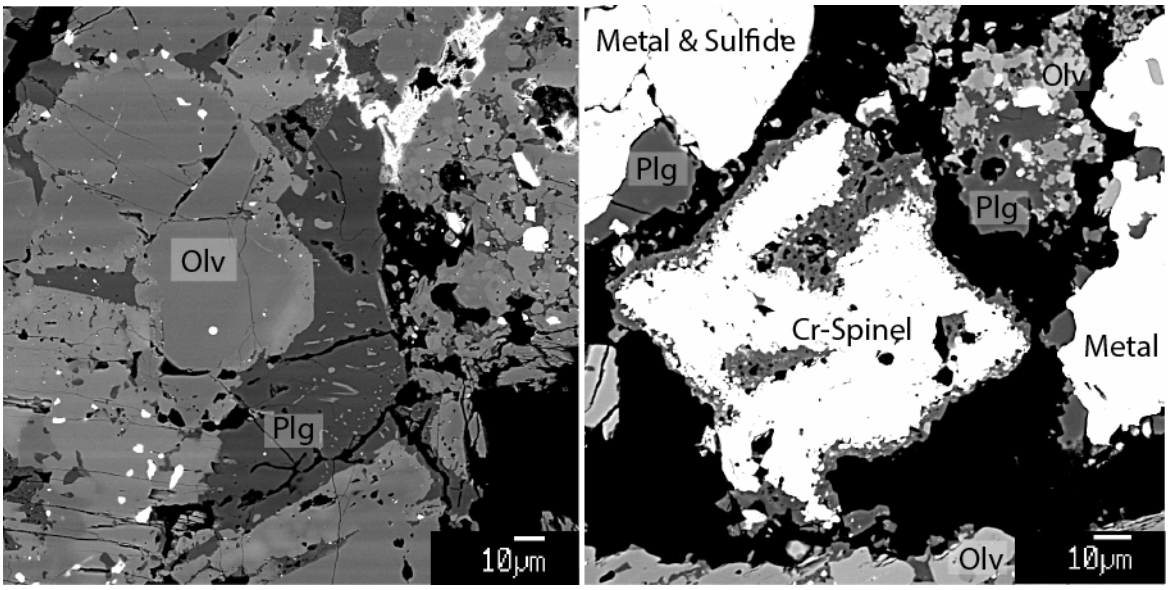

Figure 5.5. Backscattered-electron images of plagioclase grains from Forest Vale that were measured for ^{26}Al-^{26}Mg systematics, (left) FVMT-1 and (right) FVMT-17. Plagioclase (Plg) grains in this chondrite are associated with both chondrules (left) and metal, sulfide, and Cr-spinel assemblages (right). Olivine (Olv) grains were analyzed for the intercept value. Black areas are epoxy.

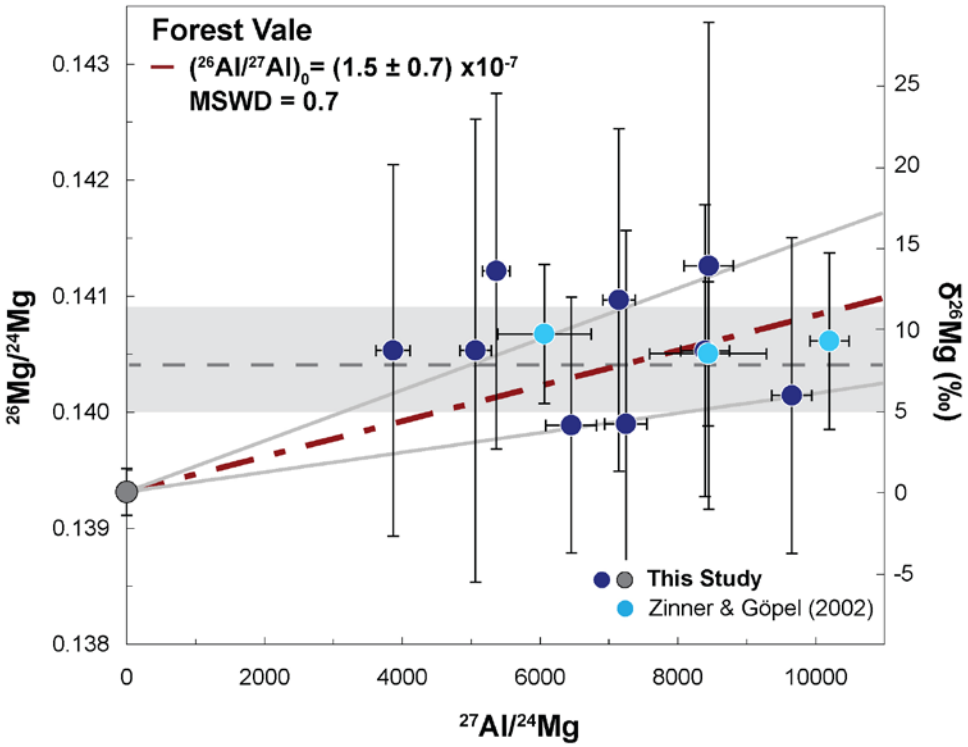

Figure 5.6. $^{26}Mg/^{24}Mg$ vs. $^{27}Al/^{24}Mg$ for plagioclase and olivine grains from Forest Vale (H4). The $(^{26}Al/^{27}Al)_0$ inferred from this study is $(1.5\pm0.7)\times10^{-7}$ (2σ) with a MSWD of 0.7. The grey dashed line in the grey shaded bar corresponds to the average $^{26}Mg/^{24}Mg$ ratio for the plagioclase grains. Data from Zinner and Göpel (2002), which are in light blue, are not included in the regression.

Table 5.2. Al-Mg isotopic composition of olivine and plagioclase from Forest Vale

Name/ Mineral	$^{27}Al/^{24}Mg$	$^{26}Mg/^{24}Mg$
FVMT-16		
olv	0.00020 ± 0.00002	0.13932 ± 0.00002
	0.0040 ± 0.0003	0.13931 ± 0.00002
	0.00026 ± 0.00002	0.139308 ± 0.000014
FVMT-8		
olv	0.0038 ± 0.0003	0.13931 ± 0.00002
	0.00045 ± 0.00003	0.13932 ± 0.00002
FVMT-1		
olv	0.0060 ± 0.0004	0.13932 ± 0.00003
	0.0045 ± 0.0003	0.13932 ± 0.00003
plag	6452 ± 370	0.1399 ± 0.0011
	7245 ± 304	0.1399 ± 0.0017
	5062 ± 230	0.1405 ± 0.0020
FVMT-17		
plag	8449 ± 357	0.1413 ± 0.0021
	9656 ± 291	0.1401 ± 0.0014
	7144 ± 235	0.1410 ± 0.0015
	3864 ± 248	0.1405 ± 0.0016
FVMT-15		
plag	8395 ± 359	0.1405 ± 0.0013
FVED-4		
plag	5363 ± 199	0.1412 ± 0.0015
$(^{26}Al/^{27}Al)_0$	$(1.5 \pm 0.7)\times10^{-7}$ (2σ)	
MSWD	0.7	

5.4.3 *Beaver Creek*

The average anorthite number of plagioclase grains from Beaver Creek is An_{12}, with a range from An_6 to An_{22}. Only two out of the 25 plagioclase grains analyzed have An# values above 10 (Figure 5.1). Typical regions chosen for isotopic analyses are shown in Figure 5.7. Implications of the compositional homogeneity of plagioclase in Beaver Creek are considered in the Discussion.

We analyzed olivine, pyroxene and plagioclase from 5 regions in Beaver Creek with the ion probe (Table 5.3). There is a limited spread in the Al/Mg ratio, and the

$^{26}Mg/^{24}Mg$ ratios for many of the individual measurements are unresolved from the terrestrial value. When the data are plotted on an isochron diagram, there is no clear correlation between the $^{27}Al/^{24}Mg$ and $^{26}Mg/^{24}Mg$ ratios (Figure 5.8). A regression through the data gives an $(^{26}Al/^{27}Al)_0$ of $(0.9\pm0.7)\times 10^{-7}$, consistent with $<2.4\times10^{-7}$ (2σ) inferred from Zinner and Göpel (2002). The $(^{26}Al/^{27}Al)_0$ corresponds to a time difference of 6.5 (+1.7/-0.6) Myr after CAIs.

The $^{27}Al/^{24}Mg$ ratios of plagioclase grains from Beaver Creek are relatively uniform, around ~3000 (see Table 5.3). The ^{24}Mg counts/cycle are ~12,000 (200 cycles). The ratio biases from averaging ratios and from total counts are $+4\times10^{-5}$ (+0.04‰) and $+2\times10^{-7}$ (+0.2 ppm), respectively.

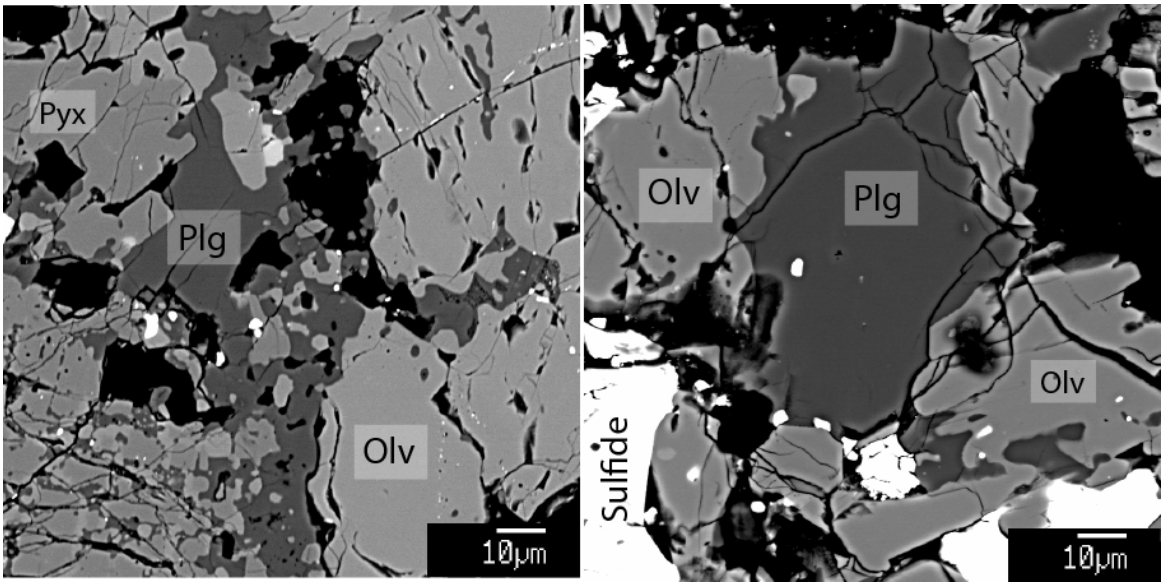

Figure 5.7. Backscattered-electron images of plagioclase grains from Beaver Creek that were analyzed for ^{26}Al-^{26}Mg systematics, (left) BC-r15 and (right) BC-r4. Plagioclase (Plg) grains in this chondrite are relatively uniform in composition (Figure 5.1). Olivine (Olv) and pyroxene (Pyx) grains were analyzed for the intercept value. White phases are mostly sulfide and black areas are epoxy.

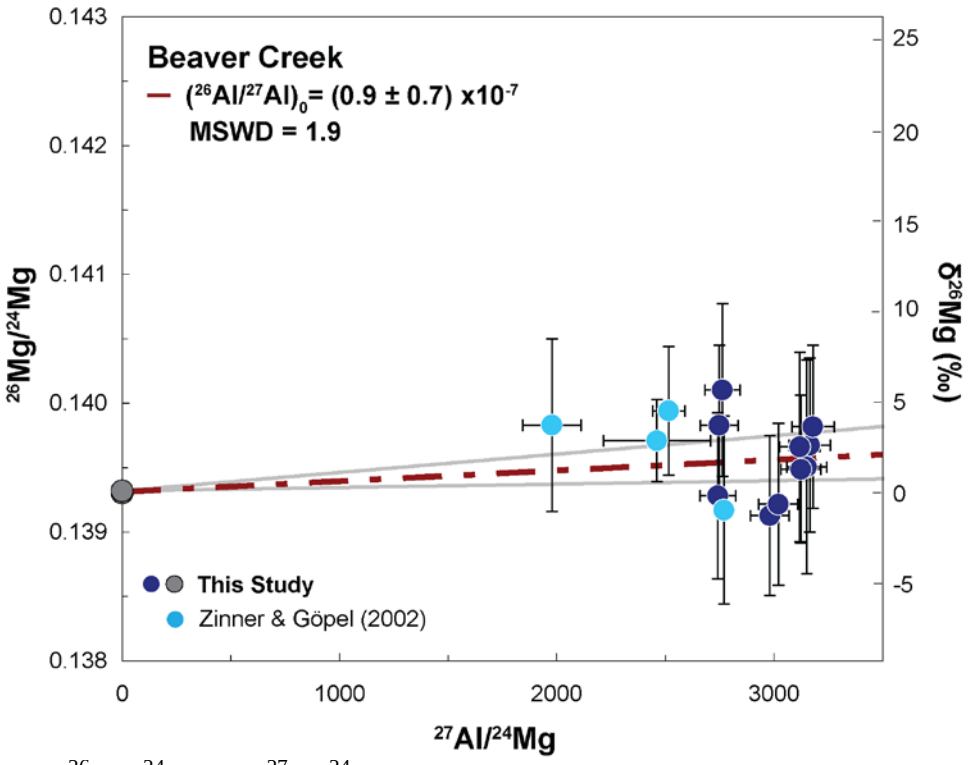

Figure 5.8. $^{26}Mg/^{24}Mg$ vs. $^{27}Al/^{24}Mg$ for plagioclase, olivine, and pyroxene grains from Beaver Creek. There is a limited spread in the Al/Mg ratio, making it difficult to precisely constrain the $(^{26}Al/^{27}Al)_0$ ratio. The $(^{26}Al/^{27}Al)_0$ inferred from this study is $(0.9\pm0.7)\times10^{-7}$ (2σ) with a MSWD of 1.9. These results are consistent with data from Zinner and Göpel (2002), which are shown in light blue, but not included in the regression.

Table 5.3. Al-Mg isotopic composition of olivine, pyroxene and plagioclase from Beaver Creek

Name/ Mineral		$^{27}Al/^{24}Mg$	$^{26}Mg/^{24}Mg$
BC r4			
	pyx	0.0039 ± 0.0002	0.13933 ± 0.00002
		0.0091 ± 0.0005	0.13933 ± 0.00002
		0.00286 ± 0.00012	0.13933 ± 0.00002
	plag	3045 ± 92	0.13951 ± 0.00083
		3019 ± 93	0.13950 ± 0.00063
		2919 ± 89	0.13922 ± 0.00063
		2670 ± 81	0.14011 ± 0.00067
BC r14			
	olv	0.0032 ± 0.0003	0.13931 ± 0.00002
	pyx	0.043 ± 0.004	0.13932 ± 0.00002
	plag	3058 ± 96	0.13968 ± 0.00067
		2656 ± 86	0.13985 ± 0.00062
BC r7			
	olv	0.0177 ± 0.0010	0.13931 ± 0.00002
		0.00279 ± 0.00011	0.13930 ± 0.00002

	plag	2881 ± 89	0.13914 ± 0.00062
BC r2			
	olv	0.00035 ± 0.00002	0.13930 ± 0.00002
		0.0109 ± 0.0006	0.13930 ± 0.00002
		0.112 ± 0.005	0.13931 ± 0.00002
	plag	2650 ± 83	0.13929 ± 0.00064
BC r15			
	olv	0.0061 ± 0.0004	0.13931 ± 0.00002
	pyx	0.0062 ± 0.0003	0.13933 ± 0.00002
		0.0086 ± 0.0004	0.13931 ± 0.00002
	plag	3073 ± 97	0.13983 ± 0.00063
		3014 ± 93	0.13967 ± 0.00074
$(^{26}Al/^{27}Al)_0$		$(0.9 \pm 0.7)\times10^{-7}$ (2σ)	
MSWD		1.9	

5.4.4 *Sena*

The compositions of plagioclase grains in Sena show the least amount of variation among the chondrites measured in this study. Their compositions range from An_8 to An_{15}, but the average is An_{12} (Figure 5.1).

We measured 3 plagioclase and 4 olivine grains in this meteorite and found no evidence for the former presence of ^{26}Al. Examples of the grains we analyzed are shown in Figure 5.9. The $(^{26}Al/^{27}Al)_0$ of $< 0.3\times10^{-7}$ (2σ upper limit) is lower than the 2σ lower limits on the initial ratios for Ste. Marguerite and Forest Vale. The $(^{26}Al/^{27}Al)_0$ for Sena corresponds to a time of formation more than 7.7 Myr after CAIs.

Plagioclase grains from Sena-1 (see Table 5.4) have very high $^{27}Al/^{24}Mg$ ratios (~10,000), with ^{24}Mg counts per cycle around 6600 (200 cycles). Measurements with $^{27}Al/^{24}Mg$ ratios of <1000 are due to beam overlap with an Mg-rich phase. The magnitude of the ratio bias from averaging ratios is $+1.5\times10^{-4}$ (+0.15‰) and from total counts is $+7\times10^{-7}$ (+0.7 ppm).

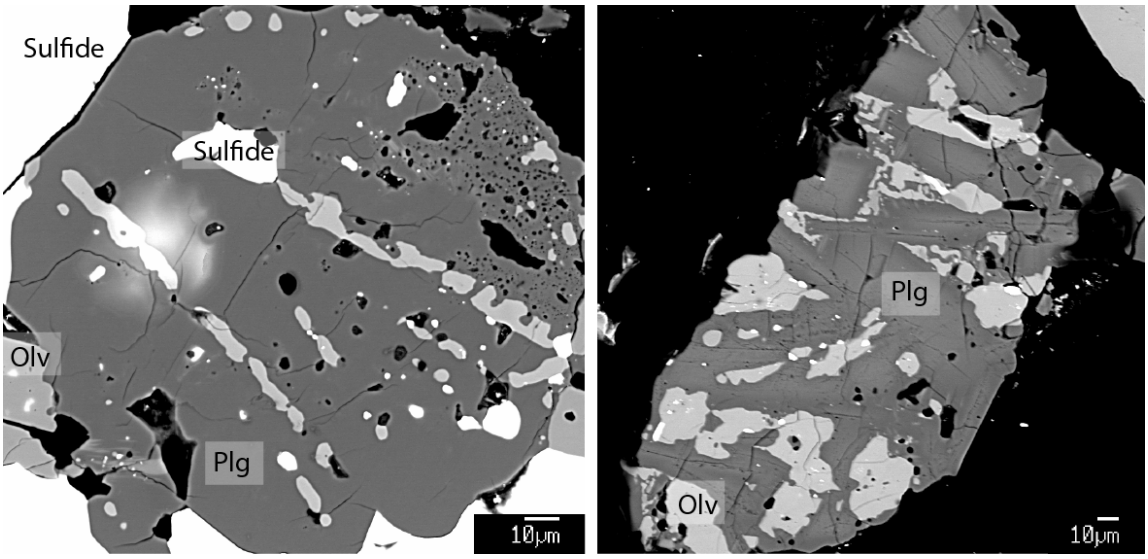

Figure 5.9. Backscattered-electron images of plagioclase (Plg) grains from Sena that were analyzed for ^{26}Al-^{26}Mg systematics, (left) Sena-1 and (right) Sena-9. Plagioclase (Plg) grains in this chondrite show little variation in composition (Figure 5.1). Olivine (Olv) grains were analyzed to constrain the intercept value. White phases are mostly sulfide and black areas are epoxy.

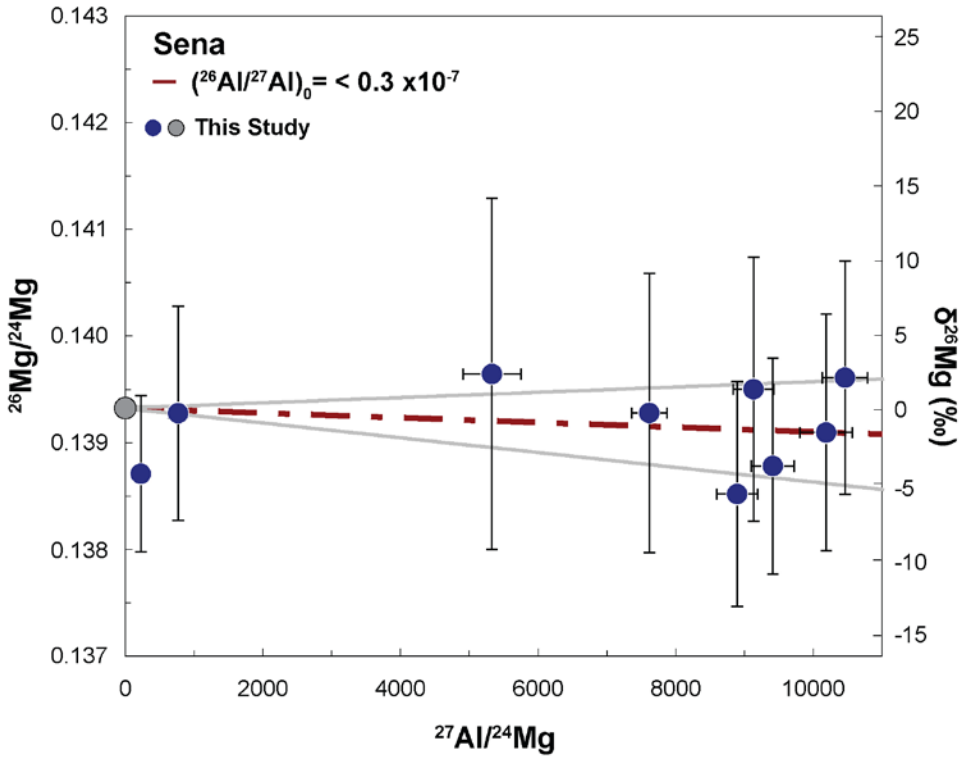

Figure 5.10. ^{26}Al-^{26}Mg systematics of plagioclase and olivine grains from Sena. The $(^{26}Al/^{27}Al)_0$ inferred from the data is unresolved from zero with a 2σ (two-sided) upper-limit of 0.3×10^{-7}, which is lower than the 2σ lower-limits on the $(^{26}Al/^{27}Al)_0$ values for Ste. Marguerite and Forest Vale.

Table 5.4. Al-Mg isotopic data for olivine and plagioclase from Sena

Name/ Mineral		$^{27}Al/^{24}Mg$	$^{26}Mg/^{24}Mg$
Sena-6			
	olv	0.0022 ± 0.0002	0.13931 ± 0.00002
		0.037 ± 0.003	0.13932 ± 0.00003
Sena-1			
	olv	0.0036 ± 0.0003	0.13933 ± 0.00003
		0.0045 ± 0.0004	0.13933 ± 0.00003
	plag	7616 ± 257	0.1393 ± 0.0013
		10460 ± 330	0.1396 ± 0.0011
		9413 ± 311	0.1388 ± 0.0010
		9129 ± 293	0.1395 ± 0.0012
Sena-15			
	olv	0.00013 ± 0.00002	0.13932 ± 0.00002
		0.0052 ± 0.0005	0.13933 ± 0.00003
	plag	10187 ± 381	0.1391 ± 0.0011
Sena-3			
	olv	0.024 ± 0.002	0.13933 ± 0.00002
		0.0157 ± 0.0014	0.13932 ± 0.00002
Sena-11			
	olv	0.0140 ± 0.0014	0.13932 ± 0.00002
		0.026 ± 0.002	0.13933 ± 0.00002
Sena-9			
	plag	224 ± 48	0.13871 ± 0.00073
		8894 ± 297	0.1385 ± 0.0011
		5331 ± 418	0.1396 ± 0.0016
		768 ± 136	0.1393 ± 0.0010
$(^{26}Al/^{27}Al)_0$		$< 0.3\times10^{-7}$ (2σ upper limit)	

5.5 Discussion

5.5.1 *Comparison with Previous Measurements*

We analyzed the ^{26}Al-^{26}Mg systematics of plagioclase, olivine, pyroxene and Cr-spinel from thin sections of H4 chondrites to constrain their $(^{26}Al/^{27}Al)_0$ ratios. Since plagioclase grains in H4 chondrites can have low Mg concentrations, it is important to

consider the influence of ratio bias to accurately constrain the $(^{26}Al/^{27}Al)_0$ for these chondrites. The ^{24}Mg counts per cycle in our measurements of plagioclase range from ~4,800 for Forest Vale to ~20,000 for Ste. Marguerite. For these counts, the magnitude of the ratio bias from averaging the ratios (the inverse of the counts per cycle of ^{24}Mg) is $+2\times10^{-4}$ (0.2‰) for Forest Vale and $+5\times10^{-5}$ (0.05‰) for Ste. Marguerite. The ratio bias from averaging ratios is insignificant compared to the statistical uncertainty of the $^{26}Mg/^{24}Mg$ ratios (~4‰). Using the sum of the counts from all cycles of the measurement reduces the magnitude of the bias on the ratios to very small values (+1 ppm and +0.4 ppm for Forest Vale and Ste. Marguerite, respectively).

In order to determine the amount of radiogenic ^{26}Mg and calculate the $(^{26}Al/^{27}Al)_0$ ratios, we must correct the Mg isotope ratios for mass-dependent fractionation. Ratio bias from low counts in ^{24}Mg will bias the $^{25}Mg/^{24}Mg$ and $^{26}Mg/^{24}Mg$ by the same amount and will propagate into the slope of the isochron in different ways, depending on how the mass-dependent fractionation correction is applied (Telus et al., 2012a). We applied an internal mass fractionation correction, which uses the ratio of non-radiogenic isotopes ($^{25}Mg/^{24}Mg$) to determine the amount of mass-dependent fractionation. Using a biased $^{25}Mg/^{24}Mg$ ratio for the internal mass fractionation correction over-corrects the $^{26}Mg/^{24}Mg$ ratio, resulting in an apparent deficit in $\delta^{26}Mg$ and a lower the inferred $(^{26}Al/^{27}Al)_0$ (see Figure 5.2a in Telus et al., 2012a).

Since Zinner and Göpel (2002) used the mean of the ratios to calculate the Mg isotope ratios, we expect the inferred $(^{26}Al/^{27}Al)_0$ ratios from their study to be less than those determined from using total counts (this study). However, the initial ratios inferred from the two studies are consistent. Although Zinner and Göpel (2002) used lower count

times (1 s/cycle for ^{24}Mg, 5 s/cycle for ^{25}Mg, and 5 s/cycle for ^{26}Mg) and had a lower transmission ion microprobe (Cameca ims 3f), they used a beam current of 2 to 5 nA, an order of magnitude higher than the beam current used in this study. This combination of conditions results in similar number of counts compared to our measurements (as shown by similar measurement uncertainties in Figure 5.4), and may explain the lack of significant ratio bias in their data. We calculated our data using both the mean of the ratios and the total counts to compare the magnitude of the bias on the isochrons from using both methods. When the mean of the ratios is used, the magnitude of the bias on the $(^{26}Al/^{27}Al)_0$ ratios ranges from -3.7 ‰ for Ste. Marguerite to -22 ‰ for Forest Vale, but drops to less than a fraction of a permil when total counts are used. If the precision of the initial ratios were a few permil, the bias from using the mean of the ratios would be a problem. However, given that the relative uncertainties on the slopes of the isochrons are >10 %, we cannot detect a bias in these data sets.

5.5.2 *Compositional Variation and Petrology of Plagioclase in H4 Chondrites*

To accurately interpret the $(^{26}Al/^{27}Al)_0$, we must also evaluate whether the plagioclase grains in H4 chondrites are primary igneous minerals or metamorphic in origin. At the lowest metamorphic grade of ordinary chondrites (type 3.0), glass in chondrule mesostasis is the predominant alkali-rich phase. Primary unaltered glass in Semarkona (LL3.00) is K-rich with coexisting microcrystals of albite (Grossman and Brearley, 2005). Primary plagioclase is rare and mainly appears in Al-rich chondrules. This primary plagioclase has compositions of An_{70} to An_{100} and $^{27}Al/^{24}Mg$ ratios of less than 300 (e.g., Huss et al., 2001). With thermal metamorphism, mesostasis glass begins to recrystallize to Na-rich plagioclase and igneous plagioclase becomes increasingly Mg-

poor. Primary plagioclase in ordinary chondrites of types 3.4 to 3.7 has compositions ranging from An_{75} to An_{95}, with $^{27}Al/^{24}Mg$ ratios up to 500. At the thermal conditions for type 4-6 ordinary chondrites, mesostasis glass has largely recrystallized to form oligoclase, which also forms in the matrix (Huss et al., 2005; Grossman and Brearley, 2005). The $^{27}Al/^{24}Mg$ ratios in both primary and secondary plagioclase in type 4 chondrites are above 500 (Tables 5.2-5.5; Zinner and Göpel, 2002). The increase in the Al/Mg ratios naturally occurs with increasing metamorphism because Mg diffuses out of the feldspar crystal structure at temperatures above 450 °C (LaTourrette and Wasserburg, 1998) and is either excluded from the crystal or forms tiny Mg-rich inclusions within the plagioclase crystal.

Details about the petrology and composition of plagioclase in fast-cooled H4 chondrites are lacking in the literature. Zinner and Göpel (2002) used mineral separates of plagioclase grains for their Al-Mg isotopic analyses. However, the petrographic context of these grains remains unknown. Because we used thin sections for our SIMS analyses and collected compositional data with the electron microprobe, we can provide some details on the composition and petrographic context of plagioclase grains in these chondrites. Plagioclase grains in Ste. Marguerite and Forest Vale are mainly found within chondrules (see Figures 5.2 and 5.5). They have a wide range in composition, An_4 to An_{77} and An_5 to An_{84}, respectively. The distributions appear to be bimodal (Figure 5.1). Grains with high An content (>50) are almost always associated with Na-rich plagioclase (see Figure 5.3). Plagioclase from Beaver Creek and Sena is fairly uniform in composition, ~An_{12} (Figure 5.1) and it is generally associated with isolated aggregates of olivine, metal and sulfide, and regions between chondrules (see Figures 5.7 and 5.9). We

find a wide range of $^{27}Al/^{24}Mg$ ratios (up to 10,000) for plagioclase in all of these chondrites, consistent with results from Zinner and Göpel (2002). The high abundance of Na-rich plagioclase and the high Al/Mg ratios compared to type 3 ordinary chondrites clearly indicate that much of the plagioclase in these H4 chondrites is secondary and metamorphic in origin and surviving primary plagioclase has been significantly affected by metamorphism, as Zinner and Göpel (2002) also reasoned.

Similar observations of the petrology and composition of plagioclase grains in H chondrites have been reported by Kovach and Jones (2010). They analyzed plagioclase in chondrules from Avanhandava (H4), Richardton (H5), and Nazareth (H6) and found that the composition of plagioclase from H chondrites is the same, regardless of the petrologic type of these chondrites. The average composition of plagioclase from their measurements is ~An_{12}, which is consistent with our results for Beaver Creek and Sena, but not consistent with results for Ste. Marguerite and Forest Vale. They also observed coexisting oligoclase and anorthite in one out of seven chondrules from Avanhandava (H4).

We analyzed ^{26}Al-^{26}Mg systematics for anorthite and oligoclase grains in Ste. Marguerite. Within the uncertainties, there is no obvious difference in their ages despite the different compositions. The presence of both forms of plagioclase in Ste. Marguerite and Forest Vale likely reflects the survival of primary, but altered, igneous plagioclase along with secondary oligoclase produced during metamorphism. Since the isochron for Ste. Marguerite includes both primary and secondary plagioclase, the ^{26}Al-^{26}Mg systematics for primary plagioclase has been completely reset. Diffusion of alkalis and Mg isotopes during slow cooling from metamorphic temperatures likely erased any

compositional heterogeneity from plagioclase in the other H chondrites like Beaver Creek and Sena, which have homogeneous plagioclase composition. This interpretation is consistent with Beaver Creek and Sena having lower $(^{26}Al/^{27}Al)_0$ than Ste. Marguerite and Forest Vale.

5.5.3 *Interpretation of the Isochron Data*

H chondrites are categorized into petrologic types (3 to 6), which are typically thought of as reflecting peak metamorphic temperatures. Early silicate thermometric studies indicated that peak temperatures for H chondrites increase systematically from type 4 to type 6, with peak temperatures of 600-700 °C for type 4 chondrites, 700-750 °C for type 5s, and 750-950 °C for type 6 chondrites (Dodd 1981). However, results from recent thermometric studies show that there is actually little difference between the peak temperatures of H chondrites of different petrologic types. Peak temperatures inferred from modeling Fe-Mg and Cr-Al exchange in coexisting Cr spinel and chromite grains range from 700 to 820 °C for H4-6 chondrites, with the average temperature for H4s at 766 °C (Wlotzka, 2005). Ganguly et al. (2013) inferred a similar range in peak temperatures for all H chondrites of 750-850 °C (750 °C for Forest Vale) based on compositional profiles across coexisting orthopyroxene-clinopyroxene, olivine-spinel, and orthopyroxene-spinel. An even smaller range in peak temperatures of 730-760 °C, with a maximum temperature for H4s of 730 °C, is inferred for H4-6 chondrites from Fe-Mg exchange between olivine-spinel mineral pairs (Kessel et al., 2007).

Dating the metamorphic cooling history of the H4 chondrites with the ^{26}Al-^{26}Mg system requires peak temperatures that were sufficiently high to equilibrate Mg isotopes and cooling rates that were sufficiently fast to freeze in the Al and Mg isotopes while ^{26}Al

was still alive. These conditions are necessary so that any excesses in ^{26}Mg only reflect the decay of ^{26}Al. If the chondrite does not experience any subsequent disturbances, the Al-Mg isotope data will produce a linear correlation between $^{26}Mg/^{24}Mg$ and $^{27}Al/^{24}Mg$ ratios on an isochron diagram. If the peak temperature was not high enough to equilibrate the Mg isotopes, ^{26}Mg excesses due to radiogenic ^{26}Mg from earlier in the meteorite's history may be preserved, resulting in a disturbed isochron. If the cooling time is too long, the Mg isotopes will equilibrate after the ^{26}Al has decayed, leaving no record of its presence.

Details about the thermal conditions necessary to preserve radiogenic ^{26}Mg in anorthite (An_{95}) are provided by LaTourrette and Wasserburg (1998), who carried out experiments to determine the self-diffusion coefficient of Mg in anorthite. They show that Mg in anorthite grains of 10, 50 and 250 μm will equilibrate with surrounding Mg-rich phases within 10^5 years at temperatures of 550 °C, 650 °C, and 750 °C, respectively (see Figure 5.6 in LaTourrette and Wasserburg, 1998). Below 450 °C, the approximate closure temperature, Mg in anorthite grains of these sizes will not exchange. The range in sizes of plagioclase grains analyzed for this study is similar to those studied by LaTourrette and Wasserburg. A recent study by Van Orman et al. (2014) shows that the Mg diffusion rate in plagioclase increases with decreasing anorthite content. The closure temperature for Mg diffusion in oligoclase can be up to 150 °C lower than that for anorthite. Different closure temperatures for Mg diffusion in oligoclase and anorthite are not reflected in different ^{26}Al-^{26}Mg cooling times for oligoclase and anorthite in Ste. Marguerite. The strong correlation between the $^{26}Mg/^{24}Mg$ and the $^{27}Al/^{24}Mg$ ratio for Ste. Marguerite (Figure 5.4) indicates that plagioclase in this chondrite experienced high

enough temperatures to homogenize Mg isotopes and that it cooled to ~450 °C sufficiently quickly to lock in the Mg isotopes and preserve evidence for ^{26}Al.

Although the inferred $(^{26}Al/^{27}Al)_0$ values for Ste. Marguerite, Forest Vale, and Beaver Creek are all resolved from zero, the isochrons may not all give chronological information. Plagioclase grains from Ste. Marguerite have the largest spread in $^{27}Al/^{24}Mg$ ratios (300 to 7000) and a clear correlation between excess ^{26}Mg and the Al/Mg ratio (MSWD ~1). The inferred $(^{26}Al/^{27}Al)_0$ of $(3.0\pm0.5)\times10^{-7}$ for Ste. Marguerite (Figure 5.4) indicates that plagioclase in this chondrite cooled to below the closure temperature for the Al-Mg system 5.2±0.2 Myr after CAIs or 4562.1±0.3 Ma (inferred from a U-corrected ^{207}Pb-^{206}Pb age of 4567.30±0.16 Ma for CAIs by Connelly et al., 2012). This is consistent with the ^{207}Pb-^{206}Pb cooling age of 4562.7±0.6 Ma based on analyses of phosphates from Ste. Marguerite (Göpel et al., 1994).

Isochrons for Forest Vale and Beaver Creek are not as straight-forward to interpret. Forest Vale gives an $(^{26}Al/^{27}Al)_0$ of $(1.5\pm0.7)\times10^{-7}$. The $^{27}Al/^{24}Mg$ ratios for plagioclase grains from Forest Vale (4000-10,000) are larger than the ratios from Ste. Marguerite. The average $^{26}Mg/^{24}Mg$ composition of the plagioclase grains in Forest Vale corresponds to a δ^{26}Mg value of ~8‰ (grey dashed line and grey bar in Figure 5.6), which is clear evidence for the former presence of ^{26}Al. However, when the Forest Vale plagioclase data are regressed by themselves, they give a slope of $(-0.5\pm3.0)\times10^{-7}$, which is unresolved from zero. This may be due to the large uncertainties on the $^{26}Mg/^{24}Mg$ ratios, but it may also reflect incomplete resetting of a former isochron. Although the Al-Mg systematics of Forest Vale may be disturbed, the inferred $(^{26}Al/^{27}Al)_0$ corresponds to 5.9

(+0.6/-0.4) Myr after CAIs, consistent with the ^{207}Pb-^{206}Pb phosphate age of 4560.9±0.7 Myr (Göpel et al., 1994).

The inferred $(^{26}Al/^{27}Al)_0$ for Beaver Creek is $(0.9\pm0.7)\times10^{-7}$ (Figure 5.8), which corresponds to a time of 6.5 (+1.7/-0.6) Myr after CAIs. This isochron is difficult to interpret chronologically because the plagioclase grains have a very limited range in $^{27}Al/^{24}Mg$ ratios (~3000) and Mg-isotope ratios. Here, we have effectively a two-point isochron with a slope that is barely resolved from zero. Isotopic disturbance, if present, is masked by the large measurement uncertainties and the limited range in $^{27}Al/^{24}Mg$.

The $(^{26}Al/^{27}Al)_0$ for Sena is $<0.3\times10^{-7}$ (Figure 5.10). The $^{27}Al/^{24}Mg$ ratio in plagioclase from Sena ranges from 7000 to 10,000, but the Mg-isotope ratios for all the grains are consistent with the terrestrial value. The 2σ upper limit on the isochron slope indicates that Sena cooled to below the Mg closure temperature ≥8 Myr after CAIs, which agrees with the ^{207}Pb-^{206}Pb phosphate age of 4556±0.1 Myr for Sena reported by Trieloff et al. (2003). The Al-Mg data for Sena are consistent with those for Quenggouk, an H4 chondrite with a similar cooling rate (Zinner and Göpel, 2002; Scott et al., 2014).

In summary, the ^{26}Al-^{26}Mg systematics of Ste. Marguerite indicate that this chondrite experienced sufficiently high temperatures to equilibrate the Mg isotopes in plagioclase and that it cooled to below ~450 °C at 5.2±0.2 Myr after CAIs. Sena cooled to below the closure temperature ≥8 Myr after CAIs. Interpretation of isochrons for Forest Vale and Beaver Creek is ambiguous given the large uncertainties on the $^{26}Mg/^{24}Mg$ ratios; but, the ^{26}Al-^{26}Mg data provide clear evidence for live ^{26}Al in these chondrites.

5.5.4 *Comparison with Cooling Rate Data*

Cooling rates of H chondrites have been principally determined from ^{244}Pu fission track and metallographic studies. Fission track studies compare cooling ages based on ^{244}Pu fission track densities in adjacent phosphate and pyroxene crystals, which have closure temperatures of 280 °C to 120 °C, respectively. Cooling rates from ^{244}Pu-fission-track data from Trieloff et al. (2003) indicate that Ste. Marguerite, Forest Vale and Beaver Creek cooled from 280 °C to 120 °C at rates >20 °C/Myr, faster than H5s and H6s, which cooled at ~3 °C/Myr. Metallographic cooling rates are determined from diffusion models of Ni compositional profiles across coexisting taenite and kamacite grains. They record cooling to below a higher temperature of 500 °C. Cooling rates for H4 chondrites from metallographic studies are mostly consistent with estimates from fission track analyses. They indicate that almost all H chondrites cooled to below 500 °C at rates of 10-50 °C/Myr (Taylor et al., 1987; Krot et al., 2012; Scott et al., 2014). The only exceptions are H4 chondrites Ste. Marguerite, Forest Vale and Beaver Creek, which metallographic studies indicate cooled at >5000 °C/Myr (Taylor et al., 1987; Krot et al., 2012; Scott et al., 2014).

The ^{26}Al-^{26}Mg ages of Ste. Marguerite, Forest Vale and Beaver Creek also indicate rapid cooling to below the Al-Mg closure temperature for plagioclase at 5-7 Myr after CAIs (Zinner and Göpel, 2002; this study). Ste. Marguerite has the highest initial ^{26}Al/^{27}Al ratio, $(^{26}Al/^{27}Al)_0$, of these three, followed by Forest Vale, then Beaver Creek. This is consistent with the metallographic cooling rates of these chondrites that indicate Ste. Marguerite cooled at >10,000 °C/Myr, Forest Vale at ~10,000 °C/Myr, and Beaver Creek cooled at ~5,000 °C/Myr (Taylor et al., 1987; Krot et al., 2012; Scott et al., 2014). The ^{26}Al-^{26}Mg ages of H4 chondrites Sena (from this study) and Quenggouk (Zinner and

Göpel, 2002) do not show evidence for the former presence of ^{26}Al. Sena and Quenggouk require >8 Myr after CAIs to cool below the Al-Mg closure temperature. The differences in the $(^{26}Al/^{27}Al)_0$ inferred for Ste. Marguerite, Forest Vale and Beaver Creek, and those inferred for Sena and Quenggouk, are consistent with cooling rates from metallographic studies, that indicate Ste. Marguerite, Forest Vale and Beaver Creek cooled to below 500 °C at rates exceptionally higher than most H4 chondrites.

5.5.5 *Thermal Evolution of the H Chondrite Parent Body*

Thermal-evolution models help to constrain the size and structure of the H chondrite parent body. These models generally assume that the H chondrite parent body was internally heated by the energy from the decay of ^{26}Al and that it accreted 2-3 Myr after CAIs. Model constraints on the accretion time are mainly from the $(^{26}Al/^{27}Al)_0$ ratio necessary to reach the peak temperature of H6 chondrites, which corresponds to ~2 Myr after CAIs (Miyamoto et al., 1981; Bennett and McSween, 1996). This time frame is consistent with the ages of chondrules from unequilibrated ordinary chondrites (Kita et al., 2000; Connelly et al., 2012), which must have formed prior to the accretion of the chondrite parent bodies. The 3 Myr upper limit is from the ^{207}Pb-^{206}Pb ages of chondrules from Ste. Marguerite (Göpel et al., 1994; Bouvier et al., 2007). Assuming that all H chondrites originate from the same body, their peak temperatures provide constraints on their depth of cooling within the parent body and their cooling ages constrain the duration of cooling within the parent body. The high peak temperature of >750 °C for H6 chondrites (Dodd 1981) constrains the size of the parent body to ~100 km (e.g., Miyamoto et al., 1981; Bennett and McSween, 1996; Harrison and Grimm, 2010; Henke et al., 2012). Their ^{207}Pb-^{206}Pb cooling ages require >60 Myr of cooling to below the Pb-

Pb closure temperature of ~450 °C within the parent body (Göpel et al., 1994; Bouvier et al. 2007). These numerical models support the onion-shell model, which proposes that the H chondrite parent asteroid cooled, undisturbed by major impacts, to form concentric layers where the most metamorphosed type 6 chondrites cooled at the center of the asteroid and the least metamorphosed type 3 chondrites cooled at the surface (Pellas and Storzer, 1981).

One of the testable predictions of the onion-shell model is that the cooling rates of H chondrites should decrease with increasing petrologic type. Trieloff et al., (2003) and Kleine et al. (2008) combined cooling ages from ^{40}Ar-^{39}Ar, ^{207}Pb-^{206}Pb, ^{182}Hf-^{182}W and ^{244}Pu fission tracks to constrain the cooling rates of H chondrites. These studies find an inverse correlation between cooling ages and petrologic types of H chondrites, providing substantial support for the onion-shell model. Cooling rates of H chondrites within the parent body are then estimated by modifying thermal evolution models of asteroids (e.g., Miyamoto et al., 1981) so that the model results are consistent with the cooling ages. They find that Ste. Marguerite and Forest Vale chondrites cooled to below 120 °C (the ^{244}Pu fission track closure temperature) at a rate of ~50 °C/Myr over ~10 Myr at ~7 km depth within a parent body ~50-100 km in radius (Trieloff et al., 2003; Kleine et al., 2008). Sena, which is classified as an H4 by Van Schmus and Wood (1967), but as an H5 by Trieloff et al. (2003), is found to have cooled to below 120 °C at depths of 16-23 km over at least 75 Myr. Metallographic studies, however, find that cooling rates for all types of H chondrites overlap and do not correlate significantly with metamorphic grade, contrary to the onion-shell model's prediction (Taylor et al., 1987; Scott et al., 2014). Scott et al. (2014) compared the metallographic cooling rates to numerical models of

cooling at 500 °C within a parent body 50-100 km in radius. They show that the cooling rates for Ste. Marguerite, Forest Vale, and Beaver Creek are too high for cooling at the depths estimated by Trieloff et al. (2003) and Kleine et al. (2008). However, the cooling rates of many other H4 chondrites, like Sena and Quenggouk, are more consistent with cooling at these depths. These observations indicate that all H4 chondrites cannot be understood in terms of a simple onion-shell model, consistent with the conclusions of previous workers (e.g., Scott and Rajan, 1981; Taylor et al., 1987; Ganguly et al., 2013; Scott et al., 2014).

Analyses of Ste. Marguerite, Forest Vale and/or Beaver Creek are widely used to estimate the cooling history of all H4 chondrites (e.g., Pellas and Storzer, 1981; Trieloff et al., 2003; Kleine et al., 2008; Ganguly et al., 2013). Figure 5.11 shows heating and cooling of H chondrites within an onion-shell parent body that accreted instantaneously ~2 Myr after CAIs to a size of ~100 km in radius (from Figure 5.2 of Harrison and Grimm, 2010). It shows that H4 chondrites reach peak temperature ~5 Myr after CAIs and require a minimum of ~10 Myr after CAIs to cool below the closure temperature of Mg isotopes in plagioclase (dashed horizontal line). The upper limits on the $(^{26}Al/^{27}Al)_0$ ratios of Sena and Quenggouk indicate that they cooled to below the closure temperature of Mg isotopes in anorthite more than 8 Myr after CAIs (vertical solid line in Figure 5.11). This is consistent with undisturbed cooling of H4 chondrites within an onion-shell parent body ~100 km in radius (dashed arrow; white star in Figure 5.11). However, the ^{26}Al-^{26}Mg ages of Ste. Marguerite, Forest Vale and Beaver Creek require cooling to below the closure temperature 5.2±0.2, 5.9 (+0.6/-0.4), and 6.5 (+1.7/-0.6) Myr after CAIs, respectively, earlier than the time required for undisturbed cooling within the

parent body. This indicates that any rock that cooled undisturbed at the depths and at the cooling rates indicated by the onion-shell model would cool to below the closure temperature of Mg isotopes in plagioclase too slowly to preserve evidence for the former presence of ^{26}Al. The ^{26}Al-^{26}Mg systematics and the metallographic cooling rates of H4 chondrites indicate that Ste. Marguerite, Forest Vale and Beaver Creek experienced a thermal history distinctly different from most H4 chondrites.

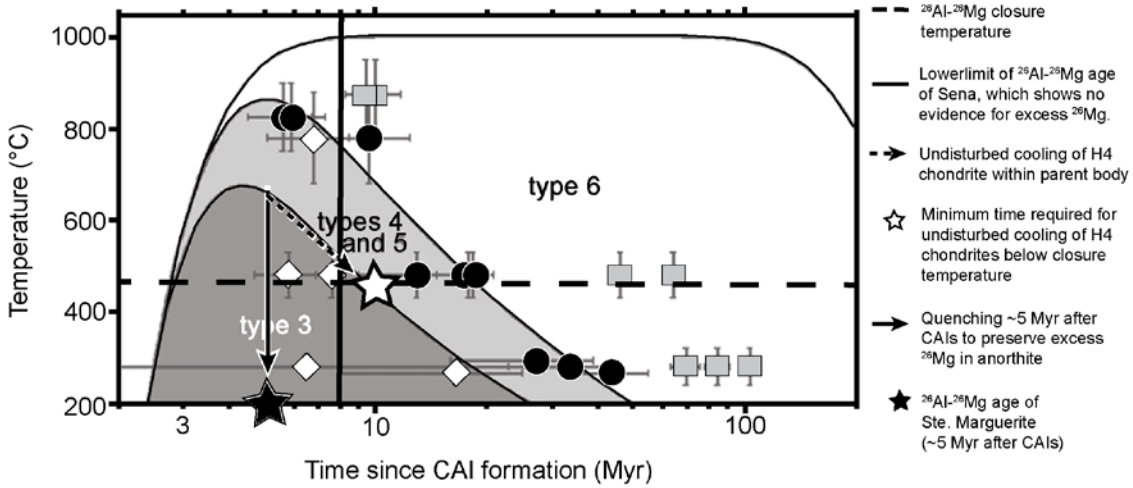

Figure 5.11. This modified version of Figure 5.2 from Harrison and Grimm (2010) compares the ^{40}Ar-^{39}Ar, ^{207}Pb-^{206}Pb, and ^{182}Hf-^{182}W cooling ages of H4-6 chondrites (diamonds are H4s, circles are H5s, and squares are H6s) to the calculated heating and cooling curves of H chondrites within a ~100 km radius parent body that accreted 2.2 Myr after CAIs. This figure schematically illustrates that the ^{26}Al-^{26}Mg systematics of Ste. Marguerite, Forest Vale, and Beaver Creek cannot be explained by undisturbed cooling within an onion-shell parent body. Cooling below the closure temperature (dashed horizontal line) while ^{26}Al is extant is required to preserve excess ^{26}Mg in anorthite. The unresolved $(^{26}Al/^{27}Al)_0$ ratios of Sena and Quenggouk indicate that if chondrites in the H chondrite parent body cooled more than ~8 Myr after CAIs, they do not preserve resolvable evidence for ^{26}Al (vertical solid line). However, cooling of H4 chondrites within the onion-shell parent body requires a minimum of ~10 Myr after CAIs to reach the ^{26}Al-^{26}Mg closure temperature (dashed arrow; white star). In order for Ste. Marguerite to have an Al-Mg age of 5.2±0.2 Myr after CAIs in this scenario, it must have been extracted from its parent body and quenched. This also applies for Forest Vale and Beaver Creek, which are not shown on this diagram. Impact excavation is indicated.

The rapid cooling of Ste. Marguerite, Forest Vale and Beaver Creek can be made consistent with an onion-shell model if an impact exhumed them from the depth at which they formed and placed them near the surface of the parent body, as proposed by various studies (e.g., Akridge et al., 1998; Scott et al., 2010; Harrison and Grimm, 2010; Ciesla et al., 2013). The exact depth within the parent body that these chondrites formed is not critical. The time scale for heating to and cooling from the peak temperature of H4 chondrites within the parent body that allows for preservation of excess ^{26}Mg from the decay of ^{26}Al is the key point here. The ^{26}Al-^{26}Mg systematics of Ste. Marguerite and its rapid metallographic cooling rate of >10,000 °C/Myr suggest that it formed at ~7 km depth within the parent body for homogenization of Mg in anorthite, but was excavated 5.2±0.2 Myr after CAIs, allowing it to quench and freeze in the Mg isotopes in anorthite (solid arrow and black star in Figure 5.11). Forest Vale and Beaver Creek also require excavation and rapid cooling to below the closure temperature to preserve evidence for excess ^{26}Mg within anorthite. However, their $(^{26}Al/^{27}Al)_0$ ratios require slightly longer cooling times of 5.9 (+0.6/-0.4) and 6.5 (+1.7/-0.6) Myr after CAIs, respectively. The differences in the $(^{26}Al/^{27}Al)_0$ ratios and metallographic cooling rates of Ste. Marguerite, Forest Vale and Beaver Creek are consistent with excavation at different times or burial near the surface at increasing depths after a single excavation from the parent body. With the large uncertainties on the ^{26}Mg/^{24}Mg ratios for Forest Vale and Beaver Creek it is also possible that the lower $(^{26}Al/^{27}Al)_0$ ratios are due to a reheating event after excavation that disturbed the original isochrons. Sena and Quenggouk require formation at depth for homogenization of Mg in anorthite, but they do not require impact excavation. Their metallographic cooling rates of 10-50 °C/Myr and the lack of evidence for ^{26}Al when

they cooled are consistent with undisturbed cooling within a parent body 100 km in radius. Other mechanisms for rapid cooling can potentially explain the preservation of ^{26}Mg excess in anorthite and the rapid metallographic cooling rates for Ste. Marguerite, Forest Vale and Beaver Creek (e.g., Scott and Rajan, 1981; Taylor et al., 1987; Ganguly et al., 2013), but it is clear that these fast-cooled H4 chondrites did not cool within an onion-shell asteroid and that the ^{26}Al data for these chondrites do not provide a constraint on the cooling history of that asteroid. Instead ^{26}Al-^{26}Mg systematics of Ste. Marguerite, Forest Vale and Beaver Creek date rapid cooling near the surface of the parent-body, likely due to impact excavation of these chondrites.

5.6 Conclusions

We used the ion microprobe to analyze the Al-Mg isotopic composition of plagioclase from thin sections of H4 chondrites to assess the influence of ratio bias in published data and to reevaluate the initial interpretation of these measurements. We inferred $(^{26}Al/^{27}Al)_0$ ratios of $(3.0\pm0.5)\times10^{-7}$, $(1.5\pm0.7)\times10^{-7}$, and $(0.9\pm0.7)\times10^{-7}$ for Ste. Marguerite, Forest Vale, and Beaver Creek, respectively (Figures 5.4, 5.6, and 5.8). Our results are consistent with those previously reported by Zinner and Göpel (2002), indicating that there is no significant issue with ratio bias in these datasets. These chondrites cooled to below the ^{26}Al-^{26}Mg closure temperature at 5-7 Myr after CAIs. Sena has an $(^{26}Al/^{27}Al)_0$ ratio of $<0.3\times10^{-7}$ (Figures 5.10), consistent with results for Quenggouk (Zinner and Göpel, 2002). Cooling to below the closure temperature for Sena and Quenggouk required more than 8 Myr after CAIs.

The ^{26}Al-^{26}Mg systematics of plagioclase from Ste. Marguerite, Forest Vale, and Beaver Creek require high temperatures for metamorphic resetting of Mg isotopes in plagioclase, but also cooling below the Al-Mg closure temperature while ^{26}Al was extant. However, the cooling time of H4 chondrites in an onion-shell parent body ~100 km in radius is much longer than the lifetime of ^{26}Al, indicating that H4 chondrites that cooled undisturbed in an onion-shell parent body would not preserve evidence for live ^{26}Al (Figure 5.11). We conclude that Ste. Marguerite, Forest Vale and Beaver Creek did not cool within an onion-shell parent body, as assumed by previous studies, and that the ^{26}Al-^{26}Mg systematics of these chondrites do not constrain the cooling history of the H chondrite parent body. A model for the H chondrite parent body that allows for both high peak temperatures and rapid cooling of Ste. Marguerite, Forest Vale, and Beaver Creek involves impact excavation of these chondrites from the region of the parent asteroid where the H4 chondrites were forming, as some studies have already proposed.

CHAPTER 6. **CONCLUSIONS**

The work presented in this dissertation represents a comprehensive effort to understand the ^{60}Fe-^{60}Ni systematics of chondrules in order to constrain the initial ^{60}Fe/^{56}Fe ratio of the solar system, which has important implications for understanding the environment of solar system formation, constraining the source of short-lived radionuclides and dating early solar system events. We collected *in situ* ion microprobe analyses of the Fe and Ni isotopic composition of chondrule olivine and pyroxene from unequilibrated ordinary chondrites, UOCs (Chapter 2). We focused our analyses on these samples primarily because UOCs are the least metamorphosed chondrites. We were looking for excesses in ^{60}Ni that correlate with the Fe/Ni ratio to constrain the initial ^{60}Fe/^{56}Fe for UOCs, which can then be used to calculate the initial solar system ratio.

We found that only a few chondrules have resolved excesses in ^{60}Ni and the correlation with the Fe/Ni ratio is poor, indicating that the Fe-Ni isotopic system was disturbed (Chapter 2). To evaluate the degree of this disturbance, we collected synchrotron X-ray fluorescence (XRF) maps of Fe, Ni and other elements in UOC chondrules (Chapter 3; Telus et al., 2015a). The XRF maps show enrichments of Fe and/or Ni along chondrule fractures, indicating that late-stage open-system redistribution of Fe and Ni is the likely source of the poorly correlated *in situ* data and the source for the discrepancies in the initial ratios inferred from bulk and *in situ* analyses. Ratio bias, which produced erroneous results in previous published SIMS studies, should not be an issue here because isotope ratios were calculated using total counts (Chapter 4; Telus et al., 2012a). Despite the complications from Fe-Ni mobilization in UOCs, we show that the initial ^{60}Fe/^{56}Fe ratio of UOCs is likely between 0.5×10^{-7} and 2.6×10^{-7} (Chapter 2).

Appropriate sample selection is critical for further progress in developing the ^{60}Fe-^{60}Ni for early solar system chronology. Given the pervasiveness of Fe-Ni mobilization in UOCs, it is appears that these samples may not be suitable for constraining the initial solar system ratio. For now, it is not clear which samples have escaped this alteration. Synchrotron XRF mapping is currently the best approach for characterizing samples prior to isotopic analyses. It provides the resolution and sensitivity necessary for mapping Ni in olivine and pyroxene. It also provides 3-dimensional information that other techniques do not readily provide. Finally, it is a very efficient approach, allowing for dozens of chondrules to be thoroughly characterized in 1-2 days.

Finally, this dissertation also includes a study on the ^{26}Al-^{26}Mg systematics of plagioclase from H4 chondrites and the implications for the onion shell parent body (Chapter 5; Telus et al., 2014a). This work stems directly from the study on ratio bias (Chapter 4). Plagioclase in these chondrites can have very high Al/Mg ratios and low Mg concentrations, making these ion probe analyses susceptible to ratio bias. Additionally, previous results by Zinner and Göpel (2002) were calculated using the mean of the ratios. We calculated the isotope ratios using total counts, a less-biased method of calculating isotope ratios. The data are consistent with the previous results, indicating that ratio bias is not significant for this dataset. We argue that ^{26}Al-^{26}Mg ages of fast-cooled H4 chondrites are inconsistent with undisturbed cooling at depth within an onion shell structured parent body. Instead, they likely date impact excavation and cooling at the surface of the parent body.

APPENDIX A. **SYNTHETIC PYROXENE STANDARDS & FE-NI SIMS CHONDRULE DATA**

Table Appendix A.1. Composition of synthetic pyroxene standards[1,2]

Name	SiO_2	Al_2O_3	MgO	Cr_2O_3	NiO	TiO_2	FeO	MnO	CaO
JHpx1	53.54	1.90	28.09	0.80	0.03	0.01	13.33	0.31	0.33
JHpx2	54.61	1.70	28.85	0.72	0.03	0.28	12.82	0.28	1.79

[1] Averaged from electron probe analyses (20 nA, 15keV)

[2] Synthesis technique: Both held at 85 degrees above computed liquidus (1426 ^{o}C at QFM-1) for ~20 minutes after long, slow ramp (120 ^{o}C/h) to setpoint. The fO_2 maintained at QFM-1 starting about 50 minutes after insertion (corresponding to 1050 ^{o}C), in both cases.

Table Appendix A.2. Fe-Ni SIMS data for each chondrule are listed below in order of appearance in Table 2.1

SMK312B-E

Mineral	$^{56}Fe/^{61}Ni$ ($\times10^6$)	± 2σ	$^{60}Ni/^{61}Ni$	± 2σ	$^{56}Fe/^{62}Ni$ ($\times10^6$)	± 2σ	$^{60}Ni/^{62}Ni$	± 2σ
pyx	0.504	0.025	22.896	0.381	0.158	0.008	7.177	0.200
	0.457	0.023	23.267	0.288	0.142	0.007	7.297	0.148
	0.379	0.019	22.875	0.319	0.120	0.006	7.176	0.168
	0.409	0.020	22.812	0.260	0.129	0.006	7.156	0.137
	0.869	0.043	23.209	0.573	0.268	0.013	7.276	0.293
	0.987	0.049	23.164	0.547	0.306	0.015	7.249	0.280
	0.361	0.018	22.830	0.421	0.114	0.006	7.156	0.222
	0.503	0.025	23.209	0.395	0.158	0.008	7.279	0.207
	0.456	0.023	23.376	0.417	0.141	0.007	7.322	0.213
	0.453	0.023	22.840	0.415	0.143	0.007	7.155	0.219
	0.756	0.038	22.697	0.527	0.237	0.012	7.111	0.277
	1.026	0.051	23.682	0.507	0.316	0.016	7.437	0.258
	0.821	0.041	22.439	0.541	0.260	0.013	7.039	0.287

	0.595	0.030	22.632	0.480	0.189	0.009	7.101	0.257
	0.491	0.025	22.821	0.341	0.155	0.008	7.150	0.180
	0.568	0.028	22.881	0.278	0.178	0.009	7.177	0.145
	0.620	0.031	23.259	0.512	0.192	0.010	7.282	0.263
	0.610	0.031	22.837	0.406	0.193	0.010	7.160	0.216
	0.528	0.026	23.416	0.287	0.165	0.008	7.343	0.147
	0.357	0.018	22.705	0.387	0.113	0.006	7.115	0.206
	0.453	0.023	22.989	0.344	0.143	0.007	7.213	0.182
	0.436	0.022	22.830	0.385	0.138	0.007	7.163	0.203
	0.628	0.031	22.861	0.553	0.197	0.010	7.164	0.290
	0.647	0.032	22.554	0.415	0.206	0.010	7.069	0.222
	1.158	0.058	23.081	0.637	0.360	0.018	7.232	0.329
	0.829	0.041	22.841	0.587	0.262	0.013	7.170	0.310
	0.890	0.044	22.484	0.495	0.284	0.014	7.044	0.267
	0.876	0.044	22.978	0.402	0.275	0.014	7.208	0.211
olv	0.206	0.001	23.061	0.275	0.065	0.003	7.229	0.143
	0.208	0.001	23.082	0.228	0.065	0.003	7.238	0.119
	0.205	0.001	22.718	0.174	0.065	0.003	7.124	0.092
	0.226	0.001	23.348	0.287	0.070	0.003	7.323	0.146
	0.223	0.001	22.937	0.228	0.070	0.004	7.187	0.120
	0.217	0.001	23.073	0.166	0.068	0.003	7.234	0.086
	0.192	0.010	23.000	0.084	0.061	0.003	7.215	0.044

SMK312B-Q

Mineral	$^{56}Fe/^{61}Ni$ ($\times10^6$) ± 2σ		$^{60}Ni/^{61}Ni$ ± 2σ		$^{56}Fe/^{62}Ni$ ($\times10^6$) ± 2σ		$^{60}Ni/^{62}Ni$ ± 2σ	
pyx	0.380	0.019	22.824	0.937	0.120	0.006	7.163	0.495
	0.593	0.030	22.711	1.038	0.185	0.009	7.120	0.541
	0.360	0.018	23.230	0.592	0.113	0.006	7.271	0.307
	0.292	0.015	23.193	0.671	0.091	0.005	7.263	0.345
	0.395	0.020	23.088	0.678	0.124	0.006	7.242	0.354
	0.367	0.018	22.691	0.637	0.116	0.006	7.114	0.337
	0.475	0.024	22.547	0.910	0.149	0.007	7.068	0.477
	0.474	0.024	22.478	0.744	0.150	0.008	7.045	0.397

	0.106	0.005	22.885	0.456	0.034	0.002	7.182	0.240
	0.300	0.015	23.647	0.776	0.092	0.005	7.396	0.390
	0.358	0.018	22.899	0.893	0.112	0.006	7.174	0.467
	0.379	0.019	22.956	0.734	0.119	0.006	7.199	0.383
	0.273	0.014	22.933	0.580	0.086	0.004	7.191	0.305
	0.434	0.022	22.847	0.855	0.136	0.007	7.159	0.449
	0.416	0.021	22.579	0.759	0.132	0.007	7.084	0.406
	0.361	0.018	22.623	0.636	0.114	0.006	7.093	0.338
	0.455	0.023	22.648	1.007	0.143	0.007	7.102	0.530
	0.419	0.021	22.759	0.800	0.133	0.007	7.135	0.425
	0.371	0.019	22.918	1.012	0.116	0.006	7.189	0.527
	0.407	0.020	22.565	0.955	0.129	0.006	7.070	0.506
	0.202	0.010	22.636	0.609	0.064	0.003	7.097	0.321
	0.422	0.021	23.223	0.871	0.131	0.007	7.278	0.449
	0.337	0.017	22.675	0.823	0.107	0.005	7.101	0.438
	0.292	0.015	22.951	0.522	0.092	0.005	7.197	0.273
	0.369	0.018	23.262	0.838	0.114	0.006	7.297	0.428
	0.377	0.019	23.057	0.702	0.119	0.006	7.242	0.371
	0.262	0.013	22.631	0.517	0.083	0.004	7.092	0.275
olv	0.110	0.006	23.026	0.186	0.034	0.002	7.222	0.097
	0.111	0.006	22.819	0.156	0.035	0.002	7.152	0.082
	0.166	0.008	22.906	0.264	0.052	0.003	7.182	0.138
	0.168	0.008	22.994	0.213	0.053	0.003	7.205	0.112
FeS	0.213	0.011	22.990	0.184	0.067	0.003	7.227	0.096
	0.228	0.011	23.131	0.171	0.072	0.004	7.257	0.089

SMK1805-T

Mineral	$^{56}Fe/^{61}Ni$ ($\times 10^6$) ± 2σ		$^{60}Ni/^{61}Ni$ ± 2σ		$^{56}Fe/^{62}Ni$ ($\times 10^6$) ± 2σ		$^{60}Ni/^{62}Ni$ ± 2σ	
pyx	0.354	0.018	22.969	0.383	0.112	0.006	7.205	0.201
	0.346	0.017	23.037	0.296	0.109	0.005	7.222	0.154
	0.312	0.016	22.988	0.291	0.098	0.005	7.209	0.153
	0.368	0.018	22.973	0.365	0.115	0.006	7.202	0.190
	0.372	0.019	23.045	0.295	0.116	0.006	7.228	0.154

0.334	0.017	22.985	0.262	0.105	0.005	7.207	0.137
0.338	0.017	22.465	0.338	0.108	0.005	7.043	0.181
0.356	0.018	22.706	0.284	0.113	0.006	7.118	0.152
0.270	0.014	22.987	0.265	0.085	0.004	7.207	0.139
0.339	0.017	23.079	0.360	0.105	0.005	7.235	0.186
0.318	0.016	22.753	0.284	0.100	0.005	7.146	0.149
0.345	0.017	22.544	0.336	0.109	0.005	7.071	0.179
0.350	0.018	22.834	0.285	0.110	0.006	7.163	0.151
0.280	0.014	22.915	0.268	0.088	0.004	7.187	0.140
0.708	0.035	22.614	0.401	0.223	0.011	7.091	0.212
0.760	0.038	22.677	0.358	0.240	0.012	7.107	0.189
0.668	0.033	23.050	0.332	0.208	0.010	7.228	0.171
0.365	0.018	22.633	0.367	0.115	0.006	7.099	0.194
0.365	0.018	22.997	0.292	0.114	0.006	7.218	0.152
0.318	0.016	23.110	0.273	0.100	0.005	7.248	0.142
0.394	0.020	23.062	0.325	0.123	0.006	7.229	0.168
0.446	0.022	22.892	0.299	0.140	0.007	7.180	0.157
0.403	0.020	23.161	0.357	0.125	0.006	7.267	0.185
0.574	0.029	22.439	0.376	0.182	0.009	7.026	0.200
0.562	0.028	22.976	0.331	0.176	0.009	7.206	0.174
0.469	0.023	23.066	0.301	0.147	0.007	7.237	0.157
0.398	0.020	22.822	0.321	0.125	0.006	7.150	0.168
0.448	0.022	22.860	0.303	0.141	0.007	7.164	0.159
0.401	0.020	22.954	0.288	0.126	0.006	7.198	0.151
0.994	0.050	22.884	0.671	0.312	0.016	7.175	0.352
0.926	0.046	22.053	0.712	0.298	0.015	6.901	0.391
0.560	0.028	22.812	0.381	0.175	0.009	7.160	0.199
0.627	0.031	22.990	0.342	0.196	0.010	7.211	0.178
0.559	0.028	23.059	0.344	0.176	0.009	7.234	0.180
0.515	0.026	23.001	0.397	0.161	0.008	7.215	0.206
0.584	0.029	22.923	0.342	0.183	0.009	7.187	0.179
0.536	0.027	23.284	0.354	0.167	0.008	7.307	0.183
0.417	0.021	22.682	0.330	0.131	0.007	7.115	0.174
0.439	0.022	22.879	0.282	0.138	0.007	7.169	0.148
0.389	0.019	23.147	0.274	0.121	0.006	7.258	0.142
0.562	0.028	22.727	0.369	0.176	0.009	7.128	0.194
0.467	0.023	23.740	0.285	0.144	0.007	7.445	0.144

	0.576	0.029	22.756	0.380	0.182	0.009	7.133	0.200
	0.505	0.025	22.813	0.349	0.158	0.008	7.239	0.183
	0.560	0.028	22.753	0.378	0.177	0.009	7.134	0.200
	0.740	0.037	23.108	0.392	0.233	0.012	7.246	0.206
	0.732	0.037	22.581	0.584	0.231	0.012	7.084	0.310
	0.124	0.006	23.049	0.206	0.039	0.002	7.251	0.108
	0.431	0.022	22.535	0.385	0.136	0.007	7.064	0.205
	0.489	0.024	22.769	0.321	0.154	0.008	7.138	0.169
	0.422	0.021	23.035	0.300	0.132	0.007	7.223	0.157
olv	0.170	0.008	22.803	0.205	0.054	0.003	7.150	0.108
	0.175	0.009	22.863	0.169	0.055	0.003	7.166	0.089
	0.176	0.009	23.041	0.151	0.055	0.003	7.227	0.079

SMKMT r1

Mineral	$^{56}Fe/^{61}Ni$ ($\times10^6$) ± 2σ		$^{60}Ni/^{61}Ni$ ± 2σ		$^{56}Fe/^{62}Ni$ ($\times10^6$) ± 2σ		$^{60}Ni/^{62}Ni$ ± 2σ	
pyx	0.296	0.015	23.016	0.127	0.093	0.005	7.218	0.062
	0.051	0.003	23.007	0.043	0.016	0.001	7.215	0.021
	0.226	0.011	23.010	0.062	0.071	0.004	7.216	0.030
	0.253	0.013	22.958	0.077	0.079	0.004	7.200	0.037
	0.254	0.013	23.093	0.074	0.079	0.004	7.242	0.036
	0.120	0.006	23.067	0.055	0.038	0.002	7.234	0.027
	0.318	0.016	23.082	0.086	0.100	0.005	7.239	0.042
	0.187	0.009	22.910	0.059	0.059	0.003	7.185	0.029

DAP1 Sept2011

Mineral	$^{56}Fe/^{61}Ni$ ($\times10^6$) ± 2σ		$^{60}Ni/^{61}Ni$ ± 2σ		$^{56}Fe/^{62}Ni$ ($\times10^6$) ± 2σ		$^{60}Ni/^{62}Ni$ ± 2σ	
pyx	1.646	0.082	23.461	0.169	0.513	0.026	7.357	0.081
	0.875	0.044	23.556	0.246	0.273	0.014	7.386	0.117
	0.416	0.021	23.206	0.103	0.131	0.007	7.278	0.050
	0.051	0.003	23.167	0.054	0.016	0.001	7.266	0.026

	0.342	0.017	23.416	0.070	0.107	0.005	7.343	0.033
	0.813	0.041	23.299	0.104	0.255	0.013	7.307	0.050
	0.343	0.017	23.144	0.077	0.108	0.005	7.258	0.037
	0.257	0.013	23.287	0.067	0.081	0.004	7.303	0.032
	0.632	0.032	23.557	0.105	0.197	0.010	7.387	0.050
	0.951	0.048	23.539	0.127	0.296	0.015	7.381	0.061
	0.453	0.023	23.479	0.088	0.142	0.007	7.363	0.042
	0.829	0.041	23.112	0.114	0.261	0.013	7.248	0.055
	0.920	0.046	23.246	0.129	0.288	0.014	7.290	0.062
	0.496	0.025	23.472	0.086	0.155	0.008	7.360	0.041
	0.693	0.035	23.191	0.105	0.203	0.010	7.262	0.057
	0.475	0.024	23.393	0.103	0.149	0.007	7.336	0.050
	1.097	0.055	23.371	0.138	0.343	0.017	7.329	0.066
	0.851	0.043	23.155	0.122	0.268	0.013	7.262	0.059
	0.007	0.000	23.115	0.067	0.002	0.000	7.249	0.033

DAP1 July2010

Mineral	$^{56}Fe/^{61}Ni$ ($\times 10^6$) ± 2σ		$^{60}Ni/^{61}Ni$ ± 2σ		$^{56}Fe/^{62}Ni$ ($\times 10^6$) ± 2σ		$^{60}Ni/^{62}Ni$ ± 2σ	
pyx	0.303	0.015	23.138	0.195	0.095	0.005	7.256	0.094
	0.136	0.007	23.136	0.135	0.043	0.002	7.255	0.065
	0.134	0.007	22.869	0.160	0.042	0.002	7.172	0.078
	0.137	0.007	23.047	0.145	0.043	0.002	7.228	0.070
	1.837	0.092	23.316	0.503	0.574	0.029	7.312	0.241
	3.112	0.156	22.676	0.647	0.985	0.049	7.110	0.319
	0.174	0.009	22.704	0.166	0.055	0.003	7.119	0.082
	0.199	0.010	22.895	0.150	0.063	0.003	7.180	0.073
	0.479	0.024	22.742	0.232	0.152	0.008	7.131	0.114
	0.143	0.007	22.956	0.132	0.045	0.002	7.199	0.064
	0.422	0.021	23.275	0.225	0.132	0.007	7.299	0.108
	0.379	0.019	22.864	0.210	0.120	0.006	7.170	0.102
	1.168	0.058	23.447	0.415	0.365	0.018	7.353	0.199
	5.010	0.250	22.784	0.826	1.588	0.079	7.145	0.405
	0.225	0.011	22.885	0.197	0.071	0.004	7.177	0.096
	1.310	0.066	23.405	0.416	0.411	0.021	7.340	0.199

	0.856	0.043	23.137	0.339	0.269	0.013	7.256	0.164
	0.297	0.015	22.949	0.193	0.094	0.005	7.197	0.094
	1.277	0.064	22.945	0.373	0.404	0.020	7.196	0.182
	0.525	0.026	23.027	0.255	0.165	0.008	7.221	0.124

DAP1 March2010

Mineral	$^{56}Fe/^{61}Ni$ ($\times 10^6$) ± 2σ		$^{60}Ni/^{61}Ni$ ± 2σ		$^{56}Fe/^{62}Ni$ ($\times 10^6$) ± 2σ		$^{60}Ni/^{62}Ni$ ± 2σ	
pyx	0.398	0.020	23.011	0.214	0.125	0.006	7.216	0.104
	0.182	0.009	23.018	0.144	0.057	0.003	7.219	0.070
	0.453	0.023	23.178	0.230	0.142	0.007	7.269	0.111
	0.177	0.009	22.902	0.142	0.056	0.003	7.182	0.069
	0.226	0.011	23.012	0.151	0.071	0.004	7.217	0.073
	0.271	0.014	22.550	0.168	0.086	0.004	7.070	0.083
	0.204	0.010	22.800	0.145	0.064	0.003	7.150	0.071
	0.195	0.010	22.745	0.154	0.062	0.003	7.132	0.075
	0.281	0.014	22.776	0.190	0.089	0.004	7.142	0.093
	0.780	0.039	23.027	0.327	0.246	0.012	7.221	0.159
	0.299	0.015	22.932	0.194	0.094	0.005	7.192	0.094
	0.664	0.033	23.134	0.262	0.208	0.010	7.255	0.127
	1.431	0.072	22.743	0.384	0.454	0.023	7.131	0.190
	0.135	0.007	22.776	0.119	0.043	0.002	7.142	0.058
	1.853	0.093	22.862	0.443	0.589	0.029	7.169	0.219
	0.159	0.008	22.939	0.131	0.050	0.002	7.194	0.064
	0.507	0.025	22.960	0.277	0.160	0.008	7.200	0.135
	0.430	0.022	23.055	0.219	0.135	0.007	7.230	0.106
	0.242	0.012	22.785	0.168	0.076	0.004	7.145	0.083
	0.855	0.043	22.774	0.319	0.271	0.014	7.141	0.157
	0.243	0.012	22.890	0.159	0.077	0.004	7.178	0.078
	0.257	0.013	22.870	0.168	0.081	0.004	7.172	0.082
	0.146	0.007	22.878	0.127	0.046	0.002	7.175	0.062

DAP2 July2011

Mineral	$^{56}Fe/^{61}Ni$ ($\times 10^6$) ± 2σ		$^{60}Ni/^{61}Ni$ ± 2σ		$^{56}Fe/^{62}Ni$ ($\times 10^6$) ± 2σ		$^{60}Ni/^{62}Ni$ ± 2σ	
pyx	0.873	0.044	22.996	0.164	0.273	0.014	7.212	0.079
	0.749	0.037	22.911	0.135	0.235	0.012	7.185	0.065
	0.982	0.049	23.337	0.286	0.305	0.015	7.318	0.136
	0.127	0.006	22.983	0.127	0.040	0.002	7.207	0.062
	0.447	0.022	23.049	0.155	0.140	0.007	7.228	0.075
	0.046	0.002	23.127	0.067	0.014	0.001	7.253	0.032
	0.861	0.043	23.196	0.203	0.269	0.013	7.274	0.097
	0.079	0.004	23.068	0.064	0.025	0.001	7.234	0.031
	0.686	0.034	23.131	0.161	0.214	0.011	7.254	0.077
	0.046	0.002	23.061	0.043	0.015	0.001	7.232	0.021
	0.190	0.009	22.839	0.122	0.060	0.003	7.162	0.060
	0.176	0.009	23.028	0.059	0.055	0.003	7.222	0.028
	0.249	0.012	23.049	0.071	0.079	0.004	7.228	0.035
	0.113	0.006	23.090	0.056	0.036	0.002	7.241	0.027
	0.621	0.031	22.835	0.155	0.195	0.010	7.161	0.075
	0.352	0.018	22.967	0.096	0.111	0.006	7.202	0.046
	0.625	0.031	23.000	0.152	0.196	0.010	7.213	0.074
	0.669	0.033	22.963	0.154	0.210	0.010	7.201	0.075
	0.136	0.007	22.906	0.101	0.043	0.002	7.184	0.049

DAP2 March2010

Mineral	$^{56}Fe/^{61}Ni$ ($\times 10^6$) ± 2σ		$^{60}Ni/^{61}Ni$ ± 2σ		$^{56}Fe/^{62}Ni$ ($\times 10^6$) ± 2σ		$^{60}Ni/^{62}Ni$ ± 2σ	
pyx	2.953	0.148	22.876	0.398	0.959	0.048	7.322	0.193
	0.581	0.029	22.964	0.313	0.189	0.009	7.199	0.152
	1.304	0.065	22.841	0.303	0.422	0.021	7.161	0.147
	0.384	0.019	22.861	0.195	0.125	0.006	7.166	0.095
	1.191	0.060	22.548	0.367	0.390	0.020	7.067	0.182
	0.348	0.017	23.030	0.170	0.113	0.006	7.220	0.082
	0.323	0.016	22.869	0.202	0.105	0.005	7.169	0.099

	2.028	0.101	23.039	0.377	0.656	0.033	7.223	0.183
	0.849	0.042	22.449	0.234	0.279	0.014	7.035	0.117
	0.277	0.014	23.214	0.215	0.089	0.004	7.277	0.104
	1.296	0.065	22.771	0.277	0.423	0.021	7.138	0.136
	2.738	0.137	22.693	0.373	0.894	0.045	7.113	0.183
	0.324	0.016	22.940	0.251	0.105	0.005	7.191	0.123

SMK1805-1 Dec2010

Mineral	$^{56}Fe/^{61}Ni$ ($\times 10^6$) ± 2σ		$^{60}Ni/^{61}Ni$ ± 2σ		$^{56}Fe/^{62}Ni$ ($\times 10^6$) ± 2σ		$^{60}Ni/^{62}Ni$ ± 2σ	
pyx	0.393	0.020	23.038	0.111	0.124	0.006	7.225	0.054
	0.189	0.009	22.989	0.083	0.060	0.003	7.210	0.040
	0.209	0.010	22.881	0.093	0.066	0.003	7.175	0.046
	0.170	0.008	22.871	0.083	0.054	0.003	7.172	0.041
	0.846	0.042	23.187	0.229	0.266	0.013	7.272	0.111
	0.530	0.026	23.023	0.126	0.167	0.008	7.220	0.061
	1.026	0.051	23.028	0.181	0.323	0.016	7.222	0.088

SMK1805-1 July2010

Mineral	$^{56}Fe/^{61}Ni$ ($\times 10^6$) ± 2σ		$^{60}Ni/^{61}Ni$ ± 2σ		$^{56}Fe/^{62}Ni$ ($\times 10^6$) ± 2σ		$^{60}Ni/^{62}Ni$ ± 2σ	
pyx	2.236	0.112	22.954	0.442	0.702	0.035	7.199	0.214
	2.065	0.103	23.208	0.430	0.644	0.032	7.278	0.206
	2.628	0.131	22.716	0.437	0.833	0.042	7.123	0.215
	1.103	0.055	23.164	0.290	0.346	0.017	7.265	0.140
	1.841	0.092	23.422	0.387	0.571	0.029	7.344	0.183
	2.707	0.135	22.692	0.463	0.855	0.043	7.116	0.227
	1.328	0.066	23.261	0.332	0.414	0.021	7.295	0.159
	1.773	0.089	23.240	0.389	0.554	0.028	7.288	0.186
	1.707	0.085	23.232	0.380	0.535	0.027	7.286	0.183

QUE ch3

Mineral	$^{56}Fe/^{61}Ni$ ($\times10^6$) ± 2σ		$^{60}Ni/^{61}Ni$ ± 2σ		$^{56}Fe/^{62}Ni$ ($\times10^6$) ± 2σ		$^{60}Ni/^{62}Ni$ ± 2σ	
pyx	0.916	0.046	23.518	0.577	0.279	0.014	7.361	0.293
	0.671	0.034	23.240	0.371	0.217	0.011	7.296	0.189
	0.086	0.004	22.956	0.142	0.027	0.001	7.219	0.074
	1.164	0.058	22.524	0.374	0.372	0.019	7.068	0.201
	0.863	0.043	22.920	0.249	0.270	0.013	7.199	0.128
	1.126	0.056	22.987	0.328	0.345	0.017	7.210	0.172
	0.019	0.001	23.006	0.025	0.006	0.000	7.221	0.013
	0.010	0.001	22.953	0.022	0.003	0.000	7.194	0.011
	0.473	0.047	23.203	0.448	0.148	0.015	7.276	0.215
	0.190	0.019	23.160	0.455	0.059	0.006	7.263	0.219
	0.559	0.056	23.378	0.534	0.173	0.017	7.330	0.253
	0.201	0.020	22.893	0.378	0.063	0.006	7.283	0.183
	0.257	0.026	22.922	0.497	0.082	0.008	7.188	0.245
	0.694	0.069	23.278	0.497	0.218	0.022	7.300	0.239
	0.189	0.019	23.002	0.258	0.060	0.006	7.214	0.126
	0.443	0.044	23.195	0.406	0.138	0.014	7.274	0.195
	0.184	0.018	22.753	0.462	0.058	0.006	7.135	0.227
	0.320	0.016	23.099	0.171	0.100	0.005	7.244	0.083
	0.443	0.022	23.069	0.181	0.139	0.007	7.235	0.087
	0.978	0.049	23.004	0.236	0.307	0.015	7.214	0.114
	0.691	0.035	23.216	0.203	0.216	0.011	7.280	0.097
	1.232	0.062	23.232	0.400	0.386	0.019	7.286	0.193
	0.067	0.003	23.124	0.087	0.021	0.001	7.252	0.042
	0.645	0.032	22.867	0.216	0.203	0.010	7.171	0.106

QUE ch5

Mineral	$^{56}Fe/^{61}Ni$ ($\times10^6$) ± 2σ		$^{60}Ni/^{61}Ni$ ± 2σ		$^{56}Fe/^{62}Ni$ ($\times10^6$) ± 2σ		$^{60}Ni/^{62}Ni$ ± 2σ	
pyx	0.085	0.004	23.382	0.085	0.026	0.001	7.332	0.041
	0.519	0.026	23.935	0.200	0.160	0.008	7.501	0.093

	0.264	0.013	23.712	0.219	0.082	0.004	7.434	0.104
	0.490	0.024	23.606	0.243	0.152	0.008	7.401	0.115
	0.069	0.003	22.793	0.095	0.022	0.001	7.148	0.046
	0.209	0.010	23.328	0.157	0.065	0.003	7.315	0.075
	0.200	0.010	23.429	0.189	0.062	0.003	7.345	0.089
	0.129	0.006	23.415	0.214	0.040	0.002	7.341	0.101
	0.125	0.006	23.193	0.092	0.039	0.002	7.273	0.044
	0.054	0.003	23.102	0.079	0.017	0.001	7.245	0.038
	0.069	0.003	22.993	0.051	0.022	0.001	7.211	0.025
	0.162	0.008	23.181	0.099	0.051	0.003	7.269	0.047
	0.064	0.003	23.023	0.118	0.020	0.001	7.220	0.057

QUE chK

Mineral	$^{56}Fe/^{61}Ni$ ($\times 10^6$) ± 2σ		$^{60}Ni/^{61}Ni$ ± 2σ		$^{56}Fe/^{62}Ni$ ($\times 10^6$) ± 2σ		$^{60}Ni/^{62}Ni$ ± 2σ	
pyx	0.386	0.019	22.775	0.115	0.126	0.006	7.142	0.056
	0.326	0.016	22.942	0.112	0.106	0.005	7.195	0.054
	0.429	0.021	22.886	0.121	0.140	0.007	7.177	0.059
	0.146	0.007	23.007	0.075	0.047	0.002	7.215	0.036
	0.270	0.013	23.079	0.107	0.088	0.004	7.238	0.052
	0.238	0.012	23.109	0.153	0.078	0.004	7.249	0.074
	0.386	0.019	22.935	0.118	0.126	0.006	7.193	0.057
	0.336	0.017	23.037	0.111	0.110	0.005	7.225	0.054
	0.308	0.015	23.016	0.114	0.100	0.005	7.218	0.055
	0.321	0.016	23.057	0.120	0.105	0.005	7.231	0.058
	0.467	0.023	22.945	0.127	0.152	0.008	7.196	0.062
	0.222	0.011	23.016	0.092	0.072	0.004	7.218	0.045
	0.359	0.018	23.116	0.115	0.117	0.006	7.249	0.055
	0.156	0.008	23.057	0.075	0.051	0.003	7.231	0.036
	0.083	0.004	22.995	0.057	0.027	0.001	7.211	0.028

QUE chI

Mineral	$^{56}Fe/^{61}Ni$ (×10^6) ± 2σ		$^{60}Ni/^{61}Ni$ ± 2σ		$^{56}Fe/^{62}Ni$ (×10^6) ± 2σ		$^{60}Ni/^{62}Ni$ ± 2σ	
pyx	0.402	0.040	22.884	0.145	0.127	0.013	7.177	0.071
	0.350	0.035	22.923	0.136	0.110	0.011	7.189	0.066
	0.043	0.004	22.871	0.085	0.014	0.001	7.172	0.042
	0.083	0.008	22.890	0.085	0.026	0.003	7.178	0.041
	0.067	0.007	22.879	0.069	0.021	0.002	7.175	0.034
	0.420	0.042	22.865	0.158	0.132	0.013	7.170	0.077
	0.502	0.050	22.983	0.157	0.157	0.016	7.208	0.076
	0.427	0.043	22.873	0.151	0.134	0.013	7.173	0.073
	0.277	0.028	22.991	0.105	0.087	0.009	7.210	0.051
	0.241	0.024	22.872	0.105	0.076	0.008	7.173	0.051
	0.166	0.017	22.980	0.095	0.052	0.005	7.207	0.046
	0.062	0.006	22.939	0.096	0.020	0.002	7.194	0.047
	0.175	0.017	22.985	0.085	0.055	0.005	7.208	0.041

QUE chM

Mineral	$^{56}Fe/^{61}Ni$ (×10^6) ± 2σ		$^{60}Ni/^{61}Ni$ ± 2σ		$^{56}Fe/^{62}Ni$ (×10^6) ± 2σ		$^{60}Ni/^{62}Ni$ ± 2σ	
pyx	0.176	0.018	23.107	0.091	0.055	0.006	7.247	0.044
	0.174	0.017	23.058	0.091	0.055	0.005	7.231	0.044
	0.239	0.024	23.097	0.109	0.075	0.007	7.243	0.052
	0.164	0.016	23.105	0.100	0.051	0.005	7.246	0.048
	0.176	0.018	23.066	0.088	0.055	0.006	7.234	0.042
	0.171	0.017	23.116	0.069	0.054	0.005	7.249	0.033

QUE chC

Mineral	$^{56}Fe/^{61}Ni$ (×10^6) ± 2σ		$^{60}Ni/^{61}Ni$ ± 2σ		$^{56}Fe/^{62}Ni$ (×10^6) ± 2σ		$^{60}Ni/^{62}Ni$ ± 2σ	
pyx	3.153	0.315	23.206	0.277	0.984	0.098	7.277	0.133

	3.543	0.354	23.096	0.302	1.108	0.111	7.243	0.145
	3.391	0.339	22.725	0.292	1.068	0.107	7.126	0.143
	3.346	0.335	22.813	0.286	1.052	0.105	7.154	0.139
	4.441	0.444	23.072	0.390	1.388	0.139	7.235	0.188

QUE chF

Mineral	$^{56}Fe/^{61}Ni$ ($\times 10^6$) ± 2σ		$^{60}Ni/^{61}Ni$ ± 2σ		$^{56}Fe/^{62}Ni$ ($\times 10^6$) ± 2σ		$^{60}Ni/^{62}Ni$ ± 2σ	
pyx	1.068	0.107	22.995	0.166	0.335	0.033	7.212	0.080
	0.096	0.010	23.147	0.056	0.030	0.003	7.259	0.027
	1.272	0.127	22.994	0.158	0.400	0.040	7.211	0.077
	1.629	0.163	23.044	0.176	0.512	0.051	7.227	0.085
	1.551	0.155	23.386	0.163	0.483	0.048	7.333	0.078

QUE ch6

Mineral	$^{56}Fe/^{61}Ni$ ($\times 10^6$) ± 2σ		$^{60}Ni/^{61}Ni$ ± 2σ		$^{56}Fe/^{62}Ni$ ($\times 10^6$) ± 2σ		$^{60}Ni/^{62}Ni$ ± 2σ	
pyx	0.753	0.038	22.941	0.131	0.236	0.012	7.194	0.064
	1.361	0.068	22.916	0.208	0.428	0.021	7.187	0.101
	0.767	0.038	23.109	0.212	0.240	0.012	7.247	0.102
	0.954	0.048	23.121	0.146	0.298	0.015	7.251	0.070
	0.608	0.030	23.040	0.126	0.190	0.010	7.226	0.061
	0.534	0.027	23.225	0.178	0.167	0.008	7.283	0.085
	0.162	0.008	23.091	0.116	0.051	0.003	7.241	0.056
	0.899	0.045	23.005	0.150	0.282	0.014	7.214	0.073
	0.291	0.015	23.085	0.090	0.091	0.005	7.240	0.043
	0.963	0.048	22.995	0.151	0.302	0.015	7.211	0.073
	0.949	0.047	22.966	0.165	0.298	0.015	7.202	0.080
	0.703	0.035	22.928	0.238	0.221	0.011	7.190	0.116
	0.317	0.016	22.973	0.123	0.099	0.005	7.204	0.059
	0.697	0.035	22.981	0.131	0.218	0.011	7.207	0.063
	0.353	0.018	22.980	0.094	0.111	0.006	7.207	0.046
	0.456	0.023	22.804	0.135	0.144	0.007	7.151	0.066

QUE ch1

Mineral	$^{56}Fe/^{61}Ni$ ($\times10^6$) ± 2σ		$^{60}Ni/^{61}Ni$ ± 2σ		$^{56}Fe/^{62}Ni$ ($\times10^6$) ± 2σ		$^{60}Ni/^{62}Ni$ ± 2σ	
pyx	0.121	0.006	22.943	0.122	0.038	0.002	7.195	0.059
	0.129	0.006	22.898	0.121	0.041	0.002	7.181	0.059
	0.121	0.006	22.975	0.120	0.038	0.002	7.205	0.058
	0.140	0.007	22.837	0.124	0.044	0.002	7.162	0.060
	0.149	0.007	22.872	0.133	0.047	0.002	7.173	0.064
	0.167	0.008	22.898	0.195	0.052	0.003	7.181	0.095
	0.136	0.007	22.994	0.124	0.042	0.002	7.211	0.060
	0.109	0.005	22.864	0.115	0.034	0.002	7.170	0.056
	0.132	0.007	22.941	0.129	0.042	0.002	7.195	0.063
	0.135	0.007	22.853	0.126	0.043	0.002	7.167	0.061
	0.156	0.008	22.823	0.127	0.049	0.002	7.157	0.062
	0.112	0.006	22.934	0.157	0.035	0.002	7.192	0.076
	0.072	0.004	22.922	0.132	0.023	0.001	7.188	0.064
	0.120	0.006	22.877	0.138	0.038	0.002	7.174	0.067
	0.013	0.001	23.070	0.077	0.004	0.000	7.235	0.037

EET r1

Mineral	$^{56}Fe/^{61}Ni$ ($\times10^6$) ± 2σ		$^{60}Ni/^{61}Ni$ ± 2σ		$^{56}Fe/^{62}Ni$ ($\times10^6$) ± 2σ		$^{60}Ni/^{62}Ni$ ± 2σ	
pyx	0.371	0.019	22.993	0.109	0.117	0.006	7.211	0.053
	0.331	0.017	22.855	0.097	0.104	0.005	7.167	0.047
	1.243	0.062	22.731	0.200	0.392	0.020	7.128	0.098
	1.809	0.090	22.778	0.244	0.569	0.028	7.143	0.120
	0.583	0.029	22.785	0.270	0.183	0.009	7.145	0.132
	0.740	0.037	23.108	0.209	0.231	0.012	7.247	0.101
	0.439	0.022	23.023	0.175	0.138	0.007	7.220	0.085
	0.246	0.012	22.848	0.123	0.077	0.004	7.165	0.060
	2.680	0.134	23.052	0.293	0.838	0.042	7.229	0.141

	1.537	0.077	22.861	0.221	0.483	0.024	7.169	0.108
	1.017	0.051	22.824	0.177	0.320	0.016	7.158	0.087
	2.303	0.115	23.078	0.248	0.722	0.036	7.237	0.120
	0.540	0.027	22.792	0.128	0.170	0.009	7.147	0.062
	0.297	0.015	23.004	0.097	0.093	0.005	7.214	0.047

EET r4

Mineral	$^{56}Fe/^{61}Ni$ ($\times 10^6$) ± 2σ		$^{60}Ni/^{61}Ni$ ± 2σ		$^{56}Fe/^{62}Ni$ ($\times 10^6$) ± 2σ		$^{60}Ni/^{62}Ni$ ± 2σ	
pyx	0.497	0.050	22.811	0.126	0.114	0.006	7.153	0.062
	0.518	0.052	22.934	0.130	0.118	0.006	7.192	0.063
	0.136	0.014	22.916	0.066	0.031	0.002	7.187	0.032
	0.651	0.065	22.909	0.129	0.149	0.007	7.184	0.063
	0.446	0.045	22.980	0.104	0.102	0.005	7.206	0.050

BM80 r40

Mineral	$^{56}Fe/^{61}Ni$ ($\times 10^6$) ± 2σ		$^{60}Ni/^{61}Ni$ ± 2σ		$^{56}Fe/^{62}Ni$ ($\times 10^6$) ± 2σ		$^{60}Ni/^{62}Ni$ ± 2σ	
pyx	0.480	0.024	22.881	0.154	0.151	0.008	7.176	0.075
	0.298	0.015	22.838	0.133	0.094	0.005	7.162	0.065
	0.397	0.020	22.807	0.124	0.125	0.006	7.152	0.061
	0.451	0.023	23.038	0.149	0.141	0.007	7.225	0.072
	0.276	0.014	22.836	0.104	0.087	0.004	7.161	0.051
	0.317	0.016	22.977	0.143	0.100	0.005	7.210	0.071
	0.236	0.012	22.790	0.088	0.074	0.004	7.147	0.043
	0.207	0.010	22.785	0.115	0.065	0.003	7.145	0.056
	0.463	0.023	22.893	0.137	0.146	0.007	7.179	0.067
	0.233	0.012	23.036	0.109	0.073	0.004	7.224	0.053
	0.363	0.018	22.780	0.136	0.114	0.006	7.143	0.067

BM23 ch13

Mineral	$^{56}Fe/^{61}Ni$ ($\times10^6$) ± 2σ		$^{60}Ni/^{61}Ni$ ± 2σ		$^{56}Fe/^{62}Ni$ ($\times10^6$) ± 2σ		$^{60}Ni/^{62}Ni$ ± 2σ	
pyx	2.112	0.106	22.848	0.265	0.664	0.033	7.165	0.129
	2.436	0.122	22.997	0.298	0.762	0.038	7.212	0.144
	3.403	0.170	23.253	0.352	1.057	0.053	7.292	0.168
	1.380	0.069	22.988	0.255	0.430	0.021	7.209	0.122
	0.959	0.048	23.004	0.188	0.300	0.015	7.214	0.091
	2.071	0.104	22.640	0.284	0.651	0.033	7.100	0.139
	0.932	0.047	22.964	0.191	0.292	0.015	7.202	0.092

BM23 ch9

Mineral	$^{56}Fe/^{61}Ni$ ($\times10^6$) ± 2σ		$^{60}Ni/^{61}Ni$ ± 2σ		$^{56}Fe/^{62}Ni$ ($\times10^6$) ± 2σ		$^{60}Ni/^{62}Ni$ ± 2σ	
pyx	1.616	0.081	23.261	0.309	0.504	0.025	7.294	0.148
	1.577	0.079	22.858	0.315	0.495	0.025	7.169	0.153
	1.973	0.099	22.876	0.329	0.619	0.031	7.174	0.160
	1.635	0.082	22.666	0.312	0.517	0.026	7.108	0.153
	1.022	0.051	23.098	0.254	0.320	0.016	7.244	0.122
	0.676	0.034	22.951	0.147	0.212	0.011	7.197	0.071
	0.635	0.032	22.982	0.145	0.199	0.010	7.207	0.070
	1.159	0.058	22.567	0.235	0.367	0.018	7.076	0.116
	2.056	0.103	22.950	0.315	0.644	0.032	7.197	0.152
	2.126	0.106	23.017	0.341	0.664	0.033	7.218	0.164
	2.428	0.121	22.826	0.383	0.763	0.038	7.158	0.187
	2.670	0.133	23.061	0.413	0.836	0.042	7.232	0.199

BM23 ch25

Mineral	$^{56}Fe/^{61}Ni$ ($\times10^6$) ± 2σ		$^{60}Ni/^{61}Ni$ ± 2σ		$^{56}Fe/^{62}Ni$ ($\times10^6$) ± 2σ		$^{60}Ni/^{62}Ni$ ± 2σ	
pyx	0.294	0.015	23.028	0.120	0.092	0.005	7.222	0.058
	0.250	0.013	22.972	0.144	0.079	0.004	7.204	0.070
	0.300	0.015	22.700	0.142	0.095	0.005	7.118	0.070
	0.358	0.018	22.793	0.143	0.113	0.006	7.148	0.070
	0.346	0.017	22.904	0.131	0.109	0.005	7.183	0.063
	0.351	0.018	22.843	0.123	0.111	0.006	7.164	0.060
	0.322	0.016	23.060	0.141	0.101	0.005	7.232	0.068

BM23 ch12

Mineral	$^{56}Fe/^{61}Ni$ ($\times10^6$) ± 2σ		$^{60}Ni/^{61}Ni$ ± 2σ		$^{56}Fe/^{62}Ni$ ($\times10^6$) ± 2σ		$^{60}Ni/^{62}Ni$ ± 2σ	
pyx	0.506	0.025	22.832	0.175	0.159	0.008	7.160	0.086
	0.628	0.031	23.079	0.191	0.197	0.010	7.238	0.092
	1.686	0.084	22.757	0.299	0.533	0.027	7.136	0.147
	1.315	0.066	22.589	0.270	0.416	0.021	7.083	0.133
	1.707	0.085	22.475	0.300	0.542	0.027	7.046	0.149
	1.020	0.051	23.117	0.296	0.319	0.016	7.250	0.143
	0.177	0.009	22.903	0.191	0.056	0.003	7.183	0.093
	0.967	0.048	22.858	0.302	0.304	0.015	7.168	0.147
	0.274	0.014	22.922	0.237	0.086	0.004	7.188	0.116
	2.593	0.130	22.980	0.406	0.813	0.041	7.207	0.197

BVG ch1

Mineral	$^{56}Fe/^{61}Ni$ ($\times10^6$) ± 2σ		$^{60}Ni/^{61}Ni$ ± 2σ		$^{56}Fe/^{62}Ni$ ($\times10^6$) ± 2σ		$^{60}Ni/^{62}Ni$ ± 2σ	
pyx	0.911	0.046	22.417	0.247	0.289	0.014	7.028	0.122
	1.258	0.063	22.654	0.248	0.398	0.020	7.104	0.122
	0.466	0.023	22.674	0.162	0.147	0.007	7.110	0.079
	0.184	0.009	22.670	0.099	0.058	0.003	7.109	0.048

	0.514	0.026	22.680	0.170	0.163	0.008	7.112	0.084
	1.035	0.052	23.153	0.421	0.324	0.016	7.261	0.202
	2.014	0.101	22.697	0.373	0.636	0.032	7.118	0.183
	1.603	0.080	23.255	0.318	0.501	0.025	7.293	0.153
	0.482	0.024	22.746	0.167	0.152	0.008	7.133	0.082

BVG ch18

Mineral	$^{56}Fe/^{61}Ni$ (×10^6) ± 2σ		$^{60}Ni/^{61}Ni$ ± 2σ		$^{56}Fe/^{62}Ni$ (×10^6) ± 2σ		$^{60}Ni/^{62}Ni$ ± 2σ	
pyx	0.115	0.006	22.784	0.149	0.036	0.002	7.145	0.073
	0.149	0.007	22.851	0.118	0.047	0.002	7.166	0.058
	0.132	0.007	22.947	0.123	0.041	0.002	7.196	0.060
	0.154	0.008	22.938	0.102	0.049	0.002	7.194	0.049
	0.200	0.010	22.972	0.097	0.063	0.003	7.204	0.047
	0.117	0.006	22.943	0.092	0.037	0.002	7.195	0.045
	0.143	0.007	23.048	0.094	0.045	0.002	7.228	0.046
	0.113	0.006	22.954	0.099	0.036	0.002	7.198	0.048

BM80 ch18

Mineral	$^{56}Fe/^{61}Ni$ (×10^6) ± 2σ		$^{60}Ni/^{61}Ni$ ± 2σ		$^{56}Fe/^{62}Ni$ (×10^6) ± 2σ		$^{60}Ni/^{62}Ni$ ± 2σ	
pyx	0.064	0.003	23.073	0.106	0.020	0.001	7.236	0.051
	0.219	0.011	22.936	0.160	0.069	0.003	7.193	0.078
	0.378	0.019	23.660	0.347	0.117	0.006	7.417	0.163
	0.235	0.012	23.133	0.185	0.074	0.004	7.254	0.089
	0.267	0.013	23.030	0.161	0.083	0.004	7.222	0.078
	0.553	0.028	22.390	0.404	0.175	0.009	7.019	0.200
	0.457	0.023	22.839	0.392	0.144	0.007	7.162	0.190
	0.248	0.012	22.864	0.160	0.078	0.004	7.170	0.078

BM80 ch37 Mono

Mineral	$^{56}Fe/^{61}Ni$ ($\times 10^6$) ± 2σ		$^{60}Ni/^{61}Ni$ ± 2σ		$^{56}Fe/^{62}Ni$ ($\times 10^6$) ± 2σ		$^{60}Ni/^{62}Ni$ ± 2σ	
pyx	0.874	0.044	22.839	1.031	0.275	0.014	7.168	0.469
	0.546	0.027	23.245	0.713	0.170	0.009	7.285	0.318
	0.199	0.010	23.094	0.415	0.062	0.003	7.239	0.187
	1.038	0.052	22.819	1.491	0.325	0.016	7.161	0.675
	0.126	0.006	22.002	1.108	0.040	0.002	6.895	0.525
	0.249	0.012	23.558	0.631	0.077	0.004	7.390	0.277
	0.109	0.005	22.784	0.626	0.034	0.002	7.142	0.284
	0.101	0.005	22.684	0.501	0.032	0.002	7.110	0.230
	0.242	0.012	23.163	0.675	0.076	0.004	7.264	0.303
	1.440	0.072	23.329	1.214	0.449	0.022	7.315	0.541
	1.239	0.062	23.791	1.256	0.383	0.019	7.452	0.547
	0.498	0.025	22.987	0.675	0.157	0.008	7.201	0.305
	0.415	0.021	24.791	1.331	0.125	0.006	7.753	0.556
	1.016	0.051	23.568	1.360	0.311	0.016	7.393	0.594
	0.112	0.006	23.051	0.368	0.035	0.002	7.228	0.166
	0.117	0.006	23.068	0.424	0.037	0.002	7.235	0.191
	0.580	0.029	24.072	0.830	0.178	0.009	7.541	0.358
	0.673	0.034	22.639	0.852	0.213	0.011	7.100	0.391
	0.120	0.006	22.907	0.420	0.038	0.002	7.180	0.190
	0.826	0.041	24.330	1.095	0.251	0.013	7.615	0.465
	0.566	0.028	24.617	1.503	0.171	0.009	7.704	0.634
	0.178	0.009	23.161	0.416	0.056	0.003	7.267	0.187
	0.564	0.028	22.592	0.714	0.179	0.009	7.090	0.328
	0.416	0.021	24.506	0.859	0.127	0.006	7.680	0.365
	0.245	0.012	22.471	0.829	0.077	0.004	7.062	0.381
	0.555	0.028	23.260	1.655	0.173	0.009	7.295	0.740
	0.653	0.033	22.818	0.853	0.206	0.010	7.165	0.389
	0.521	0.026	23.073	0.782	0.164	0.008	7.230	0.353
	0.627	0.031	22.774	1.022	0.198	0.010	7.302	0.463
	0.057	0.003	23.470	0.351	0.018	0.001	7.360	0.156

BM80 ch37 Multi

Mineral	$^{56}Fe/^{61}Ni$ ($\times10^6$) ± 2σ		$^{60}Ni/^{61}Ni$ ± 2σ		$^{56}Fe/^{62}Ni$ ($\times10^6$) ± 2σ		$^{60}Ni/^{62}Ni$ ± 2σ	
pyx	0.923	0.046	23.128	0.490	0.289	0.014	7.253	0.236
	0.704	0.035	23.151	0.458	0.220	0.011	7.260	0.220
	0.730	0.036	23.112	0.437	0.229	0.011	7.248	0.211
	0.907	0.045	23.235	0.469	0.283	0.014	7.287	0.225
	0.685	0.034	22.855	0.424	0.215	0.011	7.167	0.206
	0.602	0.030	23.247	0.363	0.187	0.009	7.290	0.173

KRM94 ch1

Mineral	$^{56}Fe/^{61}Ni$ ($\times10^6$) ± 2σ		$^{60}Ni/^{61}Ni$ ± 2σ		$^{56}Fe/^{62}Ni$ ($\times10^6$) ± 2σ		$^{60}Ni/^{62}Ni$ ± 2σ	
pyx	2.837	0.142	22.776	0.181	0.891	0.045	7.143	0.088
	1.935	0.097	22.746	0.163	0.608	0.030	7.133	0.079
	2.149	0.107	22.901	0.184	0.672	0.034	7.182	0.089
	2.618	0.131	23.190	0.180	0.816	0.041	7.272	0.086
	2.050	0.102	22.997	0.156	0.643	0.032	7.212	0.075
	1.817	0.091	23.025	0.144	0.569	0.028	7.221	0.070
	2.630	0.132	22.845	0.179	0.827	0.041	7.164	0.087
	2.801	0.140	22.811	0.164	0.881	0.044	7.154	0.080
	2.129	0.106	22.694	0.197	0.672	0.034	7.116	0.097
	1.507	0.075	22.838	0.125	0.475	0.024	7.162	0.061
	1.158	0.058	22.838	0.115	0.364	0.018	7.162	0.056
	2.047	0.102	23.001	0.166	0.640	0.032	7.213	0.080
	0.527	0.026	22.999	0.083	0.165	0.008	7.213	0.040

KRM94 ch3

Mineral	$^{56}Fe/^{61}Ni$ ($\times10^6$) ± 2σ		$^{60}Ni/^{61}Ni$ ± 2σ		$^{56}Fe/^{62}Ni$ ($\times10^6$) ± 2σ		$^{60}Ni/^{62}Ni$ ± 2σ	
pyx	0.130	0.007	23.167	0.072	0.041	0.002	7.265	0.035
	0.131	0.007	23.148	0.067	0.041	0.002	7.259	0.032
	0.137	0.007	23.159	0.071	0.043	0.002	7.263	0.034

	0.187	0.009	22.970	0.084	0.059	0.003	7.203	0.041
	0.128	0.006	22.995	0.071	0.040	0.002	7.211	0.034
	0.166	0.008	23.087	0.077	0.052	0.003	7.240	0.037
	0.106	0.005	22.838	0.066	0.033	0.002	7.162	0.032

KRM93 ch1

Mineral	$^{56}Fe/^{61}Ni$ ($\times 10^6$) ± 2σ		$^{60}Ni/^{61}Ni$ ± 2σ		$^{56}Fe/^{62}Ni$ ($\times 10^6$) ± 2σ		$^{60}Ni/^{62}Ni$ ± 2σ	
pyx	4.120	0.206	22.946	0.282	1.291	0.065	7.196	0.136
	4.440	0.222	23.006	0.314	1.389	0.069	7.215	0.152
	3.329	0.166	22.936	0.253	1.046	0.052	7.193	0.123
	2.405	0.120	22.823	0.213	0.758	0.038	7.157	0.104
	3.242	0.162	22.906	0.242	1.017	0.051	7.184	0.117

KRM93 ch11 July2011

Mineral	$^{56}Fe/^{61}Ni$ ($\times 10^6$) ± 2σ		$^{60}Ni/^{61}Ni$ ± 2σ		$^{56}Fe/^{62}Ni$ ($\times 10^6$) ± 2σ		$^{60}Ni/^{62}Ni$ ± 2σ	
pyx	0.746	0.037	23.176	0.132	0.233	0.012	7.268	0.064
	0.297	0.015	23.069	0.079	0.093	0.005	7.235	0.038
	0.605	0.030	23.149	0.093	0.189	0.009	7.260	0.045
	0.629	0.031	23.041	0.117	0.197	0.010	7.226	0.057

KRM93 ch11 Dec2008

Mineral	$^{56}Fe/^{61}Ni$ ($\times 10^6$) ± 2σ		$^{60}Ni/^{61}Ni$ ± 2σ		$^{56}Fe/^{62}Ni$ ($\times 10^6$) ± 2σ		$^{60}Ni/^{62}Ni$ ± 2σ	
pyx	0.562	0.028	23.226	0.078	0.173	0.009	7.284	0.037
	0.432	0.022	23.321	0.075	0.113	0.006	7.314	0.036
	0.425	0.021	23.194	0.065	0.111	0.006	7.275	0.031
	0.320	0.016	23.131	0.057	0.084	0.004	7.255	0.028
	0.991	0.050	23.232	0.105	0.259	0.013	7.286	0.050

	0.718	0.036	23.181	0.093	0.188	0.009	7.271	0.045
	1.844	0.092	23.222	0.158	0.482	0.024	7.283	0.076
	0.949	0.047	23.272	0.199	0.248	0.012	7.299	0.095
	0.654	0.033	23.162	0.085	0.171	0.009	7.265	0.041
	0.866	0.043	23.163	0.097	0.227	0.011	7.265	0.047
	0.536	0.027	23.091	0.080	0.140	0.007	7.243	0.038
	0.503	0.025	23.214	0.079	0.131	0.007	7.281	0.038
	0.124	0.006	23.046	0.040	0.032	0.002	7.228	0.019
	0.349	0.017	22.920	0.023	0.092	0.005	7.189	0.033

APPENDIX B. **ADDITIONAL X-RAY FLUORESCENCE MAPS OF UOC CHONDRULES**

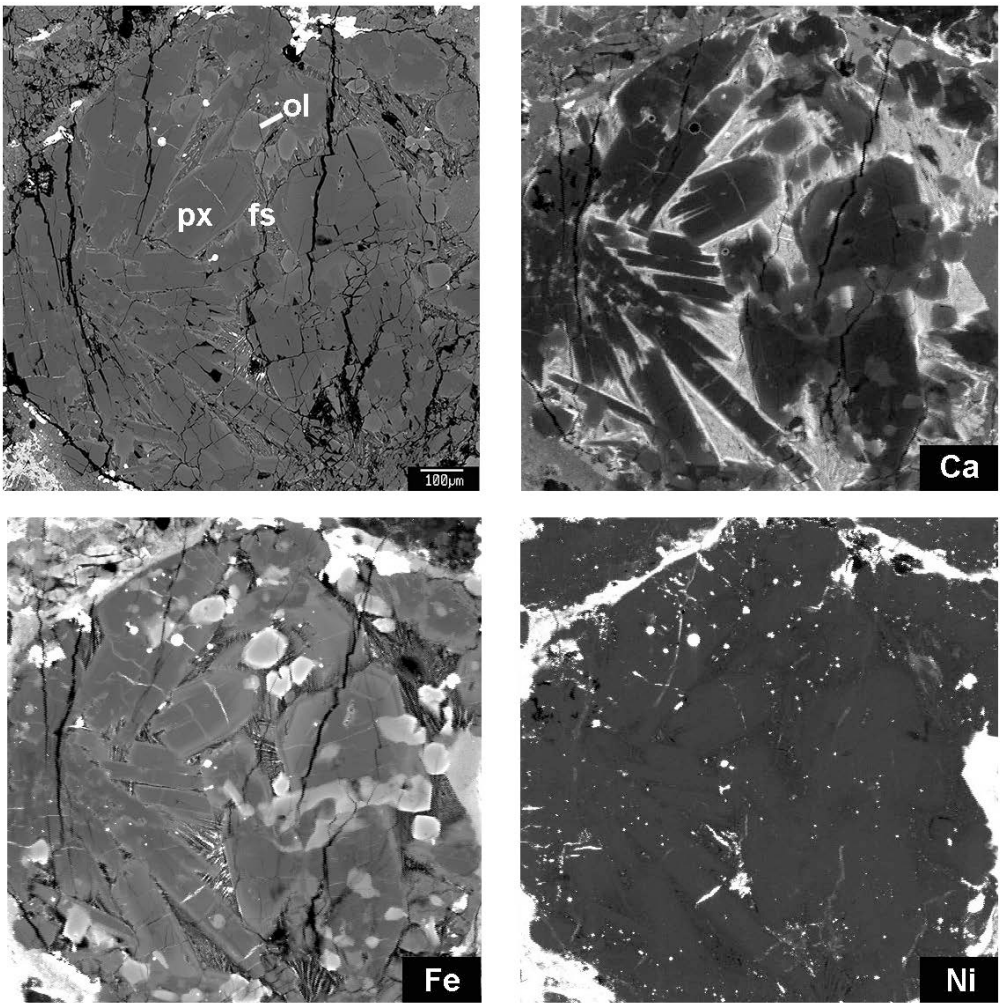

Appendix B.1. BSE and elemental maps for a type II porphyritic olivine-pyroxene chondrule from Semarkona (SMK1805 80040) obtained at the AS (ol: olivine, px: pyroxene, and fs: feldspar). The X-ray maps show that Fe is concentrated in blebs and along fractures in the pyroxene grains. Nickel is concentrated in blebs throughout the chondrule, but it is also associated with fractures.

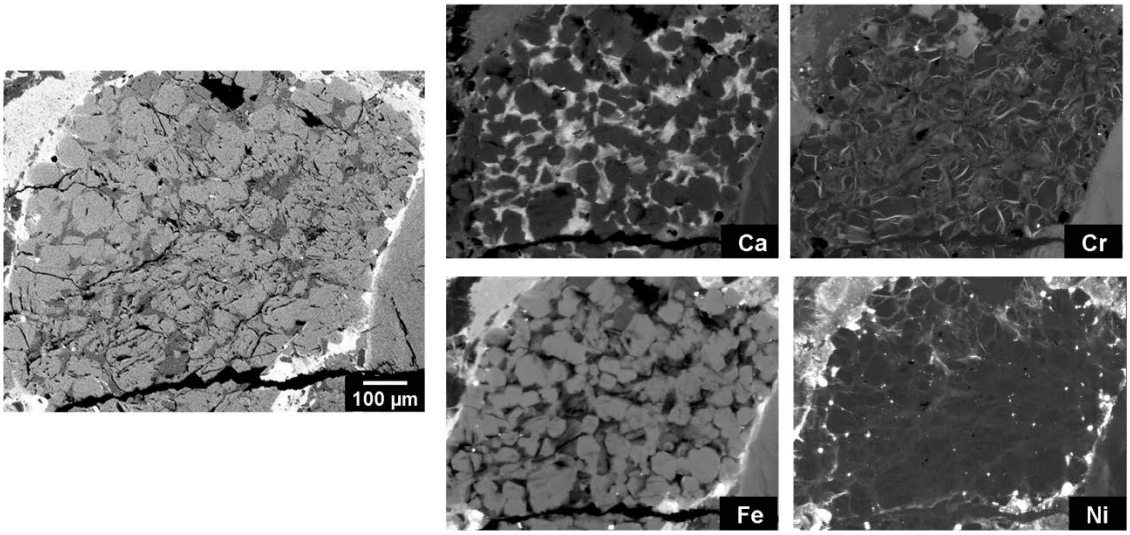

Appendix B.2. BSE and elemental maps for a bleached type II porphyritic olivine chondrule from Krymka (KRM94 80041) obtained at the AS. Nickel is concentrated in blebs and along fractures mainly on the left side of the chondrule. There some Ca zoning in the matrix. Chromium exsolution features are prevalent.

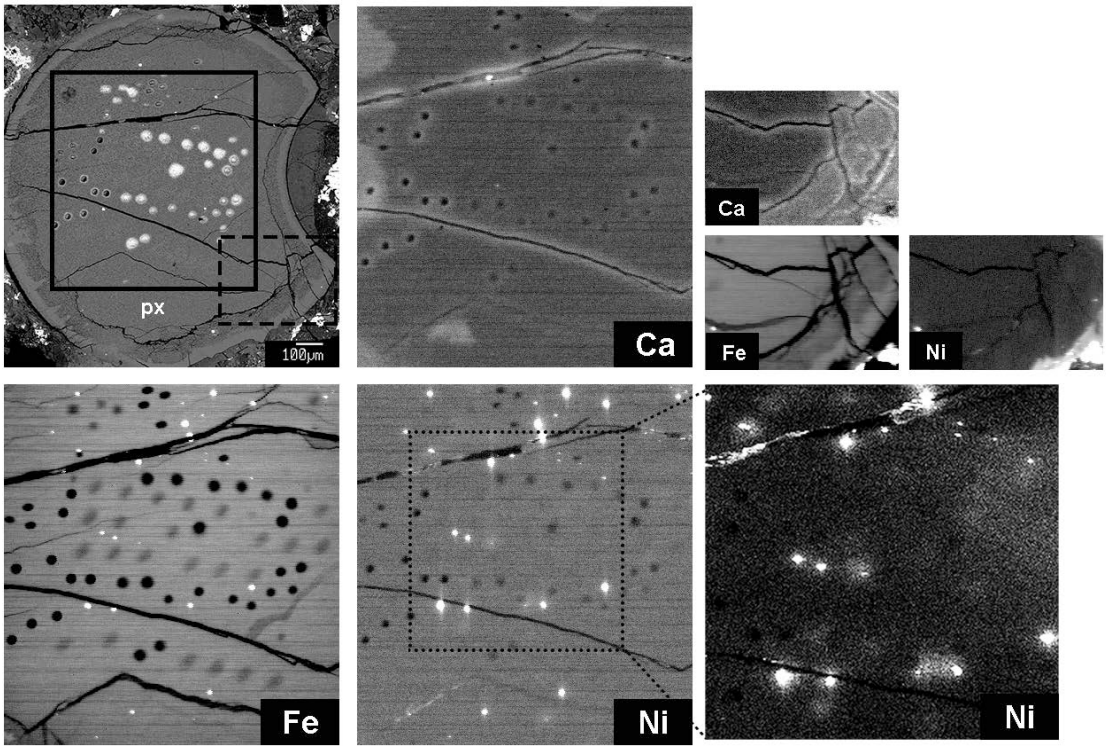

Appendix B.3. BSE and elemental maps for a bleached type II cryptocrystalline-pyroxene chondrule from Semarkona (SMK1805 ch1) obtained at the AS and the APS (Ni map in bottom right corner). The bleached region is depleted in Fe, but enriched in Ca. Calcium also appears to be enriched along the chondrule fractures, but this is likely due to edge effects and or Ca signal from the glass substrate. Nickel is concentrated in blebs mostly, but there are also minor amounts of Ni along the chondrule fractures. White ovals in the BSE image (black ovals in the X-ray maps) are from ion probe analyses.

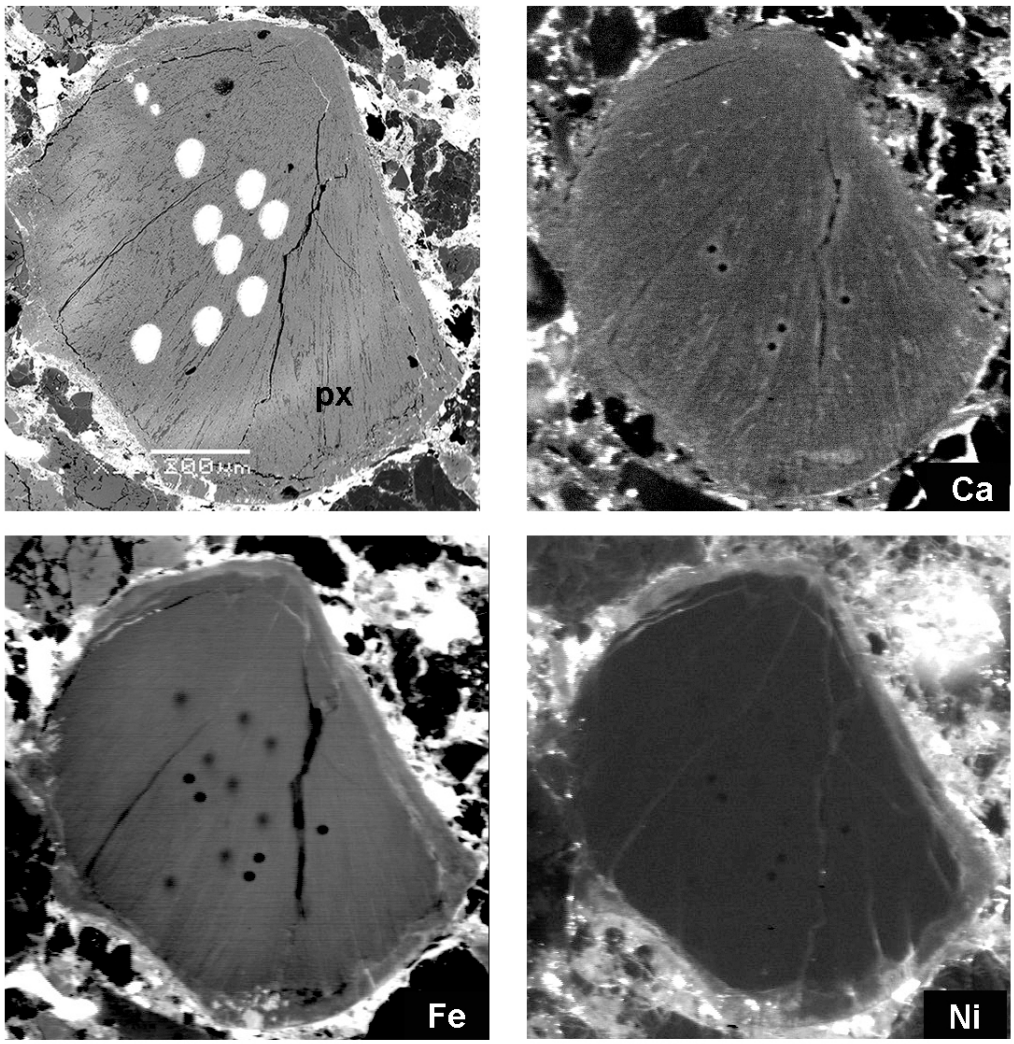

Appendix B.4. BSE and elemental maps for a bleached type II cryptocrystalline-pyroxene chondrule from Krymka (KRM9-3 ch3) obtained at the AS. The bleached region of the chondrule is not obvious. It may be associated with the diffusive Fe depleted zone along the chondrule rim. This chondrule has a large outer zone that is enriched in Fe and Ni. Iron and Ni are also concentrated along the chondrule fractures. White ovals in the BSE image (black ovals in the X-ray maps) are from ion probe analyses.

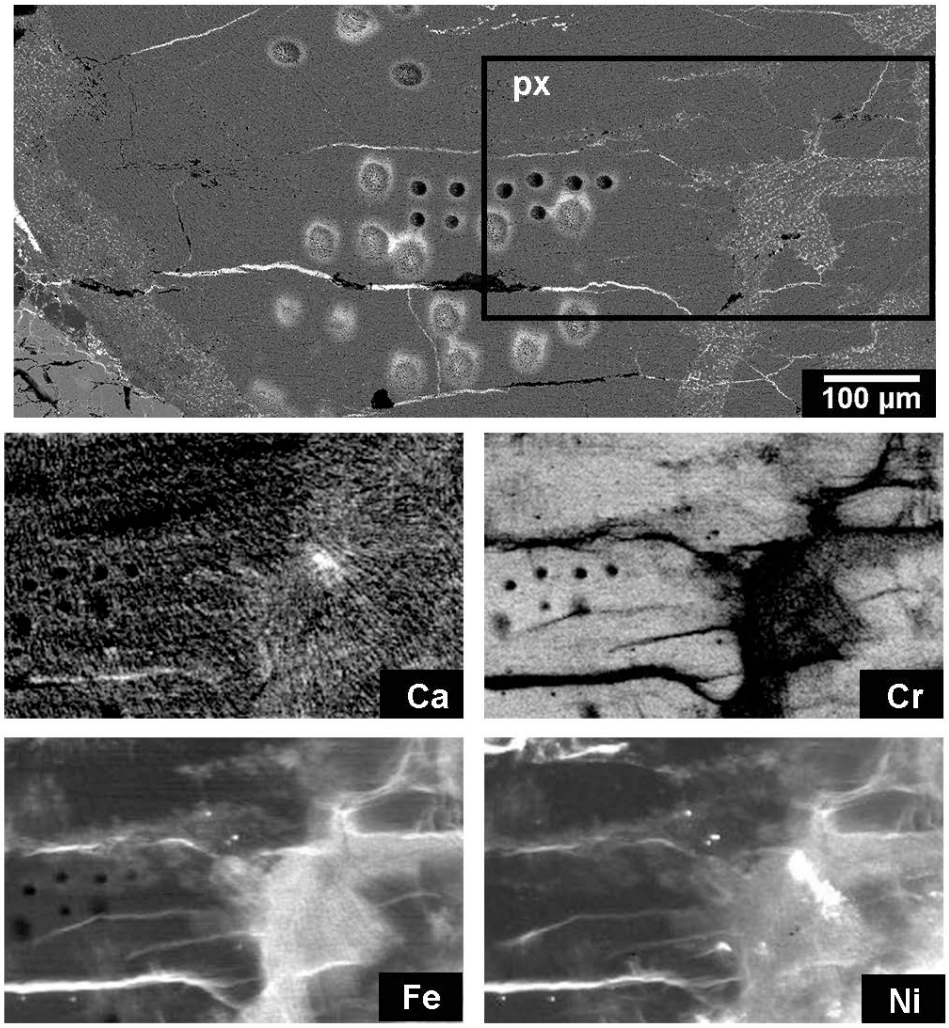

Appendix B.5. BSE and elemental maps for a bleached type II cryptocrystalline-pyroxene chondrule from Bishunpur (BM80 ch37) obtained at the AS. The bleached region and the chondrule fractures have been filled with a Fe- and Ni-rich mineral. Cr is depleted in the bleached region. Calcium may be enriched in the bleached region, but the Ca map is ambiguous. White ovals in the BSE image (black ovals in the X-ray maps) are from ion probe analyses.

APPENDIX C. **RE-CALCULATED SIMS DATA**

Table Appendix C.1: ^{53}Mn-^{53}Cr pallasite data (Hsu 2005)

As published

Albin

$(^{53}Mn/^{55}Mn)_0 = (1.3 \pm 1.0) \times 10^{-5}$

Mineral	^{53}Cr/^{52}Cr	^{55}Mn/^{52}Cr
Intercept*	0.11339±0.00023	0±0.01
Olivine	0.11381±0.00045	36±2
Olivine	0.11415±0.00065	55±3
Olivine	0.11376±0.00036	13±1

Brenham

$(^{53}Mn/^{55}Mn)_0 = (1.9 \pm 1.3) \times 10^{-5}$

Mineral	^{53}Cr/^{52}Cr	^{55}Mn/^{52}Cr
Intercept*	0.11339±0.00023	0±0.01
Olivine	0.11368±0.00047	13±1
Olivine	0.11384±0.00051	24±1
Olivine	0.11404±0.00045	36±2

Eagle Station

$(^{53}Mn/^{55}Mn)_0 = (0.6 \pm 0.8) \times 10^{-5}$

Mineral	^{53}Cr/^{52}Cr	^{55}Mn/^{52}Cr
Intercept*	0.11339±0.00023	0±0.01
Olivine	0.11362±0.00050	21±1
Olivine	0.11363±0.00079	57±3
Olivine	0.11396±0.00087	94±5

Glorieta Mountain

$(^{53}Mn/^{55}Mn)_0 = (1.5 \pm 1.0) \times 10^{-5}$

Mineral	^{53}Cr/^{52}Cr	^{55}Mn/^{52}Cr

Recalculated

Albin

$(^{53}Mn/^{55}Mn)_0 = (-0.0 \pm 0.9) \times 10^{-5}$

Mineral	^{53}Cr/^{52}Cr	^{55}Mn/^{52}Cr
Intercept*	0.11339±0.00023	0±0.01
Olivine	0.11334±0.00041	36±2
Olivine	0.11343±0.00058	55±3
Olivine	0.11359±0.00041	12±1

Brenham

$(^{53}Mn/^{55}Mn)_0 = (0.2 \pm 1.3) \times 10^{-5}$

Mineral	^{53}Cr/^{52}Cr	^{55}Mn/^{52}Cr
Intercept*	0.11339±0.00023	0±0.01
Olivine	0.11340±0.00041	14±1
Olivine	0.11347±0.00055	24±1
Olivine	0.11345±0.00048	36±2

Eagle Station

$(^{53}Mn/^{55}Mn)_0 = (-0.1 \pm 1.0) \times 10^{-5}$

Mineral	^{53}Cr/^{52}Cr	^{55}Mn/^{52}Cr
Intercept*	0.11339±0.00023	0±0.01
Olivine	0.11348±0.00061	20±1
Olivine	0.11353±0.00095	56±3
Olivine	0.11306±0.00105	88±4

Glorieta Mountain

$(^{53}Mn/^{55}Mn)_0 = (0.4 \pm 1.1) \times 10^{-5}$

Mineral	^{53}Cr/^{52}Cr	^{55}Mn/^{52}Cr

Intercept*	0.11339±0.00023	0±0.01	Intercept*	0.11339±0.00023	0±0.01
Olivine	0.11354±0.00026	11±1	Olivine	0.11343±0.00024	11±1
Olivine	0.11372±0.00027	26±1	Olivine	0.11343±0.00029	27±1
Olivine	0.11404±0.00045	40±2	Olivine	0.11361±0.00048	40±2

Imilac

$(^{53}Mn/^{55}Mn)_0 = (0.8 \pm 0.8) \times 10^{-5}$			$(^{53}Mn/^{55}Mn)_0 = (-0.3 \pm 0.9) \times 10^{-5}$		
Mineral	$^{53}Cr/^{52}Cr$	$^{55}Mn/^{52}Cr$	Mineral	$^{53}Cr/^{52}Cr$	$^{55}Mn/^{52}Cr$
Intercept*	0.11339±0.00023	0±0.01	Intercept*	0.11339±0.00023	0±0.01
Olivine	0.11345±0.00026	12±1	Olivine	0.11332±0.00028	12±1
Olivine	0.11364±0.00032	34±2	Olivine	0.11331±0.00034	34±2
Olivine	0.11380±0.00042	50±3	Olivine	0.11320±0.00044	50±3

Springwater

$(^{53}Mn/^{55}Mn)_0 = (0.9 \pm 0.6) \times 10^{-5}$			$(^{53}Mn/^{55}Mn)_0 = (0.3 \pm 0.5) \times 10^{-5}$		
Mineral	$^{53}Cr/^{52}Cr$	$^{55}Mn/^{52}Cr$	Mineral	$^{53}Cr/^{52}Cr$	$^{55}Mn/^{52}Cr$
Intercept*	0.11339±0.00023	0±0.01	Intercept*	0.11339±0.00023	0±0.01
Olivine	0.11347±0.00034	17±1	Olivine	0.11331±0.00031	17±1
Olivine	0.11362±0.00023	42±2	Olivine	0.11354±0.00020	42±2
Olivine	0.11439±0.00059	91±5	Olivine	0.11352±0.00052	91±5

* Although minerals with low Mn/Cr ratios such as chromite and troilite were measured and the data were reported in Hsu (2005), the regressions were done using the $^{53}Cr/^{52}Cr$ ratio for normal chromium with an uncertainty derived from the standard measurements. We followed the same procedure during the recalculation so as not to introduce differences between the two calculations.

Table Appendix C.2: ^{60}Fe-^{60}Ni sulfide data Tachibana & Huss (2003b)

As published **Recalculated**

Bishunpur 2359-6-Tr41

$(^{60}Fe/^{56}Fe)_0 = (1.10 \pm 0.32) \times 10^{-7}$*			$(^{60}Fe/^{56}Fe)_0 = (0.16 \pm 0.37) \times 10^{-7}$		
Mineral	$^{60}Ni/^{61}Ni$	$^{56}Fe/^{61}Ni$ ($\times 10^4$)	Mineral	$^{60}Ni/^{61}Ni$	$^{56}Fe/^{61}Ni$ ($\times 10^4$)
Metal	23.07±0.10	0.142±0.016	Metal	23.06±0.04	0.147±0.015
Metal	23.09±0.14	0.152±0.018	Metal	23.08±0.05	0.168±0.017
Metal	23.16±0.09	0.193±0.022	Metal	23.13±0.03	0.194±0.019
Troilite	23.15±0.08	4.21±0.20	Troilite	23.18±0.07	3.50±0.18
Troilite	23.14±0.19	13.3±0.7	Troilite	23.11±0.09	5.41±0.27

Troilite	23.79±0.44	479±19	Troilite	23.51±0.54	477±19
Troilite	23.81±0.93	572±23	Troilite	23.04±1.08	550±22
Troilite	23.77±0.36	628±24	Troilite	23.30±0.44	590±24
Troilite	24.55±0.54	652±26	Troilite	23.72±0.57	598±24
Troilite	23.36±0.53	702±27	Troilite	22.87±0.62	698±28
Troilite	23.87±0.46	778±30	Troilite	22.85±0.50	761±30

^{62}Ni Normalization

Bishunpur 2359-6-Tr41

$(^{60}Fe/^{56}Fe)_0 = (0.12 \pm 0.40)\times10^{-7}$			$(^{60}Fe/^{56}Fe)_0 = (0.21 \pm 0.63)\times10^{-7}$		
Mineral	$^{60}Ni/^{62}Ni$	$^{56}Fe/^{62}Ni$ ($\times10^4$)	Mineral	$^{60}Ni/^{62}Ni$	$^{56}Fe/^{62}Ni$ ($\times10^4$)
Metal	7.22±0.03	0.045±0.041	Metal	7.26±0.02	0.047±0.042
Metal	7.23±0.06	0.048±0.043	Metal	7.27±0.03	0.053±0.048
Metal	7.25±0.04	0.062±0.056	Metal	7.28±0.02	0.062±0.056
Troilite	7.29±0.19	1.34±0.07	Troilite	7.30±0.04	1.11±0.06
Troilite	7.29±0.10	4.18±0.21	Troilite	7.28±0.05	1.69±0.08
Troilite	7.41±0.14	155±6	Troilite	7.43±0.29	148±6
Troilite	7.12±0.42	184±7	Troilite	7.26±0.58	174±7
Troilite	7.26±0.12	202±8	Troilite	7.34±0.24	186±7
Troilite	7.34±0.34	209±8	Troilite	7.47±0.31	189±8
Troilite	7.13±0.18	230±9	Troilite	7.21±0.34	224±9
Troilite	7.09±0.39	252±10	Troilite	7.19±0.28	243±10

Bishunpur 2359-6-Tr2

$(^{60}Fe/^{56}Fe)_0 = (1.06 \pm 0.66)\times10^{-7}$*			$(^{60}Fe/^{56}Fe)_0 = (-0.04 \pm 0.79)\times10^{-7}$		
Mineral	$^{60}Ni/^{61}Ni$	$^{56}Fe/^{61}Ni$ ($\times10^4$)	Mineral	$^{60}Ni/^{61}Ni$	$^{56}Fe/^{61}Ni$ ($\times10^4$)
Metal	23.08±0.05	0.119±0.005	Metal	23.07±0.05	0.119±0.005
Troilite	23.12±0.15	26.8±3.0	Troilite	23.16±0.16	19.8±2.0
Troilite	23.11±0.12	55.9±3.8	Troilite	23.07±0.13	46.6±3.1
Troilite	23.31±0.19	87.7±6.0	Troilite	23.35±0.20	61.1±4.1
Troilite	23.43±0.25	362±17	Troilite	22.98±0.28	349±16

^{62}Ni Normalization

Bishunpur 2359-6-Tr2

$(^{60}Fe/^{56}Fe)_0 = (-0.28 \pm 1.17)\times10^{-7}$			$(^{60}Fe/^{56}Fe)_0 = (-0.04 \pm 1.36)\times10^{-7}$		
Mineral	$^{60}Ni/^{62}Ni$	$^{56}Fe/^{62}Ni$ ($\times10^4$)	Mineral	$^{60}Ni/^{62}Ni$	$^{56}Fe/^{62}Ni$ ($\times10^4$)

Metal	7.27±0.03	0.038±0.001	Metal	7.26±0.03	0.038±0.001
Troilite	7.27±0.08	8.50±0.96	Troilite	7.29±0.09	6.22±0.62
Troilite	7.26±0.07	17.9±1.2	Troilite	7.27±0.07	14.9±1.0
Troilite	7.30±0.11	28.0±1.9	Troilite	7.35±0.11	18.8±1.3
Troilite	7.22±0.14	116±6	Troilite	7.23±0.16	112±5

Bishunpur 2359-6-Tr47

$(^{60}Fe/^{56}Fe)_0 = (1.28 \pm 0.67)\times10^{-7}$*			$(^{60}Fe/^{56}Fe)_0 = (0.46 \pm 0.79)\times10^{-7}$		
Mineral	$^{60}Ni/^{61}Ni$	$^{56}Fe/^{61}Ni$ ($\times10^4$)	Mineral	$^{60}Ni/^{61}Ni$	$^{56}Fe/^{61}Ni$ ($\times10^4$)
Metal	23.10±0.05	0.142±0.005	Metal	23.09±0.06	0.142±0.005
Troilite	23.10±0.14	12.8±1.6	Troilite	23.10±0.16	12.6±1.5
Troilite	23.15±0.18	29.8±2.7	Troilite	23.10±0.21	29.6±2.6
Troilite	23.14±0.23	82.9±10.6	Troilite	23.14±0.23	66±7.9
Troilite	22.93±0.34	125±15	Troilite	22.91±0.40	119±14
Troilite	23.30±0.21	204±12	Troilite	23.02±0.24	199±11
Troilite	23.64±0.27	283±31	Troilite	23.46±0.30	267±28
Troilite	23.44±0.59	305±33	Troilite	23.24±0.67	301±32

^{62}Ni Normalization

Bishunpur 2359-6-Tr47

$(^{60}Fe/^{56}Fe)_0 = (0.36 \pm 1.16)\times10^{-7}$			$(^{60}Fe/^{56}Fe)_0 = (0.37 \pm 1.34)\times10^{-7}$		
Mineral	$^{60}Ni/^{62}Ni$	$^{56}Fe/^{62}Ni$ ($\times10^4$)	Mineral	$^{60}Ni/^{62}Ni$	$^{56}Fe/^{62}Ni$ ($\times10^4$)
Metal	7.27±0.05	0.045±0.001	Metal	7.27±0.03	0.045±0.001
Troilite	7.27±0.14	4.04±0.49	Troilite	7.27±0.09	3.95±0.47
Troilite	7.28±0.18	9.38±0.86	Troilite	7.27±0.11	9.33±0.83
Troilite	7.25±0.23	26.6±3.4	Troilite	7.29±0.12	20.8±2.5
Troilite	7.17±0.34	40.2±5.0	Troilite	7.21±0.22	37.8±4.5
Troilite	7.23±0.21	65.2±3.8	Troilite	7.25±0.13	63.2±3.5
Troilite	7.41±0.27	88.1±9.6	Troilite	7.36±0.16	83.3±8.8
Troilite	7.32±0.59	95.6±10.3	Troilite	7.31±0.36	94.6±10.1

Krymka 1729-3-Tr1

$(^{60}Fe/^{56}Fe)_0 = (1.82 \pm 0.78)\times10^{-7}$*			$(^{60}Fe/^{56}Fe)_0 = (-0.23 \pm 0.96)\times10^{-7}$		
Mineral	$^{60}Ni/^{61}Ni$	$^{56}Fe/^{61}Ni$ ($\times10^4$)	Mineral	$^{60}Ni/^{61}Ni$	$^{56}Fe/^{61}Ni$ ($\times10^4$)

Metal	23.09±0.07	0.133±0.007	Metal	23.09±0.07	0.129±0.008
Troilite	23.41±0.35	182±13	Troilite	23.24±0.47	164±11
Troilite	23.40±0.37	212±13	Troilite	23.00±0.46	207±12
Troilite	24.17±0.79	406±29	Troilite	23.45±0.94	398±28
Troilite	24.98±1.16	1104±63	Troilite	22.45±1.19	946±57

^{62}Ni Normalization

Krymka 1729-3-Tr1

$(^{60}Fe/^{56}Fe)_0 = (-0.61 \pm 1.34)\times10^{-7}$			$(^{60}Fe/^{56}Fe)_0 = (-0.12 \pm 1.67)\times10^{-7}$		
Mineral	$^{60}Ni/^{62}Ni$	$^{56}Fe/^{62}Ni$ ($\times10^4$)	Mineral	$^{60}Ni/^{62}Ni$	$^{56}Fe/^{62}Ni$ ($\times10^4$)
Metal	7.27±0.04	0.042±0.003	Metal	7.27±0.04	0.041±0.002
Troilite	7.31±0.20	57.7±4.0	Troilite	7.32±0.25	51.9±2.0
Troilite	7.22±0.21	67.5±4.1	Troilite	7.24±0.25	65.6±2.4
Troilite	7.36±0.45	130±9	Troilite	7.39±0.51	125±8.7
Troilite	6.87±0.61	340±20	Troilite	7.11±0.65	292±18

Krymka 1729-3-Tr12

$(^{60}Fe/^{56}Fe)_0 = (1.64 \pm 0.93)\times10^{-7}$*			$(^{60}Fe/^{56}Fe)_0 = (-0.12 \pm 0.96)\times10^{-7}$		
Mineral	$^{60}Ni/^{61}Ni$	$^{56}Fe/^{61}Ni$ ($\times10^4$)	Mineral	$^{60}Ni/^{61}Ni$	$^{56}Fe/^{61}Ni$ ($\times10^4$)
Troilite	23.10±0.12	3.83±0.36	Troilite	23.09±0.13	3.82±0.38
Troilite	23.11±0.39	42.9±4.2	Troilite	23.00±0.41	42.2±4.2
Troilite	25.71±1.45	1590±157	Troilite	22.94±1.44	1502±150

^{62}Ni Normalization

Krymka 1729-3-Tr12

$(^{60}Fe/^{56}Fe)_0 = (-0.71 \pm 1.57)\times10^{-7}$			$(^{60}Fe/^{56}Fe)_0 = (-0.12 \pm 1.65)\times10^{-7}$		
Mineral	$^{60}Ni/^{62}Ni$	$^{56}Fe/^{62}Ni$ ($\times10^4$)	Mineral	$^{60}Ni/^{62}Ni$	$^{56}Fe/^{62}Ni$ ($\times10^4$)
Troilite	7.27±0.06	1.21±0.12	Troilite	7.27±0.07	1.21±0.12
Troilite	7.24±0.22	13.7±1.4	Troilite	7.24±0.22	13.5±1.3
Troilite	6.91±0.81	522±52	Troilite	7.22±0.78	477±48

*Initial ratios published in Huss and Tachibana (2003b) were calculated using errors corrected for the correlated component. For easier comparison, we calculated all regressions using the measured errors for each ratio.

Table Appendix C.3: ^{53}Mn-^{53}Cr sulfide data (Guan et al. 2007)

As published * **Recalculated**

MAC88136 M3641-1

$(^{53}Mn/^{55}Mn)_0 = (4.56\pm0.75)\times10^{-7}$			$(^{53}Mn/^{55}Mn)_0 = (3.42\pm0.83)\times10^{-7}$		
Mineral	$^{53}Cr/^{52}Cr$	$^{55}Mn/^{52}Cr$	Mineral	$^{53}Cr/^{52}Cr$	$^{55}Mn/^{52}Cr$
Tr-1a	0.1120±0.0003	0.093±0.009	Tr-1a	0.1120±0.0003	0.093±0.009
Tr-1b	0.1122±0.0005	0.093±0.009	Tr-1b	0.1122±0.0005	0.093±0.009
Sphal-1a	0.1152±0.0027	11016±1102	Sphal-1a	0.1136±0.0027	10176±1018
Sphal-1b	0.132±0.015	45160±4516	Sphal-1b	0.127±0.015	41955±4195
Sphal-1c	0.1412±0.0059	54991±5499	Sphal-1c	0.1349±0.0064	51174±5117
Sphal-1d	0.1247±0.0044	32788±3279	Sphal-1d	0.1207±0.0045	30380±3038
Sphal-2a	0.1220±0.0042	17492±1749	Sphal-2a	0.1187±0.0045	16181±1618
Sphal-2b	0.1175±0.0037	12119±1212	Sphal-2b	0.1154±0.0041	11692±1169
Sphal-2c	0.1148±0.0036	9628±963	Sphal-2c	0.1121±0.0039	9245±924

MAC88136 M3645-5

$(^{53}Mn/^{55}Mn)_0 = (1.75\pm0.50)\times10^{-7}$			$(^{53}Mn/^{55}Mn)_0 = (0.41\pm0.58)\times10^{-7}$		
Mineral	$^{53}Cr/^{52}Cr$	$^{55}Mn/^{52}Cr$	Mineral	$^{53}Cr/^{52}Cr$	$^{55}Mn/^{52}Cr$
Tr-1a	0.1120±0.0003	0.079±0.009	Tr-1a	0.1120±0.0003	0.080±0.008
Tr-1b	0.1122±0.0005	0.079±0.009	Tr-1b	0.1123±0.0005	0.079±0.008
Sphal-1a	0.129±0.011	67680±6768	Sphal-1a	0.120±0.012	58117±5812
Sphal-1b	0.1231±0.0071	65761±6576	Sphal-1b	0.1134±0.0072	58896±5890
Sphal-1c	0.1314±0.0085	71788±7179	Sphal-1c	0.1199±0.0085	63340±6334
Sphal-2a	0.1231±0.0076	74210±7421	Sphal-2a	0.1139±0.0076	64240±6424
Sphal-2b	0.1223±0.0079	71925±7193	Sphal-2b	0.1129±0.0079	63708±6371
Sphal-2c	0.1134±0.0056	31020±3102	Sphal-2c	0.1091±0.0056	24385±2438

* We were not able to precisely reproduce the published numbers, most likely due to slight differences in editing the data. The same data reduction was used for both mean of ratios and total counts so data can be directly compared.

Table Appendix C.4: ^{60}Fe-^{60}Ni sulfide data (Guan et al. 2007)

As published*

MAC88136 M3641-2

$(^{60}Fe/^{56}Fe)_0 = (8.5 \pm 6.1)\times10^{-7}$

Mineral	^{60}Ni/^{61}Ni	^{56}Fe/^{61}Ni (×10^4)
FeNi-1a	23.15±0.13	0.115±0.012
FeNi-1b	23.21±0.13	0.146±0.015
FeNi-2a	23.12±0.16	0.138±0.014
FeNi-3b	23.17±0.16	0.113±0.011
FeNi-3a	23.09±0.13	0.132±0.013
Tr-1a	24.54±0.97	84.4±8.4
Tr-1b	23.58±57	80.7±8.1

^{62}Ni Normalization

MAC88136 M3641-2

$(^{60}Fe/^{56}Fe)_0 = (0.4 \pm 10.0)\times10^{-7}$

Mineral	^{60}Ni/^{62}Ni	^{56}Fe/^{62}Ni (×10^4)
FeNi-1a	7.31±0.06	0.037±0.004
FeNi-1b	7.33±0.07	0.046±0.005
FeNi-2a	7.28±0.09	0.044±0.004
FeNi-3b	7.31±0.04	0.036±0.004
FeNi-3a	7.30±0.05	0.042±0.004
Tr-1a	7.32±0.53	26.5±2.7
Tr-1b	7.32±0.29	25.6±2.6

Qingzhen QZ02-03

$(^{60}Fe/^{56}Fe)_0 = (6.1 \pm 2.1)\times10^{-7}$

Mineral	^{60}Ni/^{61}Ni	^{56}Fe/^{61}Ni (×10^4)
CDT-1a	23.02±0.11	0.317±0.032
CDT-2a	22.95±0.08	0.318±0.032
CDT-2b	23.09±0.12	0.311±0.031
CDT-3a	23.11±0.08	0.318±0.032

Recalculated

MAC88136 M3641-2

$(^{60}Fe/^{56}Fe)_0 = (1.8 \pm 9.0)\times10^{-7}$

Mineral	^{60}Ni/^{61}Ni	^{56}Fe/^{61}Ni (×10^4)
FeNi-1a	23.03±0.09	0.115±0.012
FeNi-1b	23.09±0.11	0.145±0.015
FeNi-2a	23.03±0.11	0.138±0.014
FeNi-3b	23.08±0.07	0.113±0.011
FeNi-3a	23.13±0.07	0.132±0.013
Tr-1a	23.31±1.34	81.2±8.1
Tr-1b	23.19±0.87	80.6±8.1

$(^{60}Fe/^{56}Fe)_0 = (1.8 \pm 14)\times10^{-7}$

Mineral	^{60}Ni/^{62}Ni	^{56}Fe/^{62}Ni (×10^4)
FeNi-1a	7.27±0.05	0.037±0.004
FeNi-1b	7.29±0.06	0.046±0.005
FeNi-2a	7.27±0.06	0.044±0.004
FeNi-3b	7.28±0.03	0.036±0.004
FeNi-3a	7.30±0.04	0.042±0.004
Tr-1a	7.36±0.66	25.9±2.6
Tr-1b	7.32±0.42	25.9±2.6

$(^{60}Fe/^{56}Fe)_0 = (-4.2 \pm 2.9)\times10^{-7}$

Mineral	^{60}Ni/^{61}Ni	^{56}Fe/^{61}Ni (×10^4)
CDT-1a	23.03±0.09	0.315±0.031
CDT-2a	22.95±0.09	0.317±0.032
CDT-2b	23.08±0.08	0.311±0.031
CDT-3a	23.11±0.09	0.316±0.032

CDT-3b	23.15±0.09	0.311±0.031	CDT-3b	23.15±0.08	0.311±0.031
CDT-4a	23.17±0.10	0.318±0.032	CDT-4a	23.15±0.09	0.316±0.032
CDT-4b	23.01±0.13	0.311±0.031	CDT-4b	23.02±0.08	0.311±0.031
Sph-1a	24.92±0.91	414±41	Sph-1a	20.58±2.05	354±35
Sph-1b	28.11±1.79	667±67	Sph-1b	22.53±2.83	588±59
Sph-1c	26.33±3.15	656±66	Sph-1c	19.16±2.95	560±56
Sph-1d	26.38±2.88	447±45	Sph-1d	23.22±4.22	396±40
Sph-1e	23.54±2.52	55.6±5.6	Sph-1e	23.16±0.53	13.1±1.3

^{62}Ni Normalization

Qingzhen QZ02-03

$(^{60}Fe/^{56}Fe)_0 = (-6.7 \pm 3.6)\times10^{-7}$			$(^{60}Fe/^{56}Fe)_0 = (-3.7 \pm 3.6)\times10^{-7}$		
Mineral	$^{60}Ni/^{62}Ni$	$^{56}Fe/^{62}Ni$ ($\times10^4$)	Mineral	$^{60}Ni/^{62}Ni$	$^{56}Fe/^{62}Ni$ ($\times10^4$)
CDT-1a	5.97±0.04	0.099±0.010	CDT-1a	7.27±0.044	0.098±0.010
CDT-2a	7.24±0.04	0.101±0.010	CDT-2a	7.24±0.044	0.100±0.010
CDT-2b	7.28±0.04	0.097±0.010	CDT-2b	7.28±0.038	0.097±0.010
CDT-3a	7.29±0.04	0.100±0.010	CDT-3a	7.29±0.044	0.099±0.010
CDT-3b	7.30±0.04	0.097±0.010	CDT-3b	7.30±0.039	0.097±0.010
CDT-4a	7.30±0.04	0.100±0.010	CDT-4a	7.30±0.044	0.099±0.010
CDT-4b	7.26±0.04	0.097±0.010	CDT-4b	7.26±0.040	0.097±0.010
Sph-1a	5.97±1.04	139±14	Sph-1a	6.44±1.11	120±12
Sph-1b	6.64±1.37	232±23	Sph-1b	7.10±1.45	196±20
Sph-1c	5.09±1.66	254±25	Sph-1c	5.92±1.67	194±19
Sph-1d	6.29±2.06	167±17	Sph-1d	7.33±2.15	131±13
Sph-1e	6.88±0.48	18.7±1.9	Sph-1e	7.31±0.26	4.2±0.4

* These data ratios do not match the values published by Guan et al. (2007) because we were unable to fully duplicate the original data reduction. The data in these tables differ only in the method of ratio calculation and are directly comparable.

Table Appendix C.5: ^{60}Fe-^{60}Ni chondrule data (Tachibana et al. 2006)

As published *

Recalculated

Semarkona SMK 1-4

$(^{60}Fe/^{56}Fe)_0 = (2.7 \pm 1.0)\times10^{-7}$			$(^{60}Fe/^{56}Fe)_0 = (0.7 \pm 1.1)\times10^{-7}$		
Mineral	$^{60}Ni/^{61}Ni$	$^{56}Fe/^{61}Ni$ ($\times10^4$)	Mineral	$^{60}Ni/^{61}Ni$	$^{56}Fe/^{61}Ni$ ($\times10^4$)
Silicate[1]	23.09±0.05	0.195±0.019	Silicate[1]	23.11±0.04	0.194±0.019

Silicate[1]	23.09±0.11	0.373±0.037	Silicate[1]	23.09±0.11	0.364±0.036
Silicate	23.13±0.40	36.5±3.7	Silicate	23.02±0.48	34.8±3.5
Silicate	23.23±0.23	57.8±5.8	Silicate	23.17±0.25	55.6±5.6
Silicate	23.25±0.22	58.1±5.8	Silicate	23.22±0.22	51.7±5.2
Silicate	23.63±0.55	95.8±9.6	Silicate	23.35±0.67	93.8±9.4
Silicate	23.36±0.29	130±13	Silicate	23.13±0.32	126±13
Silicate	23.37±0.60	156±16	Silicate	23.06±0.66	149±15
Silicate	23.71±0.74	159±16	Silicate	23.16±0.83	155±15
Silicate	23.85±0.42	183±18	Silicate	23.35±0.47	169±17
Silicate	23.55±0.37	185±18	Silicate	23.17±0.41	175±18
Silicate	23.48±0.37	189±19	Silicate	23.19±0.41	181±18

^{62}Ni Normalization

Semarkona SMK 1-4

$(^{60}Fe/^{56}Fe)_0 = (0.2 \pm 1.6)\times10^{-7}$ $(^{60}Fe/^{56}Fe)_0 = (0.7 \pm 1.8)\times10^{-7}$

Mineral	^{60}Ni/^{62}Ni	^{56}Fe/^{62}Ni (×10^4)	Mineral	^{60}Ni/^{62}Ni	^{56}Fe/^{62}Ni (×10^4)
Silicate[1]	7.30±0.03	0.062±0.006	Silicate[1]	7.31±0.02	0.061±0.006
Silicate[1]	7.27±0.06	0.118±0.012	Silicate[1]	7.27±0.04	0.115±0.012
Silicate	7.24±0.22	11.5±1.2	Silicate	7.24±0.18	11.3±1.1
Silicate	7.31±0.12	18.1±1.8	Silicate	7.32±0.13	17.5±1.7
Silicate	7.33±0.11	18.2±1.8	Silicate	7.34±0.11	16.2±1.6
Silicate	7.33±0.29	30.1±3.0	Silicate	7.35±0.24	29.5±3.0
Silicate	7.30±0.15	40.7±4.1	Silicate	7.31±0.17	39.4±3.9
Silicate	7.23±0.31	48.8±4.9	Silicate	7.29±0.35	46.8±4.7
Silicate	7.22±0.41	50.2±5.0	Silicate	7.29±0.30	48.8±4.9
Silicate	7.37±0.21	56.9±5.7	Silicate	7.38±0.24	53.0±5.3
Silicate	7.27±0.19	57.8±5.8	Silicate	7.32±0.22	55.0±5.5
Silicate	7.30±0.19	59.1±5.9	Silicate	7.33±0.21	56.6±5.7

Semarkona SMK 2-1

$(^{60}Fe/^{56}Fe)_0 = (2.0 \pm 1.1)\times10^{-7}$ $(^{60}Fe/^{56}Fe)_0 = (-1.3 \pm 1.5)\times10^{-7}$

Mineral	^{60}Ni/^{61}Ni	^{56}Fe/^{61}Ni (×10^4)	Mineral	^{60}Ni/^{61}Ni	^{56}Fe/^{61}Ni (×10^4)
Silicate[1]	23.15±0.04	0.171±0.017	Silicate[1]	23.12±0.02	0.163±0.016
Silicate	23.34±0.64	123±12	Silicate	23.20±0.65	80.4±8.0
Silicate	23.62±0.65	137±14	Silicate	22.90±0.72	117±12

Silicate	23.44±0.51	146±15	Silicate	23.04±0.53	116±12
Silicate	23.38±0.47	176±18	Silicate	22.96±0.47	130±13
Silicate	23.47±0.50	186±19	Silicate	23.06±0.42	86.1±8.6
Silicate	23.63±0.57	260±26	Silicate	22.98±0.48	146±15
Silicate	23.79±1.10	265±27	Silicate	22.51±1.27	256±26
Silicate	23.87±0.81	269±27	Silicate	22.72±0.76	215±21

^{62}Ni Normalization

Semarkona SMK 2-1

$(^{60}Fe/^{56}Fe)_0 = (-4.7 \pm 2.0)\times10^{-7}$			$(^{60}Fe/^{56}Fe)_0 = (-1.3 \pm 2.6)\times10^{-7}$		
Mineral	$^{60}Ni/^{62}Ni$	$^{56}Fe/^{62}Ni$ ($\times10^4$)	Mineral	$^{60}Ni/^{62}Ni$	$^{56}Fe/^{62}Ni$ ($\times10^4$)
Silicate[1]	7.32±0.02	0.054±0.005	Silicate[1]	7.31±0.01	0.052±0.005
Silicate	7.23±0.35	39.2±3.9	Silicate	7.33±0.34	25.1±2.5
Silicate	6.89±0.36	44.1±4.4	Silicate	7.24±0.38	36.8±3.7
Silicate	7.07±0.27	46.4±4.6	Silicate	7.28±0.28	36.6±3.7
Silicate	7.08±0.26	55.4±5.5	Silicate	7.26±0.25	40.7±4.1
Silicate	7.09±0.28	59.5±5.9	Silicate	7.29±0.22	27.1±2.7
Silicate	7.12±0.31	81.7±8.2	Silicate	7.26±0.25	45.7±4.6
Silicate	6.44±0.61	84.1±8.4	Silicate	7.12±0.68	81.2±8.1
Silicate	6.83±0.41	85.0±8.5	Silicate	7.18±0.41	68.5±6.8

Semarkona SMK 2-4

$(^{60}Fe/^{56}Fe)_0 = (2.8 \pm 2.3)\times10^{-7}$			$(^{60}Fe/^{56}Fe)_0 = (-0.2 \pm 2.8)\times10^{-7}$		
Mineral	$^{60}Ni/^{61}Ni$	$^{56}Fe/^{61}Ni$ ($\times10^4$)	Mineral	$^{60}Ni/^{61}Ni$	$^{56}Fe/^{61}Ni$ ($\times10^4$)
Silicate[1]	23.12±0.10	0.00016±0.00002	Silicate[1]	23.12±0.08	0.00016±0.00002
Silicate	22.99±0.20	18.0±1.8	Silicate	22.96±0.20	16.2±1.6
Silicate	23.11±0.25	44.2±4.4	Silicate	23.04±0.26	33.6±3.4
Silicate	23.33±0.34	60.7±6.1	Silicate	23.12±0.30	31.1±3.1
Silicate	23.58±0.53	116±12	Silicate	23.27±0.49	81.7±8.2
Silicate	23.44±0.50	142±14	Silicate	23.09±0.58	130±13
Silicate	23.76±0.77	174±17	Silicate	23.05±0.85	163±16

^{62}Ni Normalization

Semarkona SMK 2-4

$(^{60}Fe/^{56}Fe)_0 = (-1.4 \pm 3.8)\times10^{-7}$			$(^{60}Fe/^{56}Fe)_0 = (-0.2 \pm 4.7)\times10^{-7}$		
Mineral	$^{60}Ni/^{62}Ni$	$^{56}Fe/^{62}Ni$ ($\times10^4$)	Mineral	$^{60}Ni/^{62}Ni$	$^{56}Fe/^{62}Ni$ ($\times10^4$)
Silicate*	7.30±0.05	0.00005±0.00001	Silicate[1]	7.31±0.04	0.000049±0.000005
Silicate	7.24±0.10	5.65±0.56	Silicate	7.26±0.11	5.12±0.51
Silicate	7.22±0.13	13.8±1.4	Silicate	7.28±0.14	10.5±1.1
Silicate	7.36±0.18	18.9±1.9	Silicate	7.31±0.16	9.78±0.98
Silicate	7.24±0.27	36.2±3.6	Silicate	7.35±0.26	25.6±2.6
Silicate	7.28±0.28	44.4±4.4	Silicate	7.30±0.30	40.8±4.1
Silicate	7.18±0.40	54.8±5.5	Silicate	7.29±0.45	51.3±5.1

Bishunpur BIS-21

$(^{60}Fe/^{56}Fe)_0 = (4.4 \pm 2.5)\times10^{-7}$			$(^{60}Fe/^{56}Fe)_0 = (-1.7 \pm 2.7)\times10^{-7}$		
Mineral	$^{60}Ni/^{61}Ni$	$^{56}Fe/^{61}Ni$ ($\times10^4$)	Mineral	$^{60}Ni/^{61}Ni$	$^{56}Fe/^{61}Ni$ ($\times10^4$)
Silicate[1]	23.15±0.12	1.52±0.15	Silicate[1]	23.22±0.08	1.35±0.13
Silicate	23.19±0.35	35.3±3.5	Silicate	22.66±0.32	31.1±3.1
Silicate	23.15±0.36	39.1±3.9	Silicate	22.90±0.38	36.9±3.7
Silicate	23.22±0.34	40.5±4.0	Silicate	23.10±0.38	38.5±3.8
Silicate	24.19±0.62	164±16	Silicate	23.53±0.72	160±16
Silicate	23.59±0.96	178±18	Silicate	22.51±1.05	166±17
Silicate	23.96±0.82	200±20	Silicate	23.16±0.89	194±19

^{62}Ni Normalization

Bishunpur BIS-21

$(^{60}Fe/^{56}Fe)_0 = (-3.5 \pm 4.0)\times10^{-7}$			$(^{60}Fe/^{56}Fe)_0 = (-1.6 \pm 4.6)\times10^{-7}$		
Mineral	$^{60}Ni/^{62}Ni$	$^{56}Fe/^{62}Ni$ ($\times10^4$)	Mineral	$^{60}Ni/^{62}Ni$	$^{56}Fe/^{62}Ni$ ($\times10^4$)
Silicate[1]	7.32±0.06	0.48±0.05	Silicate[1]	7.34±0.04	0.42±0.04
Silicate	7.21±0.18	11.1±1.1	Silicate	7.16±0.17	9.9±1.0
Silicate	7.25±0.19	12.3±1.2	Silicate	7.24±0.20	11.7±1.2
Silicate	7.27±0.18	12.6±1.3	Silicate	7.30±0.20	12.1±1.2
Silicate	7.24±0.32	50.9±5.1	Silicate	7.44±0.37	49.8±5.0
Silicate	6.77±0.50	57.5±5.7	Silicate	7.11±0.57	53.3±5.3
Silicate	7.24±0.42	62.5±6.3	Silicate	7.32±0.47	61.0±6.1

[1]silicate plus metal and/or sulfide

* These data ratios do not match the values published by Tachibana et al. (2006) because we were unable to fully duplicate the original data reduction. The data in these tables differ only in the method of ratio calculation and are directly comparable.

Table Appendix C.6: ^{60}Fe-^{60}Ni chondrule data (Tachibana et al. 2007; Tachibana et al. 2009; Telus et al. 2011)

Mean of Ratios **Total counts**

Bishunpur BIS 32

$(^{60}Fe/^{56}Fe)_0 = (1.9 \pm 1.1)\times10^{-7}$*			$(^{60}Fe/^{56}Fe)_0 = (0.0 \pm 1.2)\times10^{-7}$		
Mineral	$^{60}Ni/^{61}Ni$	$^{56}Fe/^{61}Ni$ ($\times10^4$)	Mineral	$^{60}Ni/^{61}Ni$	$^{56}Fe/^{61}Ni$ ($\times10^4$)
Silicate	23.30±0.34	45.0±4.5	Silicate	23.16±0.37	43.8±4.4
Silicate	23.09±0.02	0.618±0.062	Silicate	23.09±0.02	0.618±0.062
Silicate	23.16±0.22	40.4±4.0	Silicate	23.09±0.26	39.4±3.9
Silicate	23.70±0.44	119±12	Silicate	23.42±0.45	119±12
Silicate	23.33±0.43	99.7±10.0	Silicate	23.11±0.43	98.1±9.8
Silicate	23.33±0.29	62.2±6.2	Silicate	23.20±0.32	62.3±6.2
Silicate	23.04±0.38	94.1±9.4	Silicate	22.91±0.42	89.0±8.9
Silicate	23.37±0.41	87.0±8.7	Silicate	23.13±0.42	85.2±8.5
Silicate	22.98±0.26	33.0±3.3	Silicate	22.94±0.19	18.1±1.8
Silicate	23.14±0.35	103±10	Silicate	22.96±0.38	102±10
Silicate	23.11±0.02	0.090±0.009	Silicate	23.11±0.01	0.089±0.009
Silicate	23.25±0.38	53.4±5.3	Silicate	23.15±0.40	51.2±5.1
Silicate	23.06±0.41	125±12	Silicate	22.80±0.40	122±12
Silicate	23.27±0.32	82.0±8.2	Silicate	23.20±0.38	79.6±8.0
Silicate	23.53±0.36	98.9±9.9	Silicate	23.41±0.40	94.5±9.4
Silicate	23.43±0.32	71.2±7.1	Silicate	23.29±0.36	69.8±7.0
Silicate	23.10±0.36	87.6±8.8	Silicate	22.95±0.37	81.0±8.1

*Data as published by Tachibana et al. (2007)

^{62}Ni Normalization

Bishunpur BIS 32

$(^{60}Fe/^{56}Fe)_0 = (-0.1 \pm 1.9)\times10^{-7}$			$(^{60}Fe/^{56}Fe)_0 = (0.1 \pm 2.1)\times10^{-7}$		
Mineral	$^{60}Ni/^{62}Ni$	$^{56}Fe/^{62}Ni$ ($\times10^4$)	Mineral	$^{60}Ni/^{62}Ni$	$^{56}Fe/^{62}Ni$ ($\times10^4$)
Silicate	7.29±0.18	14.2±1.4	Silicate	7.30±0.20	13.8±1.4
Silicate	7.28±0.01	0.197±0.020	Silicate	7.28±0.01	0.197±0.020
Silicate	7.28±0.11	12.7±1.3	Silicate	7.28±0.14	12.4±1.2

Silicate	7.39±0.22	37.1±3.7	Silicate	7.38±0.23	37.1±3.7
Silicate	7.26±0.22	31.4±3.1	Silicate	7.28±0.23	30.9±3.1
Silicate	7.31±0.14	19.5±2.0	Silicate	7.31±0.17	19.5±2.0
Silicate	7.20±0.20	29.8±3.0	Silicate	7.22±0.22	28.1±2.8
Silicate	7.28±0.21	27.3±2.7	Silicate	7.29±0.22	26.8±2.7
Silicate	7.22±0.13	10.4±1.0	Silicate	7.23±0.10	5.72±0.57
Silicate	7.23±0.19	32.8±3.3	Silicate	7.24±0.20	32.5±3.3
Silicate	7.28±0.01	0.029±0.003	Silicate	7.28±0.01	0.028±0.003
Silicate	7.29±0.19	16.7±1.7	Silicate	7.30±0.21	16.1±1.6
Silicate	7.18±0.22	39.4±3.9	Silicate	7.19±0.22	38.5±3.9
Silicate	7.30±0.16	25.7±2.6	Silicate	7.31±0.20	25.0±2.5
Silicate	7.36±0.18	31.1±3.1	Silicate	7.38±0.21	29.6±3.0
Silicate	7.35±0.17	22.3±2.2	Silicate	7.34±0.19	21.9±2.2
Silicate	7.23±0.19	27.7±2.8	Silicate	7.23±0.20	25.6±2.6

Semarkona SMK1-5

$(^{60}Fe/^{56}Fe)_0 = (3.2 \pm 1.6)\times10^{-7}$*			$(^{60}Fe/^{56}Fe)_0 = (0.1 \pm 1.9)\times10^{-7}$		
Mineral	$^{60}Ni/^{61}Ni$	$^{56}Fe/^{61}Ni$ ($\times10^4$)	Mineral	$^{60}Ni/^{61}Ni$	$^{56}Fe/^{61}Ni$ ($\times10^4$)
Silicate	23.70±0.43	94.7±9.5	Silicate	23.44±0.43	94.2±9.4
Silicate	23.37±0.28	31.4±3.1	Silicate	23.28±0.28	31.0±3.1
Silicate	23.08±0.36	59.6±6.0	Silicate	22.90±0.37	59.2±5.9
Silicate	23.20±0.35	73.0±7.3	Silicate	22.96±0.41	71.2±7.1
Silicate	23.14±0.16	9.39±0.94	Silicate	23.11±0.17	9.32±0.93
Silicate	23.44±0.42	41.8±4.2	Silicate	23.13±0.45	41.3±4.1
Silicate	23.94±0.48	70.2±7.0	Silicate	23.64±0.54	68.6±6.9
Silicate	23.24±0.48	54.9±5.5	Silicate	22.92±0.49	53.4±5.3
Silicate	22.24±0.24	32.3±3.2	Silicate	23.17±0.26	31.5±3.1
Silicate	23.57±0.42	64.1±6.4	Silicate	23.35±0.43	64.0±6.4
Silicate	22.94±0.17	29.8±3.0	Silicate	22.88±0.19	29.8±3.0
Silicate	23.12±0.05	0.68±0.07	Silicate	23.12±0.06	0.67±0.07
Silicate	23.61±0.34	80.5±8.1	Silicate	23.43±0.38	80.3±8.0
Silicate	23.02±0.25	30.0±3.0	Silicate	22.95±0.27	29.8±3.0
Silicate	22.95±0.35	65.8±6.6	Silicate	22.78±0.34	65.2±6.5
Silicate	22.96±0.26	35.6±3.6	Silicate	22.89±0.28	35.5±3.5
Silicate	23.47±0.37	75.6±7.6	Silicate	23.27±0.41	74.6±7.5
Silicate	23.29±0.36	82.7±8.3	Silicate	23.09±0.38	82.2±8.2

*Data as published by Tachibana et al. (2007)

^{62}Ni Normalization

Semarkona SMK1-5

$(^{60}Fe/^{56}Fe)_0 = (0.0 \pm 2.8)\times10^{-7}$			$(^{60}Fe/^{56}Fe)_0 = (0.1 \pm 3.1)\times10^{-7}$		
Mineral	$^{60}Ni/^{62}Ni$	$^{56}Fe/^{62}Ni$ ($\times10^4$)	Mineral	$^{60}Ni/^{62}Ni$	$^{56}Fe/^{62}Ni$ ($\times10^4$)
Silicate	7.36±0.22	29.3±2.9	Silicate	7.37±0.23	29.4±2.9
Silicate	7.31±0.15	9.78±0.98	Silicate	7.32±0.15	9.64±0.96
Silicate	7.19±0.18	18.8±1.9	Silicate	7.20±0.20	18.6±1.9
Silicate	7.24±0.18	22.8±2.3	Silicate	7.22±0.22	22.3±2.2
Silicate	7.27±0.08	2.94±0.29	Silicate	7.27±0.09	2.91±0.29
Silicate	7.29±0.22	13.0±1.3	Silicate	7.28±0.24	12.9±1.3
Silicate	7.42±0.25	21.4±2.1	Silicate	7.44±0.28	21.0±2.1
Silicate	7.19±0.25	17.2±1.7	Silicate	7.21±0.26	16.7±1.7
Silicate	7.29±0.13	10.1±1.0	Silicate	7.29±0.14	9.80±1.0
Silicate	7.36±0.22	19.8±2.0	Silicate	7.34±0.23	19.8±2.0
Silicate	7.19±0.09	9.37±0.94	Silicate	7.19±0.10	9.37±0.94
Silicate	7.27±0.03	0.213±0.021	Silicate	7.27±0.03	0.211±0.021
Silicate	7.37±0.18	25.1±2.5	Silicate	7.37±0.20	25.0±2.5
Silicate	7.21±0.13	9.41±0.94	Silicate	7.22±0.14	9.33±0.93
Silicate	7.15±0.18	20.7±2.1	Silicate	7.17±0.18	20.5±2.0
Silicate	7.19±0.14	11.2±1.1	Silicate	7.20±0.15	11.2±1.1
Silicate	7.33±0.19	23.5±2.3	Silicate	7.32±0.21	23.2±2.3
Silicate	7.26±0.18	25.8±2.6	Silicate	7.26±0.20	25.6±2.6

Semarkona SMK1-6

$(^{60}Fe/^{56}Fe)_0 = (0.5 \pm 4.2)\times10^{-7}$*			$(^{60}Fe/^{56}Fe)_0 = (0.6 \pm 3.2)\times10^{-7}$		
Mineral	$^{60}Ni/^{61}Ni$	$^{56}Fe/^{61}Ni$ ($\times10^4$)	Mineral	$^{60}Ni/^{61}Ni$	$^{56}Fe/^{61}Ni$ ($\times10^4$)
Silicate	23.19±0.15	13.6±1.4	Silicate	23.17±0.17	13.6±1.4
Silicate	22.94±0.14	17.3±1.7	Silicate	22.90±0.17	17.3±1.7
Silicate	23.20±0.10	13.0±1.3	Silicate	23.20±0.09	1.61±0.16
Silicate	23.12±0.12	7.10±0.71	Silicate	23.02±0.04	0.742±0.074
Silicate	23.03±0.19	17.4±1.7	Silicate	22.98±0.19	17.4±1.7
Silicate	23.08±0.20	16.4±1.6	Silicate	23.02±0.19	16.3±1.6

Silicate	23.04±0.18	15.2±1.5	Silicate	22.96±0.19	14.6±1.5
Silicate	23.10±0.16	15.9±1.6	Silicate	23.06±0.20	15.7±1.6
Silicate	23.22±0.13	5.55±0.56	Silicate	23.23±0.13	5.50±0.55
Silicate	22.91±0.41	41.3±4.1	Silicate	22.69±0.44	41.1±4.1
Silicate	23.32±0.18	19.6±2.0	Silicate	23.27±0.20	19.6±2.0
Silicate	23.11±0.25	15.1±1.5	Silicate	23.01±0.27	15.0±1.5
Silicate	23.11±0.22	17.0±1.7	Silicate	23.01±0.25	17.0±1.7
Silicate	23.20±0.19	16.5±1.6	Silicate	23.15±0.23	16.5±1.6
Silicate	23.21±0.23	15.4±1.5	Silicate	23.15±0.25	15.4±1.5
Silicate	23.21±0.22	15.7±1.6	Silicate	23.13±0.25	15.7±1.6
Silicate	23.39±0.23	15.7±1.6	Silicate	23.31±0.25	15.7±1.6
Silicate	23.08±0.17	18.4±1.8	Silicate	23.03±0.19	18.4±1.8
Silicate	23.03±0.18	17.3±1.7	Silicate	23.00±0.19	17.3±1.7
Silicate	23.27±0.21	17.4±1.7	Silicate	23.25±0.21	15.7±1.6
Silicate	23.17±0.14	9.02±0.90	Silicate	23.16±0.15	8.96±0.90
Silicate	23.08±0.20	16.8±1.7	Silicate	23.02±0.22	16.8±1.7
Silicate	23.11±0.24	18.1±1.8	Silicate	23.06±0.25	18.1±1.8
Silicate	23.23±0.18	17.4±1.7	Silicate	23.18±0.19	17.3±1.7
Silicate	23.26±0.21	15.6±1.6	Silicate	23.19±0.24	15.6±1.6
Silicate	23.17±0.26	18.9±1.9	Silicate	23.09±0.28	18.9±1.9
Silicate	22.95±0.24	16.0±1.6	Silicate	22.87±0.29	15.9±1.6
Silicate	23.09±0.07	1.44±0.14	Silicate	23.08±0.08	1.43±0.14
Silicate	23.22±0.15	10.1±1.0	Silicate	23.19±0.17	10.0±1.0
Silicate	23.20±0.27	20.0±2.0	Silicate	23.12±0.29	20.0±2.0
Silicate	23.21±0.60	66.0±6.6	Silicate	22.91±0.73	65.6±6.6
Silicate	23.11±0.21	18.1±1.8	Silicate	23.05±0.21	18.1±1.8

* These data ratios do not match the values published by Tachibana et al. (2007) because we were unable to fully duplicate the original data reduction. The data for this chondrule are consistent with those published by Mishra et al. (2010). The data in these tables differ only in the method of ratio calculation and are directly comparable.

^{62}Ni Normalization

Semarkona SMK1-6

$(^{60}Fe/^{56}Fe)_0 = (-3.9 \pm 7.1)\times10^{-7}$			$(^{60}Fe/^{56}Fe)_0 = (0.6 \pm 5.4)\times10^{-7}$		
Mineral	$^{60}Ni/^{62}Ni$	$^{56}Fe/^{62}Ni$ ($\times10^4$)	Mineral	$^{60}Ni/^{62}Ni$	$^{56}Fe/^{62}Ni$ ($\times10^4$)
Silicate	7.30±0.08	4.30±0.43	Silicate	7.29±0.09	4.28±0.43
Silicate	7.22±0.07	5.47±0.55	Silicate	7.20±0.09	5.46±0.55
Silicate	7.31±0.05	3.83±0.38	Silicate	7.30±0.05	0.507±0.05

Silicate	7.29±0.07	2.24±0.22	Silicate	7.24±0.02	0.234±0.023
Silicate	7.24±0.10	5.51±0.55	Silicate	7.23±0.10	5.49±0.55
Silicate	7.25±0.10	5.17±0.52	Silicate	7.24±0.10	5.16±0.52
Silicate	7.25±0.09	4.80±0.48	Silicate	7.22±0.10	4.60±0.46
Silicate	7.27±0.09	5.01±0.50	Silicate	7.25±0.10	4.96±0.50
Silicate	7.31±0.07	1.75±0.18	Silicate	7.31±0.07	1.73±0.17
Silicate	7.13±0.22	13.2±1.3	Silicate	7.14±0.24	13.1±1.3
Silicate	7.34±0.09	6.14±0.61	Silicate	7.32±0.10	6.14±0.61
Silicate	7.25±0.13	4.78±0.48	Silicate	7.24±0.14	4.77±0.48
Silicate	7.26±0.11	5.37±0.54	Silicate	7.24±0.13	5.37±0.54
Silicate	7.29±0.10	5.20±0.52	Silicate	7.28±0.12	5.19±0.52
Silicate	7.29±0.12	4.87±0.49	Silicate	7.28±0.13	4.85±0.48
Silicate	7.29±0.12	4.95±0.50	Silicate	7.27±0.13	4.94±0.49
Silicate	7.35±0.12	4.92±0.49	Silicate	7.33±0.13	4.91±0.49
Silicate	7.26±0.09	5.79±0.58	Silicate	7.24±0.10	5.79±0.58
Silicate	7.25±0.10	5.46±0.55	Silicate	7.23±0.10	5.45±0.55
Silicate	7.31±0.11	5.49±0.55	Silicate	7.31±0.11	4.92±0.49
Silicate	7.29±0.07	2.86±0.29	Silicate	7.28±0.08	2.83±0.28
Silicate	7.26±0.10	5.33±0.53	Silicate	7.24±0.12	5.32±0.53
Silicate	7.27±0.13	5.72±0.57	Silicate	7.25±0.13	5.71±0.57
Silicate	7.31±0.09	5.46±0.55	Silicate	7.29±0.10	5.45±0.54
Silicate	7.30±0.11	4.89±0.49	Silicate	7.29±0.12	4.89±0.49
Silicate	7.27±0.13	6.00±0.60	Silicate	7.26±0.15	5.98±0.60
Silicate	7.21±0.13	5.07±0.51	Silicate	7.19±0.15	5.06±0.51
Silicate	7.28±0.04	0.46±0.05	Silicate	7.26±0.04	0.453±0.045
Silicate	7.31±0.07	3.19±0.32	Silicate	7.29±0.09	3.15±0.32
Silicate	7.27±0.14	6.31±0.63	Silicate	7.27±0.15	6.29±0.63
Silicate	7.21±0.32	21.1±2.1	Silicate	7.21±0.39	20.8±2.1
Silicate	7.26±0.11	5.7±0.57	Silicate	7.25±0.11	5.71±0.57

Semarkona SMK3-6

$(^{60}Fe/^{56}Fe)_0 = (1.7 \pm 1.1)\times10^{-7}$*			$(^{60}Fe/^{56}Fe)_0 = (0.6 \pm 1.2)\times10^{-7}$		
Mineral	$^{60}Ni/^{61}Ni$	$^{56}Fe/^{61}Ni$ ($\times10^4$)	Mineral	$^{60}Ni/^{61}Ni$	$^{56}Fe/^{61}Ni$ ($\times10^4$)
Silicate	23.34±0.19	62.0±6.2	Silicate	23.37±0.20	61.7±6.2
Silicate	23.53±0.28	61.6±6.2	Silicate	23.46±0.31	61.6±6.2
Silicate	23.29±0.19	64.8±6.5	Silicate	23.22±0.20	64.7±6.5

Silicate	23.15±0.22	45.0±4.5	Silicate	23.08±0.22	45.0±4.5
Silicate	23.22±0.24	52.5±5.3	Silicate	23.14±0.26	52.3±5.2
Silicate	23.28±0.20	42.0±4.2	Silicate	23.20±0.23	42.0±4.2
Silicate	23.05±0.20	54.3±5.4	Silicate	23.01±0.19	54.2±5.4
Silicate	23.11±0.04	0.091±0.009	Silicate	23.11±0.04	0.091±0.009
Silicate	23.03±0.18	61.5±6.2	Silicate	22.97±0.21	61.4±6.1
Silicate	23.17±0.08	5.69±0.57	Silicate	23.17±0.08	5.65±0.56
Silicate	23.23±0.25	95.8±9.6	Silicate	23.15±0.26	95.7±9.6
Silicate	23.06±0.28	59.8±6.0	Silicate	22.98±0.29	59.8±6.0
Silicate	23.48±0.23	54.3±5.4	Silicate	23.42±0.25	54.3±5.4
Silicate	23.01±0.20	56.0±5.6	Silicate	22.94±0.23	56.4±5.6
Silicate	23.24±0.23	54.1±5.4	Silicate	23.17±0.26	54.1±5.4
Silicate	23.38±0.21	41.0±4.1	Silicate	23.31±0.21	40.1±4.0
Silicate	23.07±0.27	51.7±5.2	Silicate	22.98±0.32	50.0±5.0
Silicate	23.30±0.36	37.8±3.8	Silicate	23.23±0.39	37.8±3.8

*Data as published by Tachibana et al. (2007)

^{62}Ni Normalization

Semarkona SMK3-6

$(^{60}Fe/^{56}Fe)_0 = (0.5 \pm 1.9)\times10^{-7}$			$(^{60}Fe/^{56}Fe)_0 = (0.6 \pm 2.0)\times10^{-7}$		
Mineral	$^{60}Ni/^{62}Ni$	$^{56}Fe/^{62}Ni$ ($\times10^4$)	Mineral	$^{60}Ni/^{62}Ni$	$^{56}Fe/^{62}Ni$ ($\times10^4$)
Silicate	7.34±0.10	19.4±1.9	Silicate	7.32±0.10	19.4±1.9
Silicate	7.39±0.14	19.3±1.9	Silicate	7.38±0.16	19.2±1.9
Silicate	7.32±0.10	20.3±2.0	Silicate	7.30±0.10	20.3±2.0
Silicate	7.27±0.11	14.2±1.4	Silicate	7.26±0.12	14.2±1.4
Silicate	7.29±0.12	16.5±1.7	Silicate	7.28±0.14	16.5±1.6
Silicate	7.32±0.10	13.2±1.3	Silicate	7.30±0.12	13.2±1.3
Silicate	7.24±0.10	17.2±1.7	Silicate	7.24±0.10	17.1±1.7
Silicate	7.29±0.02	0.029±0.003	Silicate	7.27±0.02	0.029±0.003
Silicate	7.24±0.09	19.4±1.9	Silicate	7.22±0.11	19.4±1.9
Silicate	7.30±0.04	1.79±0.18	Silicate	7.29±0.04	1.78±0.18
Silicate	7.30±0.13	30.2±3.0	Silicate	7.28±0.14	30.1±3.0
Silicate	7.24±0.15	18.9±1.9	Silicate	7.23±0.16	18.9±1.9
Silicate	7.38±0.11	16.9±1.7	Silicate	7.37±0.13	16.9±1.7
Silicate	7.24±0.10	17.8±1.8	Silicate	7.21±0.12	17.8±1.8
Silicate	7.30±0.12	17.1±1.7	Silicate	7.29±0.14	17.0±1.7
Silicate	7.35±0.10	12.9±1.3	Silicate	7.33±0.11	12.6±1.3

Silicate	7.25±0.14	16.3±1.6	Silicate	7.23±0.17	15.8±1.6
Silicate	7.32±0.18	11.9±1.2	Silicate	7.31±0.21	11.9±1.2

Semarkona SMK3-2

$(^{60}Fe/^{56}Fe)_0 = (2.0 \pm 1.9)\times10^{-7}$*			$(^{60}Fe/^{56}Fe)_0 = (0.2 \pm 2.0)\times10^{-7}$		
Mineral	$^{60}Ni/^{61}Ni$	$^{56}Fe/^{61}Ni$ ($\times10^4$)	Mineral	$^{60}Ni/^{61}Ni$	$^{56}Fe/^{61}Ni$ ($\times10^4$)
Silicate	23.15±0.25	45.8±4.6	Silicate	23.07±0.26	45.4±4.5
Silicate	23.13±0.19	25.5±2.6	Silicate	23.09±0.23	25.5±2.5
Silicate	23.06±0.04	2.49±0.25	Silicate	23.06±0.04	2.45±0.25
Silicate	22.97±0.22	24.2±2.4	Silicate	22.91±0.23	23.7±2.4
Silicate	23.07±0.09	1.62±0.16	Silicate	23.07±0.09	1.56±0.16
Silicate	23.08±0.09	6.16±0.62	Silicate	23.07±0.09	4.47±0.45
Silicate	23.25±0.31	34.6±3.5	Silicate	23.22±0.34	33.0±3.3
Silicate	23.12±0.14	18.6±1.9	Silicate	23.09±0.15	18.3±1.8
Silicate	23.11±0.21	39.4±3.9	Silicate	23.05±0.23	39.4±3.9
Silicate	23.26±0.29	68.8±6.9	Silicate	23.16±0.30	68.6±6.9
Silicate	23.18±0.42	63.4±6.3	Silicate	23.04±0.44	63.1±6.3
Silicate	22.99±0.24	34.7±3.5	Silicate	22.90±0.26	34.6±3.5
Silicate	23.04±0.17	25.6±2.6	Silicate	22.97±0.19	25.1±2.5
Silicate	23.19±0.23	37.9±3.8	Silicate	23.12±0.24	37.9±3.8
Silicate	23.13±0.16	15.7±1.6	Silicate	23.11±0.20	15.6±1.6
Silicate	23.05±0.17	16.2±1.6	Silicate	23.01±0.17	15.2±1.5
Silicate	23.07±0.02	0.293±0.029	Silicate	23.06±0.02	0.292±0.029
Silicate	23.05±0.01	0.056±0.006	Silicate	23.05±0.01	0.055±0.006

* These data ratios do not match the values published by Tachibana et al. (2007) because we were unable to fully duplicate the original data reduction. The data in these tables differ only in the method of ratio calculation and are directly comparable.

^{62}Ni Normalization

Semarkona SMK3-2

$(^{60}Fe/^{56}Fe)_0 = (0.1 \pm 3.0)\times10^{-7}$			$(^{60}Fe/^{56}Fe)_0 = (0.3 \pm 3.4)\times10^{-7}$		
Mineral	$^{60}Ni/^{62}Ni$	$^{56}Fe/^{62}Ni$ ($\times10^4$)	Mineral	$^{60}Ni/^{62}Ni$	$^{56}Fe/^{62}Ni$ ($\times10^4$)

Silicate	7.28±0.13	14.4±1.4	Silicate	7.25±0.14	14.3±1.4
Silicate	7.27±0.10	8.04±0.80	Silicate	7.26±0.12	8.02±0.80
Silicate	7.27±0.02	0.79±0.08	Silicate	7.25±0.02	0.776±0.078
Silicate	7.22±0.12	7.68±0.77	Silicate	7.20±0.13	7.52±0.75
Silicate	7.27±0.04	0.51±0.05	Silicate	7.26±0.05	0.495±0.050
Silicate	7.28±0.05	1.95±0.19	Silicate	7.26±0.05	1.42±0.14
Silicate	7.31±0.16	10.9±1.1	Silicate	7.30±0.18	10.4±1.0
Silicate	7.28±0.07	5.86±0.59	Silicate	7.26±0.08	5.77±0.58
Silicate	7.26±0.11	12.5±1.2	Silicate	7.25±0.12	12.4±1.2
Silicate	7.29±0.15	21.7±2.2	Silicate	7.28±0.16	21.6±2.2
Silicate	7.26±0.22	20.1±2.0	Silicate	7.25±0.24	20.0±2.0
Silicate	7.23±0.13	11.0±1.1	Silicate	7.20±0.14	11.0±1.1
Silicate	7.25±0.09	8.11±0.81	Silicate	7.22±0.10	7.95±0.79
Silicate	7.28±0.12	12.0±1.2	Silicate	7.27±0.13	12.0±1.2
Silicate	7.28±0.09	4.94±0.49	Silicate	7.27±0.10	4.92±0.49
Silicate	7.25±0.09	5.14±0.51	Silicate	7.24±0.09	4.81±0.48
Silicate	7.27±0.01	0.093±0.009	Silicate	7.25±0.01	0.093±0.009
Silicate	7.27±0.01	0.018±0.002	Silicate	7.25±0.01	0.018±0.002

Bishunpur BIS-1*

$(^{60}Fe/^{56}Fe)_0 = (0.5 \pm 1.0)\times10^{-7}$			$(^{60}Fe/^{56}Fe)_0 = (-0.5 \pm 1.1)\times10^{-7}$		
Mineral	$^{60}Ni/^{61}Ni$	$^{56}Fe/^{61}Ni$ ($\times10^4$)	Mineral	$^{60}Ni/^{61}Ni$	$^{56}Fe/^{61}Ni$ ($\times10^4$)
Silicate	23.07±0.12	19.1±1.9	Silicate	23.05±0.14	18.7±1.9
Silicate	23.07±0.27	59.8±6.0	Silicate	22.97±0.26	56.6±5.7
Silicate	22.96±0.17	16.8±1.7	Silicate	22.94±0.18	16.5±1.7
Silicate	23.15±0.22	47.2±4.7	Silicate	23.08±0.25	46.6±4.7
Silicate	23.38±0.24	127±13	Silicate	23.32±0.26	126±13
Silicate	22.89±0.18	57.8±5.8	Silicate	22.86±0.19	56.7±5.7
Silicate	23.25±0.24	65.0±6.5	Silicate	23.19±0.25	64.8±6.5
Silicate	23.20±0.21	101±10	Silicate	23.15±0.23	100±10
Silicate	23.12±0.45	84.6±8.5	Silicate	23.06±0.46	81.7±8.2
Silicate	23.02±0.12	13.5±1.4	Silicate	23.01±0.12	13.3±1.3
Silicate	22.91±0.12	16.7±1.7	Silicate	22.89±0.13	16.6±1.7
Silicate	23.22±0.25	69.4±6.9	Silicate	23.08±0.27	68.3±6.8
Silicate	22.80±0.22	78.4±7.8	Silicate	22.72±0.24	71.5±7.2
Silicate	23.28±0.16	35.3±3.5	Silicate	23.23±0.18	35.1±3.5

Silicate	22.93±0.24	43.2±4.3	Silicate	23.17±0.10	11.4±1.1
Silicate	23.28±0.21	30.1±3.0	Silicate	22.83±0.24	42.1±4.2
Silicate	23.30±0.27	39.4±3.9	Silicate	23.20±0.21	29.1±2.9
Silicate	23.10±0.02	0.693±0.069	Silicate	23.21±0.27	39.0±3.9
Silicate	23.18±0.11	12.3±1.2	Silicate	23.10±0.02	0.681±0.068

*Data reported by Tachibana et al. (2007)

^{62}Ni Normalization

Bishunpur BIS-1

$(^{60}Fe/^{56}Fe)_0 = (-0.4 \pm 1.6)\times10^{-7}$			$(^{60}Fe/^{56}Fe)_0 = (-0.5 \pm 1.8)\times10^{-7}$		
Mineral	$^{60}Ni/^{62}Ni$	$^{56}Fe/^{62}Ni$ ($\times10^4$)	Mineral	$^{60}Ni/^{62}Ni$	$^{56}Fe/^{62}Ni$ ($\times10^4$)
Silicate	7.27±0.06	6.01±0.60	Silicate	7.27±0.07	5.90±0.59
Silicate	7.23±0.14	18.9±1.9	Silicate	7.24±0.14	17.9±1.8
Silicate	7.23±0.09	5.31±0.53	Silicate	7.23±0.10	5.24±0.52
Silicate	7.27±0.11	14.9±1.5	Silicate	7.28±0.13	14.7±1.5
Silicate	7.34±0.12	39.9±4.0	Silicate	7.35±0.14	39.4±3.9
Silicate	7.20±0.10	18.4±1.8	Silicate	7.20±0.10	18.0±1.8
Silicate	7.30±0.12	20.3±2.0	Silicate	7.31±0.13	20.2±2.0
Silicate	7.29±0.11	31.7±3.2	Silicate	7.30±0.12	31.5±3.1
Silicate	7.27±0.25	26.9±2.7	Silicate	7.27±0.24	25.9±2.6
Silicate	7.25±0.06	4.27±0.43	Silicate	7.25±0.07	4.20±0.42
Silicate	7.22±0.06	5.27±0.53	Silicate	7.22±0.07	5.24±0.52
Silicate	7.29±0.13	21.8±2.2	Silicate	7.28±0.14	21.5±2.2
Silicate	7.17±0.12	24.8±2.5	Silicate	7.16±0.13	22.7±2.3
Silicate	7.32±0.08	11.0±1.1	Silicate	7.32±0.10	11.0±1.1
Silicate	7.30±0.05	3.87±0.39	Silicate	7.30±0.05	3.56±0.36
Silicate	7.20±0.13	13.7±1.4	Silicate	7.19±0.13	13.4±1.3
Silicate	7.32±0.10	9.42±0.94	Silicate	7.31±0.11	9.14±0.91
Silicate	7.32±0.14	12.4±1.2	Silicate	7.32±0.15	12.3±1.2
Silicate	7.28±0.01	0.219±0.022	Silicate	7.28±0.01	0.215±0.022

Bishunpur BIS-38

$(^{60}Fe/^{56}Fe)_0 = (1.2 \pm 0.9)\times10^{-7}$*	$(^{60}Fe/^{56}Fe)_0 = (0.4 \pm 1.1)\times10^{-7}$

Mineral	$^{60}Ni/^{61}Ni$	$^{56}Fe/^{61}Ni$ ($\times10^4$)	Mineral	$^{60}Ni/^{61}Ni$	$^{56}Fe/^{61}Ni$ ($\times10^4$)
Silicate	23.12±0.08	10.2±1.0	Silicate	23.11±0.07	9.38±0.94
Silicate	23.31±0.33	164±16	Silicate	23.17±0.35	156±16
Silicate	23.45±0.25	108±11	Silicate	23.32±0.25	101±1.0
Silicate	23.17±0.14	44.3±4.4	Silicate	23.10±0.15	42.0±4.2
Silicate	23.10±0.30	132±13	Silicate	23.02±0.31	128±13
Silicate	23.12±0.11	13.4±1.3	Silicate	23.11±0.08	10.3±1.0
Silicate	23.02±0.12	28.1±2.8	Silicate	23.04±0.13	26.9±2.7
Silicate	23.25±0.21	67.1±6.7	Silicate	23.20±0.24	63.8±6.4
Silicate	23.30±0.14	25.3±2.5	Silicate	23.25±0.13	24.4±2.4
Silicate	23.45±0.27	92.3±9.2	Silicate	23.34±0.26	88.4±8.8
Silicate	23.03±0.11	16.9±1.7	Silicate	23.02±0.11	16.9±1.7
Silicate	23.13±0.06	4.13±0.41	Silicate	23.12±0.05	4.07±0.41
Silicate	23.56±0.53	140±14	Silicate	23.43±0.52	138±14
Silicate	23.13±0.38	185±18	Silicate	22.98±0.40	182±18
Silicate	23.10±0.29	88.9±8.9	Silicate	22.98±0.31	86.6±8.7
Silicate	23.03±0.13	31.0±3.1	Silicate	23.00±0.15	30.9±3.1

*Data published by Tachibana et al. (2007)

^{62}Ni Normalization

Bishunpur BIS-38

$(^{60}Fe/^{56}Fe)_0 = (-0.2 \pm 1.7)\times10^{-7}$ $(^{60}Fe/^{56}Fe)_0 = (0.4 \pm 1.8)\times10^{-7}$

Mineral	$^{60}Ni/^{62}Ni$	$^{56}Fe/^{62}Ni$ ($\times10^4$)	Mineral	$^{60}Ni/^{62}Ni$	$^{56}Fe/^{62}Ni$ ($\times10^4$)
Silicate	7.28±0.05	3.21±0.32	Silicate	7.28±0.04	2.95±0.30
Silicate	7.30±0.16	51.7±5.2	Silicate	7.30±0.18	49.2±4.9
Silicate	7.37±0.13	33.8±3.4	Silicate	7.35±0.13	31.9±3.2
Silicate	7.31±0.14	14.0±1.4	Silicate	7.28±0.08	13.3±1.3
Silicate	7.24±0.14	41.8±4.2	Silicate	7.26±0.17	40.4±4.0
Silicate	7.31±0.06	4.20±0.42	Silicate	7.28±0.04	3.23±0.32
Silicate	7.14±0.07	8.87±0.89	Silicate	7.26±0.07	8.49±0.85
Silicate	7.30±0.11	21.1±2.1	Silicate	7.31±0.12	20.1±2.0
Silicate	7.40±0.13	7.94±0.79	Silicate	7.33±0.07	7.67±0.77
Silicate	7.31±0.12	29.0±2.9	Silicate	7.36±0.14	27.8±2.3
Silicate	7.30±0.06	5.31±0.53	Silicate	7.26±0.06	5.29±0.53
Silicate	7.30±0.05	1.30±0.13	Silicate	7.29±0.03	1.28±0.13
Silicate	7.28±0.26	43.8±4.4	Silicate	7.38±0.27	43.3±4.3
Silicate	7.25±0.18	58.3±5.8	Silicate	7.24±0.21	57.6±5.8

Silicate	7.17±0.14	28.2±2.8	Silicate	7.24±0.16	27.5±2.7
Silicate	7.22±0.07	9.81±0.98	Silicate	7.25±0.08	9.76±0.98

Krymka 3-1

$(^{60}Fe/^{56}Fe)_0 = (1.41 \pm 0.21)\times10^{-7}$			$(^{60}Fe/^{56}Fe)_0 = (1.14 \pm 0.22)\times10^{-7}$		
Mineral	$^{60}Ni/^{61}Ni$	$^{56}Fe/^{61}Ni$ ($\times10^4$)	Mineral	$^{60}Ni/^{61}Ni$	$^{56}Fe/^{61}Ni$ ($\times10^4$)
Intercept[1]	23.10±0.01	0.317±0.032	Intercept[1]	23.10±0.01	0.317±0.032
Silicate	23.88±0.27	530±53	Silicate	23.69±0.28	498±50
Silicate	24.11±0.40	864±86	Silicate	23.80±0.38	801±80
Silicate	23.38±0.25	405±41	Silicate	23.34±0.26	390±39
Silicate	23.74±0.24	415±41	Silicate	23.64±0.25	407±41
Silicate	23.67±0.27	437±44	Silicate	23.49±0.25	416±42
Silicate	23.86±0.27	379±38	Silicate	23.72±0.26	366±37
Silicate	23.80±0.32	438±44	Silicate	23.59±0.30	426±43
Silicate	24.06±0.30	543±54	Silicate	23.91±0.31	525±53

[1]Data forced through zero

^{62}Ni Normalization

Krymka 3-1

$(^{60}Fe/^{56}Fe)_0 = (0.88 \pm 0.31)\times10^{-7}$*			$(^{60}Fe/^{56}Fe)_0 = (0.94 \pm 0.33)\times10^{-7}$		
Mineral	$^{60}Ni/^{62}Ni$	$^{56}Fe/^{62}Ni$ ($\times10^4$)	Mineral	$^{60}Ni/^{62}Ni$	$^{56}Fe/^{62}Ni$ ($\times10^4$)
Intercept[1]	7.28±0.01	0.100±0.010	Intercept[1]	7.28±0.01	0.100±0.010
Silicate	7.46±0.14	164±16	Silicate	7.45±0.13	155±15
Silicate	7.48±0.18	265±27	Silicate	7.48±0.18	247±25
Silicate	7.31±0.12	127±13	Silicate	7.33±0.12	123±12
Silicate	7.41±0.11	129±13	Silicate	7.42±0.12	127±13
Silicate	7.38±0.13	136±14	Silicate	7.37±0.12	130±13
Silicate	7.44±0.12	117±12	Silicate	7.44±0.12	114±11
Silicate	7.39±0.15	136±14	Silicate	7.40±0.14	133±13
Silicate	7.48±0.14	168±17	Silicate	7.49±0.15	163±16

*Data published by Tachibana et al. (2009)

[1]Data forced through zero

Krymka 3-9*

$(^{60}Fe/^{56}Fe)_0 = (0.95 \pm 0.42)\times10^{-7}$			$(^{60}Fe/^{56}Fe)_0 = (0.63 \pm 0.44)\times10^{-7}$		
Mineral	$^{60}Ni/^{61}Ni$	$^{56}Fe/^{61}Ni$ ($\times10^4$)	Mineral	$^{60}Ni/^{61}Ni$	$^{56}Fe/^{61}Ni$ ($\times10^4$)

Silicate	23.44±0.32	491±49	Silicate	23.19±0.31	466±47
Silicate	23.36±0.29	439±44	Silicate	23.24±0.29	400±40
Silicate	23.68±0.23	262±26	Silicate	23.58±0.21	227±23
Silicate	23.38±0.29	456±46	Silicate	23.23±0.29	423±42
Silicate	23.41±0.17	132±13	Silicate	23.34±0.16	125±12
Silicate	23.07±0.09	46.3±4.6	Silicate	23.06±0.09	45.2±4.5
Silicate	23.33±0.27	367±37	Silicate	23.32±0.24	336±34
Silicate	23.52±0.24	337±34	Silicate	23.37±0.24	319±32

^{62}Ni Normalization

Krymka 3-9

$(^{60}Fe/^{56}Fe)_0 = (0.54 \pm 0.64)\times10^{-7}$			$(^{60}Fe/^{56}Fe)_0 = (0.62 \pm 0.68)\times10^{-7}$		
Mineral	$^{60}Ni/^{62}Ni$	$^{56}Fe/^{62}Ni$ ($\times10^4$)	Mineral	$^{60}Ni/^{62}Ni$	$^{56}Fe/^{62}Ni$ ($\times10^4$)
Silicate	7.32±0.15	154±15	Silicate	7.31±0.15	146±15
Silicate	7.31±0.14	138±14	Silicate	7.33±0.14	126±13
Silicate	7.43±0.11	81.7±8.2	Silicate	7.43±0.10	71.2±7.1
Silicate	7.31±0.14	143±14	Silicate	7.32±0.14	133±13
Silicate	7.36±0.08	41.5±4.2	Silicate	7.36±0.08	39.3±3.9
Silicate	7.27±0.04	14.6±1.5	Silicate	7.27±0.04	14.2±1.4
Silicate	7.31±0.13	115±12	Silicate	7.35±0.12	105±11
Silicate	7.38±0.11	105±11	Silicate	7.37±0.12	100±10

*Data reported by Tachibana et al. (2009)

Krymka 3-11

$(^{60}Fe/^{56}Fe)_0 = (2.76 \pm 0.44)\times10^{-7}$			$(^{60}Fe/^{56}Fe)_0 = (2.35 \pm 0.44)\times10^{-7}$		
Mineral	$^{60}Ni/^{61}Ni$	$^{56}Fe/^{61}Ni$ ($\times10^4$)	Mineral	$^{60}Ni/^{61}Ni$	$^{56}Fe/^{61}Ni$ ($\times10^4$)
Intercept[1]	23.10±0.001	0.317±0.002	Intercept[1]	23.10±0.001	0.317±0.002
Silicate	23.45±0.21	84.2±8.4	Silicate	23.36±0.20	82.0±8.2
Silicate	23.28±0.09	58.5±5.8	Silicate	23.25±0.08	56.5±5.6
Silicate	23.29±0.10	79.2±7.9	Silicate	23.25±0.10	74.8±7.5
Silicate	23.19±0.08	48.1±4.8	Silicate	23.18±0.08	46.3±4.6
Silicate	23.33±0.08	44.2±4.4	Silicate	23.30±0.08	43.4±4.3
Silicate	23.14±0.04	10.9±1.1	Silicate	23.13±0.04	10.7±1.1
Silicate	23.26±0.06	37.6±3.8	Silicate	23.21±0.06	36.7±3.7

Silicate	23.18±0.06	28.8±2.9	Silicate	23.15±0.06	27.6±2.8
Silicate	23.27±0.12	89.3±8.9	Silicate	23.25±0.10	85.4±8.5
Silicate	23.22±0.09	63.0±6.3	Silicate	23.20±0.09	61.8±6.2
Silicate	23.33±0.17	163±16	Silicate	23.24±0.16	159±16
Silicate	23.24±0.07	48.9±4.9	Silicate	23.26±0.08	48.5±4.8
Silicate	23.34±0.08	38.1±3.8	Silicate	23.35±0.07	37.2±3.7

[1]Data forced through zero

^{62}Ni Normalization

Krymka 3-11

$(^{60}Fe/^{56}Fe)_0 = (2.37 \pm 0.68)\times10^{-7}$*			$(^{60}Fe/^{56}Fe)_0 = (2.37 \pm 0.68)\times10^{-7}$		
Mineral	$^{60}Ni/^{62}Ni$	$^{56}Fe/^{62}Ni$ ($\times10^4$)	Mineral	$^{60}Ni/^{62}Ni$	$^{56}Fe/^{62}Ni$ ($\times10^4$)
Intercept[1]	7.28±0.0001	0.100±0.010	Intercept[1]	7.28±0.0001	0.100±0.010
Silicate	7.36±0.11	26.4±2.6	Silicate	7.36±0.10	25.8±0.08
Silicate	7.33±0.04	18.4±1.8	Silicate	7.33±0.04	17.8±0.02
Silicate	7.33±0.05	24.9±2.5	Silicate	7.33±0.05	23.6±0.04
Silicate	7.30±0.04	15.1±1.5	Silicate	7.31±0.04	14.6±0.02
Silicate	7.35±0.04	13.9±1.4	Silicate	7.35±0.04	13.6±0.02
Silicate	7.29±0.02	3.42±0.34	Silicate	7.29±0.02	3.37±0.34
Silicate	7.32±0.03	11.8±1.2	Silicate	7.32±0.03	11.5±1.2
Silicate	7.29±0.03	9.07±0.91	Silicate	7.30±0.03	8.69±0.87
Silicate	7.32±0.06	28.1±2.8	Silicate	7.33±0.05	26.9±2.7
Silicate	7.31±0.05	19.9±2.0	Silicate	7.31±0.04	19.5±1.9
Silicate	7.33±0.08	51.3±5.1	Silicate	7.33±0.08	50.1±5.0
Silicate	7.33±0.04	15.3±1.5	Silicate	7.33±0.04	15.2±1.5
Silicate	7.36±0.04	11.9±1.2	Silicate	7.36±0.04	11.7±1.2

* These data ratios do not match the values published by Tachibana et al. (2009) because we were unable to fully duplicate the original data reduction. The data in these tables differ only in the method of ratio calculation and are directly comparable.

[1]Data forced through zero

Semarkona DAP-1

$(^{60}Fe/^{56}Fe)_0 = (4.5 \pm 1.3)\times10^{-7}$			$(^{60}Fe/^{56}Fe)_0 = (2.1 \pm 1.2)\times10^{-7}$*		
Mineral	$^{60}Ni/^{61}Ni$	$^{56}Fe/^{61}Ni$ ($\times10^4$)	Mineral	$^{60}Ni/^{61}Ni$	$^{56}Fe/^{61}Ni$ ($\times10^4$)

Silicate	22.91±0.18	18.6±1.9	Silicate	22.86±0.18	16.2±1.6
Silicate	23.07±0.17	20.5±2.0	Silicate	23.07±0.15	17.8±1.8
Silicate	23.03±0.27	51.2±5.1	Silicate	22.93±0.23	42.7±4.3
Silicate	23.14±0.15	16.0±1.6	Silicate	23.13±0.13	12.7±1.3
Silicate	23.65±0.25	47.9±4.8	Silicate	23.47±0.23	37.6±3.8
Silicate	23.03±0.23	38.9±3.9	Silicate	23.05±0.21	33.8±3.4
Silicate	24.13±0.53	123±12	Silicate	23.69±0.42	104±10
Silicate	23.06±0.07	1.22±0.12	Silicate	23.07±0.03	0.30±0.03
Silicate	24.57±0.97	500±50	Silicate	23.32±0.84	450±45
Silicate	23.15±0.19	18.2±1.8	Silicate	23.20±0.15	15.7±1.6
Silicate	24.15±0.47	144±14	Silicate	23.65±0.42	117±12
Silicate	23.54±0.41	100±1.0	Silicate	23.38±0.34	77.3±7.7
Silicate	23.18±0.21	29.1±2.9	Silicate	23.13±0.19	26.5±2.6
Silicate	23.43±0.42	131±13	Silicate	23.17±0.38	114±11
Silicate	23.31±0.30	54.5±5.4	Silicate	23.22±0.26	46.8±4.7

*Data reported by Telus et al. (2011)

^{62}Ni Normalization

Semarkona DAP-1

$(^{60}Fe/^{56}Fe)_0 = (1.1 \pm 1.9)\times10^{-7}$			$(^{60}Fe/^{56}Fe)_0 = (2.1 \pm 1.9)\times10^{-7}$		
Mineral	$^{60}Ni/^{62}Ni$	$^{56}Fe/^{62}Ni$ ($\times10^4$)	Mineral	$^{60}Ni/^{62}Ni$	$^{56}Fe/^{62}Ni$ ($\times10^4$)
Silicate	7.21±0.09	5.93±0.59	Silicate	7.20±0.09	5.18±0.52
Silicate	7.26±0.08	6.52±0.65	Silicate	7.27±0.07	5.65±0.56
Silicate	7.22±0.13	16.3±1.6	Silicate	7.23±0.12	13.6±1.4
Silicate	7.29±0.07	5.09±0.51	Silicate	7.29±0.06	4.03±0.40
Silicate	7.42±0.12	15.0±1.5	Silicate	7.40±0.11	11.9±1.2
Silicate	7.23±0.11	12.4±1.2	Silicate	7.27±0.10	10.8±1.1
Silicate	7.45±0.23	38.5±3.8	Silicate	7.47±0.20	32.9±3.3
Silicate	7.27±0.04	0.386±0.039	Silicate	7.27±0.02	0.093±0.009
Silicate	7.22±0.43	160±16	Silicate	7.35±0.41	142±14
Silicate	7.28±0.09	5.79±0.58	Silicate	7.31±0.07	4.99±0.50
Silicate	7.48±0.22	45.2±4.5	Silicate	7.45±0.20	36.9±3.7
Silicate	7.32±0.20	31.8±3.2	Silicate	7.37±0.16	24.5±2.4
Silicate	7.29±0.10	9.23±0.92	Silicate	7.29±0.10	8.41±0.84
Silicate	7.28±0.20	41.3±4.1	Silicate	7.31±0.18	36.1±3.6
Silicate	7.29±0.15	17.3±1.7	Silicate	7.32±0.13	14.8±1.5

Table Appendix C.7: ^{10}Be-^{10}B CAI data (MacPherson et al. 2003)[1]

As published **Recalculated**

Efremovka 6456-1

$(^{10}Be/^{9}Be)_0 = (0.76 \pm 0.16) \times 10^{-3}$			$(^{10}Be/^{9}Be)_0 = (0.76 \pm 0.16) \times 10^{-3}$		
Mineral	$^{10}B/^{11}B$	$^{9}Be/^{11}B$	Mineral	$^{10}B/^{11}B$	$^{9}Be/^{11}B$
Melilite #1	0.297±0.034	38.2±4.6	Melilite #1	0.297±0.034	38.1±4.6
Melilite #2	0.298±0.019	65.9±7.0	Melilite #2	0.298±0.019	65.9±7.0
Melilite #3	0.266±0.009	24.6±2.5	Melilite #3	0.266±0.009	24.6±2.5
Melilite #4	0.302±0.016	42.0±4.2	Melilite #4	0.302±0.016	42.0±4.2
Melilite #5	0.459±0.044	261±30	Melilite #5	0.458±0.044	260±30
Melilite #6	0.348±0.021	137±14	Melilite #6	0.348±0.021	137±14

Vigarano 1623-9

$(^{10}Be/^{9}Be)_0 = (0.58 \pm 0.19) \times 10^{-3}$			$(^{10}Be/^{9}Be)_0 = (0.57 \pm 0.19) \times 10^{-3}$		
Mineral	$^{10}B/^{11}B$	$^{9}Be/^{11}B$	Mineral	$^{10}B/^{11}B$	$^{9}Be/^{11}B$
Melilite #1	0.279±0.027	24.2±2.8	Melilite #1	0.279±0.027	24.2±2.8
Melilite #2	0.236±0.027	33.8±4.0	Melilite #2	0.236±0.027	33.8±4.0
Melilite #3	0.519±0.125	470±96	Melilite #3	0.510±0.125	461±96
Melilite #4	0.347±0.055	161±23	Melilite #4	0.345±0.055	160±13
Melilite #5	0.294±0.036	110±14	Melilite #5	0.293±0.036	110±14
Melilite #6	0.250±0.019	16.1±1.8	Melilite #6	0.249±0.019	16.1±1.8
Melilite #7	0.290±0.029	69.2±8.0	Melilite #7	0.290±0.029	69.1±8.0
Pyroxene #1	0.243±0.013	0.60±0.07	Pyroxene #1	0.243±0.013	0.60±0.07

Vigarano 477-4b

$(^{10}Be/^{9}Be)_0 = (0.53 \pm 0.17) \times 10^{-3}$			$(^{10}Be/^{9}Be)_0 = (0.53 \pm 0.17) \times 10^{-3}$		
Mineral	$^{10}B/^{11}B$	$^{9}Be/^{11}B$	Mineral	$^{10}B/^{11}B$	$^{9}Be/^{11}B$
Melilite #1	0.264±0.019	23.6±2.5	Melilite #1	0.264±0.019	23.6±2.5
Melilite #2	0.250±0.008	7.7±0.8	Melilite #2	0.250±0.008	7.7±0.8
Melilite #3	0.249±0.016	15.7±1.6	Melilite #3	0.249±0.016	15.7±1.6
Melilite #4	0.270±0.015	13.4±1.4	Melilite #4	0.270±0.015	13.4±1.4
Melilite #5	0.279±0.034	83±10	Melilite #5	0.278±0.034	83±10

Melilite #6	0.261±0.023	26.8±3.0	Melilite #6	0.261±0.023	26.8±3.0
Melilite #7	0.264±0.016	18.5±1.9	Melilite #7	0.264±0.016	18.5±1.9
Melilite #8	0.292±0.037	85±11	Melilite #8	0.291±0.037	85±11
Melilite #9*	0.250±0.016	14.9±1.6	Melilite #9	0.250±0.016	14.8±1.6
Melilite #10	0.265±0.025	42.5±4.8	Melilite #10	0.265±0.025	42.5±4.8
Melilite #11	0.250±0.013	23.4±2.4	Melilite #11	0.250±0.013	23.3±2.4
Melilite #12	0.330±0.046	170±22	Melilite #12	0.329±0.046	169±22
Pyroxene #1	0.244±0.002	0.021±0.002	Pyroxene #1	0.244±0.002	0.021±0.002

*Original published $^{10}B/^{11}B$ number for Melilite #9 (0.248±0.016) was not reproduced in recalculation.

Vigarano 477-5

$(^{10}Be/^{9}Be)_0 = (0.73^* \pm 0.19) \times 10^{-3}$			$(^{10}Be/^{9}Be)_0 = (0.72 \pm 0.19) \times 10^{-3}$		
Mineral	$^{10}B/^{11}B$	$^{9}Be/^{11}B$	Mineral	$^{10}B/^{11}B$	$^{9}Be/^{11}B$
Melilite #1	0.405±0.058	147±20	Melilite #1	0.404±0.058	146±20
Melilite #2	0.309±0.042	103±13	Melilite #2	0.309±0.042	103±13
Melilite #3	0.276±0.027	29.1±3.3	Melilite #3	0.276±0.027	29.0±3.3
Melilite #4	0.264±0.020	19.8±2.2	Melilite #4	0.264±0.020	19.8±2.2
Melilite #5	0.285±0.038	35.7±4.5	Melilite #5	0.285±0.038	35.6±4.5
Melilite #6*	0.282±0.035	77.3±9.4	Melilite #6	0.281±0.035	77.2±9.4
Melilite #7	0.322±0.038	144±17	Melilite #7	0.321±0.038	143±17
Melilite #8*	0.253±0.016	37.7±4.0	Melilite #8	0.253±0.016	37.7±4.0
Melilite #9	0.225±0.051	38.9±6.5	Melilite #9	0.226±0.051	38.6±6.5
Melilite #10	0.518±0.081	342±49	Melilite #10	0.514±0.081	340±49
Melilite #11	0.340±0.042	143±18	Melilite #11	0.339±0.042	143±18

*Original published numbers for Melilite #6 (0.288±0.035, 76.7±9.4) and Melilite #8 (0.255±0.016, 37.6±4.0) were incorrect, resulting in an inferred initial ratio of $(0.75\pm0.19)\times10^{-3}$, rather than the value listed here.

Leoville 3535-3b

$(^{10}Be/^{9}Be)_0 = (0.67 \pm 0.24) \times 10^{-3}$			$(^{10}Be/^{9}Be)_0 = (0.67 \pm 0.28) \times 10^{-3}$		
Mineral	$^{10}B/^{11}B$	$^{9}Be/^{11}B$	Mineral	$^{10}B/^{11}B$	$^{9}Be/^{11}B$
Melilite #1	0.283±0.042	38.3±4.7	Melilite #1	0.282±0.042	38.2±4.7
Melilite #2	0.266±0.024	16.8±1.8	Melilite #2	0.266±0.024	16.8±1.8
Melilite #3	0.300±0.072	103±16	Melilite #3	0.298±0.072	102±16
Melilite #4	0.263±0.021	7.5±0.8	Melilite #4	0.263±0.021	7.5±0.8
Melilite #5	0.368±0.057	166±20	Melilite #5	0.367±0.057	165±20
Melilite #6	0.308±0.033	90±10	Melilite #6	0.307±0.033	90±10

Melilite #7	0.269±0.020	27.5±2.9	Melilite #7	0.268±0.020	27.5±2.9
Melilite #8	0.310±0.029	77.4±8.6	Melilite #8	0.309±0.029	77.3±8.6
Melilite #9	0.235±0.024	29.9±3.3	Melilite #9	0.234±0.024	29.8±3.3

Allende 3898

$(^{10}Be/^{9}Be)_0 = (0.48 \pm 0.17) \times 10^{-3}$			$(^{10}Be/^{9}Be)_0 = (0.48 \pm 0.17) \times 10^{-3}$		
Mineral	$^{10}B/^{11}B$	$^{9}Be/^{11}B$	Mineral	$^{10}B/^{11}B$	$^{9}Be/^{11}B$
Melilite #1	0.326±0.038	119±15	Melilite #1	0.325±0.038	119±15
Melilite #2	0.304±0.035	93±11	Melilite #2	0.304±0.035	92±11
Melilite #3	0.325±0.038	130±16	Melilite #3	0.324±0.038	130±16
Melilite #4	0.258±0.008	2.5±0.3	Melilite #4	0.258±0.008	2.5±0.3
Melilite #5	0.272±0.040	32±4	Melilite #5	0.271±0.040	32±4
Melilite #6	0.298±0.022	98±11	Melilite #6	0.298±0.022	98±11
Spinel #1	0.275±0.037	5.3±0.7	Spinel #1	0.274±0.037	5.2±0.7

Axtell 2771

$(^{10}Be/^{9}Be)_0 = (0.30 \pm 0.12) \times 10^{-3}$			$(^{10}Be/^{9}Be)_0 = (0.29 \pm 0.13) \times 10^{-3}$		
Mineral	$^{10}B/^{11}B$	$^{9}Be/^{11}B$	Mineral	$^{10}B/^{11}B$	$^{9}Be/^{11}B$
Melilite #1	0.288±0.033	18.9±2.3	Melilite #1	0.287±0.033	18.8±2.3
Melilite #2	0.313±0.056	30.6±4.7	Melilite #2	0.311±0.056	30.4±4.7
Melilite #3	0.547±0.111	767±137	Melilite #3	0.536±0.111	753±137
Melilite #4	0.213±0.043	99±16	Melilite #4	0.211±0.043	99±16
Melilite #5	0.259±0.032	117±14	Melilite #5	0.258±0.032	117±14
Melilite #6	0.580±0.161	1014±241	Melilite #6	0.556±0.161	973±241

[1]Initial ratios published in MacPherson et al (2003) and the revised initial ratios published in this study were calculated using errors corrected for the correlated component.

REFERENCES

Akridge G., Benoit P. H., Sears D. W. G. (1998) Regolith and megaregolith formation of H-chondrites: Thermal constraints on the parent body. *Icarus* **132,** 185–195.

Alexander C. M. O.'D., Barber D. J., and Hutchison R. H. (1989) The microstructure of Semarkona and Bishunpur. *Geochim. Cosmochim. Acta* **53**, 3045–3057.

Alexander C. M. O'D., Bowden R., Fogel M. L., Howard K. T., Herd C. D. K., and Nittler L. R. (2012). The provenances of asteroids, and their contributions to the volatile inventories of the terrestrial planets. *Science* **337,** 721-723.

Beale E. (1962) Some uses of computer in operational research. *Industrielle Organsation* **31**, 51-52.

Bennet M. E. and McSween H. Y. Jr. (1996). Revised model calculations for the thermal histories of ordinary chondrite parent bodies. *Meteorit. Planet. Sci.* **31**, 83–792.

Birck J. L. and Lugmair G. W. (1988) Nickel and chromium isotopes in Allende inclusions. *Earth. Planet. Sci. Lett.* **90**, 131-143.

Bizzarro M., Ulfbeck D., Trinquier A., Thrane K., Connelly J. N., Meyer B. S. (2007) Evidence for a late supernova injection of ^{60}Fe into the protoplanetary disk. *Science*. **316**, 1178-1181.

Bland P. A., Collins G. S., Davison T. M., Abreu N. M., Ciesla F. J., Muxworthy A. R., Moore J. (2014) Pressure-temperature evolution of primordial solar system solids during impact-induced compaction. *Nature. Comm.* **5,** 5451.

Bouvier A., Blichert-Toft J., Moynier F., Vervoort J. D. and Albaréde F. (2007) Pb–Pb dating constraints on the accretion and cooling history of chondrites. *Geochim. Cosmochim. Acta* **71**, 1583–1604.

Catanzaro E. J., Murphy T. J., Garner E. L. and Shields W. R. (1966) Absolute isotopic abundance ratios and atomic weights of magnesium. *Journal of Research of the National Bureau of Standards* **70a**, 453–458.

Chakroborty S. (2010) Diffusion coefficients in olivine, wadsleyite and ringwoodite. *Rev. Mineral. Geochem.* **72**, 603-639.

Chen J. H., Papanastassiou D. A. and Wasserburg G. J. (2009) A search for nickel isotopic anomalies in iron meteorites and chondrites. *Geochim. Cosmochim. Acta.* **73,** 1461-1471.

Chen J. H. and Papanastassiou D. (2013) Fe-Ni isotopic systematics in UOC QUE97008 and Semarkona chondrules. (abstract #2649). 44th Lunar and Planetary Science Conference. CD-ROM.

Cherniak D. J. and Dimanov A. (2010) Diffusion in pyroxene, mica and amphibole *Rev. Mineral. Geochem.* **72**, 641-690.

Chmeleff J., von Blanckenburg F., Kossert K. an Jakob D. (2009) Determination of the ^{10}Be half-life by multicollector ICP-MS and liquid scintillation counting. *Nuclear Instruments and Methods in Physics Research Section B: Beam Interactions with Materials and Atoms*. **268,** 192-199.

Ciesla F. J., Davison T. M., Collins G. S., and O'Brien D. P. (2013) Thermal consequences of impacts in the early solar system. *Meteorit. Planet. Sci.* **48**, 2559–2576.

Clayton D. D. (1983) Extinct radioactivities – a three-phase mixing model. *Astrophys. J.* **268**, 381–384.

Coath C. D., Steele R. C, and Lunnon W. F. (2013) Statistical bias in isotope ratios. *Journal of Analytical Atomic Spectrometry* **28**, 52–58.

Cody G. D., Alexander C. M. O. D., Yabuta H., Kilcoyne A. L. D., Araki T., Ade H., Dera P., Fogel M., Militzer B., and Mysen B. O. (2008) Organic thermometry for chondritic parent bodies. *Earth. Planet. Sci. Lett.* **272**, 446-455.

Connelly J. N., Bizzarro M., Krot A. N., Nordlund A., Wielandt D., and Ivanova M. A. 2012. The Absolute Chronology and Thermal Processing of Solids in the Solar Protoplanetary Disk. *Science* **338**, 651–655.

Dauphas N., Cook D. L., Sacarabany A., Frohlich C., Davis A. M., Wadwha M., Pourmand A., Rausher T., and Gallino R. (2008) Iron 60 evidence for early injection and efficient mixing of stellar debris in the protosolar nebula. *Astrophys. J.* **686**, 560-569.

Davis A. M., Richter F. M., Mendybaev R. A., Janney P. E., Wadhwa M. and McKeegan K. D. 2005. Isotopic mass fractionation laws and the initial solar system $^{26}Al/^{27}Al$ ratio (abstract #2334). 36th Lunar and Planetary Science Conference. CD-ROM.

Diehl R., Halloin H., Kretschmer K., Lichti G. G., Scho¨nfelder B., Strong A. W., von Kienlin A., Wang W., Jean P., Knödlseder J., Roques J.-P., Weidenspointner G., Schanne S., Hartmann D. H., Winkler C. and Wunderer C. (2006) Radioactive ^{26}Al from massive stars in the galaxy. *Nature* **439**, 45–47.

Dodd R. T. 1981. *Meteorites, A Petrologic-chemical Synthesis.* Cambridge University Press, Cambridge pp.90-97.

Dohmen R. and Milke R. (2010) Diffusion in polycrystalline materials: grain boundaries, mathematical models, and experimental data. *Rev Mineral Geochem* **72**, 921-970.

Dyl K. A., Cleverley J. S., Bland P. A., Ryan C. G., Fisher L. A., Hough R. M. (2014) Quantified, whole section trace element mapping of carbonaceous chondrites by Synchrotron X-ray fluorescence microscopy: 1. CV meteorites. *Geochim. Cosmochim. Acta* **134**, 100–119.

Faure F. and Messing T. M. (2005) *Isotopes: Principles and Applications.* John Wiley and Sons, 897 pp.

Ganguly J., Tirone M., Chakraborty S., and Domanik K. (2013) H-chondrite parent asteroid: A multistage cooling, fragmentation and re-accretion history constrained by thermometric studies, diffusion kinetic modeling and geochronological data. *Geochim. Cosmochim. Acta* **105**, 206–220.

Ganguly J., Motoo I., and Zhang X. (2007) Cr diffusion in orthopyroxene: Experimental determination, ^{53}Mn–^{53}Cr thermochronology, and planetary applications. *Geochim. et Cosmochim. Acta* **71**, 3915–3925.

Göpel C., Manhes G., and Allegre C. J. (1994) U-Pb systematics of phosphates from equilibrated ordinary chondrites. *Earth & Planetary Science Letters* **121**, 153–171.

Grossman J. N., Alexander C. M. O. D., Wang J., and Brearley A. J. (2000) Bleached chondrules: Evidence for widespread aqueous processes on the parent asteroids of ordinary chondrites. *Meteorit. Planet. Sci.* **35**, 467–486.

Grossman J. N. and Brearley A. J. (2005) The onset of metamorphism in ordinary and carbonaceous chondrites. *Meteorit. Planet. Sci.* **40**, 87–122.

Guan Y., Huss G. R., Leshin L A. and MacPherson G. J. (2003a) Ni isotope anomalies and ^{60}Fe in sulfides from unequilibrated enstatite chondrites (abstract). *Meteoritics & Planetary Sci*ence **38**, A138.

Guan Y., Huss G. R., and Leshin L. A. (2003b) ^{60}Fe, ^{53}Mn, and nickel isotope anomalies in sulfides from enstatite chondrites (abstract). Presented at the NIPR International Symposium, "Evolution of solar system materials: A new perspective from Antarctic Meteorites, 33-34.

Guan Y., Huss G. R., and Leshin L. A. (2004a) Further observations of ^{60}Fe-^{60}Ni and ^{53}Mn-^{53}Cr systems in sulfides from enstatite chondrites (abstract #2003). 35th Lunar and Planetary Science Conference. CD-ROM.

Guan Y., Huss G. R. and Leshin L. A. (2004b) SIMS analyses of Mg, Cr, and Ni isotopes in primitive meteorites and short-lived radionuclides in the early solar system. *Applied Surface Science* **231-232**, 899-902.

Guan Y., Huss G. R. and Leshin L. A. (2007) ^{60}Fe-^{60}Ni and ^{53}Mn-^{53}Cr isotopic systems in sulfides from unequilibrated enstatite chondrites. *Geochim. Cosmochim. Acta* **71**, 4082-4091.

Harrison K. P. and Grimm R. E. (2010) Thermal constraints on the early history of the H-chondrite parent body reconsidered. *Geochim. Cosmochim. Acta* **74**, 5410–5423.

Henke S., Gail H. -P., Trieloff M., Schwarz W. H., and Kleine T. (2012) Thermal historymodeling of the H chondrite parent body. *Astronomy & Astrophysics* **545**, A135.

Henke S., Gail H. -P., Trieloff M., and Schwarz W. H. (2013) Thermal evolution model for the H chondrite asteroid-instantaneous formation versus protracted accretion. *Icarus* **226**, 212-228.

Hester J. J. and Desch S. J. (2005) "Understanding our origins: Star formation in H II region environments", *ASP Conference Series*, **341**, 107-127.

Hsu W., Huss G. R. and Wasserburg G. J. (1997) Mn-Cr systematics of differentiated meteorites (abstract #1783). 28th Lunar and Planetary Science Conference. CD-ROM.

Hsu W. (2005) Mn-Cr systematics of pallasites. *Geochemical Journal* **39**, 311-316.

Huss G. R. and Lewis R. S. (1994) Noble gases in presolar diamonds II: Component abundances reflect thermal processing. *Meteoritics* **29**, 811-829.

Huss G. R., MacPherson G. J., Wasserburg G. J., Russell S. S. and Srinivasan G. (2001) Aluminum-26 in calcium-aluminum-rich inclusions and chondrules from unequilibrated ordinary chondrites. *Meteorit. Planet. Sci.* **36**, 975–997.

Huss G. R. and Tachibana S. (2004) Clear evidence for ^{60}Fe in silicate from a Semarkona chondrule (abstract #1811). 35th Lunar and Planetary Science Conference. CD-ROM.

Huss G. R., Rubin A. E., and Grossman J. N. (2006) Thermal metamorphism in chondrites. In Meteorites and the Early Solar System II (eds. D.S. Lauretta and HY McSween). The University of Arizona Press, Tucson, pp. 567–586.

Huss G. R., Tachibana S. and Nagashima K. (2007) ^{26}Al and ^{60}Fe in chondrules from unequilibrated ordinary chondrites (abstract). *Meteorit. Planet. Sci.* **42**, A70.

Huss G. R., Meyer B. S., Srinivasan G., Goswami J. N., and Sahipal S. (2009) Stellar sources of short-lived radionuclides in the early solar system. *Geochim. Cosmochim. Acta.* **73,** 4922-4945.

Huss G. R., Tachibana S., Nagashima K., and Telus M. (2010a) Development of multi-collection Ni isotopic analysis of ferromagnesian silicates in the ion microprobe (abstract #1567). 41st Lunar and Planetary Science Conference. CD-ROM.

Huss G. R., Tachibana S., Nagashima K. and Telus M. (2010b) Development of routine multi-collection Ni isotopic analysis of Fe-rich silicates by ion microprobe (abstract). *Meteoritics & Planetary Science* **45**, A87.

Huss G. R., Ogliore R. C., Nagashima K., Telus M., Jilly C. E. (2011) Dangers of determining isotope ratios using means of individual ratios (abstract #2608). 42nd Lunar and Planetary Science Conference. CD-ROM.

Hutcheon I. D. and Olsen E. (1991) Cr isotopic composition of differentiated meteorites: A search for ^{53}Mn (abstract #1353). 22nd Lunar and Planetary Science Conference. CD-ROM.

Ito M. and Ganguly J. (2006) Diffusion kinetics of Cr in olivine and ^{53}Mn–^{53}Cr thermochronology of early solar system objects. *Geochim. et Cosmochim. Acta* **70**, 799–809.

Ito M. and Messenger S. R. (2010) Thermal metamorphic history of a Ca, Al-rich inclusion constrained by high spatial resolution Mg isotopic measurements with NanoSIMS 50L. *Meteorit. Planet. Sci.* **45**, 583-595.

Jacobsen B., Yin Q.-Z., Moynier F., Amelin Y., Krot A. N., Nagashima K., Hutcheon I. D., and Palme H. 2008. ^{26}Al-^{26}Mg and ^{207}Pb-^{206}Pb systematics of Allende CAIs: Canonical solar initial ^{26}Al/^{27}Al ratio reinstated. *Earth & Planetary Science Letters* **272**, 353–364.

Jilly C. E., Huss G.R., Krot A. N., Nagashima K., Yin Q.-Z., Sugiura N. (2014) ^{53}Mn-^{53}Cr dating of aqueously formed carbonates in the CM2 lithology of the Sutter's Mill carbonaceous chondrite. *Meteorit. Planet. Sci.* **49**, 2104-2117

Kastner J. H. and Myers P. C. (1994) An observational estimate of the probability of encounters between mass-losing evolved stars and molecular clouds. *Astrophys. J.* **421**, 605–614.

Kessel R., Beckett J. R., and Stolper E. M. (2007). The thermal history of equilibrated ordinary chondrites and the relationship between textural maturity and temperature. *Geochim. Cosmochim. Acta* **71**, 1855–1881.

Kita N. T., Nagahara H., Togashi S., and Morishita Y. (2000) A short duration of chondrule formation in the solar nebula: evidence from ^{26}Al in Semarkona ferromagnesian chondrules. *Geochim. Cosmochim. Acta* **64**, 3913–3922.

Kita N. T. and Ushikubo T. (2012) Evolution of protoplanetary disk inferred from ^{26}Al chronology of individual chondrules. *Meteorit. Planet. Sci.* **47**, 1108-1119.

Kleine T., Touboul M., Van Orman J. A., Bourdon B., Maden C., Mezger K., and Halliday A. N. (2008) Hf–W thermochronometry: Closure temperature and constraints on the accretion and cooling history of the H chondrite parent body. *Earth & Planetary Science Letters* **270**, 106–118.

Kleine T., Touboul M., Bourdon B., Nimmo F., Mezger K., Palme H., Jacobsen S. B., Yin Q.-Z. and Halliday A. N. (2009) Hf-W chronology of the accretion and early evolution of asteroids and terrestrial planets. *Geochim. et Cosmochim. Acta* **73**, 5150–5188.

Klinger L. and Rabkin E. (1999) Beyond the Fisher model of grain boundary diffusion: Effect of structural inhomogeneity in the bulk. *Acta Mater* **47,** 725-734.

Kovach H. A. and Jones R. H. (2010) Feldspar in type 4-6 ordinary chondrites: Metamorphic processing on the H and LL chondrite parent bodies. *Meteoritics & Planetary Science* **45**, 246–264.

Krot T. V., Goldstein J. I., Scott E. R. D., and Wakita S. (2012) Thermal histories of H3-6 chondrites and their parent asteroid from metallographic cooling rates and cloudy taenite dimensions. (abstract) *Meteorit. Planet. Sci.* **47**, A232.

Larsen K. K., Trinquier A., Paton C., Schiller M., Wielandt D., Ivanova M. A., Connelly J. N., Nordlund Ö., Krot A. N., and Bizzarro M. (2011) Evidence for magnesium isotope heterogeneity in the solar protoplanetary disk. *The Astrophysical Journal* **735**, L37.

LaTourrette T. and Wasserburg G. J. (1998) Mg diffusion in anorthite: implication for the formation of early solar system planetesimals. *Earth & Planetary Science Letters* **158**, 91–108.

LaTourrette T., Hutcheon I. D. (1999) Mg diffusion in mellilite: Thermal histories for CAIs and their parent bodies. (abstract #2003) 30th Lunar and Planetary Science Conference. CD-ROM.

Limongi M. and Chieffi A. (2006) Nucleosynthesis of ^{60}Fe in massive stars. *New Astron. Rev.* **50**, 474–476.

Ludwig, K. R. (2006) ISOPLOT/Ex ver. 3.50. A Geochronological Toolkit for Microsoft Excel.

Lugmair G. W. and Shukolyukov A. (1998) Early solar system timescales according to ^{53}Mn-^{53}Cr systematics. *Geochimica et Cosmochimica Acta* **62**, 2863-2886.

MacPherson G. J. and Huss G. R. (2001) Extinct ^{10}Be in CAIs from Vigarano, Leoville, and Axtell (abstract #1882). 32nd Lunar and Planetary Science Conference. CD-ROM.

MacPherson G. J., Huss G. R. and Davis A. M. (2003) Extinct ^{10}Be in Type A CAIs from CV chondrites. *Geochimica et Cosmochimica Acta* **67**, 3165-3179.

Makide K., Nagashima K., Krot A. N., Hutcheon I. D., and Bischoff A. (2009) Oxygen- and magnesium-isotope compositions of calcium-aluminum-rich inclusions from CR2 carbonaceous chondrites. *Geochimica et Cosmochimica Acta* **73**, 5018–5050.

Mare E. R., Tomkins A. G., and Godel B. M. (2014) Restriction of parent body heating by metal-troilite melting: Thermal models for the ordinary chondrites. *Meteorit. Planet. Sci.* **49**, 636-651.

Mishin Y. and Herzig Chr. (1999) Grain boundary diffusion: recent progress and future research. *Mater. Sci. Eng.* **A260**, 55-71.

Mishra R. K., Goswami J. N., Tachibana S., Huss G. R., and Rudraswami N. G. (2009) Fe-Ni and Al-Mg isotope systematics in chondrules from unequilibrated ordinary chondrites (abstract #1689). 40th Lunar and Planetary Science Conference. CD-ROM.

Mishra R. K., Goswami J. N., Tachibana S., Huss G. R., and Rudraswami N. G. (2010) Evidence in chondrules for contemporaneous injection of ^{26}Al and ^{60}Fe of stellar origin into the nascent solar system. *Astrophysical Journal* **714**, L217-L221.

Mishra R. K. and Goswami J. N. (2014) Fe–Ni and Al–Mg isotope records in UOC chondrules: Plausible stellar source of ^{60}Fe and other short-lived nuclides in the early Solar System. *Geochim et Cosmochim Acta* **132**, 440–457.

Mishra R. K. and Chaussidon M. (2014) Fossil record of high level of ^{60}Fe in chondrules from unequilibrated chondrites. *Earth. Planet. Sci. Lett.* **398**, 90-100.

Mittlefehldt DW (1994) The genesis of diogenites and HED parent body petrogenesis. *Geochim et Cosmochim Acta* **58**, 1537–1552.

Miyamoto M., Fujii N., and Takeda H. (1981) Ordinary chondrite parent body: An internal heating model. *Proceedings of the Lunar & Planetary Science Conference* **12B**, 1145–1152.

Monnereau M., Toplis M. J., Baratoux D., and Guignard J. (2013) Thermal history of the H-chondrite parent-body: Implications for metamorphic grade and accretionary time-scales. *Geochim. Cosmochim. Acta* **119**, 302–321.

Moskovitz N. and Gaidos E. (2011) Differentiation of planetesimals and the thermal consequences of melt migration. *Meteorit. Planet. Sci.* **46**, 903-918.

Mostefaoui S., Lugmair G. W., Hoppe P. and El Goresy A. (2003) Evidence for live ^{60}Fe in Semarkona and Chervony Kut: A NanoSIMS study (abstract #1585). 34th Lunar and Planetary Science Conference. CD-ROM.

Mostefaoui S., Lugmair G. W., Hoppe P. and El Goresy A. (2004) Evidence for live ^{60}Fe in meteorites. *New Astronomy Reviews* **48**, 155-159.

Mostefaoui S., Lugmair G. W., and Hoppe P. (2005) Fe-60: A heat source for planetary differentiation from a nearby supernova explosion. *Astrophysical Journal* **625**, 271-277.

Newville M. (2013) Larch: An analysis package for XAFS and related spectroscopies. *J. Phys.: Conf. Ser.* **430**, 012007.

Nyquist L.E., Kleine T., Shih C.-Y. and Reese Y.D. (2009) The distribution of short-lived radioisotopes in the early solar system and the chronology of asteroid accretion, differentiation, and secondary mineralization. *Geochim. Cosmochim. Acta.* **73,** 5115-5136.

Ogliore R. C., Huss G. R., and Nagashima K. (2011) Ratio estimation in SIMS analysis. *Nuclear Instruments and Methods in Physics Research B: Beam Interactions with Materials and Atoms.* **269**, 1910–1918.

Ouellette N., Desch S. J., Bizzarro M., Boss A. P., Ciesla F., Meyer B. (2009) Injection mechanisms of short-lived radionuclides and their homogenization. *Geochim. Cosmochim. Acta* **73**, 4946–4962.

Paterson, D., de Jonge, M. D., Howard, D. L., Lewis, W., McKinlay, J., Starritt, A., Kusel, M., Ryan, C. G., Kirkham, R., Moorhead, G., Siddons, D. P. (2011) The X-ray fluorescence microscopy beamline at the Australian Synchrotron. *AIP Conf. Proc.* **1365**, 219−222.

Pearson K., (1910) On the constants of index-distributions as deduced from the like constants for the components of the ratio, with special reference to the opsonic index, Biometrika **7**, 531–541.

Pellas P., and Storzer D. (1981) ^{244}Pu fission-track thermometry and its application to stony meteorites. *Proceedings of the Royal Society of London.* **374**, 253–270.

Petry C., Chakraborty S., Palme H. (2004) Experimental determination of Ni diffusion coefficients in olivine and their dependence on temperature, composition, oxygen fugacity, and crystallographic orientation. *Geochim. Cosmochim. Acta* **68**, 4179-4188.

Quitté G., Markowski A., Latkoczy C., Gabriel A. and Pack A. (2010) Iron-60 heterogeneity and incomplete isotope mixing in the early solar system. *Astrophys. J.* **720**, 1215-1224.

Quitté G., Latkoczy C., Schonbachler M., Halliday A. N. and Gunther D. (2011) ^{60}Fe-^{60}Ni systematics in the eucrite parent body: A case study of Bouvante and Juvinas. *Geochim. Cosmochim. Acta* **75**, 7698-7706.

Rugel G., Faestermann T., Knie K, Korschinek G., Poutivtsev M., Schumann D., Kivel N., Günther-Leopold I., Weinreich R., and Wohlmuther M. (2009) New measurement of the ^{60}Fe half-life. *Physical Review Letters* **103**, 072502.

Ryan C. G., Cousens D. R., Sie S. H., and Griffin W. L (1990) Quantitative-analysis of PIXE spectra in geoscience applications. *Nucl. Instrum. Methods. Phys. Res. B,* **49**, 271-276.

Ryan C. G. (2001) Developments in dynamic analysis for quantitative PIXE true elemental imaging. *Nucl. Instrum. Methods. Phys. Res. B* **181**, 170-179.

Ryan C. G. (2010) The Maia 384 detector array in a nuclear microprobe: A platform for high definition elemental imaging. *Nucl. Instrum. Methods. Phys. Res. B* **268**, 1899-1902.

Scott E. R. D. and Rajan R. S. (1981) Metallic minerals, thermal histories, and parent bodies of some xenolithic, ordinary chondrites. *Geochimica et Cosmochimica Acta* **45**, 53–67.

Scott E. R. D., Mandell D., Yang J., Goldstein J. I., Krot T. and Taylor G. J. (2010) Metamorphism and impacts on the parent asteroid of H-chondrites. (abstract #1529) 41st Lunar and Planetary Science Conference. CD-ROM.

Scott E. R. D., Krot T.V., Goldstein J. I. and Wakita S. (2014) Thermal and impact history of the H-chondrite parent asteroid during metamorphism: constraints from metallic Fe-Ni. *Geochim. Cosmochim. Acta* **136**, 13-37.

Shukolyukov A. and Lugmair G. W. (1993a) Live Iron-60 in the early Solar System. *Science* **259**, 1138-1142.

Shukolyukov A. and Lugmair G. W. (1993b) ^{60}Fe in eucrites. *Earth. Planet. Sci. Lett.* **119**, 159-166.

Spivak-Birndorf L. J., Wadhwa M. and Janney P. E. (2011) ^{60}Fe-^{60}Ni chronology of the D'Orbigny angrite: Implications for the initial solar system abundance of ^{60}Fe (abstract #2281) 42nd Lunar and Planetary Science Conference. CD-ROM.

Spivak-Birndorf L. J., Wadhwa M., and Janney P. E. (2012a) ^{60}Fe-^{60}Ni systematics of Chainpur chondrules and the plutonic angrites Northwest Africa 4590 and 4801 (abstract #2861) 43rd Lunar and Planetary Science Conference. CD-ROM.

Spivak-Birndorf L. J., Wadhwa M., and Janney P. E. (2012b) The ^{60}Fe-^{60}Ni systematics of chondrules from unequilibrated ordinary chondrites. (abstract #5365) *Meteorit. Planet. Sci.* **47**, A355.

Tachibana S., and Huss G. R. (2003) Iron-60 in troilites from an unequilibrated ordinary chondrite and the initial ^{60}Fe/^{56}Fe in the early solar system (abstract #1737). 34th Lunar and Planetary Science Conference. CD-ROM.

Tachibana S. and Huss G. R. (2003) The initial abundance of ^{60}Fe in the early solar system. *Astrophysical Journal* **588**, L41-L44.

Tachibana S., Huss G. R., Kita N. T., Shimoda H. and Morishita Y. (2005) The abundances of iron-60 in pyroxene chondrules from unequilibrated ordinary chondrites (abstract #1529). 36th Lunar and Planetary Science Conference. CD-ROM.

Tachibana S., Huss G. R., Kita N. T., Shimoda G., and Morishita Y. (2006) ^{60}Fe in chondrites: debris from a nearby supernova in the early solar system? *Astrophysical Journal* **639**, L87-L90.

Tachibana S., Huss G. R. and Nagashima K. (2007) ^{60}Fe-^{60}Ni systems in ferromagnesian chondrules in least equilibrated ordinary chondrites (abstract #1709). 38th Lunar and Planetary Science Conference. CD-ROM.

Tachibana S., Huss G. R., and Nagashima K. (2009) Ion microprobe study of ^{60}Fe-^{60}Ni system in ferromagnesium pyroxene chondrules in Krymka (LL3.1) by multicollection (abstract #1808). 40th Lunar and Planetary Science Conference. CD-ROM.

Takigawa A., Miki J., Tachibana S., Huss G.R., Tominaga N., Umeda H., and Nomoto K. (2008) Injection of short-lived radionuclides from a faint mixing-fallback supernova into the early solar system. *Astrophys. J.* **688,** 1383-1387.

Tang H. and Dauphas N. (2012a) Abundance, distribution, and origin of ^{60}Fe in the solar protoplanetary disk. *Earth Planet. Sci. Lett.* **359-360**, 248-263.

Tang H. and Dauphas N. (2012b) Low abundance and homogeneous distribution of 60Fe in the early solar system. (abstract #1703). 43rd Lunar and Planetary Science Conference. CD-ROM.

Tang H. and Dauphas N. (2015) Low ^{60}Fe abundance in Semarkona and Sahara 99555. *Astrophys. J.* **802**, 22**.**

Taylor G. J., Maggiore P., Rubin A. E., Scott E. R. D., and Keil K. (1987) Original structures, and fragmentation and reassembly history of asteroids: Evidence from meteorites. *Icarus.* **69**, 1–13.

Telus M., Huss G. R., Nagashima K., Ogliore R. C., Tachibana S. and Jilly C. E. (2011a) Possible heterogeneity of ^{60}Fe in chondrules from primitive ordinary chondrites (abstract #2559). 42nd Lunar and Planetary Science Conference. CD-ROM.

Telus, M., Huss G. R., Tachibana S., and Goswami J. (2011b) The initial abundance of ^{60}Fe in the inner solar system: evidence from chondrules (abstract #9127). Workshop on Formation of the First Solids in the Solar System.

Telus M., Huss G. R., Nagashima K. and Ogliore R. C. (2011c) ^{60}Fe-^{60}Ni analysis of porphyritic chondrules from primitive ordinary chondrites (abstract #5489). *Meteoritics & Planetary Science* **46**, A232.

Telus M., Huss G. R., Ogliore R. C., Nagashima K., and Tachibana S. (2012a) Recalculation of data for short-lived radionuclide systems using less-biased ratio estimation. *Meteorit. Planet. Sci.* **47**, 2013–2030.

Telus M., Huss G. R., Nagashima K., Ogliore R. C., and Tachibana S. (2012b) Reevaluating our understanding of the ^{60}Fe-^{60}Ni system in chondrites (abstract #2733). 43rd Lunar and Planetary Science Conference. CD-ROM.

Telus M., Huss G. R., Nagashima K., and Ogliore R. C. (2012c) A test of possible ratio bias in ^{26}Al-^{26}Mg measurements of plagioclase from the H4 chondrite, Ste. Marguerite. *Meteorit. Planet. Sci.* **47** (abstract #5364).

Telus M., Huss G. R., Nagashima K., and Ogliore R. C. (2013a) Initial abundance of ^{60}Fe in unequilibrated ordinary chondrites (abstract #2964). 44th Lunar and Planetary Science Conference. CD-ROM.

Telus M., Huss G. R., Nagashima K., Ogliore R. C., Chen J. H., and Papanasstassiou D. A. (2013b) ^{60}Fe-^{60}Ni systematics of chondrules from UOC QUE 97008: Comparing results from *in situ* and bulk analyses. *Meteorit. Planet. Sci.* **48** (abstract #5294).

Telus M., Huss G. R., Nagashima K., and Ogliore R. C. (2014a) Revisiting ^{26}Al-^{26}Mg systematics of H4 chondrites. *Meteorit. Planet. Sci.* **49**, 929–945.

Telus M., Huss G. R., Ogliore R. C., Nagashima K. (2014b) ^{26}Al-^{26}Mg systematics of plagioclase in H4 chondrites: Implications for the H-chondrite parent body (abstract #2697). 45th Lunar and Planetary Science Conference. CD-ROM.

Telus M., Huss G. R., Ogliore R. C., Nagashima K., and Tomkins A. (2014c) Synchrotron XRF mapping of Fe, Ni and other elements in UOC chondrules: Implications for interpreting ^{60}Fe-^{60}Ni data (abstract #2559). 45th Lunar and Planetary Science Conference. CD-ROM.

Telus M., Huss G. R., Ogliore R. C., and Nagashima K. (2014d) Synchrotron XRF Fe and Ni mapping and Ni XANES of UOC chondrules: Implications for ^{60}Fe-^{60}Ni analyses. *Meteorit. Planet. Sci.* **49**, (abstract #5431).

Telus M., Huss G. R., Ogliore R. C., Nagashima K., Howard D. L., Newville M. G. and Tomkins A. G. (2015a) Mobility of iron and nickel at low temperatures and

implications for ^{60}Fe-^{60}Ni systematics of UOC chondrules. *Geochim. Cosmochim. Acta. (**submitted**).*

Telus M., Huss G. R., Nagashima K., and Ogliore R. C. (2015b) The ^{60}Fe-^{60}Ni systematics of UOC chondrules, open-system redistribution compromises its usefulness (abstract #2550). 46th Lunar and Planetary Science Conference. CD-ROM.

Telus M., Huss G. R., Nagashima K., Ogliore R. C. and Tachibana S (2015c) In situ ^{60}Fe-^{60}Ni systematics of UOC chondrules. *Geochim Cosmochim Acta (**in preparation**).*

Tomiyama T. and Huss G. R. (2005) Minor element behavior of pallasite olivine: understanding pallasite thermal history and chronology (abstract #2071). 36th Lunar and Planetary Science Conference. CD-ROM.

Tomiyama T., Huss G. R., Nagashima K. and Krot A. N. (2007) Ion microprobe analysis of ^{53}Mn-^{53}Cr systematics of pallasite olivines using the Cameca ims 1280 ion microprobe (abstract #2007). 38th Lunar and Planetary Science Conference. CD-ROM.

Trieloff M., Jessberger E. K., Herrwerth I., Hopp J., Fiéni C., Ghélis M., Bourot-Denise M. and Pellas P. (2003) Structure and thermal history of the H-chondrite parent asteroid revealed by thermochronometry. *Nature* **422**, 502–506.

Trinquier A., Birck J. -L., Allegre C. -J., Göpel C. and Ulfbeck D. (2008) ^{53}Mn-^{53}Cr systematics of the early solar system revisited. *Geochim. Cosmochim. Acta* **72**, 5146–5163.

Van Orman J. A., Cherniak D. J., and Kita N. T. (2014) Magnesium diffusion in plagioclase: Dependence on composition, and implications for thermal resetting of

the ^{26}Al-^{26}Mg early solar system chronometer. *Earth & Planetary Science Letters* **385**, 79-88.

Van Schmus W. R. and Wood J. A. (1967) A chemical-petrologic classification for the chondritic meteorites. *Geochimica et Cosmochimica Acta* **31**, 747–765.

Wang W., Harris M. j., Diehl R., Halloin H., Cordier B., Strong A. W., Kretschmer K., Knödlseder J., Jean P., LIchti G. G., Roques J. P., Schanne S., von Kienlin A.,Weidenspointener G. and Wunderer C. (2007) SPI observations of the diffuse ^{60}Fe emission in the galaxy. *Astron. Astrophys.* **469**, 1005–1012.

Wasserburg G. J., Busso M., Gallino R. and Nollett K. M. (2006) Short-lived nuclei in the early solar system: possible AGB sources. *Nuc. Phys. A* **777**, 5–69.

Wyatt M. C. (2008) Evolution of debris disks. *Annu. Rev. Astron. Astrophys.* **46**, 339–83

Williams J. P. and Gaidos E. (2007) On the likelihood of supernova enrichment of protoplanetary disks. *Astrophys. J.* **663**, L33–L36.

Williams, J. P. (2010) The astrophysical environment of the solar birthplace. *Contemporary Physics*, **51**, 381 – 396.

Wlotzka F. (2005) Cr spinel and chromite as petrogenetic indicators in ordinary chondrites: equilibration temperatures of petrologic types 3.7 to 6. *Meteorit. Planet. Sci.* **40**, 1673–1702.

Wood J. A. (1967) Chondrites: their metallic minerals, thermal histories, and parent planets. *Icarus* **6**, 1–49.

York D. (1966) Least-squared fitting of a straight line. Canadian Journal of Physics **44**, 1079-1086.

Zinner E. and Göpel C. (1992) Evidence for ^{26}Al in feldspars from the H4 chondrite Ste. Marguerite. (abstract) *Meteorit. Planet. Sci.* **27**, 311–312.

Zinner E., Hoppe P., and Lugmair G. W. (2002) Radiogenic ^{26}Mg in Ste. Marguerite and Forest Vale plagioclase: Can ^{26}Al be used as chronometer? (abstract #1204). 33rd Lunar and Planetary Science Conference. CD-ROM.

Zinner E. and Göpel C. (2002) Aluminum-26 in H4 chondrites: Implications for its production and its usefulness as a fine-scale chronometer for early solar system events. *Meteorit. Planet. Sci.* **37**, 1001–1013.